Inherently Elastic Actuation for Soft Robotics

By

CHONGJING CAO

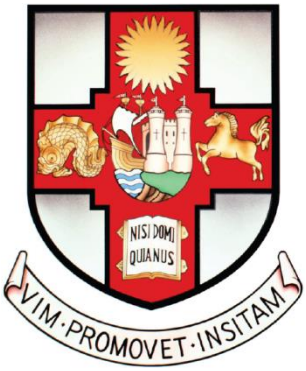

Department of Aerospace Engineering

UNIVERSITY OF BRISTOL

Department of Engineering Design and Mathematics

UNIVERSITY OF THE WEST OF ENGLAND

A dissertation submitted to the University of Bristol in accordance with the requirements for award of the degree of *Doctor of Philosophy* in the Faculty of Engineering.

July 2019.

Word count: FIFTY THOUSAND AND EIGHT

Author's Declaration

I declare that the work in this dissertation was carried out in accordance with the requirement of the University's *Regulations and Code of Practice for Research Degree Programmes* and that it has not been submitted for any other academic award. Except where indicated by specific reference in the text, the work is the candidate's own work. Work done in collaboration with, or with the assistance of, others, is indicated as such. Any views expressed in the dissertation are those of the author.

SIGNED:_____ DATE:_____

Acknowledgement

First and foremost, I want to sincerely thank my family for their mental and financial support throughout my PhD study in the UK. Without your support, this PhD could not have come true.

I am grateful for my supervisor Dr Andrew Conn for his dedicated support, enthusiasm and proofreading of all my papers and this thesis. I would like to thank Prof. Stuart Burgess for all the inspiration and valuable discussion in the flapping wing project. I am thankful to Dr Tom Hill for sharing with me his insights in nonlinear dynamics and all these successful collaborations.

The support and collaboration of the Soft Lab members means a lot for me and this thesis. I would like to specially thank my good friend Dr Krishna Manaswi Digumarti for the exchange in ideas all these years and the great moments on the collaboration for RoboSoft conference 2018. I would like to thank Dr Xing Gao for the collaborations on the EA-DEO gripper, MCDEA concept and pump designs. Thank you for insisting on the original ideas when being questioned and thank you for the enthusiasm when frustrating failures were encountered. I would also like to thank Dr Jianglong Guo, Dr Chaoqun Xiang and Mr Richard Suphapol Diteesawat for their collaborations in different projects. I appreciate the Bristol Robotics Lab for offering such a great working environment.

As a FARSCOPE CDT student, I am grateful for this wonderful programme and friendly community.

Last but certainly not least, I want to have a special thank to my lovely girlfriend Jing Li, who has been helping me passing the lowest moments of my PhD research and constantly kicking my butt to meet numerous deadlines.

Abstract

Dielectric elastomer actuators (DEAs) are an emerging type of soft actuators that have the attractive features of large actuation strains, fast response speed, and high energy density.

Soft robotics is a rapidly growing research field that seeks solutions to reduce the complexity of safely interacting with environments. In contrast to rigid robots, soft robots utilize soft materials such as silicone rubber that can deform when interacting with unknown environments. The compliance nature of DEAs makes it ideal for soft robotics.

However, despite the development of DEAs for two decades, the inherent elasticity of the dielectric elastomer has been long overlooked as a resource for improved efficiency, higher work output and resonant operation. In this work, the author investigates the principles of utilising the elasticity in DEAs and develop high performing DEAs that uses these principles for soft and bioinspired robotics.

This study is built on a comprehensive electromechanical dynamic model of generalized cone DEAs and three different configuration variations: (i) circular and planar dielectric elastomer oscillator (DEO), (ii) double cone dielectric elastomer actuators (DCDEAs), (iii) magnetically coupled dielectric elastomer actuators (MCDEAs). For each configuration, its dynamic response is analysed in-depth and physical insights are drawn with the generalized cone DEA model and experiments.

Based on the cone DEA configuration, different elastic actuation principles for different dielectric elastomer materials are proposed. For Very-High-Bond (VHB) acrylic material with high viscoelasticity, the elastic actuation is demonstrated by recovery of elastic energy via a reduced the actuation duty ratio which enables the elastic energy stored in the membranes to contribute to work output. For silicone material with low viscosity, the elastic actuation is demonstrated by driving the DEA at its resonance which amplifies the stroke/power output.

By using the three DEA configurations, along with the two elastic actuation strategies, applications that demonstrate the feasibility and clear advantage of inherently elastic actuation and the use of DEAs in soft/bioinspired robotics are developed.

Based on large out-of-plane resonant actuation of the DEO, a monolithic electroadhesion (EA) – DEO soft gripper is developed to overcome the slow de-adhesion issue of conventional EA grippers. The performance of the EA-DEO gripper is tested against different lightweight and flexible materials. By using the resonant actuation of the DEO, the release speeds of the gripper are sped up from several minutes to 100s of milliseconds, which demonstrates at least two orders of magnitude of improvement.

A bioinspired robotic leg and flapping wing mechanism driven by the DCDEA elastic artificial muscles are presented which utilizes the elastic energy recovery principle and resonant actuation principle

respectively. For the flapping wing mechanism, a peak flapping stroke of 31˚ at the resonant frequency of 30 Hz is reported, which far outperforms previously published DEA driven flappers.

Finally, the first DEA driven pneumatic pump by using the MCDEA developed in this work is proposed. A proof-of-concept prototype has a 40 mm diameter and 30 mm height. This pump design exhibits a peak pressure output of 30.5 mbar and flowrate of 0.9 SLPM at the resonance of the driving DEA with a low power consumption of 40 mW.

The inherently elastic actuation of DEAs demonstrated in this thesis shows the clear advantage of applying it for soft and bioinspired robotics applications.

Table of acronyms

CG	Carbon Grease
DCDEA	Double Cone Dielectric Elastomer Actuator
DEA	Dielectric Elastomer Actuator
DEMES	Dielectric Elastomer Minimum Energy Structure
DEO	Dielectric Elastomer Oscillator
DOF	Degree of Freedom
EA	Electro-Adhesion
EAP	Electro-Active Polymer
FEA	Fluidic Elastomer Actuator
IPMC	Ionic-Polymer/Metal Composites
MCDEA	Magnetically Coupled Dielectric Elastomer Actuator
SMA	Shape Memory Alloy
VHB	Very-High-Bond

Notation

a	Radius of the central disk in cone DEAs
A	DEA electrode area
b	Inner radius of the support ring in cone DEAs
C	Capacitance of the DEA
D	Electric displacement
d	Out-of-plane displacement of DEA membranes
E	Electric field
E_{in}	Energy input into the DEA
E_k	Kinetic energy
E_s	Elastic strain energy
F	Force
f	Excitation frequency of the DEA
F_e	Helmholtz free energy in a dielectric elastomer actuator system
f_r	Response frequency of the DEA
f_{rs}	Resonant frequency of the DEA
g	Gravitational acceleration
H	Elastomer membrane thickness
h	Distance between two DEA frames
i	Current
J	Constant related to the limit stretch
K	Constant in magnetic repulsion model
L	Rod length
$L_{1,2,3}$	Dimension of an undeformed piece of DEA
$l_{1,2,3}$	Dimension of a deformed piece of DEA
m	Mass

p	Electrostatic (Maxwell) pressure
P_l	Equivalent parallel resistance of the DEA
P_{out}	Power output of a DEA
P_x, P_y	Force in x and y direction on the ideal dielectric elastomer membrane
Q	Electrical charge
$\dot{Q}$	Rate of change in electrical charge
R_s	Equivalent surface resistance of the DEA
v	Velocity
Vol	Volume of the DEA
W	Helmholtz free energy density of the dielectric elastomer actuator system
W_{out}	Work output of the DEA
α	Angle between out-of-plane deformed membrane and the horizontal reference plane
β	Ogden model parameter
θ	Phase difference between two signals
ε	Dielectric constant
η_{em}	Electromechanical efficiency of the DEA
$\lambda_{1,2,3}$	Principle stretches in 1, 2, 3 axes
μ	Shear modulus
ξ	Strain on dashpot
$\sigma_{1,2,3}$	True stresses in 1, 2, 3 axes
Φ	Voltage

Parts of this work have been published in the following papers:

JOURNAL PUBLICATIONS

- **Cao, C**., Gao, X., Burgess, S. and Conn, A.T. Power optimization of a double cone dielectric elastomer actuator for resonating robotic systems. *Extreme Mechanics Letters*. (under review)
- **Cao, C**., Hill, T.L., Conn, A.T. Li, B. and Gao, X. Nonlinear dynamics of a magnetically coupled dielectric elastomer actuator. *Physical Review Applied*. (Accepted/In-press)
- **Cao, C**., Gao, X. and Conn, A.T., 2019. Towards efficient elastic actuation in bio-inspired robotics using dielectric elastomer artificial muscles. *Smart Materials and structures*. 28(9) p.095015.
- **Cao, C**., Hill, T.L. and Conn, A.T., 2019. On the nonlinear dynamics of a circular dielectric elastomer oscillator. *Smart Materials and Structures*. 28(7) p. 075020.
- **Cao, C**., Gao, X. and Conn, A.T., 2019. A magnetically-coupled dielectric elastomer pump for soft robotics. *Advanced Materials Technologies*. 4(8) p.1900128.
- **Cao**, C., Gao, X., Guo, J. and Conn, A.T., 2019. De-electroadhesion of flexible and lightweight materials: an experimental study. *Applied Sciences*. 9(14) p.2796.
- **Cao, C**., Burgess, S. and Conn, A.T., 2019. Towards a dielectric elastomer resonator driven flapping wing micro air vehicle. *Frontiers in Robotics and AI*. 5 p.137.
- **Cao, C**., Gao, X. and Conn, A.T., 2019. A compliantly coupled dielectric elastomer actuator using magnet repulsion. *Applied Physics Letters*. 114(1) p.011904.
- Gao, X., **Cao, C. (joint first author)**, Guo, J. and Conn, A.T., 2019. Elastic electroadhesion with rapid release by integrated resonant vibration. *Advanced Materials Technologies*. 4(1) p.1800378.
- **Cao, C**. and Conn, A.T., 2018, June. Performance Optimization of a Conical Dielectric Elastomer Actuator. *Actuators.* 7(2) p. 32.

INTERNATIONAL CONFERENCE PROCEEDINGS

- **Cao, C**., Gao, X. and Conn, A.T., 2019, March. Contactless coupling of dielectric elastomer membranes with magnetic repulsion. In Electroactive Polymer Actuators and Devices (EAPAD) XXI. International Society for Optics and Photonics.
- **Cao, C**., Diteesawat, R.S, Rossiter, J., and Conn, A.T., 2019, April. A reconfigurable crawling

robot driven by electroactive artificial muscle. In 2019 IEEE International Conference on Soft Robotics (RoboSoft). IEEE.

- **Cao, C**., Burgess, S. and Conn, A.T., 2018, April. Flapping at resonance: Realization of an electroactive elastic thorax. In 2018 IEEE International Conference on Soft Robotics (RoboSoft). IEEE.
- Digumarti, K.M., **Cao, C (joint first author)**., Guo, J., Conn, A.T. and Rossiter, J., 2018, April. Multi-directional crawling robot with soft actuators and electroadhesive grippers. In 2018 IEEE International Conference on Soft Robotics (RoboSoft). IEEE.
- **Cao, C**. and Conn, A.T., 2017, April. Elastic actuation for legged locomotion. In Electroactive Polymer Actuators and Devices (EAPAD). International Society for Optics and Photonics.

POSTER PRESENTATIONS

- **Cao, C**., Gao, X. and Conn, A.T., A dielectric elastomer actuator driven pneumatic pump for soft robotics, in EuroEAP 2019, June, Dresden, Germany.
- **Cao, C**., Gao, X. and Conn, A.T., A dielectric elastomer actuator driven pneumatic pump for soft robotics, in IEEE International Conference on Soft Robotics (RoboSoft) 2019, April, Seoul, Korea.
- **Cao, C**. Towards elastic actuation for legged and aerial locomotion. (presentation + poster). In 2017 CDT Conference for Bristol, Edinburgh and Oxford Robotics CDT Students. 7th June 2017. Lady Margaret Hall, Oxford.
- **Cao, C**. Dielectric elastomer actuators as artificial muscles in locomotion (presentation). In Joint Industry and Robotics CDT Symposium (JIRCS) 2018. 4th – 5th June. 2018. UWE Bristol Exhibition and Conference Centre (ECC).
- **Cao, C**. and Conn, A.T., Elastic actuation for legged locomotion, in SPIE, Electroactive Polymer Actuators and Devices (EAPAD) 2017, March, Portland, Oregon, United States.

Table of Contents

List of Figures

List of Tables

Chapter 1: Introduction

1.1 Motivation

Conventional rigid robots are very successful at performing repeatable tasks with high precision but their application outside of controlled environments such as factories can be challenging due to complexities arising from environmental uncertainty [1]. Another important potential limitation is unsafe human-robot interaction. Such rigid robots in factories are generally designed to move rapidly and/or exert high torques, which can be dangerous when in close contact with people or other fragile objects [2].

Soft robotics is an emerging research field that often seeks solutions from nature to reduce the complexity required for systems to safely interact with the environments. In contrast to rigid robots, soft robots utilize soft materials such as silicone rubber that can deform when interacting with unknown environments. The inherent compliance of the robot design creates the advantages of reduced control complexity, safe interaction with human beings, and the capability to manipulate fragile objects [1] [2] [3]. Soft robotics also offers the advantages of low-cost and reduced fabrication complexity due to the simple structures and reduced number of components.

The growing application of soft robotics demands compliant actuation technologies beyond conventional rigid actuators such as direct current (DC) motors. Several compliant actuators, or so called 'artificial muscles', have been adopted for soft robotics, including shape memory alloys (SMAs), fluidic elastomer actuators (FEAs) and electroactive polymers (EAPs). Dielectric elastomer actuators (DEAs) are a promising soft actuation technology which belongs to a sub-class of EAPs. DEAs response to electrical stimulations and have the advantages of large actuation strains, inherent compliance, high energy density, fast response and high bandwidth, and high electromechanical efficiency [4]. Many applications have been developed by using DEAs, for example,

- robotic locomotion, including terrestrial [5] [6] [7], aquatic [8] [9] and aerial locomotion [10] [11];
- soft grasping and manipulation [12] [13] [14] [15];
- micro fluidic control [16] [17] [18];
- acoustics [19] [20] and optical devices [21] [22] [23].

Despite the research advance in DEAs, as a type of elastomer, the inherent elasticity of the DEAs has not been widely explored. This could be due to the fact that one of the main focuses on DEA research is the accurate position control where the vibration of the DEA system due to the inherent elasticity are usually the objective to be eliminated, see [24] [25] [26] [27] for example. The complex

electromechanical coupling, nonlinearity in the elasticity and the inherent viscoelasticity in the DEA systems [28] also make dynamic modelling and characterization challenging.

On the contrary, in nature, elasticity has been widely explored to minimize the cost of transport and maximize stability. For example, legged animals take advantage of their serial muscle and tendon complex in their limbs and in a running gait, kinetic and gravitational potential energy is stored as elastic energy in tendons in limbs when an animal hits the ground, and then released in the second half of the step. Thus a great percentage of work the muscle otherwise has to do is saved [29]. Most species of flying insects achieve flight by having flight muscles deform the highly elastic thorax and the deformation of the thorax then causes the flapping of the wings. Insects naturally excite this natural muscle-thorax oscillator at its resonant frequency which amplifies the flapping stroke and greatly reduces inertial power demands [30].

Taking inspiration from nature, the use of elasticity in DEAs can potentially improve the efficiency and stability of actuation (mimicking the legged animals) and amplify the power output of a DEA device using resonance (mimicking the flying insects). This thesis aims to develop novel functional DEA configurations based on a well-developed cone DEA structure [31] [32] [33] [34] [35], and investigate the principles of utilizing the inherent elasticity in these DEA systems. To demonstrate the feasibility of using the inherent elastic actuation for soft robotics, for each DEA configuration developed in this thesis, a specific application is demonstrated.

1.2 Aim and objectives

This thesis aims to investigate the principles of the inherent elasticity in dielectric elastomer actuators, understand their dynamics with the use of numerical models and experimental methods and demonstrate the feasibility of using elastic actuation in soft and bioinspired robotics.

The objectives of this thesis are summarized as follows:

- Developing novel configurations of DEAs for soft robotics.
- Developing an electro-mechanical coupled dynamic model to describe the proposed DEAs.
- Optimizing the performance of the proposed DEAs by using the dynamic model and experimental methods.
- Proposing the principles for elastic actuation of the DEAs and developing applications using these proposed principles for soft and bioinspired robotics.

1.3 Thesis Outline

The main objective of this thesis is to explore the use of an inherently elastic actuator for bioinspired soft robotics applications. First, a generalized dynamic modelling framework of cone shaped DEAs is developed which allows the development and characterization of different variations of cone configurations. Based on this model, three different cone configurations are developed and characterized, and applications are demonstrated to take advantage of the high power output at resonance or elastic energy recovery to improve the actuation efficiency or generate novel functionalities. The structure of this thesis and the research methodology employed towards the key contributions of this thesis in Chapter 4 to 7 are summarized in **Figure 1.1**.

- Chapter 2 reviews the state of art of the soft actuation technologies with the focus on shape memory alloys, fluidic elastomer actuators, ionic polymer/metal composites and dielectric elastomer actuators.
- Chapter 3 introduces the actuation principles of dielectric elastomer actuators, reviews state of the art dielectric elastomer materials, compliant electrodes, configurations and applications of DEAs.
- Chapter 4 summarizes the free energy based modelling framework, and based on this framework, a generalized cone DEA dynamic model is developed which can be readily extended for any specific cone DEA designs.
- Chapter 5 develops a novel dielectric elastomer oscillator (DEO) based on the cone DEA structure. It features a low-profile planar configuration and can generate high-amplitude out-of-plane oscillation at resonance. Its dynamic response is characterized by the dynamic model adapted from Chapter 4 and is verified against experiments. A novel soft gripper integrating electroadhesion and the DEO is developed which uses the resonance of the DEO to significantly improve the de-adhesion speed. The evaluation of the proposed gripper on various objects is reported and discussed. Potential practical applications of this gripper are discussed.
- Chapter 6 conducts on in-depth analysis of the energetic performance of double cone DEAs (DCDEAs). Dynamic models for VHB acrylic elastomer and silicone elastomer based DCDEAs are developed and verified against experiments. For VHB acrylic DCDEAs, a novel actuation scheme that utilizes elastic energy recovery at low actuation frequencies is reported. Optimization is performed to maximize the work output of the actuator. A novel bioinspired robotic leg powered by DCDEAs which demonstrates the same elastic energy recovery principle is developed. For silicone elastomer DCDEAs, a resonant actuation scheme is demonstrated to maximize the power output. Based on the resonance actuation scheme, the first DEA driven resonant flapping wing robot is developed and its performance is characterized. Potential improvements and applications of this design are also discussed.

- Chapter 7 reports a novel magnetically coupled DEA (MCDEA) configuration with breaks the restriction of one-degree-of-freedom (DOF) actuation in DCDEAs and allows two separately controlled outputs. A dynamic model is developed based on the generalized cone DEA model in Chapter 4 and is verified against experiments. Its dynamic response is fully characterized using the developed model. The performance of the MCDEA developed in this chapter and the rigidly coupled DCDEA in Chapter 6 are compared and the pros and cons of each configuration are discussed. The first DEA driven soft pneumatic pump is reported and its performance is evaluated. The limitations of conventional rigid pump/compressors are discussed and the state of the art of soft pumping technologies are reviewed. Applications of this novel pneumatic pump in soft robotics are demonstrated.
- Chapter 8 concludes all the results and contributions before discussing future work.

In summary, by taking inspiration from nature, this thesis aims to answer the research question of can the inherent elasticity in dielectric elastomer actuators being exploited for soft and bioinspired robotics with the following methodology. 1. Proposing novel DEA configurations for soft and bioinspired robotics applications. 2. Developing comprehensive DEA model to characterize their behaviours. 3. Proposing strategies for exploiting the elasticity in DEAs. 4. Developing applications in soft/ bioinspired robotics that demonstrate the proposed strategies.

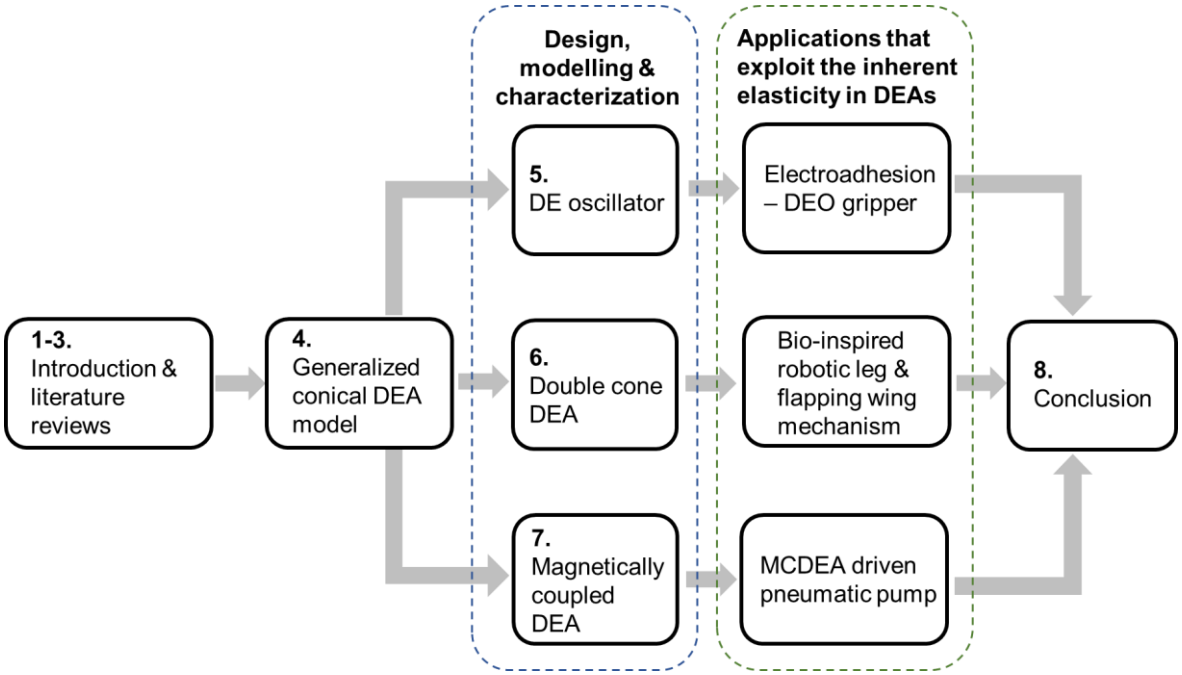

Figure 1.1. Summary of the structure of this thesis, the research methodology and key contributions of this thesis in Chapters 4 - 7.

Chapter 2: Actuation Technologies for Soft Robotics

This chapter reviews and compares different state of the art of actuation technologies for soft robotics. Many types of compliant actuators, sometimes referred to as 'artificial muscles', have been developed. Such artificial muscles can actively deform under an external stimulus such as electric field (electroactive polymers (EAPs)), magnetic field (Terfenol-D), thermal energy (Nylon fibres, shape memory alloys (SMAs), shape memory polymers (SMPs)), light (light responsive polymers) or fluid pressure (McKibben actuators, fluidic elastomer actuators (FEAs)). Several reviews focusing on the artificial muscles, functionalities, applications and limitations [1] [36] [37] [38] have been published. This chapter focuses on the three most commonly used artificial muscles in robotics, which include shape memory alloys, fluidic actuators and electroactive polymers (with the focuses on ionic polymer/metal composites and dielectric elastomer actuators). Other EAPs such as conducting polymers, ionic polymer gels, piezoelectric polymers, liquid-crystal elastomers and recently developed electro-ribbon actuators [39] and hydraulically amplified self-healing electrostatic actuators (HASEL) [40] have not been widely demonstrated for robotics applications and, hence, will not be covered here.

2.1 Shape Memory Alloys

Shape memory alloys (SMAs) represent a class of material that can retain their original form under stimulation. SMAs were originally discovered in 1932 [41] and have been extensively studied and widely adopted in applications such as aerospace, automobile, biomedical, and robotics [42]. The working mechanism of SMAs replies on their transformation between martensite and austenite phases upon thermal stimulation. Nickel-titanium (NiTi) is one of the most popular and widely adopted SMA materials which exhibits greater actuation strains than the other shape memory materials (linear strain of ~ 5 %) [43] [44].

The most common way to actuate SMAs is via Joule heating. Due to the high conductivity of SMAs, when a current is passing through the SMA, resistive heating heats up the alloy to transfer from martensite to austenite phase and causes a contraction in length. The low linear strain of SMAs can be compensated by twisting them to spring coils which have strokes up to 50 % of the nominative length [45]. The thermo heating and cooling process of SMAs limits the actuation bandwidth (< 10 Hz) and the efficiency can be very low due to the heat loss (< 16 %) [36].

SMAs have been widely adopted in robotic designs such as a micro glider robot [46], a micro robotic fish [47], a biomimetic robotic jellyfish [48], a caterpillar-inspired robot, GoQBot, that can crawl and roll [49], and an octopus inspired soft robotic arm [50]. Despite their low actuation bandwidth, SMAs

have a relatively high power-mass density and good scalability, which allow for their use in a series of micro jumping robots in [51] [52].

2.2 Fluidic Actuators

The pneumatic artificial muscle, also known as McKibben actuators, is a type of commercially available pneumatic linear contraction actuator invented in the 1950s [53] [54]. A McKibben actuator consists of a rubber inner tube covered with a flexible but non-stretchable helical weave shell. When the inner tube is pressured and inflated, the weave shell converts the radial expansion into a linear contraction, mimicking the linear contraction motion of muscles. While the design features a simple structure, it restricts potential robotic applications involving more sophisticated behaviours than one degree-of-freedom (DOF) motion [55].

Originally proposed by Koichi Suzumori in 1991 [56], a new type of pneumatic actuators called fluidic elastomer actuators (FEAs) emerged together with the field of soft robotics. Such FEAs consist of a synthetic elastomer structure with a series of embedded channels and chambers. When pressurized, these chambers expand, causing a global deformation of the FEA. The chambers can be arranged to form different patterns and, different constraints can be added to the structure to enable various forms of motion, such as bending, twisting, contraction and extension [2]. One of the most common types of FEA is the PneuNet, which includes a pneumatic network with a flexible but non-stretchable constraint on one side so that the structure is inflated anisotropically, resulting in a bending motion. The structures of FEAs can be modified to enable more functionalities. For example, textured surface of the elastomer can be adopted to improve grasping capability [57]. Origami structures can be moulded with the FEA elastomers to allow an increase in the stiffness and anisotropy of the FEAs while maintaining a lightweight and compact structure [58]. Electrical components such as LEDs can be embedded into the FEAs design to enable simple sensing of the actuation state [58].

FEAs have the advantages of high customizability, low cost, inherent compliance which allows for safe human robot interaction, capability in handling environmental uncertainty, large actuation stroke, lightweight, and good thermodynamic efficiency [1] [2]. However, limitations and drawback of FEAs also exist. The high compliance of the elastomer material makes the modelling and control of such actuators extremely challenging. The compressors, valves, and/or fluid tanks required to power these actuators can be heavy and bulky, which limits the mobility and miniaturization of robots or wearable devices with FEAs. The mismatch in stiffness between the soft elastomer and the rigid pressurization components limits the true potential for a completely soft robotic system in computational morphology and interaction with the environment and human beings.

Nevertheless, with the rapid growth of soft robotics, FEAs have been widely utilized in robotic manipulation applications such as soft robotic arms [57] [58] and hands for dexterous grasping [59] [60]. The inherent compliance of FEAs provide an adaptable morphology which is ideal for soft wearable devices for rehabilitation, as demonstrated in [61] [62] [63] [64]. FEAs have also been used in robotic locomotion including soft crawling robot [65] with impressive resilience over mechanical impact and thermal tolerance, a soft robotic fish with great maneuverability [66] and a soft EuMoBot that mimics the motion of euglenoid movement [67]. By pumping fluids with the same colours to the surroundings into the microfluidic networks, soft robots can also achieve camouflage capability [3].

2.3 Electroactive Polymer Actuators

Electroactive polymer actuators (EAPs) are a type of polymer that respond to electrical stimulations. Such actuators usually exhibit high mechanical compliance, light weight, ease of fabrication and hence they have been widely utilized in bio-inspired and soft robotics [37]. The most common EAPs can be divided into two classes based on the actuation principle:

(i) ionic EAPs driven by the migration of cations which causes the swelling of cation-rich clusters, such as ionic-polymer/metal composites (IMPCs);

(ii) non-ionic EPAs driven by electric fields or Coulomb forces, such as dielectric elastomer actuators (DEAs) and liquid crystal elastomers (LCEs).

The most widely used EAPs include IPMCs and DEAs and will be reviewed briefly in this section.

2.3.1 Ionic-Polymer/Metal Composites

The structure of an IPMC consists of an ion exchange membrane sandwiched between two electron-conductive electrodes. When hydrated, the cations in the membrane can move freely. As a voltage bias is applied across the electrodes, the cations accumulate near the cathode side, which results in swelling of the negative side of the membrane, causing a bending of the actuator [68]. IPMCs have the advantages of low actuation voltage and large bending actuation motion, and good scalability. However, it also suffers from several drawbacks including low actuation bandwidth, high-cost, limited durability in dry environments and low efficiency [69].

The inherent actuation principle of IPMCs make them more suitable for underwater applications than in air. Various bio-inspired swimming robots using IPMCs have been developed in which IPMCs are integrated to the robotic tail or fin designs and the bending motion of IPMC actuators are used to mimic the oscillatory swimming [70] [71] [72] [73] or jet propulsion [74]. A multifunctional underwater

microrobot was developed which consists of six IPMC legs and can perform underwater crawling, floating and grasping [75].

2.3.2 Dielectric Elastomer Actuators

An ideal dielectric elastomer actuator consists of a piece of dielectric elastomer sandwiched between two compliant electrodes. When a potential difference is applied across the electrodes, the generated electrostatic pressure causes the membrane to contract in thickness and expand in area.

DEAs are known to have large actuation strains (linear strains over 500 % has been reported in [76]), fast response time (< 200 μs in [21]), high bandwidth (20 kHz in [19]) and self-sensing [77] and self-healing [78] capabilities. Silicone elastomer based DEAs also show excellent thermal tolerance (-100 to 250 ˚C in [79]). DEAs can be used in various environments, the most common case being in air, however, when carefully designed, DEAs can be used underwater [80]. The application of DEAs in vacuum was also demonstrated in [80]. The capability to fit in various environments (including outer space) of DEAs can be advantageous over FEAs and IPMCs. However, the high actuation voltage (usually in kV range) require specific high voltage converters which can restrict the mobility and miniaturization of DEA driven robots. Recent development in the miniature high voltage converters (e.g. EMCO Q series, XP Power) offer lightweight and compact solutions that improve the mobility or portability of such robots. The detailed configurations and applications of DEAs will be summarized in the next chapter.

2.4 Chapter Summary

In **Table 2.1**, the characteristics of the artificial muscles reviewed in this chapter are compared against natural muscle. It is worth noting that the efficiency values for these actuators reported in literature were obtained by the *work cycle* method [44] [81] [82]. This method involves cycling an actuator at a constant velocity between two positions (the cycling is usually driven by a linear motor). Stimulation is applied in only half of the cycle so that net mechanical work is produced in a complete cycle and the efficiency of the actuator can be estimated. However, such work cycle method has the limitations in terms of simplistic loading and could not assess the efficiency of the actuators under realistic loading (such as a payload with a mass and a dashpot). In this thesis, the author takes a different approach to investigate the electromechanical efficiency of DEAs by attaching a dissipative payload to the actuator and letting the actuator to drive the payload repetitively. The mechanical work done by the actuator is the energy dissipated by the dashpot where the energy input is the electrical energy flows into the actuator. A schematic diagram of this approach is illustrated in **Figure 2.1**.

By comparing the performances of different artificial muscles in **Table 2.1**, DEAs show clear advantages over other soft actuation technologies in the following aspects.

- DEAs show much higher efficiency (theoretical) than the other common artificial muscles such as SMAs and IPMCs, which makes it a promising candidate for realizing highly efficient soft and bioinspired robots.
- The Young's modulus of DEAs lies within the same magnitude as natural muscles and body tissues, which makes DEAs ideal for biomimetic and soft robotics applications and exploiting the inherent elasticity in actuators, just like the counterparts in nature.
- DEAs also show the highest bandwidth among all artificial muscles reviewed here, and the specific power and energy of DEAs are also the highest and are comparable with the natural muscles. This allows the study of resonance actuation, which is one common technique found in flying insects to utilize the inherent elasticity to improve actuation performances.

The high bandwidth, large specific energy/power and high electromechanical efficiency of the DEAs as the artificial muscle motivates the study of exploiting the inherent elasticity in DEA systems for developing highly dynamic biomimetic/soft robotic applications. In this thesis, the author will adopt a specific configuration of DEA and focus on the optimization of its actuation performance and demonstrate the practical applications of DEAs by utilizing the inherent elasticity embedded the actuators.

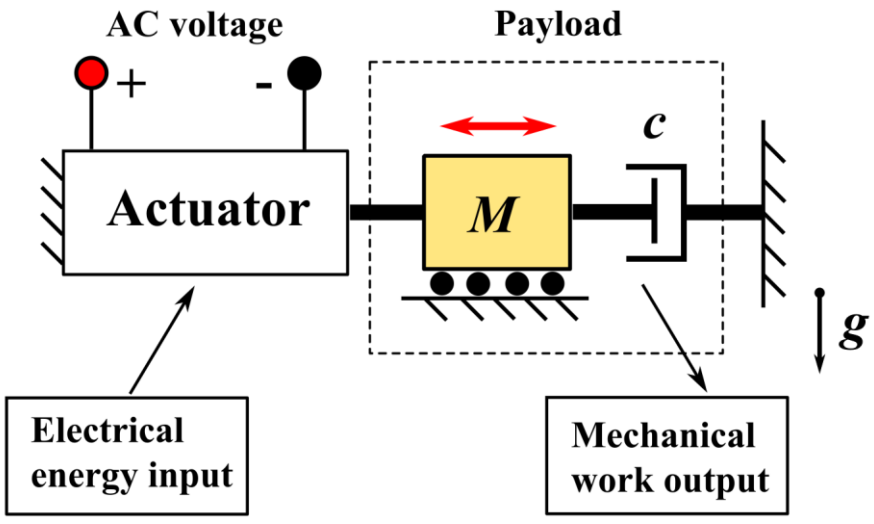

Figure 2.1. Electromechanical efficiency study setup adopted in this thesis.

Table 2.1. Comparison of different artificial muscles against natural muscle.

	SMAs [43] [44] [45] [36]	FEAs [2] [83]	IPMCs [84] [85] [86]	DEAs [19] [87] [88]	Natural muscle [89]
Young's modulus	20 – 90 GPa	~ 1 MPa	300 – 800 MPa	~ 1 MPa	10 – 60 MPa
Actuation strain (%)	< 8.5 in wire ~ 50 in coil	< 200˚ (bending) < 1000 (linear, estimated)	< 270˚	< 1000 (areal) < 500 (linear)	10 - 30
Actuation motion	Contraction	Bending, contraction, elongation, twisting	Bending	Expansion in plane and contraction in thickness	Contraction
Stimulus	Heat (Joule heating)	Fluid pressure	Voltage (charge migration)	Voltage (electric field)	Chemical reaction
Efficiency (%)	< 16	< 30	< 3	< 90 (theoretical)	< 40
Bandwidth (Hz)	< 3	< 10 (estimated)	100	< 2 kHz	2 - 180
Mass-specific Energy (J/kg)	< 10	0.5	< 4	< 20	8 - 40
Mass-specific Power (W/kg)	< 30	10	2.6	< 80	9 - 280
Cycle life	300 to 10^7	> 10^5	<10^5	> 10^6	Max > 10^9

Chapter 3: Literature Review of Dielectric Elastomer Actuators

This chapter describes the functioning principle of the dielectric elastomer actuators, lists various configurations reported in the literature and their applications in robotics.

3.1 Actuation Principle

An ideal dielectric elastomer actuator consists of a piece of dielectric elastomer sandwiched between two compliant electrodes, as illustrated in **Figure 3.1** (**a**). When a potential difference is applied across the membrane, opposite charges accumulate on both electrodes. The opposite charges are attracted to each other, which leads to an electrostatic pressure (or Maxwell pressure). Due to the elastic nature of the dielectric elastomer, the electrostatic pressure will squeeze the membrane in thickness. In the ideal case, the electrodes are assumed to be compliant enough so that their stiffness can be neglected. By the volumetric incompressibility assumption of an ideal elastomer [90], the reduction in thickness causes the membrane to expand in area, as demonstrated in **Figure 3.1** (**b**). The actuation principle was described first by Pelrine *et al* [90] in which the effective Maxwell pressure is given as

$$p = \varepsilon_0 \varepsilon_r E^2 \,, \tag{3.1}$$

where p is the Maxwell pressure, ε_0 and ε_r are the free-space permittivity and the relative permittivity of the dielectric elastomer respectively and E is the applied electric field.

This equation clearly shows the performance of a DEA can benefit from a dielectric elastomer with high relative permittivity (dielectric constant) and high dielectric breakdown strength (the maximum electric field that can be applied to a dielectric elastomer before a short circuit is formed between two electrodes).

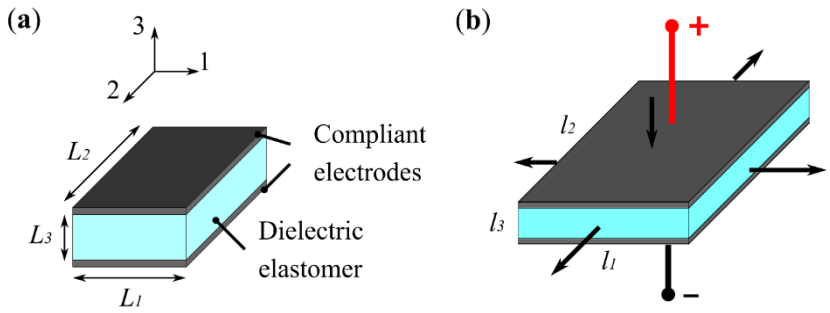

Figure 3.1. Actuation principle of an ideal DEA. (**a**) E = 0. (**b**) E >> 0.

3.2 Dielectric Materials

Many types of elastomers are used for DEAs, including acrylics, silicone, polyurethane, fluoroelastomers, polybutadiene and polyisoprene [90] [91] [4]. Acrylics and silicones are the two predominant materials for DEAs. Acrylic elastomer most commonly occurs in the form of VHB, an adhesive tape fabricated by 3M (VHB 4905 and 4910), with the thickness of 0.5 mm and 1.0 mm available. Clear advantages of VHB acrylic elastomer compared to the other dielectric elastomer materials include low-cost, high availability, relatively large dielectric constant and dielectric strength [4]. Their inherent adhesive makes it easy to bond to any support frame (hence convenient for fast prototyping). VHB acrylic elastomer has been widely studied in the last two decades and DEAs with very large actuation strains over 500 % (linear) and 1000% (areal) have been reported using VHB acrylic elastomers [76] [88]. However, VHB acrylic elastomers have the drawbacks of high viscoelasticity [4] [92] [82] [93], which causes a slow response and reduced reliability. Recent development in synthetic acrylic elastomers shows a reduced viscoelasticity thus improved response speed [94].

Table 3.1. Common fabrication techniques of silicone elastomer films.

Fabrication Technique	Description	References
Inkjet 3D Printing	• Piezoelectric inkjet printing of UV and thermal cure silicone. • A minimum thickness of 2 μm was achieved.	[95]
Blade Casting	• Adding uncured silicone mixture on substrate with even thickness. • Using applicator with adjustable height to control the thickness of the silicone membrane.	[96] [97]
Spray Deposition	• Uncured silicone is thinned with organic solvent to reduce the viscosity. • Solvent-silicone mixture is loaded in an airbrush and spray deposited onto a substrate.	[98]
Pad Printing	• Uncured silicone is pad-printed on PET substrate. • A minimum of 3 μm thickness was achieved.	[99]
Spin Coating	• Membrane thickness is controlled by the spin rate and duration.	[16] [87] [100]

Silicone elastomers, on the other hand, have significantly reduced viscoelasticity and ultrafast response time [4] (< 200 μs in [21]). However, the disadvantages are also clear. Silicone elastomers generally have a lower dielectric constant and dielectric strength than VHB acrylic elastomer [101] [102], hence a smaller actuation strain. Silicone elastomers usually come in a non-polymerized liquid state, allowing users to customize the size of the elastomer (e.g. thickness), which can be advantageous over VHB acrylic elastomers where only fixed thicknesses are available. However, a complex casting process is normally required to fabricate silicone elastomer. Different casting processes of silicone elastomers are listed in **Table 3.1**. A dedicated review on the silicone elastomer for DEAs can be found in [103]. Recently, off-the-shelf silicone membranes with the thickness ranging from 20 to 500 μm became available (ELASTOSIL® Film - Wacker Chemie AG), which benefits the DEA field by significantly reducing the fabrication complexity.

3.3 DEA Electrodes

DEAs are actuated by applying a high voltage on the electrodes. An ideal electrode material for DEAs includes:

(i) High compliance. The stiffness of the electrodes shall not affect the actuation strain of the DEA.
(ii) High conductivity over a wide range of strain. DEAs have the typical actuation strain of 10 % to over 100 %, maintaining a good conductivity during actuation can be essential for maximizing the performance of a DEA.
(iii) Good lifespan. As a reliable actuator, the dielectric elastomer as well as the electrodes must survive a large number of actuation cycles (e.g. > 10^6 cycles).

A comprehensive review on the flexible and stretchable electrodes for DEAs was done by Rosset and Shea and for detailed discussion of fabrication processes for different types of electrodes please refer to [104].

Most common compliant electrodes for DEAs include carbon-based electrodes and thin metallic film electrodes. Carbon-based electrodes received the most attention for their relatively low cost and ease of application. Such electrodes can be summarized as three categories: loose carbon powder; carbon grease (carbon particles mixed in a viscous oil) and carbon/elastomer compound (carbon particles mixed into a crosslinked elastomer) [104]. Loose carbon powder tends to have significant larger resistance at large strains (> 100 %) [105] [91] than carbon grease and carbon/elastomer compound. Commercially available carbon grease (e.g. MG 846, MG Chemicals) is cheap and easy to apply, which is ideal for fast prototyping. However, silicone oil based carbon grease, such as the widely adopted MG 846 carbon grease product, has the problem of diffusion into silicone elastomers [104] [106]. This can cause swelling of the elastomer, thus affecting the performance of the DEA. Carbon/elastomer compound is

applied to the dielectric elastomer in its non-polymerized liquid state. Pad-printing processes are normally used to transfer the liquid state carbon/elastomer compound onto the surface of the dielectric elastomer with accurate dimension, as demonstrated in [104] [15]. After curing, this type of electrode can be more robust against contamination and easier to handle than carbon grease. Carbon nanotubes (CNTs) represent another class of carbon electrodes and have been utilized extensively by the researchers at Harvard University (see e.g. [87] [100] [107] [108]). CNTs have the advantages over normal carbon particles of superior electrical conductivity [107] [108] and demonstrated self-healing capability [109]. However, the application of CNTs requires clean rooms and their relatively high cost also limits their applications in DEAs. Silver nanowires (AgNWs) share the same advantage and disadvantages as CNTs and hence are not widely adopted for DEA applications [110].

Thin metallic films are also used as the electrodes for DEAs due to the ability to create small scale patterns and higher conductivity under low strains. However, metal stiffens the dielectric elastomer and the low elasticity restricts the maximum actuation strain of the DEAs. Several approaches have been proposed to improve the performance of DEAs with metallic electrodes, such as patterned electrodes [91], output-of-plane bucked electrodes [111] and corrugated membranes [112]. However, such approaches require custom equipment, which could complicate the fabrication process of DEA devices.

3.4 DEA Configurations

In Section 3.1, the actuation principle of an idealized DEA was introduced, however, to allow a DEA to exert useful work in real applications, the dielectric elastomer membrane is usually fixed to a relatively stiff frame to withstand its shape during actuation. Ever since the introduction of DEAs by Pelrine *et al* [4] [90] [91], numerous DEA configurations have been developed. Most of these configurations can fall into the two categories: area expansion and thickness contraction. Also, based on the specific application requirements, the actuation can be either analogue (the deformation is a continuous function of the applied electric field) or binary (the deformation switches from one state to the other once the electric field passes a certain threshold).

3.4.1 Stacked DEAs

Stacked DEAs utilize the active thickness contraction of the dielectric elastomer. For a single layer of DEA, the force output can be small. To amplify its output, multiple layers of DEA membranes can be stacked together, as has been demonstrated in [113] [114] [115] and in **Figure 3.2** (**a-b**). With the advances in synthetic elastomer material and high performing electrodes such as carbon nanotubes, researchers have reported a long cylinder stacked DEA which demonstrates a peak energy density (19.8

J/kg) close to natural muscles. This could open new potential for high power biomimetic robotics and wearable devices. Apart from the advancements in material aspects, several fabrication processes have been proposed to reduce the fabrication complexity and error in each sample. Instead of fabricating individual layers separately, Carpi *et al* [116] [117] developed a folding process as illustrated in **Figure 3.2** (**c**). It begins with a strip of dielectric elastomer with compliant electrodes applied. Then the strip is folded by coating a thin layer of the dielectric material to allow bonding. Maas *et al* reported an automated production chain of stacked DEAs in [118] which enables industrial production of such DEAs.

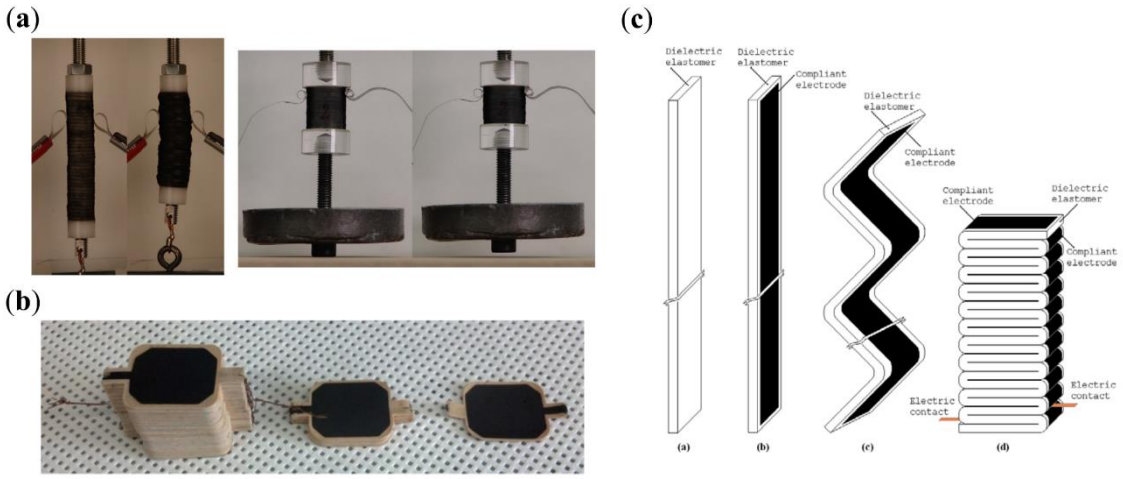

Figure 3.2. Examples of stacked DEAs. (**a**) Stacked DEAs lifting a 1 kg mass [113]. (**b**) Stacked DEA with individual units exposed [114]. (**c**) Folding process of a stacked DEA proposed by Carpi *et al* [116].

3.4.2 Planar DEAs

Planar DEA configurations utilize the area expansion of the membrane during actuation. Such designs usually involve using pre-stretched membranes and, in order to sustain the tension of the membrane in the pre-stretched directions (note that pre-stretch can be either unidirectional and bidirectional), constraints are usually added, which can be a rigid frame [119], stiff fibres [120] [121] or a deadweight [102]. Bistable elements are often added to planar DEAs to modify its performance, e.g. amplifying the actuation strokes [122] [82] (**Figure 3.3** (**a-b**)) or tuning its force-stroke response (**Figure 3.3** (**c**)) [123]. Bistable elements added to the DEA systems also transfer the actuation from analogue into binary, which allow a minimum energy consumption to maintain a position. Agonistic-antagonistic configurations (**Figure 3.3** (**d**)) can be used such that the tension of one membrane can be balanced by the tension from the other membrane, see [124] [125] [102] for example, and bi-directional actuation

can be achieved with this design, mimicking the agonistic-antagonist configuration found in natural muscle systems.

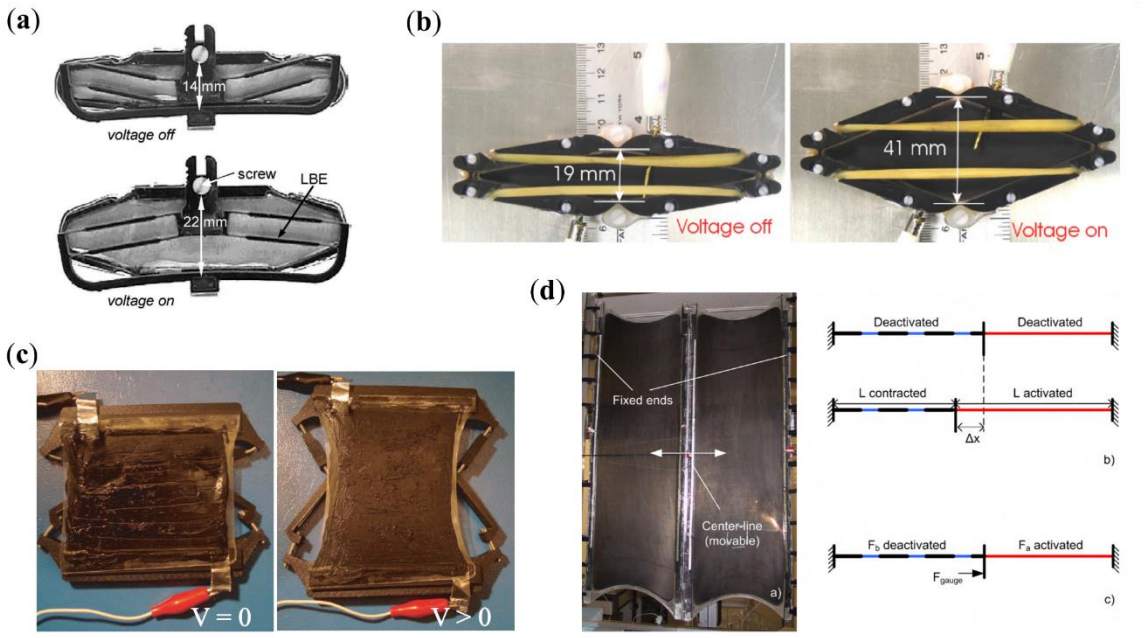

Figure 3.3. Examples of planar DEAs. (**a**) Planar DEA with linear bisable element [122]. (**b**) Diamond actuator with a rubber band bistable mechanism that can produce over 100 % extension strains [82]. (**c**) A constant force planar DEA by coupling DEA membrane with a nonlinear bowtie mechanism [123]. (**d**) Large scale agonistic-antagonistic DEA and its actuation principle [125].

3.4.3 Rolled DEAs

A rolled DEA is a pre-stretched DEA membrane rolled into a cylinder to maximize compactness. This configuration was originally developed by Pei *et al* [6] where the pre-stretched elastomer membrane is rolled around a compression spring. The electrodes can be patterned such that they align radially on two or four circumferential spans of the rolls to achieve two/three DOF actuation. Apart from using compression spring to maintain the tension on the membrane, other mechanisms can also be utilized. For example, Lau *et al* [10] developed a diamond shape mechanical amplifier that creates pulling force on the rolled membranes. Buckled carbon fibre strips were also served as the tension mechanism, which can achieve a maximum linear strain up to 142 % [126]. Rolled DEAs can also be reinforced circumferentially by Nylon fibres and then inflated to maintain its pre-stretch [127]. Zhao *et al* [100] developed a rolled DEA with combinations of different elastomers and carbon nanotube electrodes for tactile display applications which require high bandwidth and large blocked force.

3.4.4 Out-of-plane DEAs

Another way of using the active area expansion is to have biasing mechanism to deform the membrane out-of-plane and restrict the actuation strain in the desired direction. Several biasing mechanisms have been proposed in the last two decades. For example, by inflating an elastomer membrane with air, the DEA membrane expands into a balloon shape [128] [129], as illustrated in **Figure 3.4** (**a**). By taking advantage of the snap-through instability of the membrane, this configuration has been demonstrated to achieve an actuation strain of over 1000 % in area [88]. Such out-of-plane deformation can also be achieved by inserting a multilayer circular DEA into a frame with a smaller diameter, which causes the buckling in the DEA membrane [5], as shown in **Figure 3.4** (**b**). Agonistic-antagonistic configuration can also be achieved by using incompressible fluid to mechanically couple an active membrane to a passive part, where the passive part serves as the end-effector [130]. The end-effector can be remotely actuated by the active part, resulting a safer interaction with human, as demonstrated in **Figure 3.4** (**c**). By dividing the electrodes into multi-segments, the DEA can produce multi-DOF actuation, as demonstrated by [131]. The coupling media can also be solid state materials, such as the granularly coupled DEA developed by the same researchers [132].

The cone DEA is another out-of-plane actuation configuration that has received great research interest. Such configuration is achieved by having a piece of dielectric elastomer bonded to a rigid ring and a smaller central disk. A protrusion force causes the membrane together with the central disk to deform out-of-plane. Such biasing elements can be a linear compression spring [32], a deadweight [33], a bistable mechanism [34], permanent magnets [35], an antagonistic cone DEA membrane [31], or a mix of two [133]. The same multi-segment electrode principle can be applied to a cone configuration DEA to achieve multi-DOFs actuation. Conn and Rossiter [31] developed a 5 DOF double cone DEA by dividing the top and bottom electrodes into four sections. They also demonstrated that the last DOF, which is rotating around the *z* axis, can be achieved by taking advantage of the wrinkling of the membrane, as illustrated in **Figure 3.4** (**d**).

Out-of-plane DEAs represent one of the mostly adopted DEA configurations for practical applications as constraints can be easily applied to such DEAs to achieve the desired number of DOF. The biasing elements can be another passive/active membrane to achieve antagonistic configuration and bidirectional actuation, mimicking the antagonistic skeletal muscle systems in nature. These features make out-of-plane DEAs, or cone DEAs in particular, ideal candidates for studying bioinspired elastic actuations.

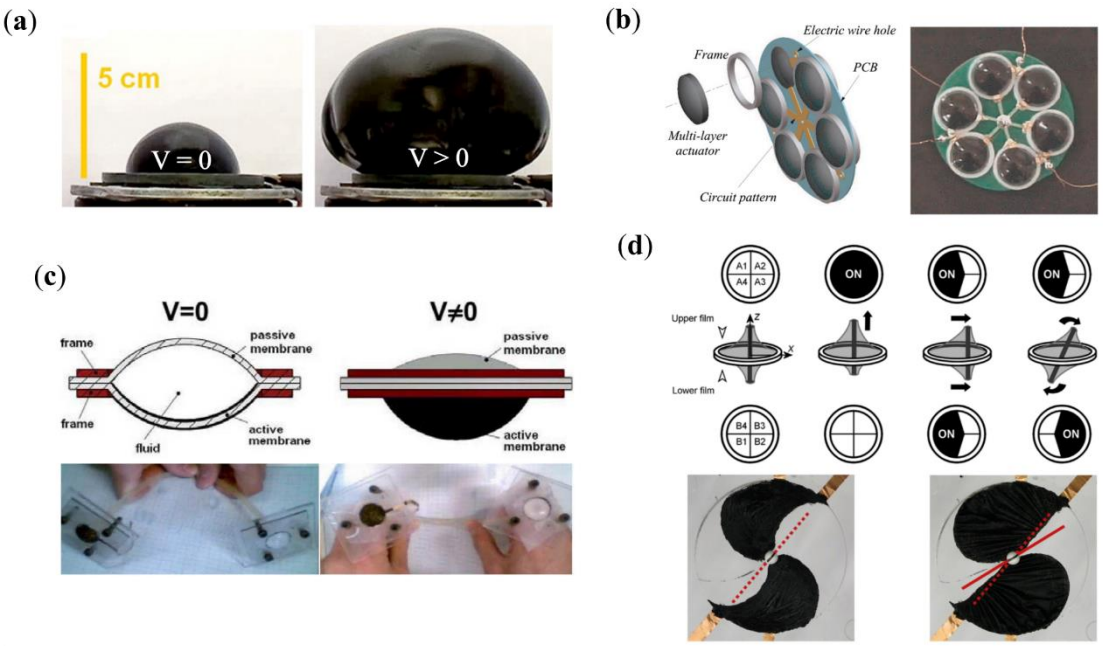

Figure 3.4. Examples of out-of-plane DEAs. (**a**) Balloon DEA experiencing giant deformation over 1000% area [88]. (**b**) Multi-layer buckling DEA pattern [5]. (**c**) Hydrostatically coupled DEA [130]. (**d**) double cone DEA with 5 DOF and potential 6th DOF demonstrated [31].

3.4.5 Compliant Bending DEAs

Unimorph/bimorph bending DEAs. Unimorph and bimorph bending DEAs are composites of multilayers of DE membranes and support layers. By employing the different expansion rate of each layer causes the whole structure to generate a bending motion [134] [135], an example of which is illustrated in **Figure 3.5** (**a**). By attaching stiff fibres with different patterns to the multilayer DE membranes, bimorphs with different forms of bending motions can be achieved [107]. Shintake *et al* [136] have integrated a bimorph DEA configuration with low-melting-point alloy. By transferring between solid and liquid state, the low-melting-point alloy serves as a stiffness changing mechanism which can fix the position of the DEA when actuated even if a heavy payload is attached. Another approach for increasing the desired stiffness of the unimorph DEAs is to use electrostatic chucking. Differing from conventional unimorph designs, this design has additional layers of electrodes and insulation to facilitate electrostatic chucking to adjacent DEA layers. Such a design can vary its stiffness up to 40 times [137]. Unimorph structures can also made to be bistable by sandwiching a non-stretchable support layer between two DEA membranes [138] [139].

Dielectric elastomer minimum energy structures (***DEMESs***). A DEMES is produced by bonding a planar pre-stretched elastomer membrane to an elastic frame. Upon release, the planar structure can deform into a 3D structure where the total energy of the system reaches its minimum. **Figure 3.5** (**b**)

illustrates an example of the DEMES structure. Different patterns of elastic frames can be designed to allow different configurations of DEMESs and various actuation motions, see [12] [140] [141] [142] [143] [144] for example. When a DEMES is released from a high energy state, more than one energy local minimum can exist, while most of the DEMES actuators only actuate around one stable state, Zhao *et al* [145] demonstrated that with a sufficient electric field and inertia on the DEMES, this actuator can transfer between two symmetrical minimum energy states, thus becoming bistable with a significantly amplified actuation stroke of over 130˚.

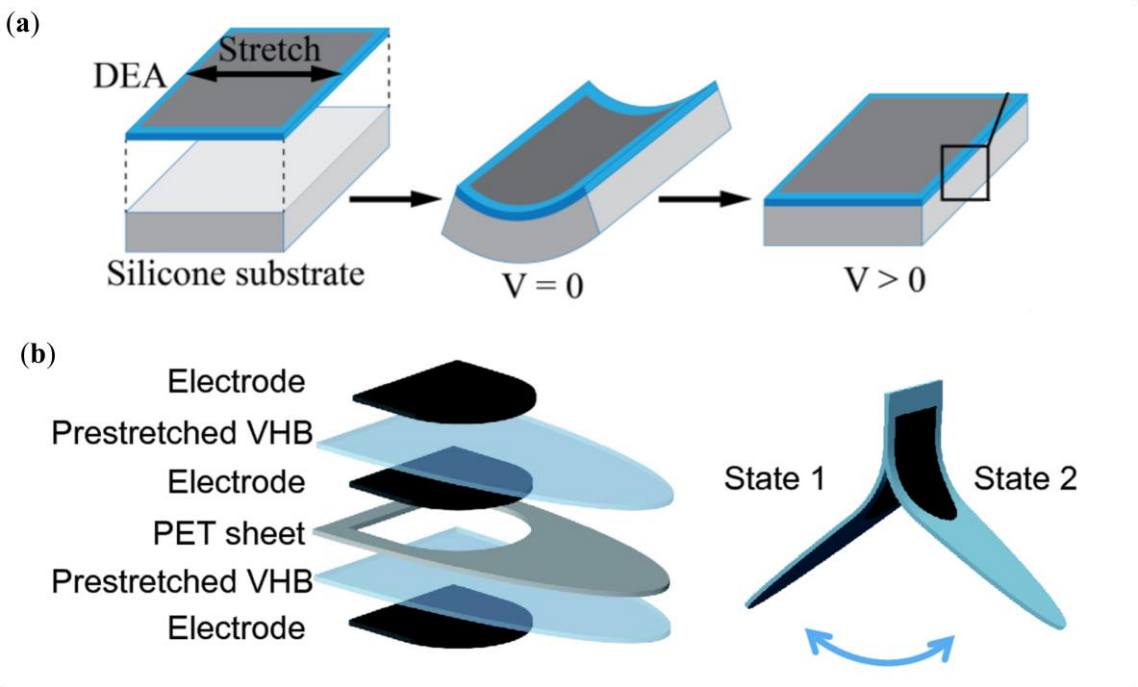

Figure 3.5. Examples of compliant bending DEAs. (**a**) Illustration of the structure of a unimorph DEA [135]. (**b**) Example structure of a DEMES [144].

3.5 DEA Applications

Due to their high energy density, large actuation strain, inherent compliance and low-cost [4], numerous applications based on DEAs have been developed in the past two decades, and many of which can fall into the following categories: robotic locomotion, including terrestrial, aquatic and aerial; soft grasping and manipulation; micro fluidic, acoustics and optical control devices.

3.5.1 Locomotion

Terrestrial. Crawling motion is one of the simplest locomotion forms. Peristaltic crawling motion and two-anchor crawling motion are the two most common motions taken by DEA driven crawling robots. Peristaltic examples include the micro earthworm robot driven by multi-segmented DEA structures (**Figure 3.6** (**a**)) [5], and rolled DEA driven earthworm robot [146]. Other robots mimic the two-anchor crawling gait of an inchworm, and can be driven by antagonistic balloon DEAs [147]; DEMES [80] and unimorph DEAs [148]. Common DEA driven crawling robots are tethered and the oscillating driving signals are pre-generated by a controller then sent to the actuator via high voltage amplifiers. Henke *et al* developed a soft crawling robot driven by soft dielectric elastomer oscillators [149]. This design only requires an external DC voltage, and it can automatically generate all signals for driving the crawling robot by a distributed, neuron-like internal control. Some researchers focus on the development of untethered DEA driven robots, for example, Cao *et al* developed an untethered soft crawling robot driven by DEMES with electroadhesion feet [150]. With the battery and electronics onboard, the robot is able to move at a speed of 0.02 body length / second.

Mimicking other forms of terrestrial locomotion using DEAs has also been attempted. Examples include walking robots such as MERbot with rolled DEA feet (**Figure 3.6** (**b**)) [6], biomimetic quadruped robot [114] and hexapod robots driven by multi-DOF double cone DEAs (**Figure 3.6** (**c**)) [7] [97] [151]. Rolling locomotion can be generated by utilizing multi-segment DEAs and actuating different segments in sequence [152] [153]. Due to the high efficiency of rolling motion, DEA driven rollers can be very fast (e.g. 0.95 body length / second in [153]). Since hopping motion requires high peak power from the actuators, hopping can be challenging if it relies solely on the power output of a DEA. A robot developed by Dubowsky *et al* [154] uses a low power cone DEA to pump energy into the power springs. When sufficient energy is stored, the power springs are released to perform hopping motion. 35 actuation cycles are required to perform one hop. This robot weighs 46 g with the fuel cell and all power electronics on board and can hop about 38 mm.

Aquatic. One of the great challenges for underwater actuation with DEAs is the isolation of high voltage. Existing isolation technique involves sandwiching the high voltage electrodes between two layers of DEA membranes and is tight sealed, while leaving the other side of the membranes directly contact with the water as the ground electrode. Several DEA driven swimming robots were developed in recent years. Undulation motion observed in some type of fish can be mimicked by biomorph DEAs, such as the biomimetic fish (**Figure 3.6** (**d**)) developed by Shintake *et al* [8] and the translucent swimming robot with ionic fluid electrodes by Christianson *et al* [155]. Jet propulsion commonly seen on jelly fish and cuttlefish can be reproduced by bistable DEAs. Yang *et al* developed an untethered cuttlefish inspired swimming robot with control strategy optimized by reinforcement learning [156].

Ray mimicking DEMES driven soft electronic fish shown in **Figure 3.6** (**e**) has the highest swimming speed up to date with the speed of 0.69 body length / second [9].

Aerial. Insect-inspired flapping wing flight requires very high power-density from the actuators. For this reason, unlike terrestrial and aquatic locomotion applications, only a few studies have looked at the potential of utilizing DEAs on flapping wing mechanisms. For example, Lau *et al* developed a series of flapping wing mechanisms driven by rolled [10] (**Figure 3.6** (**f**)) and stacked DEAs [157]. Due to the small actuation strain, the flapping stroke (3-10˚) and frequency (1-5 Hz) is significantly smaller than natural counterparts. Others have tried to use the large bending actuation of DEMES to power the wings. Zhao *et al* designed a three-segment DEMES which mimics the flapping motion of birds [158], however, no lift force was reported. It is worth noting that despite the advantages of resonant actuation of DEAs thanks to the inherent elasticity, no work has looked at the power amplification of resonant actuation of DEAs and their potential applications in flapping wing robots. Apart from using DEAs as the driving mechanism, Shintake *et al* have integrated foldable DEAs into a conventional fixed wing micro air vehicle (MAV) [11] where the DEA serves as the control elevon, a picture of this MAV is shown in **Figure 3.6** (**g**).

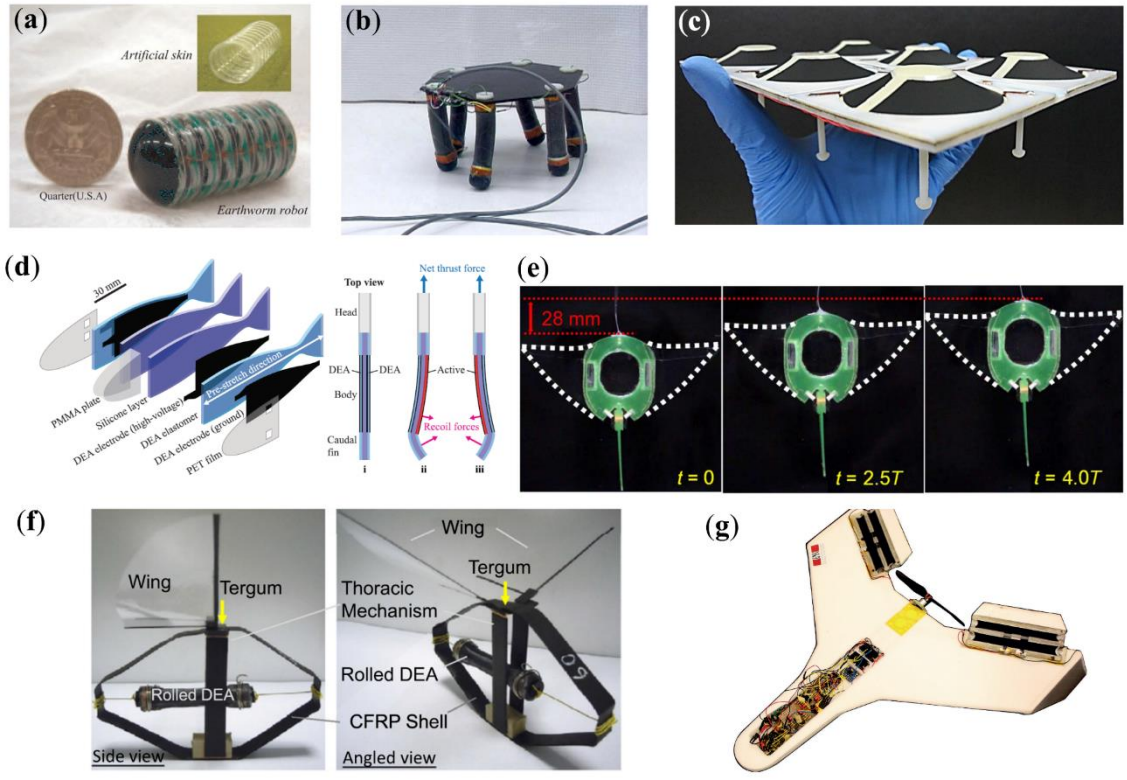

Figure 3.6. DEA applications in robotic locomotion. (**a**) Miniature earthworm robot [5]. (**b**) MERbot walking robot driven by multi-DOF rolled DEA [6]. (**c**) Hexapod robot driven by multi-DOF double cone DEAs [7]. (**d**) A bimorph DEA driven swimming robot [8]. (**e**) Untethered soft electronic fish swimming at 0.69 body length / second [9]. (**f**) Flapping wing mechanism driven by a rolled DEA [10]. (**g**) A fixed wing MAV with foldable DEA elevon [11].

3.5.2 Soft Grippers

The biggest advantages of using DEAs as soft grippers are the inherent compliance of the actuator making it safer to grasp fragile and delicate objects. Many DEMES and unimorph DEAs with no rigid supporting frames have been adopted in soft gripper designs [12] [107] [13] [14], as demonstrated in **Figure 3.7** (**a-c**). DEAs can be combined with other mechanisms to enhance the grasping performance. For example, Shintake *et al* integrated a unimorph DEA with electroadhesion in its tips (**Figure 3.7** (**d**)) [15]. When actuated, both the bending motion of the unimorph DEA and the electrostatic force of the electroadhesion cause a firm grasping of the object. The gripper weighs only 1.5 g and can pick up a wide range of objects with varying sizes and weights, including a fragile, highly deformable water-filled thin membrane balloon or a heavy metallic can (>80 g). The same group of researchers also developed a stiffness changing gripper using a DEA and low-melting-point alloy composite (**Figure 3.7** (**e**)) [136]. By transferring between solid and liquid state, the low-melting-point alloy changes its stiffness by over 90 times, allowing the grasp of very heavy payload.

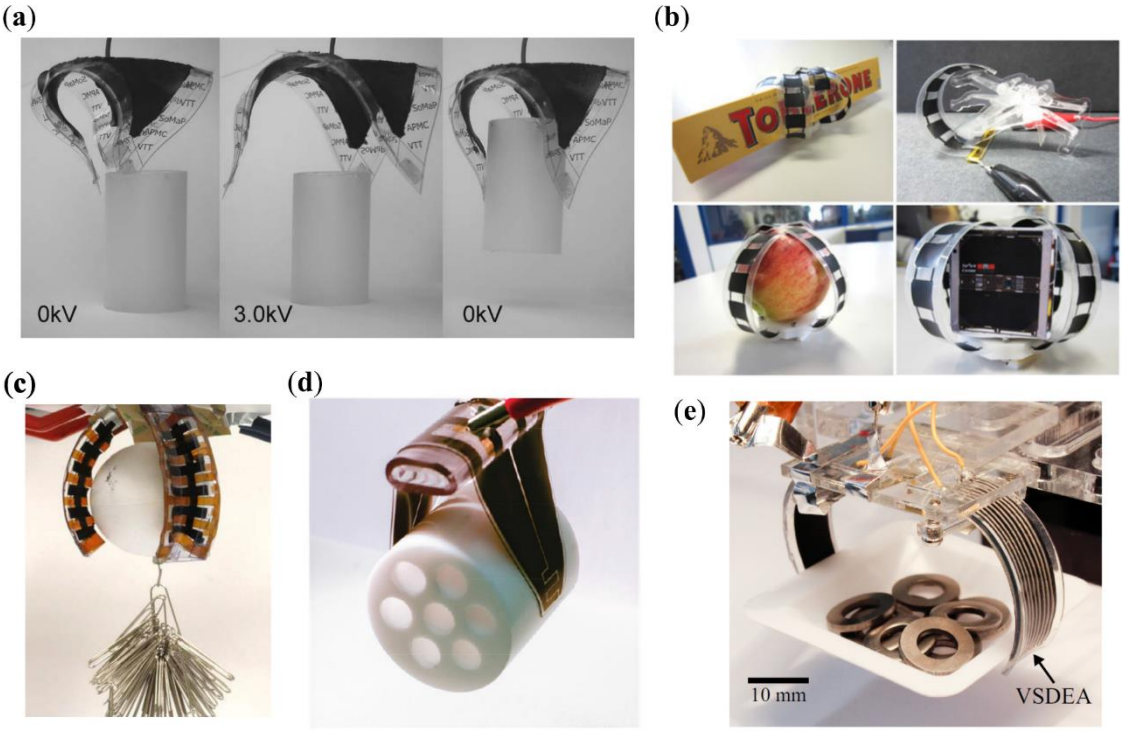

Figure 3.7. DEA applications in soft grippers. (**a-c**) DEMES serves as soft grippers [12] [13] [14]. (**d**) A unimorph DEA gripper with integrated electroadhesion in its tips [15]. (**e**) A unimorph DEA gripper with integrated variable stiffness mechanism based on low-melting-point alloy [136].

3.5.3 Fluidic, Acoustic and Optical Control

The good scalability, inherent compliance and fast response of DEAs enabled the development of several DEA driven soft micro pumps [16] [17] and valves [18] for soft robotics and biomedical applications. Thanks to the high bandwidth of the DEAs, they can also be used in acoustic applications. For example, researchers from Harvard University developed a spot DEA with ionic conducting hydrogel electrodes and utilized it as a transparent loudspeaker [19] and an active noise cancelation device [20]. The fast response and large actuation strain also make them ideal for optical applications such as ultrafast soft lenses [21] [22], switchable infrared-reflecting devices [23] and artificial chromatophore networks [159].

3.6 Chapter Summary

In this chapter, various configurations of DEAs and their applications in robotics have been reviewed. Despite the significant development of DEA since their introduction, the use of the inherent elasticity of the elastomer itself to improve its actuation efficiency and amplify output has not been investigated and demonstrated. Cone configuration based DEAs as one type of out-of-plane DEA designs allows easy restriction of its actuation DOF to one (which simplifies the control and modelling process, the 1-DOF linear actuation also mimics the natural muscle), and the potential antagonistic structure makes it an ideal design for studying inherent elastic actuation principles. In the rest of this thesis, the inherent elastic actuation principle of DEAs is investigated by using cone DEAs and a dynamic model developed for generalized cone structures. Applications demonstrating this elastic actuation principle are also developed and presented.

Chapter 4: Modelling of Dielectric Elastomer Actuators

This chapter focuses on the mathematical modelling of DEAs. First, state of the art models of hyperelastic, viscoelastic dielectric elastomer materials are reviewed. Then a generalized cone DEA dynamic modelling framework is developed which enables the further characterization and optimization of different cone DEA configurations studied in the thesis.

Statement: The cone DEA dynamic model presented in Section 4.5 in this chapter is adapted from the following publication where C. Cao is the first author.

- **Cao, C**., Hill, T.L. and Conn, A.T., 2019. On the nonlinear dynamics of a circular dielectric elastomer oscillator. *Smart Materials and Structures*. 28(7) p. 075020.

Contribution: Fabrication and testing methodology, investigation, data curation, formal analysis, writing original draft; review & editing.

4.1 Introduction to Modelling of DEAs

A dynamic model of DEAs predicts its time-dependent stroke/force output with a given actuation signal and specific boundary conditions and constraints. A complete dynamic model of DEAs should consist of a mechanical model describing the hyperelasticity and viscoelasticity of the elastomer, an electrical model describing the dynamic charge flow across the DEA, and finally an electro-mechanical coupling model describing the electric field dependent strain-stress relationship. With all three aspects considered, the dynamic response of a DEA can be fully characterized.

An accurate dynamic model of DEA can be used:

- to understand the fundamental actuation principles for a specific DEA configuration;
- as a powerful tool for performance characterization and optimization of a DEA;
- for dynamic control (e.g. outputting desired stroke/force output) of a DEA.

4.2 Free-energy Based Modelling Framework

The current free-energy based modelling framework was developed by Suo and his co-workers [160] [28] [161] [162] in which the DEA system is considered as a thermodynamic system to allow electro-mechanical coupling. A general formulation of this free-energy based material model is summarized as follows.

A schematic diagram illustrating the function of a dielectric elastomer is given in **Figure 4.1**. In its reference state, this piece of dielectric elastomer experiences no deformation and has initial dimensions of L_1, L_2, and L_3 in its length, width, and thickness directions respectively. The membrane is then deformed under forces P_1 and P_2 in axis 1 and 2 respectively. A voltage, Φ, is applied on the electrodes. The electrical charge accumulated on the electrodes is $\pm Q$. In its deformed state, its dimensions become l_1, l_2, and l_3. The strains of this dielectric elastomer are defined as $\lambda_1 = l_1/L_1$, $\lambda_2 = l_2/L_2$ and $\lambda_3 = l_3/L_3$. The Helmholtz free energy of piece of elastomer is F_E. For a small amount of change in the dimensions, δl_1, δl_2, and δl_3, the forces, P_1 and P_2, do work $P_1\delta l_1 + P_2\delta l_2$. For a small amount of change in the electrical charge, δQ, the voltage supply does work $\Phi\delta Q$.

This analysis is restricted to an isothermal process. Based on the thermodynamics law, the increase in Helmholtz free energy should equal to the sum of the work done by the forces, P_1 and P_2, and the voltage Φ (assuming no energy losses at this stage and the dielectric elastomer experiences quasi-equilibrium processes), as written as

$$\delta F_E = P_1\delta l_1 + P_2\delta l_2 + \Phi\delta Q \tag{4.2}$$

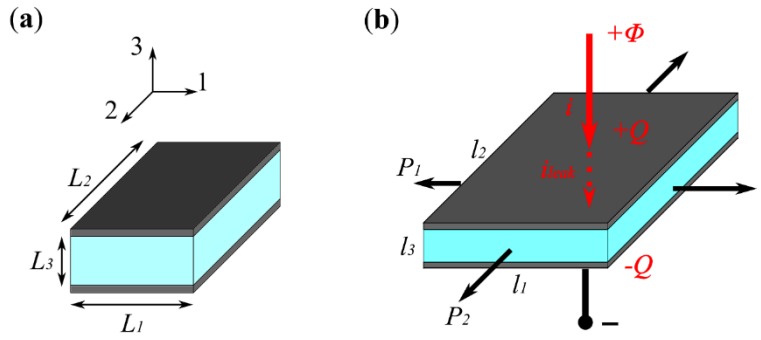

Figure 4.1. Actuation principle of dielectric elastomer actuator. (**a**) Reference state. (**b**) Actuated state.

The Helmholtz free energy density is defined as

$$W = F_E/L_1L_2L_3\ . \tag{4.3}$$

Inserting Eq. (4.4.3) into (4.4.2) and dividing by the volume of the membrane, $L_1L_2L_3$, one can obtain

$$\delta W = (\sigma_1 + ED)\lambda_2\lambda_3\delta\lambda_1 + (\sigma_2 + ED)\lambda_1\lambda_3\delta\lambda_2 + \lambda_1\lambda_2\lambda_3 E\delta D\ , \tag{4.4}$$

with

$$\sigma_1 = P_1/l_2l_3\ , \tag{4.5}$$

$$\sigma_2 = P_2/l_1l_3\ , \tag{4.6}$$

$$E = \Phi/l_3\ , \tag{4.7}$$

$$D = Q/l_1 l_2 \,, \tag{4.8}$$

where σ_1 and σ_2 are the true stresses in axis 1 and 2 respectively, E is the electric field and D is the electric displacement.

The elastomer is assumed to be incompressible, i.e. its volume is fixed when stretched, hence $\lambda_1\lambda_2\lambda_3 = 1$ [160] [28] [161] [162]. As a result, the Helmholtz free energy density, W, can be described as the function of the two in-plane principle strains λ_1 and λ_2, and electric displacement, D, as written as

$$W = W(\lambda_1, \lambda_2, D) \,. \tag{4.9}$$

Associated with small changes in these independent variables, the change in Helmholtz free energy density should satisfy

$$\delta W = \frac{\partial W}{\partial \lambda_1}\delta\lambda_1 + \frac{\partial W}{\partial \lambda_2}\delta\lambda_2 + \frac{\partial W}{\partial D}\delta D \,. \tag{4.10}$$

Combining Eq. (4.4) and (4.10), one can obtain

$$\left(\frac{\partial W}{\partial \lambda_1} - \frac{\sigma_1 + ED}{\lambda_1}\right)\delta\lambda_1 + \left(\frac{\partial W}{\partial \lambda_2} - \frac{\sigma_2 + ED}{\lambda_2}\right)\delta\lambda_2 + \left(\frac{\partial W}{\partial D} - E\right)\delta D = 0 \,. \tag{4.11}$$

The equality can be satisfied in the following way,

$$\sigma_1 + ED = \lambda_1 \frac{\partial W(\lambda_1, \lambda_2, D)}{\partial \lambda_1} \,, \tag{4.12}$$

$$\sigma_2 + ED = \lambda_2 \frac{\partial W(\lambda_1, \lambda_2, D)}{\partial \lambda_2} \,, \tag{4.13}$$

$$E = \frac{\partial W(\lambda_1, \lambda_2, D)}{\partial D} \,. \tag{4.14}$$

The material is also assumed to be an ideal dielectric elastomer, i.e. the elastomer polarizes similarly to a polymer melt. Based on such an assumption, the electric field, E, and the electric displacement, D, are a linear relationship:

$$D = \varepsilon E \,, \tag{4.15}$$

where ε is the dielectric constant.

Then Eq. (4.9) can be written as

$$W(\lambda_1, \lambda_2, D) = W_s(\lambda_1, \lambda_2) + \frac{D^2}{2\varepsilon} \,, \tag{4.16}$$

where W_s is the Helmholtz free energy density associated with the stretch of the membrane and $\frac{D^2}{2\varepsilon}$ is the part associated with the polarization of the dielectric elastomer.

Note that in this framework, the stretching and polarization of the dielectric elastomer contribute to the Helmholtz free energy independently. The two principle stresses can be written as

$$\sigma_1 + \varepsilon E^2 = \lambda_1 \frac{\partial W_s(\lambda_1,\lambda_2)}{\partial \lambda_1}, \tag{4.17}$$

$$\sigma_2 + \varepsilon E^2 = \lambda_2 \frac{\partial W_s(\lambda_1,\lambda_2)}{\partial \lambda_2}. \tag{4.18}$$

4.3 Hyperelastic Models

In this section, the most commonly used hyperelastic models are briefly described, which includes the Neo-Hookean, Gent, and Ogden models. Note that only hyperelasticity is considered at this point, while viscoelasticity will be discussed in the next section.

4.3.1 Neo-Hookean Model

The Helmholtz free energy density described by Neo-Hookean model can be written as

$$W_s = \frac{\mu}{2}(\lambda_1^2 + \lambda_2^2 + \lambda_1^{-2}\lambda_2^{-2} - 3), \tag{4.19}$$

where μ is the shear modulus.

The Neo-Hookean model has a simple structure with only one unknown parameter which makes it very easy to be implemented in DEA modelling, and it has been utilized in many DEA studies [160] [163] [164] [165] [166]. However, this simplified model is not capable of capturing the strain-stiffening effect, which occurs when the polymer chain of the elastomer reaches the stretch limit and the elastomer stiffens sharply.

4.3.2 Gent Model

The Gent model was proposed by Gent in 1996 [167], it has the advantage over Neo-Hookean model by considering the strain-stiffening effect and can be expressed as

$$W_s = -\frac{\mu J_{lim}}{2}\log\left(1 - \frac{\lambda_1^2+\lambda_2^2+\lambda_1^{-2}\lambda_2^{-2}-3}{J_{lim}}\right), \tag{4.20}$$

where μ is the shear modulus and J_{lim} is a constant related to the limit stretch, which ensures the stress stiffens deeply when the stretch approaches the limit stretch.

The Gent model also has a relatively simple form with only two unknown parameters, making it one of the most popular models for DEAs in recent years [168] [120] [169] [170] [171] [172] [173] [174].

4.3.3 Ogden Model

The Ogden model was developed by Ogden in 1972 [175]. It takes the form of

$$W_s = \sum_{n=1}^{N} \frac{\mu_n}{\beta_n}\left(\lambda_1^{\beta_n} + \lambda_2^{\beta_n} + \lambda_1^{-\beta_n}\lambda_2^{-\beta_n} - 3\right), \tag{4.21}$$

where μ_n and β_n are the model parameters and N is the model order.

It can be noted that the Ogden model differs from the Gent and Neo-Hookean models in that its parameters are purely experimentally determined with no physically meanings. Hence it is a type of phenomenological model, while the Neo-Hookean and Gent models are physical-based models [176]. The potentially infinite amount of model parameters allows the Ogden model to have a better accuracy in describing the elastomer response comparing to the other two models mentioned above, making it another popular model for DEA researchers [177] [178] [179] [82] [129].

4.4 Dissipative Dielectric Elastomer

Dissipation in the dielectric elastomer, including viscoelasticity and current leakage (where a small amount of current flows through the dielectric when a voltage is applied) is also considered by using a nonequilibrium thermodynamics framework.

4.4.1 Viscoelasticity

Such nonequilibrium thermodynamics states that the increase of the Helmholtz free energy should not exceed the total work done by the forces, P_1 and P_2, and the voltage Φ, which changes Eq. (4.2) into

$$\delta F_E \leq P_1 \delta l_1 + P_2 \delta l_2 + \Phi \delta Q \ . \tag{4.22}$$

The change in Helmholtz free energy density in Eq. (4.4.3) becomes

$$\delta W \leq (\sigma_1 + ED)\lambda_2\lambda_3\delta\lambda_1 + (\sigma_2 + ED)\lambda_1\lambda_3\delta\lambda_2 + \lambda_1\lambda_2\lambda_3 E\delta D \ . \tag{4.23}$$

To cope with the inequality in the change in the Helmholtz free energy density, W, more independent variables, namely the strains related to the dissipative damping $\xi_1, \xi_2, \ldots, \xi_n$, are introduced in function (4.16), and written as

$$W = W_s(\lambda_1, \lambda_2, \xi_1, \xi_2, \cdots, \xi_n) + \frac{D^2}{2\varepsilon} \ . \tag{4.24}$$

Combining Eq. (4.23) and (4.24), one can obtain

$$\left(\frac{\partial W}{\partial \lambda_1} - \frac{\sigma_1 + ED}{\lambda_1}\right)\delta\lambda_1 + \left(\frac{\partial W}{\partial \lambda_2} - \frac{\sigma_2 + ED}{\lambda_2}\right)\delta\lambda_2 + \left(\frac{\partial W}{\partial D} - E\right)\delta D + \sum_{i=1}^{n} \frac{\partial W}{\partial \xi_i}\delta\xi_i \leq 0\ . \qquad (4.25)$$

The inequality can be achieved by letting

$$\sum_{i=1}^{n} \frac{\partial W_s(\lambda_1, \lambda_2, \xi_1, \xi_2, \cdots, \xi_n)}{\partial \xi_i}\delta\xi_i \leq 0\ . \qquad (4.26)$$

In order to take the inequality in Eq. (4.4.26) into account, a one-dimensional Maxwell rheological model is commonly used [180] [162] [169] [181] [171]. This rheological model consists of two parallel units: nonlinear spring 1 as a unit and nonlinear spring 2 in series with a dashpot as the second unit, as depicted in **Figure 4.2** (**a**). The serial connection of the nonlinear spring and the dashpot on the second unit can capture the strain rate dependent hysteresis in the strain-stress function, stress relaxation (stress decays after a strain is applied to the dielectric elastomer) and creep (strain continues to increase after a stress is applied). For spring 1, its deformation is characterized by λ. However, for spring 2, its deformation is characterized by λ^e due to the dashpot. The strain for spring 2 is $\lambda^e = \lambda/\xi$, where ξ is the strain of the dashpot, as was defined by Zhao and Suo in [161] [182]. The net stress is the sum of the stresses on the two spring units.

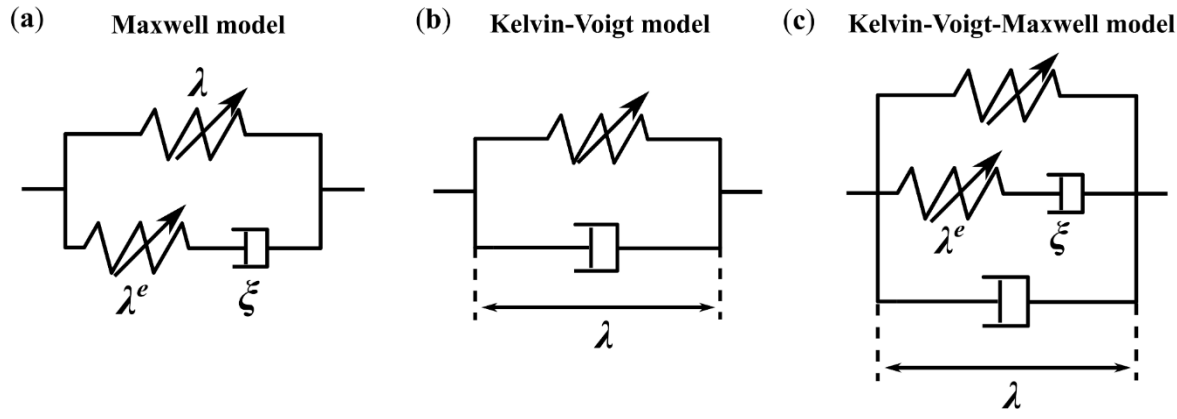

Figure 4.2. Schematic diagram of different rheological models. (**a**) Maxwell model; (**b**) Kelvin-Voigt model; (**c**) Kelvin-Voigt-Maxwell model.

Many viscoelastic models based on the Maxwell rheological model and the hyperelastic models introduced above have been proposed in recent years. Foo *et al* [162] proposed a viscoelastic model based on the Gent model where the Helmholtz free energy density associated with stretch is given as

$$W_s = -\frac{\mu_A J_A}{2}\log\left(1-\frac{\lambda_1^2+\lambda_2^2+\lambda_1^{-2}\lambda_2^{-2}-3}{J_A}\right)-\frac{\mu_B J_B}{2}\log\left(1-\frac{\lambda_1^{e^2}+\lambda_1^{e^2}+\lambda_1^{e^{-2}}\lambda_2^{e^{-2}}-3}{J_B}\right), \tag{4.27}$$

with

$$\lambda_1^e = \lambda_1/\xi_1\ , \tag{4.28}$$

$$\lambda_2^e = \lambda_2/\xi_2\ . \tag{4.29}$$

where μ_A and μ_B are the shear moduli of the two springs, J_A and J_B are constants of the limiting stretches of the two springs and λ_1^e and λ_2^e are the stretches of the spring 2 in two principle axes.

The two principles stresses are expressed as

$$\sigma_1 = \frac{\mu_A\left(\lambda_1^2-\lambda_1^{-2}\lambda_2^{-2}\right)}{1-\left(\lambda_1^2+\lambda_2^2+\lambda_1^{-2}\lambda_2^{-2}-3\right)/J_A}+\frac{\mu_B\left(\lambda_1^{e^2}-\lambda_1^{e^{-2}}\lambda_2^{e^{-2}}\right)}{1-\left(\lambda_1^{e^2}+\lambda_2^{e^2}+\lambda_1^{e^{-2}}\lambda_2^{e^{-2}}-3\right)/J_B}-\varepsilon_0\varepsilon_r E^2\ , \tag{4.30}$$

$$\sigma_2 = \frac{\mu_A\left(\lambda_2^2-\lambda_1^{-2}\lambda_2^{-2}\right)}{1-\left(\lambda_1^2+\lambda_2^2+\lambda_1^{-2}\lambda_2^{-2}-3\right)/J_A}+\frac{\mu_B\left(\lambda_2^{e^2}-\lambda_1^{e^{-2}}\lambda_2^{e^{-2}}\right)}{1-\left(\lambda_1^{e^2}+\lambda_2^{e^2}+\lambda_1^{e^{-2}}\lambda_2^{e^{-2}}-3\right)/J_B}-\varepsilon_0\varepsilon_r E^2\ . \tag{4.31}$$

By modelling the dashpot as a Newtonian fluid, the rate of deformation of the dashpot in Eq. (4.28-4.29) can be described as

$$\frac{d\xi_1}{\xi_1 dt} = \frac{1}{3\eta}\left(\frac{\mu_B\left(\lambda_1^{e^2}-\lambda_1^{e^{-2}}\lambda_2^{e^{-2}}\right)}{1-\left(\lambda_1^{e^2}+\lambda_2^{e^2}+\lambda_1^{e^{-2}}\lambda_2^{e^{-2}}-3\right)/J_B}-\frac{\mu_B\left(\lambda_2^{e^2}-\lambda_1^{e^{-2}}\lambda_2^{e^{-2}}\right)/2}{1-\left(\lambda_1^{e^2}+\lambda_2^{e^2}+\lambda_1^{e^{-2}}\lambda_2^{e^{-2}}-3\right)/J_B}\right), \tag{4.32}$$

$$\frac{d\xi_2}{\xi_2 dt} = \frac{1}{3\eta}\left(\frac{\mu_B\left(\lambda_2^{e^2}-\lambda_1^{e^{-2}}\lambda_2^{e^{-2}}\right)}{1-\left(\lambda_1^{e^2}+\lambda_2^{e^2}+\lambda_1^{e^{-2}}\lambda_2^{e^{-2}}-3\right)/J_B}-\frac{\mu_B\left(\lambda_1^{e^2}-\lambda_1^{e^{-2}}\lambda_2^{e^{-2}}\right)/2}{1-\left(\lambda_1^{e^2}+\lambda_2^{e^2}+\lambda_1^{e^{-2}}\lambda_2^{e^{-2}}-3\right)/J_B}\right), \tag{4.33}$$

where η is the viscosity of the dashpot and is greater than zero.

It should be noted that the viscoelastic model developed by Foo *et al* is not unique. For example, Zhao *et al* [182] has developed a viscoelastic model based on the Neo-Hookean model, in which the Helmholtz free energy density and the principles stresses can be written as

$$W_s = \frac{\mu_A}{2}\left(\lambda_1^2+\lambda_2^2+\lambda_1^{-2}\lambda_2^{-2}-3\right)-\frac{\mu_B}{2}\left(\lambda_1^{e^2}+\lambda_1^{e^2}+\lambda_1^{e^{-2}}\lambda_2^{e^{-2}}-3\right), \tag{4.34}$$

$$\sigma_1 = \mu_A\left(\lambda_1^2-\lambda_1^{-2}\lambda_2^{-2}\right)+\mu_B\left(\lambda_1^{e^2}-\lambda_1^{e^{-2}}\lambda_2^{e^{-2}}\right)-\varepsilon_0\varepsilon_r E^2\ , \tag{4.35}$$

$$\sigma_2 = \mu_A\left(\lambda_2^2-\lambda_1^{-2}\lambda_2^{-2}\right)+\mu_B\left(\lambda_2^{e^2}-\lambda_1^{e^{-2}}\lambda_2^{e^{-2}}\right)-\varepsilon_0\varepsilon_r E^2\ , \tag{4.36}$$

where μ_A and μ_B are the shear moduli of the two springs in Neo-Hookean model.

And the rate of deformation of the dashpot is

$$\frac{d\xi_1}{\xi_1 dt} = \frac{\mu_B}{\eta}\left(\lambda_1^{e\,2} - \lambda_1^{e\,-2}\lambda_2^{e\,-2}\right), \tag{4.37}$$

$$\frac{d\xi_2}{\xi_2 dt} = \frac{\mu_B}{\eta}\left(\lambda_2^{e\,2} - \lambda_1^{e\,-2}\lambda_2^{e\,-2}\right). \tag{4.38}$$

The Maxwell rheological model described above can be adapted for the characterization of different dielectric materials. For example, when studying silicone DEAs, which have low strain relaxation and creep effects [183], a Kelvin-Voigt model can be used instead. This model removes the nonlinear spring in the second branch in Maxwell rheological model while leaving only the dashpot, as shown in **Figure 4.2** (**b**). On the other hand, when highly viscoelastic VHB acrylic material is used, apart from the strain relaxation and creep phenomena, such material also exhibits high viscosity, as result, a hybrid Kelvin-Voigt-Maxwell rheological model can be adopted, as illustrated in **Figure 4.2** (**c**).

4.4.2 Model of Leakage Current

Electrically, a DEA can be considered as a deformable capacitor, *C*, in series with a resistor, R_s, representing the surface resistance of the compliant electrodes and the connection to the high voltage supply [162]. For ideal capacitors, no current flows through the capacitors at any time when a DC voltage is applied across. However, real capacitors have a leakage current, as a result, a parallel resistor, R_l, is added to this model to capture this phenomenon. A schematic diagram of this electrical model is illustrated in **Figure 4.3**.

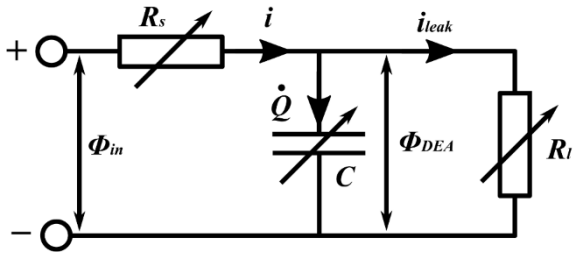

Figure 4.3. Schematic diagram of an electrical model for dissipative dielectric elastomers [162].

The total current flow in the system can be described as

$$i = \dot{Q} + i_{leak}, \tag{4.39}$$

where i is the total current, $\dot{Q}$ is the rate of change of the polarizing charge accumulated on the DEA and i_{leak} is the current leaking through the DEA.

When a voltage Φ_{in} is applied by the high voltage supply, charge flows into the DEA, and rate of charge and voltage across the DEA membrane can be expressed as

$$\dot{Q} = -\frac{1}{R_s C} Q + \frac{1}{R_s} \Phi_{in} , \tag{4.40}$$

$$\Phi_{DEA} = \frac{1}{C} Q . \tag{4.41}$$

Note that the parameters R_s and C are strain dependent. As a result, the strain caused by pre-stretch and actuation deformation should be considered in practical applications.

The current leakage through polymers has been proven to be a complex phenomenon which is affected by several factors such as molecular configuration, impurities, temperature and humidity [162]. Foo *et al* [162] proposed an exponential function based on empirical observations and the density of the leakage current is written as

$$j_{leak} = \gamma E e^{E/E_b} , \tag{4.42}$$

where γ is the conductivity at low field, and E_b is a constant with the unit of electric field.

4.5 A Generalized Cone DEA Model

A generalized cone DEA has a piece of dielectric elastomer bonded to a rigid ring and a smaller central disk. A protrusion force (can be spring force, gravitational force, magnetic force, etc.) causes the membrane together with the central disk to deform out-of-plane. When a voltage is applied across the DEA electrodes, the electrostatic pressure causes the membrane to become 'softer', hence the membrane is deformed out-of-plane further under the protrusion force. Despite the various cone DEA configurations developed, existing cone DEA models were based on specific configurations, which means that one model cannot be readily used in another variation of cone DEAs. This thesis aims to develop a generalized dynamic model for cone DEAs which can be easily adapted to different variations by utilizing the pre-developed hyperelastic and viscoelastic models and the well-studied thermodynamic framework. This generalized model offers a useful framework for studying the dynamic response and performance optimization of cone DEAs with varying biasing elements later in this thesis.

4.5.1 Cone DEA Mechanical Model

Several conical shaped DEA models have been proposed in the past, for example, a quasi-static model based on the thermodynamic equilibrium and geometric relationships [184]. This model can capture the non-truncated membrane shape and concomitant inhomogeneous stress distribution. The viscoelastic behaviour of a conical DEA has been investigated in [185] [186] by including time-dependent viscosity into this model. Despite the fact that this model can capture the inhomogeneous stress and strain distribution of a conical shaped DEA, it has the significant drawback of heavy computational cost because of the shooting method used in the numerical method to solve a set of partial differential equations and algebraic equation to meet the boundary conditions [184]. This computationally intensive model makes it challenging to predict the dynamic responses of a conical DEA with the constantly changing actuation voltage and boundary conditions (e.g. force, displacement). To cope with this issue, a commonly used approximated cone DEA model assumes a truncated cone shape and a homogeneous stress distribution on the deformed DEA membrane [32] [33] [35] [97] [169]. This model significantly reduces the computational cost for dynamic modelling and has been widely verified against experimental data. For these reasons, the proposed dynamic cone model in this work is developed based on the same assumption of a truncated cone shape.

First, the following simplifying assumptions are defined: (**i**) this is a single degree-of-freedom system, i.e. only translation along the vertical axis is modelled here; (**ii**) the deformation is truncated conical, as illustrated in **Figure 4.4** (**c**); (**iii**) the strain distribution on the membrane is homogenous; (**iv**) the circumferential deformation of the membrane does not vary.

Figure 4.4 illustrates the general concept of the formation of a cone shaped DEA. At the reference state, the dielectric elastomer does not experience any stretch, λ, and has an initial thickness H_0. The membrane is then stretched biaxially by $\lambda_p \times \lambda_p$ and bonded to a rigid circular frame with the inner radius, b, and a central disk with the radius, a. Assuming the membrane has a constant volume (i.e. the principle stretches $\lambda_1\lambda_2\lambda_3 = 1$), the current thickness is $H_1 = H_0/\lambda_p^2$. The radial stretch is $\lambda_1 = \lambda_p$ and the circumferential stretch is $\lambda_2 = \lambda_p$. An actuation voltage, Φ_{in}, is applied across the electrodes and a protrusion force, F, is applied on the central disk, causing the membrane to deform out-of-plane. As the membrane undergoes an out-of-plane deformation, d, the membrane is stretched further radially and shifted from its original position by an angle, α. The new radial stretch can be defined as

$$\lambda_1 = \frac{\sqrt{d^2+(b-a)^2}}{(b-a)}\lambda_p \,, \tag{4.43}$$

and based on assumption (**iv**), the circumferential stretch, $\lambda_2 = \lambda_p$, remains unchanged during out-of-plane deformation.

The current membrane thickness can be written as

$$H = \frac{H_0}{\lambda_1 \lambda_2} . \tag{4.44}$$

The angle between the membrane and the horizontal plane, α, can be expressed as

$$\sin \alpha = \frac{d}{\sqrt{d^2 + (b-a)^2}} . \tag{4.45}$$

The free body diagram of the central mass is shown in **Figure 4.5** and at the displacement, *d*, the force balances of the central mass in the vertical axis yields

$$m\ddot{d} + mg + \sin \alpha \int dF_{DEA} = F , \tag{4.46}$$

where m is the mass of the central mass, $\ddot{d}$ is the vertical acceleration of the central mass, g is the gravitational acceleration and $\int dF_{DEA}$ is the total radial force exerted by the membrane on the central mass.

By assumption (**iii** & **iv**), the radial stress, σ_1, is assumed to be constant with respect to the cross-sectional area, and $\int dF_{DEA}$ in Eq. (4.46) can be expressed as

$$\int dF_{DEA} = \int_0^{2\pi} aH\sigma_1 \, d\varphi \ , \ \varphi \in [0, 2\pi] , \tag{4.47}$$

which yields

$$\int dF_{DEA} = 2\pi aH\sigma_1 . \tag{4.48}$$

With a voltage Φ_{in} applied to the membrane, the instantaneous voltage on the DEA, Φ_{DEA}, can be different from the input voltage due to the charge flow in/out the DEA, as described in the last section. The instant electric field across the membrane, E, can be described as $E = \Phi_{DEA}/H$. A complete electrical model will be developed in the next section.

The radial stress, σ_1, is obtained from the viscoelastic model developed by Foo *et al* [162] as described in the last section.

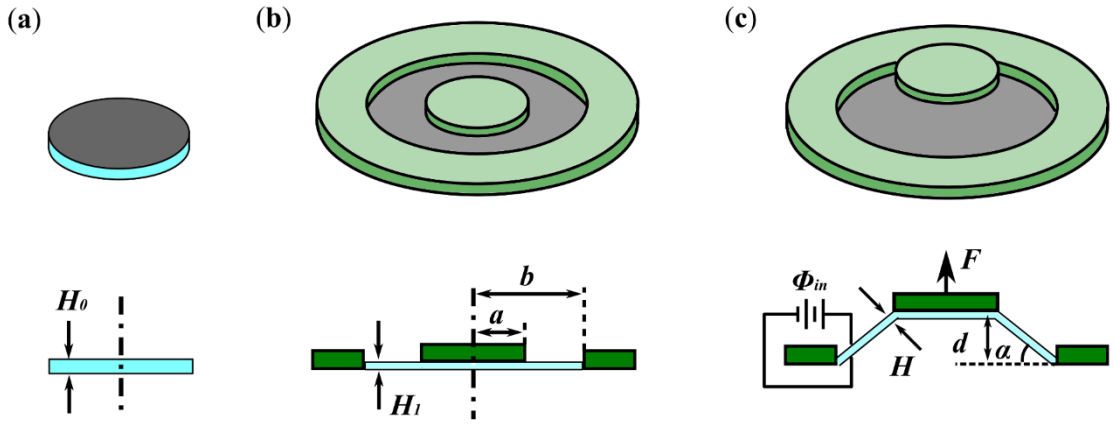

Figure 4.4. Schematic diagram of a conical DEA geometry. (**a**) A piece of circular dielectric elastomer in its initial state. (**b**) Elastomer membrane being stretched biaxially and then bonded to rigid frames. (**c**) When the centre is deformed out-of-plane, the DEA forms a conical shape.

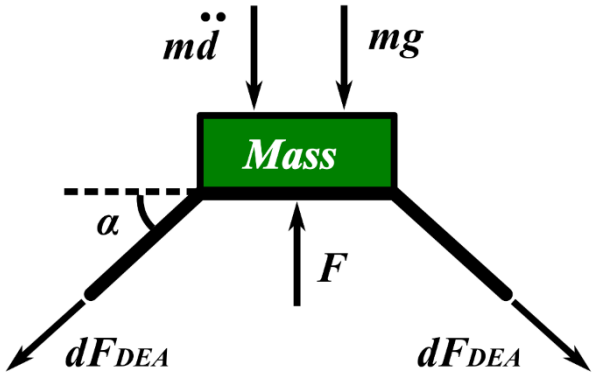

Figure 4.5. Free body diagram of the central mass on the cone DEA.

4.5.2 Cone DEA Electrical Model

Electrically, a cone DEA is a capacitor with changing capacitance. By using a parallel-plate capacitor formula, we assume the capacitance of the cone DEA is a function of the out-of-plane deformation

$$C(d) = \varepsilon_0 \varepsilon_r \frac{A}{H}, \tag{4.49}$$

where A is the area of the electrode, and is given as $A = \frac{\pi(b^2 - a^2)}{\cos\alpha}$, and H is the thickness of the membrane at the displacement d, as given in Eq. (4.44).

The leakage current is given as

$$i_{leak} = A j_{leak} = A\gamma E e^{E/E_b}. \tag{4.50}$$

The surface resistance, R_s, is assumed to be constant [169] and does not vary with the deformation, d.

The instantaneous voltage on the DEA, Φ_{DEA}, can be estimated with a given input voltage Φ_{in} by combining Eq. (4.49) with the electrical model described in the last section (Eq. (4.40, 4.41, 4.42)).

4.5.3 Cone DEA Model Summary

This section developed a numerical model that describes the dynamic response of a generalized cone DEA. This numerical model requires the actuation voltage, Φ_{in}, to be defined and this is usually the case as for most of applications where voltage input is the pre-defined control signal. For this model to be used in a specific cone configuration, the force-displacement relationship of the biasing element is required, for example, a linear spring basing element with the force-displacement function of $F = F_0 - kd$, where F_0 is a force constant and k is the stiffness. The physical meanings of each model parameters and their validation methods are summarized in **Table 4.1**. Two main experimental approaches are adopted in this thesis to validate these parameters:

- The first is the quasi-static force-displacement test, where the DEA membrane is deformed by a linear motor at a sufficiently low rate, and the reaction force on the membrane is measured simultaneously. The viscoelastic effect is neglected here and the parameters μ_A and J_A can be estimated from Eq. (4.48).
- The second is the dynamic oscillation test. The DEA is actuated by an alternating current voltage and the displacement is recorded simultaneously. The viscoelastic parameters μ_A, J_A *and* η can be estimated by fitting the modelling results with the experimental measurements.

With the initial conditions given (deformation, d, charge in the DEA, Q, radial strain of the viscoelastic element, ζ), the state of the DEA at the next time step can be estimated by solving a set of ordinary differential equations (ODEs) (Eq. (4.46, 4.32, 4.33)). If the force-displacement relationship of the biasing element is also time-dependent, for example, antagonist double cone configuration, its protrusion force at each time step can still be estimated by solving a separate set of ordinary differential equations. The structure of this cone DEA model is illustrated in **Figure 4.6**. In conclusion, this numerical model offers a simple and cost-effective dynamic framework, enables the fast performance prediction and optimization for various cone DEA designs.

Table 4.1. Physical meanings of each model parameters and their validation methods adopted in this thesis.

Model parameter	Physical meaning	Related subsystem	Validation method
μ_A	shear modulus of the spring on the first branch (Gent model)	Mechanical model	Quasi-static force-displacement tests
J_A	a constant related to the limit stretch of the spring on the first branch (Gent model)		
μ_B	shear modulus of the spring on the second branch (Gent model)		Dynamic oscillation tests
J_B	a constant related to the limit stretch of the spring on the second branch (Gent model)		
η	viscosity of the dashpot		
C	Capacitance of the DEA	Electrical model	Calculating from Eq. (4.49)
R_s	Serial resistance of the DEA		Charging/ discharging tests
ε_r	dielectric constant	Electro-mechanical coupling	Obtaining from the manufacturer

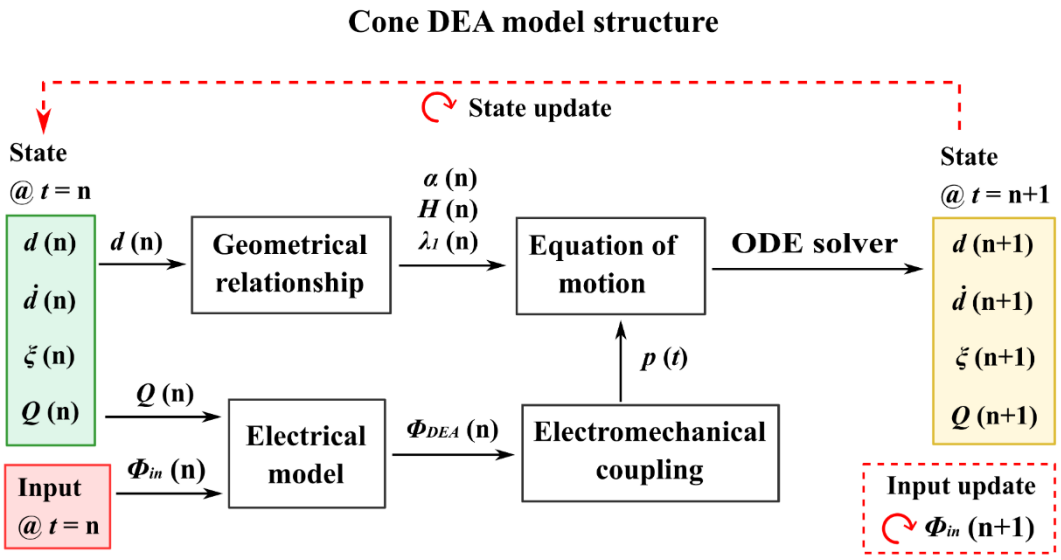

Figure 4.6. Illustration of the cone DEA model structure.

4.6 Chapter Summary

In this chapter, a free-energy based modelling framework for DEAs is reviewed, dissipation of dielectric elastomers, including viscoelasticity and leakage current are considered using a nonequilibrium thermodynamics framework. A generalized cone DEA model describing the dynamic electromechanical response is developed based on this free-energy framework. This generalized model can be applied to any cone DEA configurations by replacing the generalized protrusion force by the specific biasing element. This model offers a simple yet powerful tool to characterize the dynamic response of a cone DEA and to optimize its performance.

Chapter 5: Dielectric Elastomer Oscillator

In this chapter, the design of a novel circular dielectric elastomer oscillator (DEO) based on the cone DEA configuration is presented. The proposed DEO has a planar configuration in its rest state. However, due to the inherent elasticity of the elastomer, when excited at its resonant frequencies, the membranes can deform out-of-plane by a large amplitude. Based on the low-profile planar configuration and large out-of-plane resonance of the DEO design, a novel monolithic gripper integrating electroadhesion (EA) and the DEO is developed in this chapter. This gripper solves the slow de-adhesion issue of common EA grippers by using a DEO to force the release. The EA-DEO gripper is evaluated against various lightweight and flexible objects and an improvement in de-adhesion speed of at least two orders of magnitude is found.

Statement: The DEO design presented in Section 5.1-5.3 in this chapter is adapted from the following publication where C. Cao is the first author.

- **Cao, C**., Hill, T.L. and Conn, A.T., 2019. On the nonlinear dynamics of a circular dielectric elastomer oscillator. *Smart Materials and Structures*. 28(7) p. 075020.

Contribution: Fabrication and testing methodology, investigation, data curation, formal analysis, writing original draft; review & editing.

The EA-DEO gripper design presented in Section 5.4 in this chapter is adapted from the following publication where C. Cao is the co-first author with Dr Xing Gao.

- Gao, X., **Cao, C. (joint first author)**, Guo, J. and Conn, A.T., 2019. Elastic electroadhesion with rapid release by integrated resonant vibration. *Advanced Materials Technologies*. 4(1) p.1800378.

Contribution: Joint fabrication and testing methodology, joint investigation, joint data curation, joint formal analysis, joint writing-original draft; joint review & editing.

5.1 DEO Design

5.1.1 Design Overview

The DEO design follows the same principle as the cone DEA design described in Chapter 4, where a piece of biaxially pre-stretched elastomer is bonded to a circular frame and a central disk with a smaller diameter, as illustrated in **Figure 5.1** (**a**). Note that it differs from the other cone DEA designs in that no additional protrusion force is applied to the central disk. The mass of the elastomer, compliant electrodes and the central disk is too low to cause a noticeable out-of-plane deformation under gravity

(in contrast, a sufficiently heavy central disk can serve as the biasing element to form a conical configuration, as shown in [33]), which gives an approximately planar configuration in its rest state. This design has the advantages over other cone DEAs in terms of light weight, ease of fabrication and simplicity of structure. Despite the planar configuration in the rest state, such DEOs can exhibit out-of-plane deformation at resonance, as have been demonstrated in [19] [187] [172] [188] [189]. In [19], a stretchable and transparent DEO loudspeaker was demonstrated with the capability of operating at frequencies over 10 kHz. In [188], a vibrational robot with a DEO as the excitation source was developed and different resonant modes were utilized for steering. In contrast to the previously reported circular DEOs with no central disks, the central disk in this design restricts the boundary condition of the membrane into a conical shape, which allows a simpler modelling process, and the added inertia can potentially amplify the amplitude and tune the resonant frequency of the DEOs.

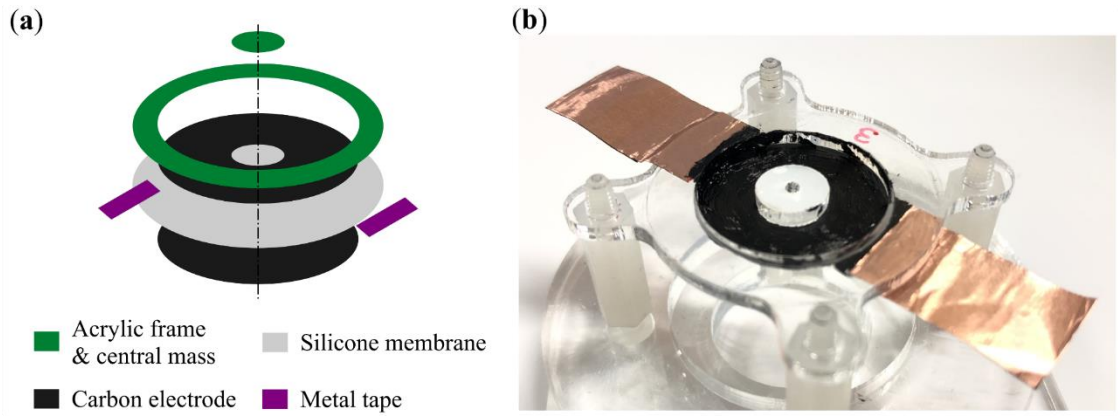

Figure 5.1. DEO design illustration. (**a**) Exposed assembly view of the dielectric elastomer oscillator. (**b**) Photo of the fabricated prototype.

5.1.2 DEO Fabrication

To fabricate the DEO, an off-the-shelf silicone elastomer (ELASTOSIL, thickness 50 μm, Wacker Chemie AG) was used as the membrane. The selection of silicone material instead of common VHB acrylic material is due the significantly lower viscoelasticity of silicone which allows it to have a faster response and a higher bandwidth, as discussed in Section 3.2. The membrane was first pre-stretched biaxially by a ratio of $\lambda_p \times \lambda_p$, and then bonded to an acrylic ring (20 mm inner diameter) using silicone adhesive (Sil-poxy, Smooth-On). An acrylic disk (0.1 g, 8 mm outer diameter) was bonded to the centre of the membrane using the same method. Copper tapes were used as the connection between the carbon electrodes and high voltage cables. A fabricated prototype of this DEO design is shown in **Figure 5.1** (**b**).

5.2 Development of Custom Electrode

As an essential part of any DEA, idealised compliant electrodes shall have good conductivity across a large range of strains and have minimum impact on the stiffness of the dielectric elastomer. Commercially available carbon grease (such as MG 846, MG Chemicals, used in this study) has the problem of diffusion into the silicone elastomer which can cause swelling of the elastomer, thus affecting the performance of the DEA [104] [106]. This is believed to be due to the silicone oil solvent being absorbed by the silicone membrane. Hence in this section, a low cost, easy-to-fabricate custom carbon grease which does not cause swelling of the silicone elastomer is developed. This section reports the fabrication process of this custom carbon grease and the comparison between it and commercially available carbon grease MG 846 and a carbon/elastomer compound.

5.2.1 Fabrication of Carbon Electrodes

In [106], castor oil and carbon black powder have been mixed to make silicone-oil-free carbon grease and it was found to be compatible with ELASTOSIL silicone films, as used in this study. Following their work, a vegetable oil solvent was adopted which is also compatible with ELASTOSIL silicone films but has a much lower viscosity (< 0.06 Pa·s at 26 ˚C [190]) with added benefits of low-cost and high commercial availability. Three custom carbon greases, with different carbon black to vegetable oil weight ratios of 10 %, 15 % and 20 %, were fabricated. The fabrication process is described as follows. First, 10/15/20 wt.% carbon black powders (1333-86-4, Cabot Corporation, USA) and 90/85/80 wt.% vegetable (rapeseed) oil (ASDA, UK) were added to a mixing cup. The mixture was first stirred by a mixer (Model 50006-13, Cole-Parmer, UK) at the speed of 100 rpm for 1 min and then 600 rpm for 5 mins to achieve a homogenous dispersion. Carbon-vegetable-oil mix with carbon powder greater than 20 wt.% was found to be too viscous to be mixed by the mixer, hence a 20 wt.% carbon powder was set as the upper limit for this custom carbon grease. Fabricated carbon grease, as well as commercial carbon grease, MG 846, were applied to the silicone elastomer by a hand brush.

A carbon/elastomer compound electrode was fabricated by mixing 10 wt.% carbon powder and 90 wt.% uncured silicone (Ecoflex 20, Smooth-on, USA) using the same method and applied on the dielectric elastomer using a mask and scraper and left to cure for 24 hours at room temperature (20 ˚C) (following [191]).

5.2.2 Effect of Electrode Type on the Mechanical Response of DEOs

First, the effects of different compliant electrodes on the mechanical properties of the silicone membrane were investigated. The experiment is described as follows. The fabricated DEO samples were fixed to the testing rig, a linear rail (X-LSQ150B-E01, ZABER) deformed the centre of the DEO membrane out-of-plane from 0 to 6 mm at a low velocity of 0.05 mm/s and a load cell (NO.1004, TEDEA) was used to measure the reaction force of the DEO. The detailed experimental setup can be found in Section 5.3.1.

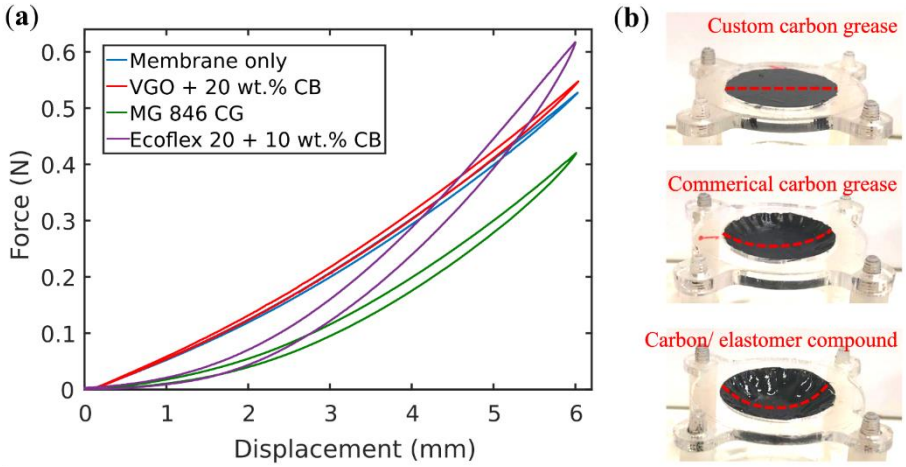

Figure 5.2. Comparison of the effects of different carbon electrodes on the mechanical properties of DEOs. (**a**) Force-displacement curves of the DEO samples with no electrode (blue), vegetable oil + 20 wt.% carbon black (red), carbon grease MG 846 (green), Ecoflex 20 + 10 wt.% carbon black (violet). Silicone elastomers were pre-stretched by λ_p = 1.2 × 1.2. (**b**) Physical appearance of the DEOs with different carbon-based electrodes. Top: custom carbon grease; middle: commercial carbon grease; bottom: carbon/elastomer compound. No pre-stretch for the membranes. Photos were taken 48 hours after the electrodes were applied. (CG = carbon grease, VGO = vegetable oil, CB = carbon black)

In **Figure 5.2** (**a**), the quasi-static force-displacement curves of the DEOs with different electrodes are shown. The custom carbon grease only caused a negligible increase in the net stiffness, while both commercial carbon grease MG 846 and the carbon/elastomer compound caused a significant softening effect on the membrane at small displacements. As the displacement increases, the added stiffness from the carbon/elastomer compound clearly increased the overall stiffness of the DEO. It can also be noted that, for these three electrodes, custom carbon grease shows the smallest hysteresis, which suggests a lower viscosity during dynamic actuation. Apart from the effect on the stiffness of the elastomer, the swelling effect can be more visible on the physical appearance. **Figure 5.2** (**b**) compares the DEOs with

the three different electrodes applied. No pre-stretch was applied to the silicone membranes to demonstrate the swelling effect more clearly. One can see that the membrane with custom carbon grease shows no wrinkles and the membrane remained flat. However, for commercial carbon grease and carbon/elastomer electrodes, wrinkles can be cleared observed, and membranes buckled due to swelling.

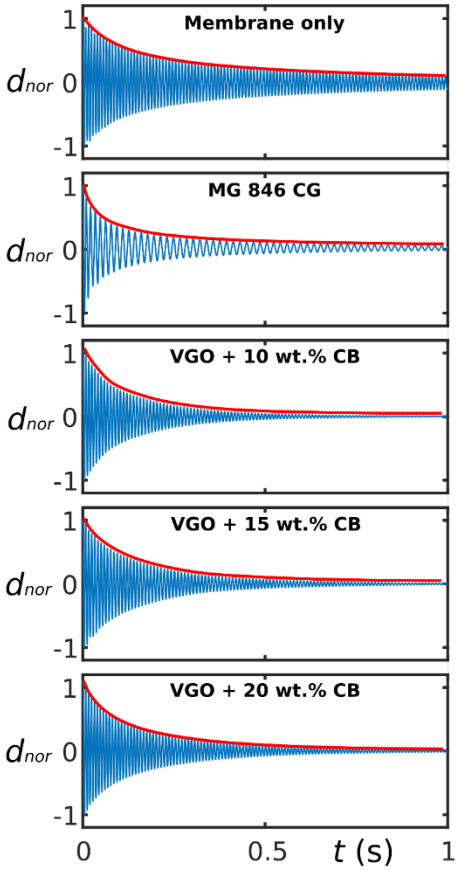

Figure 5.3. Passive step response of the DEOs with no electrode, MG 846, custom carbon grease with 10, 15 and 20 wt.% carbon black powder. d_{nor} is the normalized displacement ($d_{nor} = d/d_0$) (CG = carbon grease, VGO = vegetable oil, CB = carbon black).

A second characteristic was investigated by measuring the damping of the electrodes. Since the carbon/elastomer compound causes the most severe swelling effect in **Figure 5.2**, in the following comparison, this electrode type is not included. To investigate the effect of carbon black concentration on the damping of DEOs, a step disturbance was applied to the DEO and the decaying displacement of the DEO as a function of time was recorded. The DEO samples were fixed to the testing rig, and the central mass of each DEO sample was stretched out-of-plane by 4 mm via a string and fixed. The string was then cut off to allow the mass together with the membrane to oscillate freely. A laser displacement

sensor was used to measure the decaying displacement after the step disturbance. Detailed time-displacement results are plotted in **Figure 5.3**. For DEO samples with 10, 15 and 20 wt.% carbon greases, the decaying time constants (the time it takes for the amplitude to decay to 36.8 % of its initial value) are 0.120 s, 0.135 s and 0.138 s respectively. As a comparison, the time for DEOs with MG 846 was 0.09 s. This result suggests that despite the increase in carbon black concentration and the more viscous feel during fabrication, 20 wt.% carbon grease does not cause an increase in the damping coefficient of the system and the damping effect of the custom carbon grease is lower than MG 846. Reduced damping will allow a greater resonant amplitude of the DEO, which can be advantageous in dynamic applications.

5.2.3 Compliant Electrode Surface Resistance Measurements

In this test, the surface resistance of the custom carbon grease with different carbon concentrations and commercial carbon grease MG 846 were compared. Long and thin rectangular strips of carbon grease were hand brushed on a flat acrylic sheet and the length and width of these strips are 50 mm and 10 mm respectively (5:1 aspect ratio as recommended by [192]). Care has been taken to ensure an even electrode thickness. A high-precision LCR meter (E4980AL, Keysight) was utilized to measure the surface resistance at 1,000 Hz. Copper tapes serve as the connection between the carbon grease and the LCR meter cables. Three samples were prepared for each concentration of carbon grease.

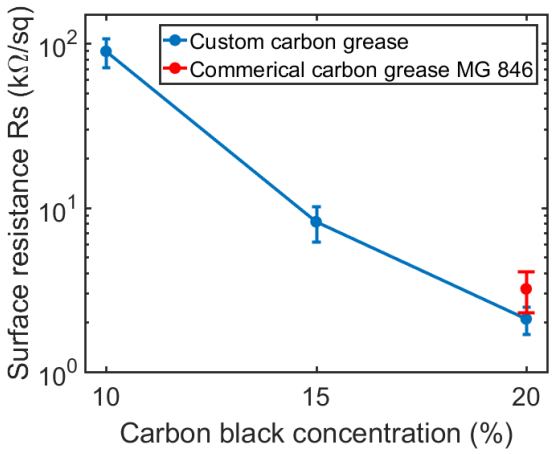

Figure 5.4. Measured surface resistance of the commercial carbon grease (20 wt.% carbon black powder), custom carbon grease with 10, 15 and 20 wt.% carbon black powder.

The experimental results are compared in **Figure 5.4**. As the concentration of the carbon black increases, the surface resistance reduces dramatically, resulting in a significantly improved

conductivity. As the concentration reached 20 wt. %, which is the same as the MG 846, the custom carbon grease shows a lower surface resistance than MG 846 (2.1 kΩ/sq comparing to 3.2 kΩ/sq). This suggested that the custom carbon grease has an improved conductivity, which can reduce the RC time constant and improve the DEO's electrical response. By considering the conductivity and the low damping effect, custom carbon grease with 20 wt.% carbon particles was considered the best-performing overall and was adopted for the rest of this thesis.

5.3 DEO Performance Characterization

5.3.1 Experimental Setups

Quasi-static force-displacement test setup. To measure its quasi-static force-displacement relationship, the DEO frame was fixed to the testing rig and a linear rail (X-LSQ150B-E01, ZABER) deformed the centre of the DEO membrane out-of-plane at a low velocity of 0.05 mm/s to ensure negligible viscoelasticity, as illustrated in **Figure 5.5**. A constant voltage was generated by a high voltage amplifier (5HV23-BP1, Ultravolt) and was applied to the DEO during deformation to analyse the effect of electric field on the force-displacement relationship. The voltage amplitude was determined by $\Phi = E\lambda_p^2/H_0$, where E = 50 V/μm. A load cell (NO.1004, TEDEA) was used to measure the reaction force of the DEO and a laser displacement sensor (LK-G152 and LKGD500, Keyence) was used to measure the deformation of the DEO membrane. All signals were collected by a DAQ device (National Instruments, BNC-2111) at a sampling frequency of 10,000 Hz and controlled by MATLAB (MathWorks).

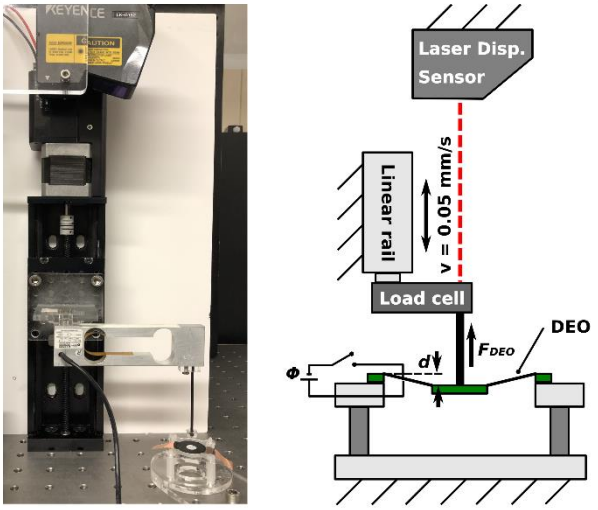

Figure 5.5. Photo and schematic diagram of the experimental setup for quasi-static force-displacement measurement.

Dynamic test setup. A frequency sweep test was performed to investigate the dynamic response of the DEO. The experimental setup is shown in **Figure 5.6**. The same laser displacement sensor and DAQ device from quasi-static test setup were used here. The DEO frame was fixed to the testing rig, while leaving the central mass to move freely. A varying-frequency sinusoidal voltage signal was generated by MATLAB and applied to the DEO via a high voltage amplifier. A laser displacement sensor measured the out-of-plane deformation of the DEO at a sampling frequency of 40,000 Hz. The excitation frequency was swept forward from 0 to 300 Hz (300 to 0 Hz for a backward sweep) at the rate of 1 Hz/s, generated by MATLAB using the 'chirp' function (the DC biasing voltage, Φ_{DC} , and the AC voltage amplitude, Φ_{AC}, are determined by $\Phi_{DC} = E_{DC}\lambda_p^2/H_0$, $\Phi_{AC} = E_{AC}\lambda_p^2/H_0$ and a value of E_{DC}=E_{AC}=25 V/μm was used in the test). As the frequency will vary continuously during this test, the system will not reach its steady state. To account for this, a second test, where the frequency was varied in discrete steps, was also adopted. These steps are given by the voltage signal : $\Phi(t) = \Phi_{DC} + \Phi_{AC} \sin 2\pi f t$ with the frequency f stepped up from 1 to 300 Hz then down to 1 Hz by steps of 0.1 Hz, 20 cycles of excitation signals were repeated at each frequency to ensure the DEO reached a steady-state response.

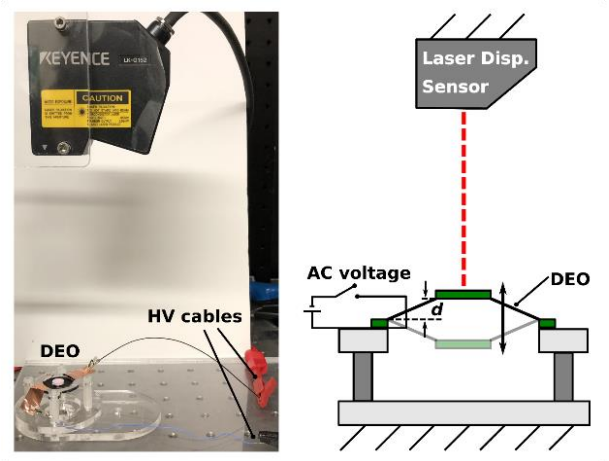

Figure 5.6. Photo and schematic diagram of the experimental setup for active dynamic tests.

5.3.2 Model Validation

The dynamic model developed in Section 4.5 is used to characterize the performance of the DEOs by having biasing force F = 0 (i.e. the only biasing element for the DEO is gravitational force, which has been taken into account apart from the additional biasing force, F, in the generalized model in Section 4.5). The adapted model is verified against quasi-static and dynamic experimental tests in this subsection.

Quasi-static response. The experimental result and model prediction of the quasi-static force-displacement relationship of the DEOs with different pre-stretch ratios are shown in **Figure 5.7**. The model parameters were determined by fitting to the experimental results using a least-mean-squares algorithm in MATLAB (following [32] [33]). The identified Gent model parameters are: μ_A = 433.6 kPa, J_A = 20.22. A relative permittivity ε_r = 2.8 was adopted in this model for ELASTOSIL elastomer, as measured by the manufacturer (Wacker Chemie AG). As can be seen in **Figure 5.7** (**a**-**c**), the model agrees very well with the experiments for all three pre-stretch ratios. Note that the force-displacement relationship is nonlinear with a stiffening effect, which suggested that its dynamic response will also be nonlinear.

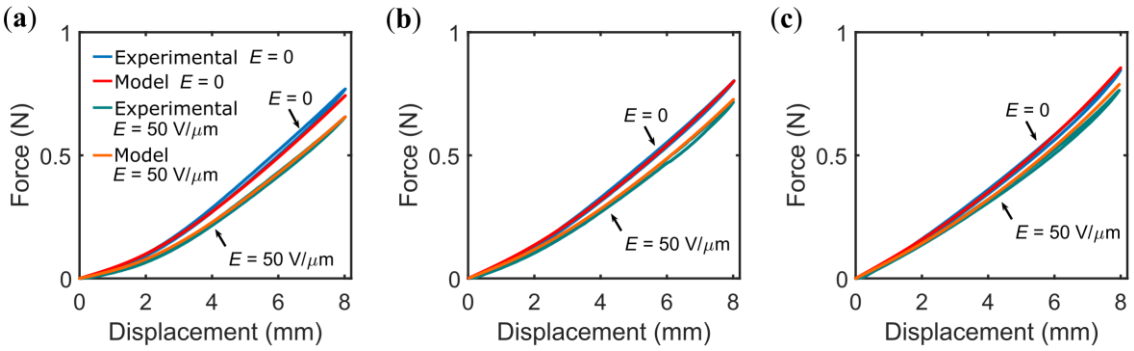

Figure 5.7. Model validation: quasi-static force-displacement relationship with and without actuation voltage. (**a**) λ_p = 1.1 × 1.1; (**b**) λ_p = 1.2 × 1.2; (**c**) λ_p = 1.3 × 1.3.

***Dynamic response*. Figure 5.8** (**a**-**b**) shows the experimental results of forward and backward frequency sweep and the model prediction is shown in **Figure 5.8** (**c**-**d**). The model parameters related to the viscoelasticity of the elastomer were identified from the forward frequency sweep test with the values μ_B = 400 kPa, J_B = 20, η= 2 kPa·s. Note that electrical response of the DEO is not considered in this dynamic model as the measured RC constant is less than 10^{-4} s, hence it is safe to be neglected within the frequency range of 1 to 1000 Hz. The nonlinearity of this DEO can be clearly observed from the frequency sweep experimental results and model predictions. The amplitude of the DEO is very close to zero at low frequencies, and large amplitudes only occur at the resonance, where the amplitude increases with the increasing frequency before dropping sharply after the resonant frequency in the forward frequency sweep. On the contrary, in the backward frequency sweep, as the frequency decreases, the amplitude jumps suddenly from an extremely low value to its peak and then reduces as the frequency decreases. Also note the peak amplitude in the backward sweep is much lower than that in the forward sweep (13.5 mm at f = 275 Hz for forward sweep and 3.8 mm at 219 Hz for backward sweep). Note that the two large peaks shown in **Figure 5.8** (**a**) belong to the first resonant mode where

the deformation of the membrane is axially symmetrical, and the largest deformation is in the centre, as demonstrated in the high-speed photos in **Figure 5.9** (**a**). Further increasing the frequency causes the DEO to vibrate at its second resonant mode, as is shown in **Figure 5.9** (**b**). The second resonant mode cannot be characterized using this numerical model where a single DOF assumption was made.

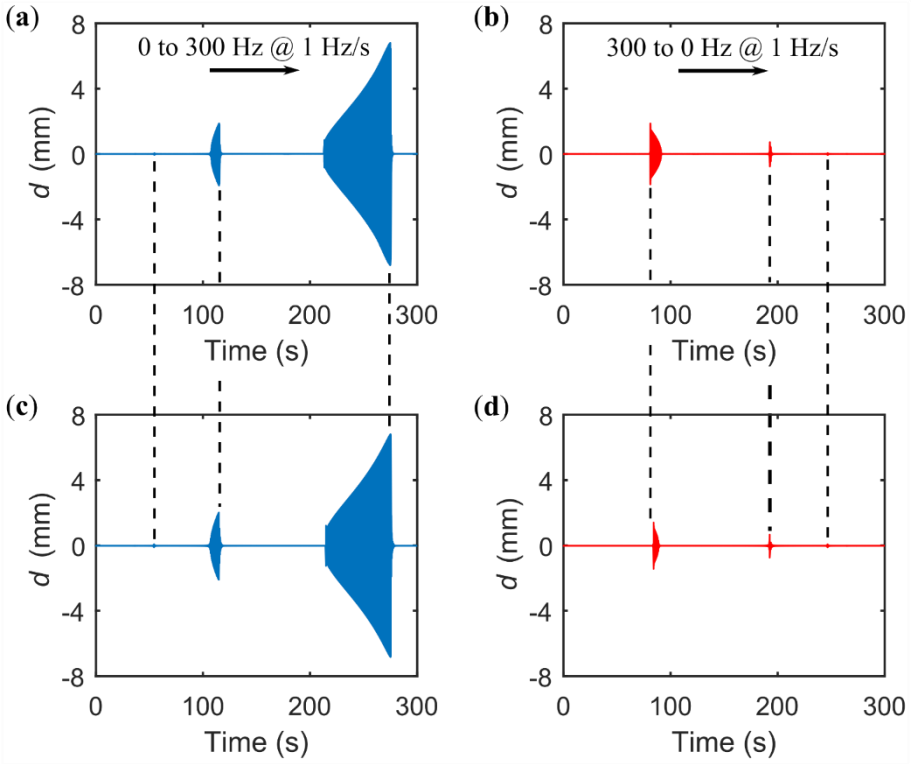

Figure 5.8. Model validation: frequency sweep test. (**a**) Measured displacement of the DEO in a forward sweep and (**b**) a backward sweep. (**c**) Modelled displacement of the DEO in a forward sweep and (**d**) a backward sweep.

It is worth noting that the maximum stroke of the DEO in the forward frequency was measured at 13.5 mm, which is 67.5 % relative to the membrane diameter. By contrast, in previous studies, the demonstrated resonant stroke was much smaller relative to the membrane diameter, for example, ~ 4 % stroke in [187] and ~ 7 % in [172] using VHB acrylic elastomer. It should be noted that the high out-of-plane deformation of the silicone can potentially lead to mechanical rupture. By using the model developed in Section 4.5, the maximum radial stretch during deformation is estimated at 1.85, which is significantly lower than the elongation at break value of 4.5 reported by the manufacturer (Wacker Chemie AG).

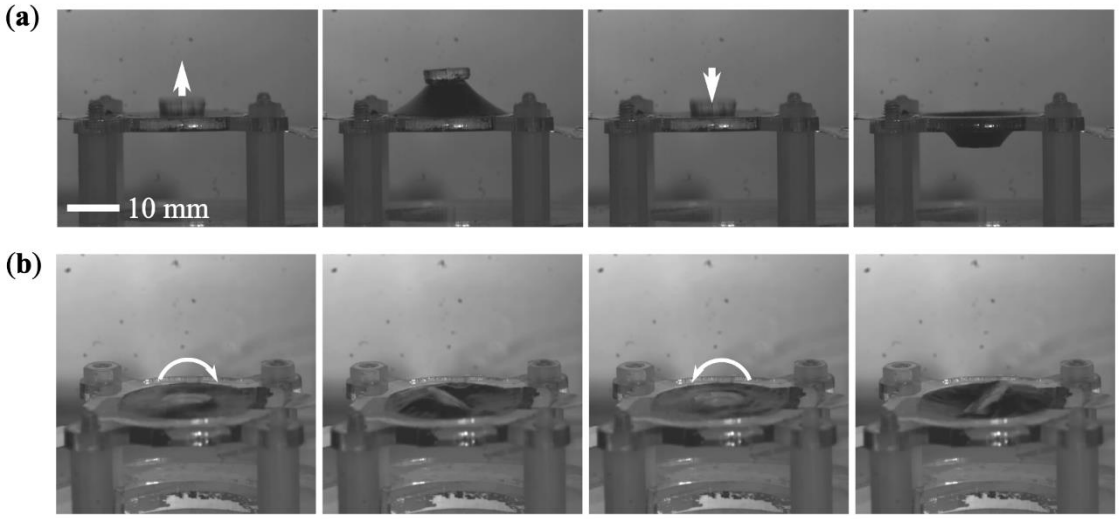

Figure 5.9. High-speed video frames of the DEO oscillating out-of-plane. (**a**) First resonate mode and (**b**) Second resonate mode.

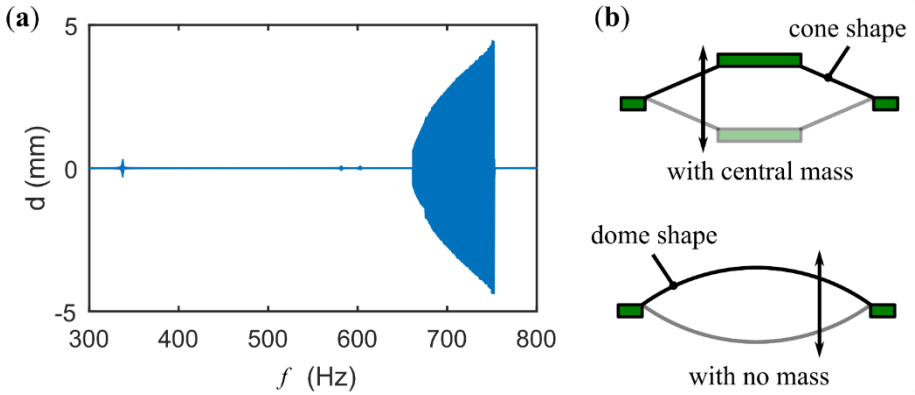

Figure 5.10. Dynamic response of the DEO with no central mass attached. (**a**) Frequency sweep of a DEO with no added mass from 300 to 800 Hz at a rate of 1 Hz/s. (**b**) Comparison of the geometrical profiles of DEOs with added central mass (top) and no added mass (bottom). With central mass attached, the geometry is close to a conical shape; when no mass is attached, it becomes a dome shape.

To illustrate the function of the central mass in this DEO design, a comparison was made by running a similar forward frequency sweep on a DEO sample with no central mass attached to the membrane and the experimental result is shown in **Figure 5.10** (**a**). One significant difference between DEOs with and without a central mass is the resonant frequency. Without the mass attached, the excitation frequency where the highest peak occurs was found at ~ 750 Hz, while the one a 0.1 g mass has its peak at 275 Hz. Another difference is in the deformation shape, as the DEOs with mass attached in the centre have an approximated conical shape, while the one without mass is closer to a dome shape, as illustrated in

Figure 5.10 (**b**). The difference between the DEOs with and without central mass suggests that the central mass adds an additional variable to the system, which can tune the resonant frequency of the system in a wide range based on the desired output in any specific applications.

5.3.3 Frequency Domain Analysis

Figure 5.11 shows the measured time domain data of the DEO in a frequency step experiment where the frequency was increased from 1 to 300 Hz at a step of 0.1 Hz. By using discrete Fourier transform (DFT), **Figure 5.12** (**a**-**b**) plots the fundamental response frequency f_r (which is defined as the frequency of the component with the largest amplitude in a DFT) and amplitude against the excitation frequency f. The last 10 cycles at each frequency (allowing 10 cycles for the DEO to reach a steady state) in a frequency step test was used in the DFTs.

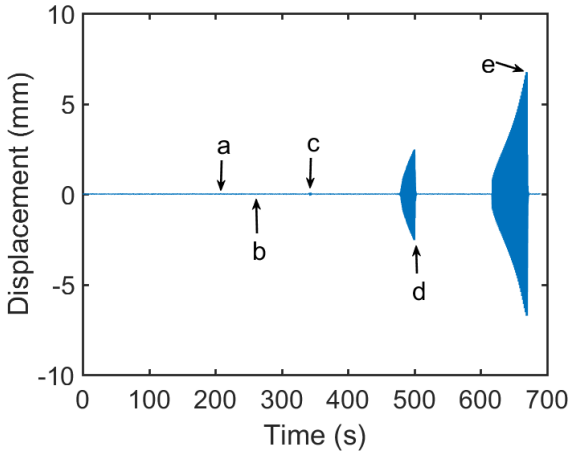

Figure 5.11. Frequency step response experimental results. Five points are marked from **a** to **e** representing five distinguishable types of responses.

It can be seen clearly from **Figure 5.12** (**a**), that for this proposed DEO, the fundamental harmonics do not always match the excitation frequency, and a subharmonic of 1/2 and super-harmonics at 2, 3, 4 can be observed. This is due to the nonlinearity that is inherent in such a system. In **Figure 5.12** (**b**), at the low frequencies (e.g. < 50 Hz), the amplitude is close to zero, a small peak of 0.15 mm can be found at 54 Hz and two significantly larger amplitude peaks occur above 100 Hz. The highest resonant peak is found at 275 Hz with an amplitude of 13.5 mm and the second highest resonant peak is at 118 Hz with an amplitude of 5 mm. It can be noted that the two resonant peaks are distorted to the right and completely different behaviors are obtained for stepping down the excitation frequencies. For example, as the excitation frequency f increases from 200 to 280 Hz, the amplitude gradually increases until it

reaches a point at f = 275 Hz. If f is increased beyond this point, a limit point is approached, and the response jumps down to a lower stable branch. However, when decreasing f from above the resonance point, the amplitude follows the lower branch until 218.8 Hz and suddenly jumps up to the upper stable branch, as illustrated in **Figure 5.12** (**b**). The region between the two jump points is a region with multiple stable solutions, which is characteristic of a forced response of a nonlinear dynamic system [193].

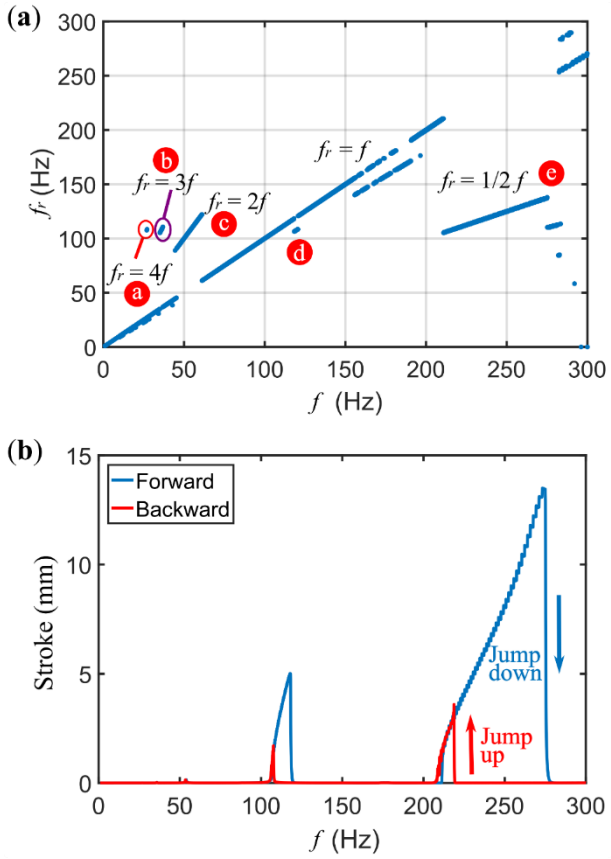

Figure 5.12. Frequency step results in frequency domain. (**a**) Fundamental response frequency against excitation frequency, subharmonics, harmonic and super-harmonic responses can be observed. (**b**) Amplitude against excitation frequency. Jump down and jump up can be noticed in the forward and backward sweep respectively.

Figure 5.13 shows the detailed time series of the input (actuation voltage) and output (displacement) signals and the frequency spectrum of the five points a-e in **Figure 5.12**. Only point d exhibits $f_r = f$ (**Figure 5.13** (**d**)), i.e. the fundamental response frequency is equal to the excitation frequency, while for the other four points a, b, c, and e, the fundamental frequency of the response is different to the excitation frequency, as indicated in the frequency spectra. For point e where the amplitude has the

highest peak (**Figure 5.13** (**e**)), the fundamental response period is twice that of the excitation period and in the frequency spectrum the highest peak is a 1/2 *f* subharmonic. In the other three cases, different integer super-harmonics are observed in **Figure 5.13** (**a**-**c**).

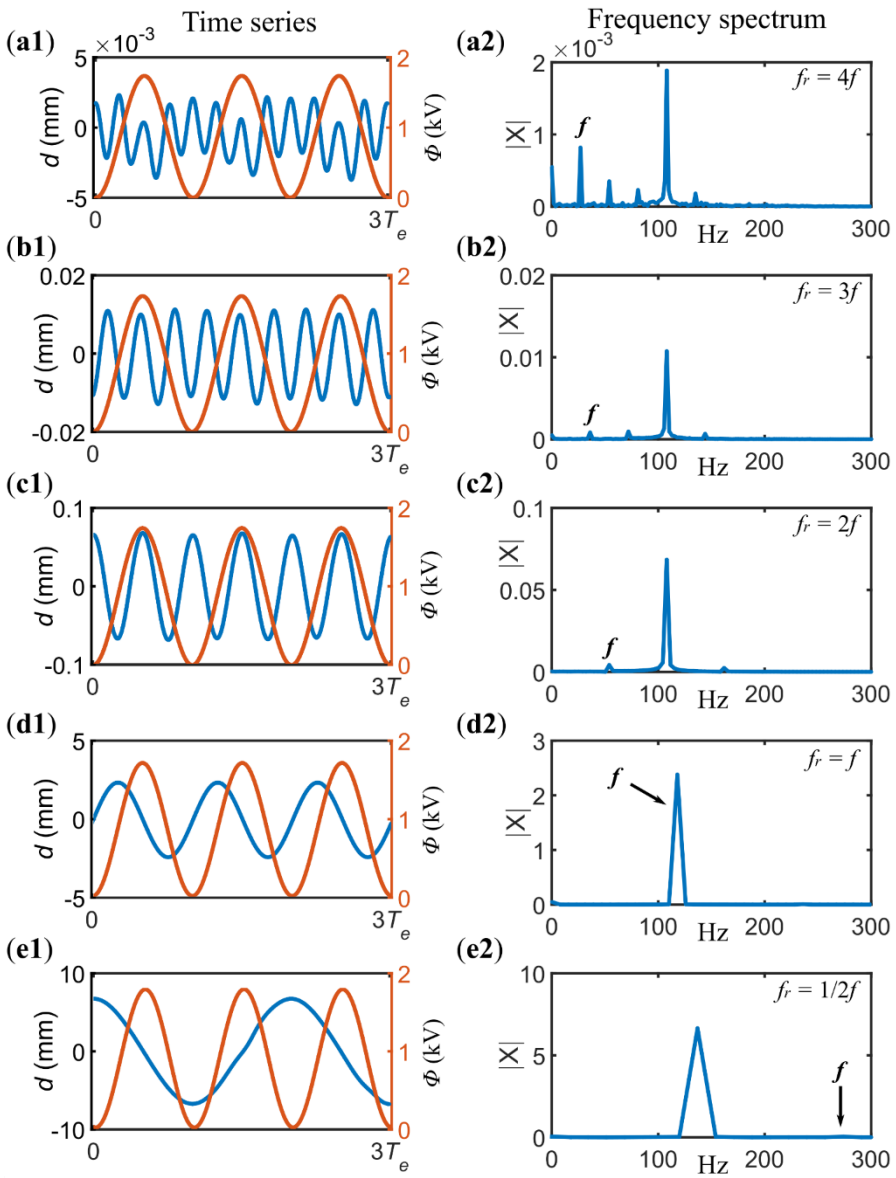

Figure 5.13. Five different frequency responses of the DEO. The time series on the left and the frequency spectra on the right, where d is the displacement of the oscillator, Φ is the actuation voltage and $|X|$ is the absolute value of DFT amplitude. (**a**) $f_r = 4\,f$, $f = 27$ Hz, (**b**) $f_r = 3\,f$, $f = 36$ Hz, (**c**) $f_r = 2\,f$, $f = 60$ Hz, (**d**) $f_r = f$, $f = 118$ Hz, (**e**) $f_r = 1/2\,f$, $f = 275$ Hz.

5.3.4 Further Studies on DEO Dynamics

In this subsection, the effects of varying the DEO parameters on the dynamic responses are investigated. First, the mechanical parameters such as the pre-stretch ratios and the weight of the mass are considered. Second, the effects of the electrical signal (i.e. the AC and DC components) are analysed.

5.3.4.1 Effects of Central Mass and Pre-stretch Ratios

Effects of central mass. First, the effects of the added mass and pre-stretch on the dynamic performance of the DEO are investigated. One parameter was fixed constant while varying the other. **Figure 5.14** (**a1-a3**) shows the experimental and simulated DEO frequency response with different masses (0.1, 0.12 and 0.2 g). The pre-stretch ratio was fixed at λ_p = 1.2 × 1.2 and the same sine wave frequency step test described in Section 5.3.1 with $E_{DC} = E_{AC}$ = 25 V/μm was adopted here. It can be noted that as the mass increases, the resonant stroke increases, and the resonant frequency reduces. The maximum stroke of 15.9 mm was measured with m = 0.2 g, which is equivalent to ~ 80 % relative to the membrane diameter. Also note that the model was able to predict the nonlinear dynamic response of the DEOs with different added masses accurately.

Effects of the pre-stretch ratios. In the second test, the performance of DEOs with different pre-stretch ratios (λ_p = 1.1 × 1.1, λ_p = 1.2 × 1.2, λ_p = 1.3 × 1.3) were compared and the results are shown in **Figure 5.14** (**b1-b3**). The central mass was fixed at m = 0.1 g, and the electric field was $E_{DC} = E_{AC}$ = 25 V/μm. It can be noted that, as the pre-stretch ratio increases, the resonant frequency increases as the membrane becomes stiffer (**Figure 5.7**); however, there is no clear effect on the resonant stroke. Note that the model underpredicted stroke of the first peak (near 100 Hz in **Figure 5.14** (**b1**)) in the case of λ_p = 1.1 × 1.1 and the second peak (near 295 Hz in **Figure 5.14** (**b3**)) in the case of λ_p = 1.3 × 1.3. Despite this, the estimated resonant frequency (295.5 Hz) is very close to the measured resonant frequency (295.3 Hz). The difference between model prediction and experimental results could be due to a slight mismatch in the force-displacement relationship with λ_p = 1.1 × 1.1 and λ_p = 1.3 × 1.3, since the model parameters were identified based on experimental results with λ_p = 1.2 × 1.2.

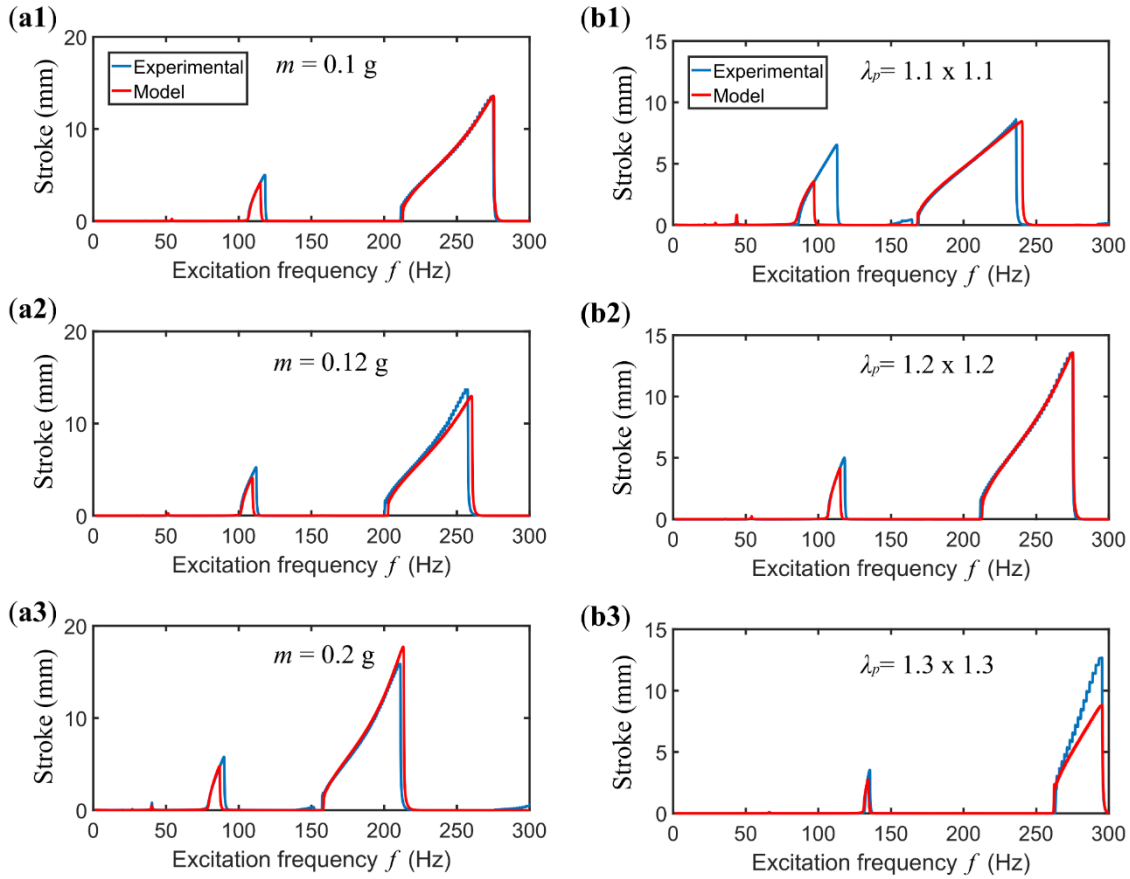

Figure 5.14. Oscillation stroke against excitation frequency of the DEOs with (**a**) different added mass and (**b**) different pre-stretch ratios.

5.3.4.2 Effects of Electrical Signals

In this subsection, the effect of the actuation signal on the dynamics of the DEOs is investigated. Here the pre-stretch ratio and the central mass were fixed at λ_p = 1.2 × 1.2 and m = 0.1 g. The input signal to the DEO is an applied electric field, E, across the dielectric elastomer and E can be considered to have both AC and DC components. The electric field parameters, AC electric field amplitude, E_{AC}, and DC biasing electric field, E_{DC}, were varied with the rule of $E_{AC} \leq E_{DC}$ (voltage must be greater than zero).

Effects of the DC signal. A DC signal would induce a constant electrostatic force on the membrane, which reduces the stresses on it, hence altering its dynamic properties. First, E_{DC} was varied from 15 to 25 V/μm while fixing E_{AC} at 15 V/μm and the result is shown in **Figure 5.15**. When the E_{DC} = 15 V/μm, a very low resonant amplitude was reached (~ 0.3 mm) and, as E_{DC} increased by 5 V/μm, the amplitude increased dramatically to a value of 6.7 mm and, as E_{DC} increased further, the amplitude continued to increase, and the high amplitude can be obtained at a wider range of excitation frequencies. This is possibly due to the fact that, as the DC biasing electric field increases, the induced Maxwell stress

(proportional to E^2) causes a greater reduction in the total stress, causing the DEO membrane to be 'softer' and an out-of-plane resonance can be triggered more easily.

Effects of the AC signals. In the second test, the DC biasing electric field, E_{DC}, was fixed at 25 V/μm and E_{AC} increased from 10 to 25 V/μm. The experimental results are shown in **Figure 5.16** and, as expected, both the resonant frequency and the amplitude increase with the increasing E_{AC} and the high amplitude region becomes broader. The results indicate that the resonant frequency and amplitudes of the DEOs can be easily tuned by the electrical signal (i.e. varying E_{AC} and E_{DC}) to meet applications where specific resonance response/amplitude is desired.

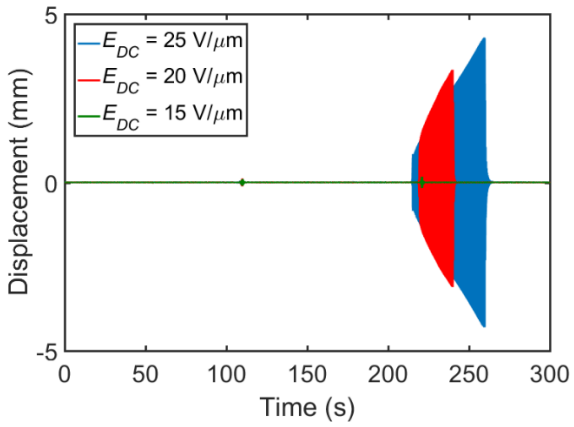

Figure 5.15. Comparison of the displacement of the DEO in a frequency sweep with different biasing DC voltage amplitudes. E_{AC} = 15 V/μm in all cases.

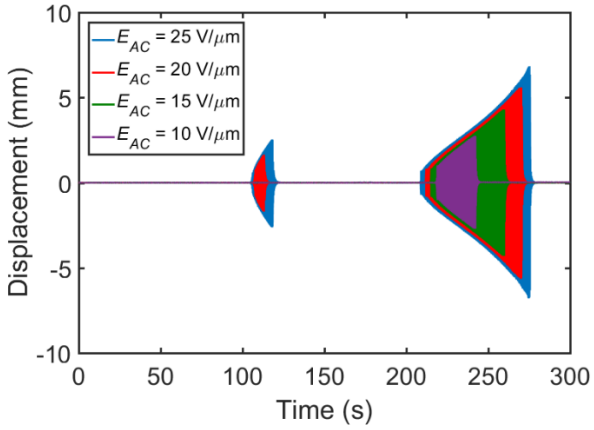

Figure 5.16. Comparison of the displacement of the DEO in a frequency sweep with different AC voltage amplitudes. E_{DC} = 25 V/μm in all cases.

5.3.5 Summary of DEO Dynamics

The experimental and numerical investigation of the DEO dynamics in this section elucidate the following conclusions:

- The developed numerical model was found to be able to accurately predict both quasi-static and dynamic responses of the DEOs.
- The hyper-elasticity of the elastomer and the complex three-dimensional deformation of this oscillator leads to highly nonlinear behaviour.
- This oscillator was found to have multiple resonant peaks and the responses at these peaks were shown to contain strong subharmonic, harmonic and super-harmonic responses.
- Resonance of the DEOs with higher pre-stretch ratios will occur at higher frequencies.
- Increasing the weight of the central mass will increase the resonant amplitude but reduce the resonant frequency.
- Adjusting the DC biasing electric field can controllably trigger significantly larger (~ 20 times) out-of-plane oscillations and increasing the AC electric field can increase the resonant amplitudes and the corresponding resonant frequencies.

5.4 DEO Application: Monolithic Electroadhesion – DEO Gripper

In the last section, a planar dielectric elastomer oscillator that exhibits large out-of-plane deformation at resonance was developed and characterized in depth. Here, we present a practical application for soft manipulations which integrates the DEO design into an electroadhesion gripper. This design takes the advantages of the DEOs with (**i**) inherent compliance of the dielectric elastomer; (**ii**) low-profile planar configuration; (**iii**) large out-of-plane oscillation; (**iv**) simple and lightweight structure.

5.4.1 Background and Problem Definition

The advancement of flexible electronic technologies (e.g. flexible chips, screens, solar panels) [194] has significantly increased the demand for gentle and precise manipulation of flat, thin and flexible substrates such as plastic films and sheets [195]. Traditional rigid robotic grippers generally have difficulty in handling flat, soft and deformable objects because of the increased mechanical and control complexity [15]. Soft robotic grippers have gained increasing interest due to their inherent compliance and adaptability which enable them to handle fragile objects safely [196]. To date, several types of soft grippers have been developed; for example, soft bending grippers using pneumatic actuation [197] and DEAs [94], jamming gripper [198], suction cup [199], gecko-adhesion [200] and electroadhesion (EA) [201]. Bending and jamming grippers are ineffective at picking-up thin, flat objects [198] [202]. Gecko-inspired adhesion has difficulty in grasping low surface-energy materials [203] (such as plastics like polypropylene) and the release of lightweight objects can also be challenging [15]. Suction cups can grasp flat objects but can be less effective when targeting a structured surface or porous substrate. Also, they cannot operate in a vacuum environment such as in chip manufacturing [201]. Electroadhesion has been previously utilized to manipulate flat, flexible and lightweight substrates [60]. This adhesion technology can potentially bring adhesion or gripping systems with enhanced adaptability, reduced complexity, low energy consumption, and gentle material handling characteristic [15].

Electroadhesion is an electrically controllable adhesion between an EA pad and a substrate, subjected to a high electric field (typically in a scale of 1 MV/m). When a high voltage is applied between the electrodes of the EA pad, counter charges are induced at the surface of any object it touches, mainly due to electric polarization that causes attractive forces between the object and the EA pad. One significant drawback of EA, which is more obvious when used for lightweight objects, is the slow de-adhesion. The slow de-adhesion phenomenon is due to the residual charge separation in the substrate after the applied voltage is removed, which diminishes slowly with dielectric relaxation [201]. Some solutions have been proposed to speed-up the de-adhesion process such as using air-jets to mechanically detach the substrate [204]. These methods tend to increase the complexity of the gripping system and are expensive. Release by vibration has been found to be feasible and effective, as reviewed in [205].

An additional vibrator can be integrated with a gripper, such as piezoelectric actuators [206] and electrostatic actuators [207]. However, these approaches are not suitable for integration into a compliant EA gripper which is capable of manipulating soft and delicate objects.

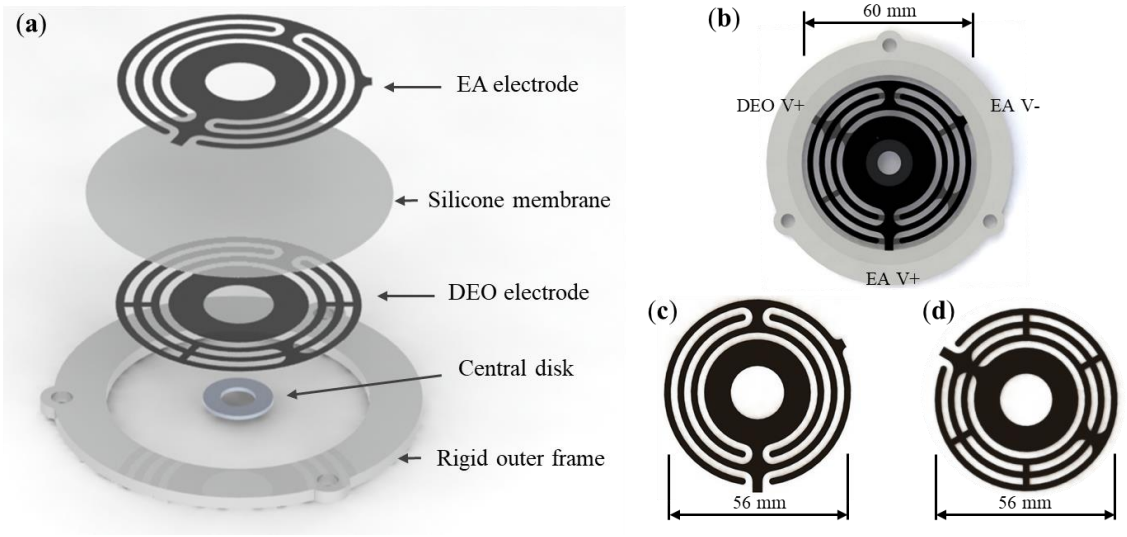

Figure 5.17. Structure of the EA-DEO soft gripper. (**a**) The gripper consists of a pre-stretched elastomer membrane bonded to a circular frame. Two EA electrodes and one DEO electrode are attached to two sides of the elastomer. A rigid disk is placed in the centre of the membrane. (**b**) A bottom view of the gripper. The gripper has an effective EA diameter of 56 mm and the gripper has an outer diameter of 80 mm. (**c**) EA electrodes design. (**d**) DEO electrode design.

5.4.2 Design Objective

With the vibrational release mechanisms proven feasible and effective for de-adhesion of an EA pad [205] [206] [207], the author proposes to take advantage of the large out-of-plane actuation deformation of a DEO device, and develop a monolithic electroadhesive device with an integrated DEO quick-release mechanism by utilizing its resonant excitation to rapidly detach substrates from the electroadhesion gripper. This technique has advantages over other vibrational actuators such as electric motors and piezoelectric actuators in terms of ease of fabrication and high deformability. Also, the same applied voltage range for both EA and DEO (usually in the order of kilovolts) can simplify the power and control systems of this gripper. This design is specialized in manipulating flexible and flat substrates with the advantages of rapid grip and release characteristics, low energy consumption, low cost and ease of fabrication.

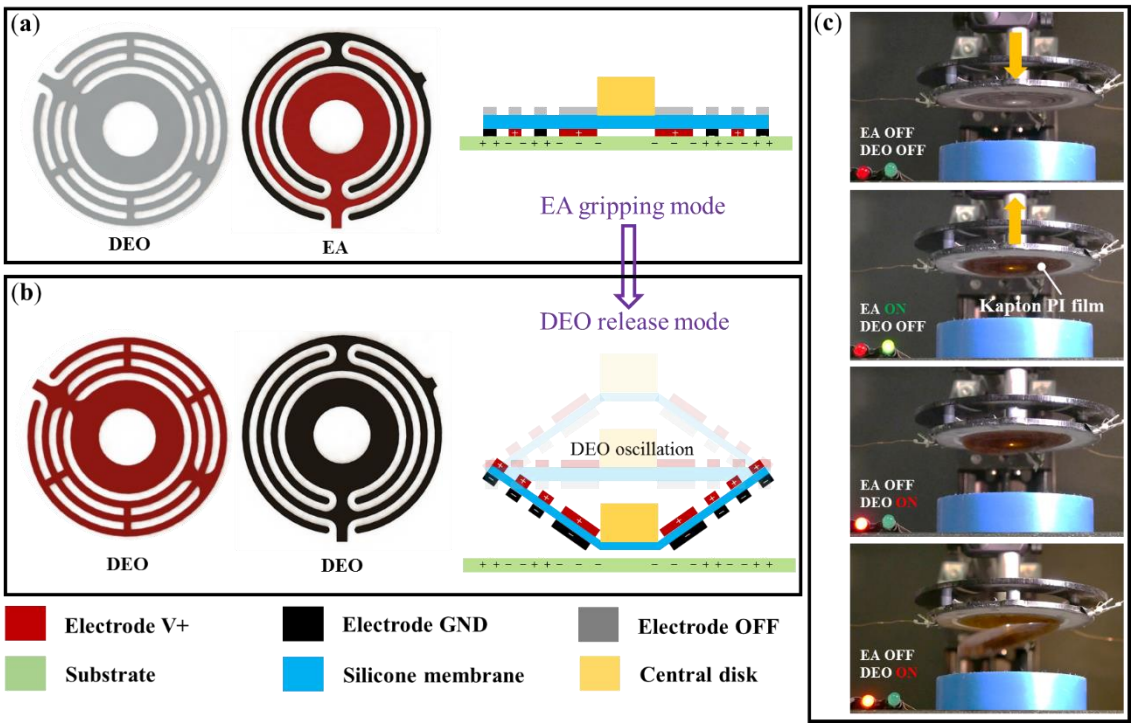

Figure 5.18. Illustration of the two actuation modes of this gripper: EA gripping mode and DEO oscillation release mode. (**a**) EA gripping mode: A voltage bias is applied across the two EA electrodes while leaving DEO OFF. An electric field is generated and homogeneous adhesion force over the surface is exerted and flat substrates can be grasped. (**b**) DEO release mode: An alternating voltage is applied across the electrodes. The out-of-plane oscillation of the DEO causes the release of the substrate. (**c**) Picking up and releasing a piece of Kapton film. The gripper is first moved downward to allow contact with the substrate. Then EA is turned on and the substrate is lifted. To release the substrate, EA is switched off and DEO is turned on. The vibration of the DEO causes the release of the substrate in less than 0.5 s.

5.4.3 Design Concept and Working Principle

The proposed gripper follows the same DEO configuration demonstrated in Section 5.1. However, a novel advancement of this design lies in the electrodes design where one electrode is divided into two parts, EA V_+ and EA V_{GND}, as a concentric-comb EA pattern, as illustrated in **Figure 5.17**. The two electrodes are interdigitated near the outer edge of the membrane, while the inner region has only one electrode. The same pattern is used on the electrodes on other side of the membrane, but instead, the electrodes are all connected and are referred to as DEO V_+. The centre is left electrode-free with a rigid central disk (1.4 g) bonded to the membrane. This configuration allows two actuation modes with this gripper. The first mode is EA gripping, and it is achieved by applying a voltage bias across the two EA electrodes EA V_+ and EA V_{GND} while leaving DEO V_+ off. An electric field is generated across the EA

electrodes and adhesion force over the surface is exerted and flat substrates can be picked-up, as shown in **Figure 5.18** (**a**). The second actuation mode, DEO out-of-plane vibration, can be triggered by applying an alternating voltage to DEO V_+ and leaving EA V_+ and EA $V_{GND} = 0$. With the appropriate actuation frequency selected to achieve resonant excitation, the DEO can vibrate out-of-plane with a large amplitude and force the substrate to release. In this design, the EA electrodes ensure that the residual adhesion force only occurs near the outer edge of the gripper. A large central DEO electrode ensures that once the DEO mode is triggered, the central disk pushes the substrate downward to create a clear gap between the EA gripper and substrate (where residual adhesion force exists), which causes a release of the substrate, as illustrated in **Figure 5.18** (**b**). The central disk helps the release process by adding mass to amplify the vibration amplitude and modifying its out-of-plane deformation profile by creating a small flat surface in the centre. This ensures a complete detachment of the substrate from the EA electrodes in a direction orthogonal to the EA gripper. A demonstration of this design in action is shown in **Figure 5.18** (**c**).

5.4.4 Fabrication of EA-DEO Gripper

For the DEO membrane, ELASTOSIL silicone (thickness 100 μm, Wacker Chemie AG), was first biaxially pre-stretched by 1.2×1.2 and bonded to a circular frame using silicone transfer tape (ARclear 93495, Adhesives Research). In this design, EA electrodes were made of conductive rubber which was formed of a mixture of 5 wt.% carbon black (VXC72R, Cabot) and silicone with a mixer (WZ-50006-01, Cole-Parmer), then cast on a laser engraved acrylic template, and finally crosslinked at 40˚C in an oven for 12 hrs after mixing. Then, a thin layer of silicone was spin-coated on the electrode to help release of the electrode from the cast mould. To minimize the effect of the electrodes on increasing the stiffness of the elastomer, a low modulus elastomer (Ecoflex-20, Smooth-on Inc.) was adopted. The fabricated electrode has a thickness of ~0.2 mm. Then the electrode was bonded to the elastomer membrane by a thin layer of spin-coated Ecoflex-20 and then crosslinked at 40˚C in the oven for an hour. As the electrode on the other side of the elastomer will not contact with the substrate, carbon grease was adopted. To avoid an inherently sticky behaviour, the EA pad's contact surface was painted with talcum powder.

5.4.5 Experimental Setups

Dynamic response of the DEO: The dynamic response of the DEO was characterized by frequency steps from 1-60 Hz with five different voltage amplitudes of 3.5 kV, 3.9 kV, 3.95 kV, 5 kV and 6 kV (electric field E = 50.4, 56.2, 56.9, 72, and 86 V/μm) and the setup is similar as in Section 5.3.1.

Measurement of Release Period: The gripper first approached the target plastic film with a 0.5 to 1 mm gap. Then, 3.5 kV was applied to the EA pad. After charging the EA pad for 10 seconds to ensure a steady gripping, the gripper was lifted. Release period recording was initiated when switching off the employed EA and was accomplished when substrates completely detached from the gripper. The whole process was recorded with a 60 frame per second Panasonic DMC-G80 camera (Panasonic UK).

5.4.6 Performance Characterization

For this gripper design, the speed and robustness of the release process mainly depend on the vibration amplitude of the DEO. **Figure 5.19** shows the DEO stroke as a function of actuation voltage and frequency. At Φ = 3.5 kV, only one resonant peak can be observed at 18 Hz. When the voltage is increased to 3.9 kV, a sub-harmonic peak occurs at ~35 Hz. The amplitude of the second peak increases significantly from 1.2 mm to 11.2 mm when the voltage is increased. The out-of-plane vibration profiles of the DEA are shown in **Figure 5.19** (**b**-**e**). A maximum relative stroke of 30 % was obtained with this DEO, which is lower than the one reported in Section 5.3.2, this is believed to be due to the reduced electrode area of the DEO and the added stiffness from the EA coating.

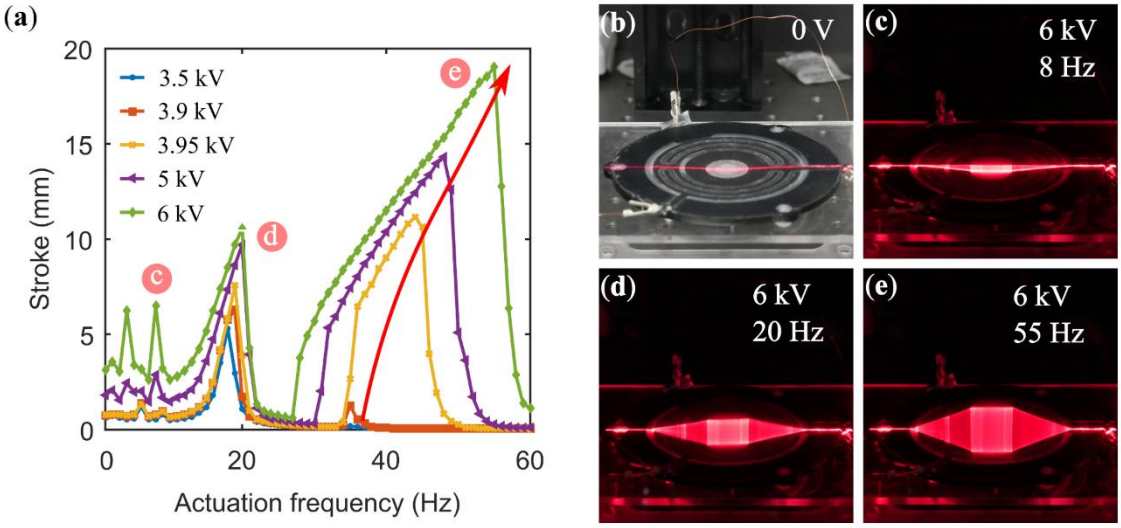

Figure 5.19. Performance investigation of the developed EA-DEO gripper. (**a**) Frequency steps from 1 to 60 Hz with five different voltage amplitudes of 3.5 kV, 3.9 kV, 3.95 kV, 5 kV and 6 kV. (**b**) Experimental setup for visual realization of the DEO oscillation geometry profiles, where a laser pointer was placed above the gripper. (**c**) Oscillation geometry profile at 8 Hz. (**d**) Oscillation geometry profile at 20 Hz. (**e**) Oscillation geometry profile at 55 Hz.

Here, the release period of this EA gripper with and without the DEO releasing mechanism were investigated against six plastic film samples with different material types and thickness (listed in **Table 5.1**). Polyimide (PI) is commonly used in flexible circuits; Polypropylene (PP), polyethylene terephthalate (Mylar), and polyvinyl chloride (PVC) are largely used in packaging. Also, PP used in this work is extremely light and flexible in order to demonstrate the functionality of the developed gripper.

Table 5.1. EA-DEO gripper testing objects' properties.

Sample NO.	***Material***	***Appellation in figures***	***Thickness (mm)***	***Mass (g)***
1.	polypropylene (**PP**, KF01121, Q-Connect)	PP	0.075	0.06
2.	polyethylene terephthalate (**Mylar**, DuPont)	Mylar 0.05	0.05	0.17
3.	polyethylene terephthalate (**Mylar**, DuPont)	Mylar 0.1	0.1	0.36
4.	polyvinyl chloride (clear **PVC**)	PVC 0.15	0.15	0.51
5.	polyvinyl chloride (clear **PVC**)	PVC 0.2	0.2	0.79
6.	polyimide (**Kapton PI**, DuPont)	Kapton PI	0.075	0.25

The measured EA-only release period (left axis) and EA+DEO release period (right axis) are compared in **Figure 5.20**. The fastest release sample is PVC 0.2 (36 ± 9.5 secs) while the longest is PP (over 30 mins). Clearly, the long release time of all tested plastic substrates restricts the applications of EA-only grippers in lightweight material manipulations where a fast release method is required. The generation of EA force on insulating material is a result of polarization, and is strongly dependent on the substrate material type and its molecular structure [201]. The poor release behavior of plastic films is likely due to their relatively high molecular weight which could cause a slow dissipation of the residual charge on the substrates [201].

With the proposed DEO oscillation release mechanism, the release of all substrates was dramatically shortened to a scale of 100 ms, as is shown in red in **Figure 5.20**. It can be noted that the EA+DEO release performance of each sample shows a similar tendency to that of EA-only release, indicating that residual charges affect DEO release behavior. With the proposed DEO release mechanism, the gripper is capable of releasing the lightest and most flexible sample (polypropylene, $m < 0.1$ g, Young's modulus ~1300 N/mm^2) in ~0.5 s, compared to the extremely long release period without this release mechanism (> 30 minutes). By comparing the release speeds of this EA+DEO gripper against the non-

DEO results, a minimum improvement of over two orders of magnitudes can be found by using the DEO release mechanism.

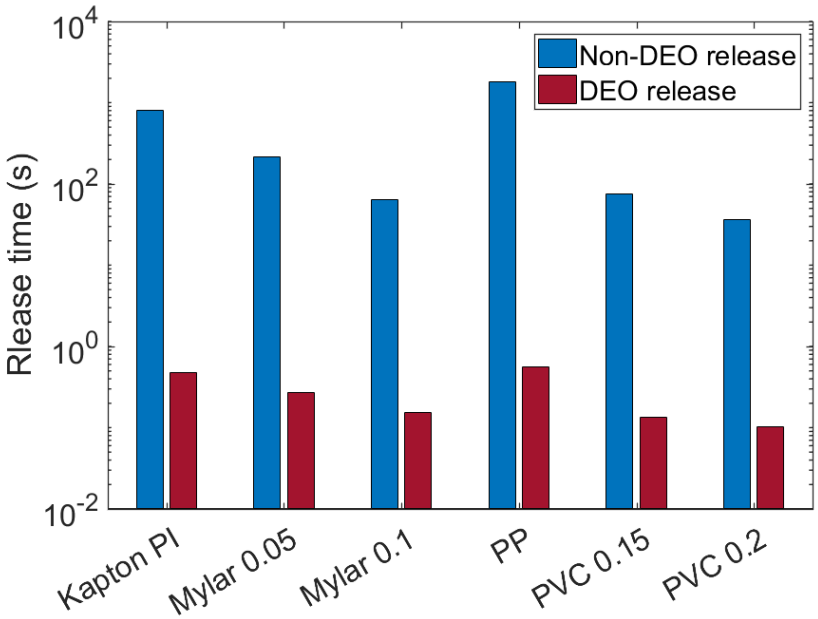

Figure 5.20. Performance investigation of the developed EA-DEO gripper for six different materials. Release periods without DEO are in blue and with DEO are in red.

5.4.7 Discussion

Compared with other vibrators, e.g. piezoelectric, electrostatic, DEO allows large out-of-plane amplitude vibration due to its inherent elasticity. EA force does not only exist on the contact surface but also in space, thus flexible substrates might vibrate along with the small amplitude vibrators. Also, a compact structure of EA-DEO provides a compliant contact surface that reduce the damage risk to the substrates. However, limitations are acknowledged for future development. Note that the large vibrational amplitudes generated in the proposed design, intrinsic to its de-adhesion performance, may not be suitable for any applications requiring the substrate needs to be dropped from a very low height (<10 mm) since the excitation stroke could exceed this. The performance of this EA-DEO device under extreme environmental conditions such as extreme temperatures (e.g. < 0 ˚C) remains untested.

The excellent mechanical and electrical properties of plastic make them promising materials in flexible electronics, such as flexible chips, screens, solar panels, etc. This also necessitates a robust yet simple gripper which can manipulate flat, flexible and lightweight plastic materials. The proposed novel EA-DEO gripper shows consistent and rapid performance on different types of plastic materials in both

gripping and releasing process. The adopted DEO speeds up the release period from several minutes to 100s of milliseconds. The low-energy consumption (gripping ~2 mJ and releasing ~50 mJ), noise-free, low-cost and ease of fabrication also allow this gripper to be a promising candidate for industrial applications in the future.

5.5 Chapter Summary

In this chapter, the design of a circular dielectric elastomer oscillator (DEO) based on cone DEA configuration was presented. The proposed DEO has a planar configuration in its rest state. However, due to the inherent elasticity of the elastomer, when excited at its resonant frequencies, the membranes can deform out-of-plane by a large amplitude. A maximum out-of-plane stroke of 67.5 % relative to the membrane diameter was observed with a very strong nonlinear dynamic response including super-harmonic, primary harmonic and sub-harmonic responses. Such nonlinear dynamic responses found in experiments were also captured accurately by the dynamic model developed Chapter 4. Based on the low-profile planar configuration and large out-of-plane resonance of the DEO design, a novel monolithic gripper integrating electroadhesion (EA) and the DEO was developed in this chapter. This gripper solved the slow de-adhesion issue of common EA grippers by using DEO to force the release. The EA-DEO gripper was evaluated against various lightweight and flexible objects and an improvement in de-adhesion speed of at least two orders of magnitude was found, which demonstrated a promising potential for industrial applications in the future.

Chapter 6: Rigidly Coupled Double Cone DEAs

In this chapter, a rigidly coupled double cone DEA (DCDEA) configuration is studied. DCDEAs have the advantages of natural antagonistic and bidirectional actuation, large stroke/force output. Despite its wide use in previous studies, the energetic performance (work/power output and electromechanical efficiency) has not been investigated and optimized. To enable its practical application in soft/bioinspired robotics, its energetic performance requires a comprehensive characterization. By using the generalized cone DEA model developed in Chapter 4, we analyse the stroke, power and electromechanical efficiency of the DCDEA. Without losing the generality, two most common DEA materials: VHB acrylic and ELASTOSIL silicone are investigated separately.

- For VHB acrylic DCDEA which exhibits high viscoelasticity, the study is focused on its output performance and electromechanical efficiency at low frequencies (0 – 10 Hz). A novel elastic energy recovery scheme for cyclic operation is proposed for VHB DCDEAs to enable the elastic energy stored in the DEA membranes to contribute to the work output. This elastic energy recovery principle is also demonstrated by a bioinspired robotic leg. It should be noted that this study restricts itself to recover the elastic energy in the DEA membranes for work output. Other forms of energy recovery, such as the electrical energy recovery, are not included in this work.
- For ELASTOSIL silicone DCDEAs, optimization is focused on the peak power output near the resonance. Its elasticity is utilized via a resonance actuation principle and is demonstrated by a biomimetic flapping wing mechanism.

Statement: The DCDEA dynamic model presented in Section 6.2 and the VHB DCDEA study in Section 6.3 in this chapter is adapted from the following publication where C. Cao is the first author.

- **Cao, C**., Gao, X. and Conn, A.T., 2019. Towards efficient elastic actuation in bio-inspired robotics using dielectric elastomer artificial muscles. *Smart Materials and structures*. 28(9) p.095015.

Contribution: Fabrication and testing methodology, investigation, data curation, formal analysis, writing original draft; review & editing.

The silicone DCDEA study presented in Section 6.4 in this chapter is adapted from the following publication where C. Cao is the first author.

- **Cao, C**., Gao, X., Burgess, S. and Conn, A.T. Power optimization of a double cone dielectric elastomer actuator for resonating robotic systems. *Extreme Mechanics Letters* (under review)

Contribution: Fabrication and testing methodology, investigation, data curation, formal analysis, writing original draft; review & editing.

6.1 Design Overview

Figure 6.1 (**a**) illustrates a schematic diagram of the DCDEA design, the DCDEA consists of two dielectric elastomer membranes bonded to circular frames with an inner radius, *b*, and the centre of the membranes are protruded by a spacer with the length, *L*. The spacer has flanges on each end with a radius, *a*. Compliant electrodes are coated on two sides of the membranes to enable actuation. A fabricated DCDEA is shown in **Figure 6.1** (**b**) with carbon grease compliant electrodes coated. As depicted in **Figure 6.1** (**c**), the actuation of a DCDEA depends on the balance of forces exerted by the two deformed DEA membranes on the central spacer. When no actuation voltage is applied, each membrane exerts an equal reaction force on the spacer, and it balances in the middle (assuming the mass of the membranes and spacer are negligible). However, when a voltage is applied across the electrodes of one DEA membrane, the generated Maxwell stress and resultant planar membrane expansion causes the spacer to move towards the actuated membrane side until another force balance is achieved.

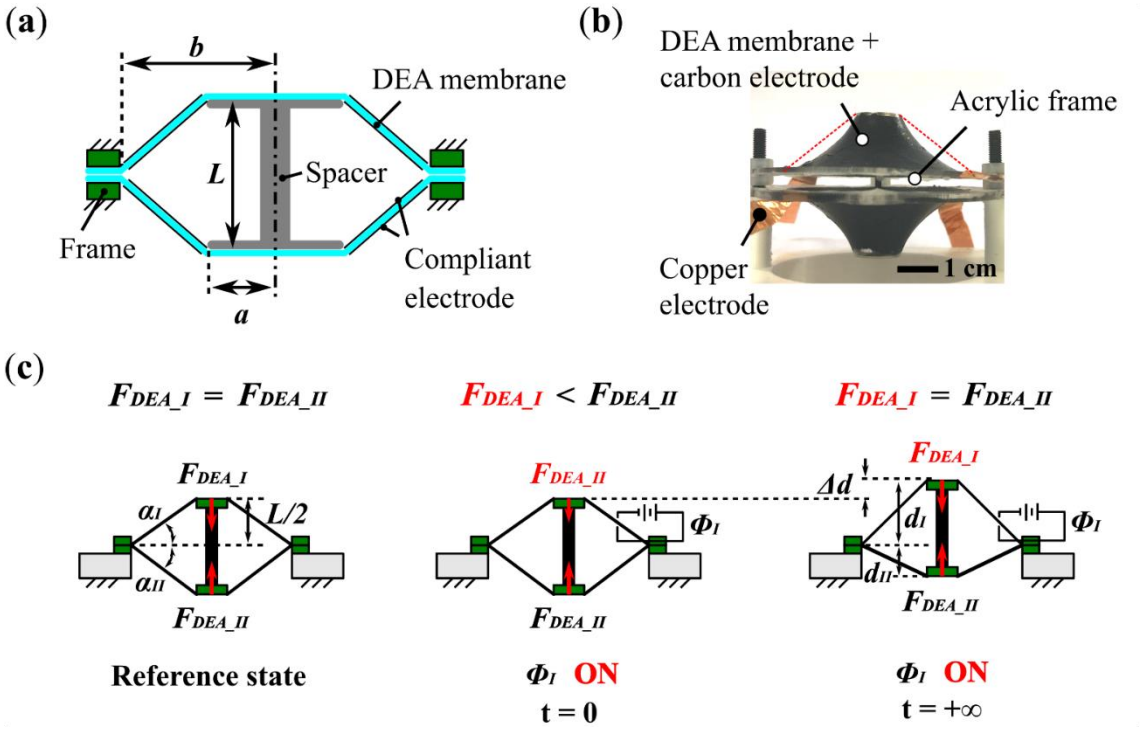

Figure 6.1. DCDEA design and actuation principle. (**a**) Schematic diagram of the DCDEA design. (**b**) Photo of a fabricated DCDEA. (**c**) Actuation principle of DCDEA.

6.2 Dynamic Modelling of DCDEA

As illustrated in **Figure 6.1** (**c**), at its passive equilibrium, the two DEA membranes are deformed out-of-plane by the spacer by the amount $d_{I\_0} = d_{II\_0} = L/2$. The tension of the membranes results in forces, F_{DEA_I} and F_{DEA_II}, on the spacer along the vertical axis. In its passive equilibrium, the two forces are balanced. When an electric field is applied across the top membrane, the reaction force of the top membrane, F_{DEA_I}, reduces, and the spacer along with the two membranes move upward. the stroke, Δd, is measured with reference to its passive position. As a result, the total out-of-plane deformation of the two membranes can be written as $d_I = d_{I\_0} + \Delta d$ and $d_{II} = d_{II\_0} - \Delta d$.

The equation of motion of this system can be written as

$$m\ddot{d} = -F_{DEA\_I} + F_{DEA\_II} \,, \tag{6.1}$$

where m is the mass of the spacer (and any payload connected to the rod) and the negative sign before F_{DEA_I} indicating a force pointing downwards. Note that gravitational force can be included in this equation of motion by adding the gravitational force component mg on the left-hand side.

The reaction force of two DEA membranes on the vertical axis can be described using the generalized cone DEA model developed in Chapter 4 and has the form

$$F_{DEA\_n} = \sin\alpha_n \int_0^{2\pi} a \frac{H_0}{\lambda_{1\_n}\lambda_{2\_n}} \sigma_{1\_n} \, d\varphi, \;\; \varphi \in [0,2\pi] \,, \tag{6.2}$$

which yields

$$F_{DEA\_n} = 2\pi a \sin\alpha_n \frac{H_0}{\lambda_{1\_n}\lambda_{2\_n}} \sigma_{1\_n} \,, \tag{6.3}$$

where $n = I, II$ for top and bottom membranes respectively, α_n is the angle between the membrane and the horizontal plane during out-of-plane deformation, $\lambda_{1,2}$ are the radial and circumferential strain, H_0 is the initial thickness of the membrane and σ_1 is the radial stress of the membrane.

For each time step, with the displacement for top and bottom membranes ($d_{I, II}$) known, the angles α_n can be estimated from Eq. (4.45) and the radial strains λ_{1_n} can be obtained from Eq. (4.42) and the radial stresses σ_{1_n} can be estimated by using the hyperelastic and viscoelastic models introduced in Section 4.3 and 4.4. This process can refer to the illustration shown in **Figure 4.6**. As a result, the equation of motion (6.1) can be obtained with the acceleration known thus the state of the DCDEA in the next time step can be predicted by solving ODE sets in MATLAB using ODE solver. The same

electrical model developed in Section 4.4.2 can be used to characterize the electrical response of the DCDEA.

6.3 VHB Acrylic DCDEA

This section focuses on the analysis of a VHB acrylic DCDEA design. As reviewed in Chapter 3, VHB acrylic material is one of the most widely adopted dielectric elastomers with relatively high dielectric constant which allows for a large force/work output at low frequencies and high viscoelasticity which limits the response speed and bandwidth. However, a comprehensive characterization on the energetic performance of the VHB based DCDEAs has not been shown in the past. In this section, an improved viscoelastic model is adopted for modelling the dynamic response of a VHB DCDEA. The DCDEA output is then evaluated and a novel actuation scheme that utilizes the elastic energy recovery of the DEA membrane is proposed and demonstrated using a bioinspired robotics leg.

6.3.1 VHB Acrylic DCDEA Modelling

To cope with the large viscoelasticity of VHB acrylic material, the Kelvin-Voigt-Maxwell rheological material [208] is adopted here. A schematic diagram of this Kelvin-Voigt-Maxwell model is illustrated in **Figure 6.2**. On the first branch is the Ogden spring that describes the hyperelasticity of this material, on the middle branch is a spring in series with a dashpot which mainly represents the stress relaxation (stress decays after a strain is applied to the dielectric elastomer) and creep (strain continues to increase after a stress is applied). A single dashpot is included in the last branch to mainly characterize the strain rate dependent hysteresis in the strain-stress function.

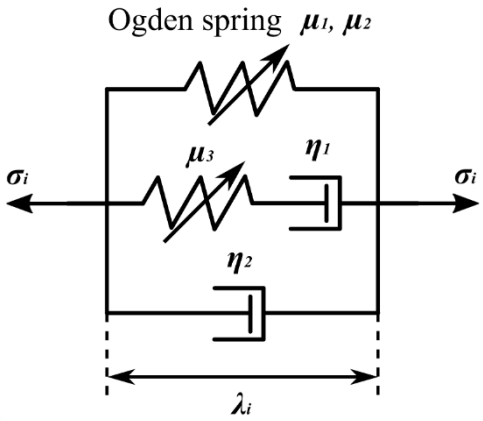

Figure 6.2. Schematic diagram of Kelvin-Voigt-Maxwell model.

For the spring on the first unit, its deformation is characterized by λ_1 and λ_2. However, for the spring in the second unit, its deformation is characterized by λ_1^e and λ_2^e due to the dashpot. Let ξ_1 and ξ_2 be the stretches of the dashpot and because the two units have the same net stretches, λ_1 and λ_2, the stretches for spring 2 can be written as

$$\lambda_1^e = \frac{\lambda_1}{\xi_1}, \tag{6.4a}$$

$$\lambda_2^e = \frac{\lambda_2}{\xi_2}. \tag{6.4b}$$

The total radial stress of the material can be represented by the summation of the stresses from the three parallel units, as written as

$$\sigma_{1\_n} = \mu_1\left(\lambda_{1\_n}^{\beta_1} - \lambda_{1\_n}^{-\beta_1}\lambda_{2\_n}^{-\beta_1}\right) + \mu_2\left(\lambda_{1\_n}^{\beta_2} - \lambda_{1\_n}^{-\beta_2}\lambda_{2\_n}^{-\beta_2}\right) - \varepsilon_0\varepsilon_r E_n^2 + \mu_3\left(\left(\frac{\lambda_{1\_n}}{\xi_{1\_n}}\right)^2 - \left(\frac{\lambda_{1\_n}}{\xi_{1\_n}}\right)^{-2}\left(\frac{\lambda_{2\_n}}{\xi_{2\_n}}\right)^{-2}\right) + \eta_2\frac{\dot{\lambda}_{1\_n}}{\lambda_{1\_n}}, \tag{6.5}$$

where $n = I, II$ for top and bottom membranes respectively, $\mu_{1,2,3}$ are shear moduli, $\beta_{1,2}$ are exponents to be determined, $\eta_{1,2}$ are the damping coefficients, ε_0 and ε_r are the absolute permittivity of a vacuum and the relative permittivity of the dielectric elastomer respectively, E_n is the applied electric field.

The rate of deformation of the dashpot in Eq. (6.4) can be described as

$$\frac{d\xi_{1\_n}}{dt} = \frac{\xi_{1\_n}}{3\eta_1}\left(\mu_3\left(\left(\frac{\lambda_{1\_n}}{\xi_{1\_n}}\right)^2 - \left(\frac{\lambda_{1\_n}}{\xi_{1\_n}}\right)^{-2}\left(\frac{\lambda_{2\_n}}{\xi_{2\_n}}\right)^{-2}\right) - \mu_3\left(\left(\frac{\lambda_{2\_n}}{\xi_{2\_n}}\right)^2 - \left(\frac{\lambda_{1\_n}}{\xi_{1\_n}}\right)^{-2}\left(\frac{\lambda_{2\_n}}{\xi_{2\_n}}\right)^{-2}\right)/2\right), \tag{6.6a}$$

$$\frac{d\xi_{2\_n}}{dt} = \frac{\xi_{2\_n}}{3\eta_1}\left(\mu_3\left(\left(\frac{\lambda_{2\_n}}{\xi_{2\_n}}\right)^2 - \left(\frac{\lambda_{1\_n}}{\xi_{1\_n}}\right)^{-2}\left(\frac{\lambda_{1\_n}}{\xi_{2\_n}}\right)^{-2}\right) - \mu_3\left(\left(\frac{\lambda_{1\_n}}{\xi_{1\_n}}\right)^2 - \left(\frac{\lambda_{1\_n}}{\xi_{1\_n}}\right)^{-2}\left(\frac{\lambda_{2\_n}}{\xi_{2\_n}}\right)^{-2}\right)/2\right). \tag{6.6b}$$

Note that based on the constant circumferential strain assumption, $\lambda_{2\_n}/\xi_{2\_n} = 1$ in Eq. (6.4 – 6.6).

6.3.2 VHB DCDEA Fabrication

The fabrication process of the DCDEAs is introduced as follows. For each membrane, a piece of 0.5 mm VHB 4905 tape (3M) was biaxially pre-stretched by 3×3 and then bonded to a rigid circular frame with an inner radius of 20 mm. A central disk with 5 mm radius was centrally aligned and bonded on

the underside of the membrane. Carbon conductive grease was hand brushed onto each side of the membrane as the compliant electrodes and copper tape was used as a connection between the compliant electrodes and high voltage cables. A spacer was fixed to each end to protrude the membranes out-of-plane and rigidly couple them together. The two circular frames were then fixed together with nylon fasteners. The assembled actuator weighs 4 g. In this work, the spacer height is determined as the characteristic design variable and the goal is to optimize the maximum work output from the DCDEA. The optimization process will be described in Section 6.3.4.

6.3.3 Experimental Setup

Quasi-static force-displacement test of a single cone DEA. A single cone DEA was fixed to the testing rig and a linear actuator (X-LSQ150B-E01, ZABER) deformed the centre of the DEA membrane out-of-plane from 0 to 20 mm then back to 0 at a low velocity of 0.01 mm/s to ensure negligible viscoelasticity. A load cell (NO.1004, TEDEA) measured the reaction force of the membrane. All signals were collected by a DAQ device (BNC-2111, National Instruments) at a sampling frequency of 500 Hz and controlled by MATLAB (MathWorks). The experimental setup is illustrated in **Figure 6.3**.

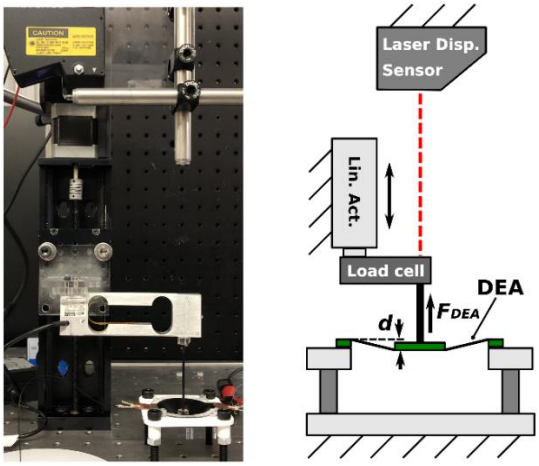

Figure 6.3. Single cone DEA membrane quasi-static force-displacement test setup.

Dynamic test of a DCDEA. The AC voltage waveform was generated by a high voltage amplifier (5HV23-BP1, Ultravolt). A laser displacement sensor (LK-G152 and LKGD500, Keyence) measured the displacement at a sampling frequency of 5 kHz. The voltage and current of the high voltage supply, Φ_{in} and i, were measured by the built-in sensors of the voltage amplifier. Square and sinusoidal waveforms with the amplitude of 3 kV were used in this experiment. It is worth noting that in antiphase sinusoidal waves, there are periods where the two membranes are acting against each other, which could

potentially lead to a reduced output. Apart from the square waves and anti-phase sinusoidal waves, other waveforms such as half sinusoidal waves and saw tooth waves can be applied, which could results in different output performances of the DCDEAs and could be investigated in the future work. The experimental setup is illustrated in **Figure 6.4**.

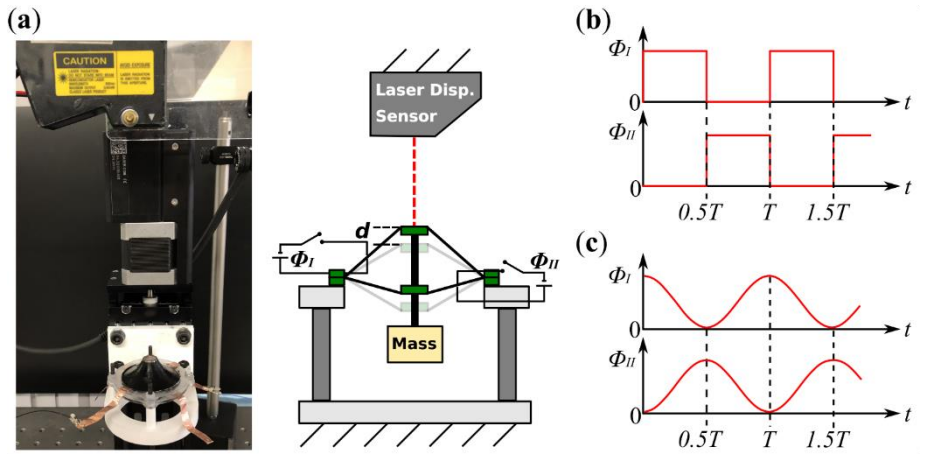

Figure 6.4. DCDEA active dynamic test setup. (**a**) DCDEA free stroke test setup. (**b**) Square wave actuation signals with antiphase. (**c**) Sinusoidal wave actuation signals with antiphase.

6.3.4 Model Validation

6.3.4.1 Quasi-static Model Parameters Identification

The measured force-displacement relationship of a single cone DEA is shown in **Figure 6.5**. The model parameters were determined by a least-mean-squares algorithm in MATLAB and the identified values are μ_1 = 47.89 kPa, μ_2 = 10.02 Pa, β_1 = 2.059 and β_2 = 5.306. As can be seen in **Figure 6.5**, a very good agreement can be found between the measurement and the model prediction. It is notable that despite the nonlinearity of the strain-stress relationship and the complex three-dimensional geometry, the force-displacement curve of a single cone DEA is close to a linear relationship.

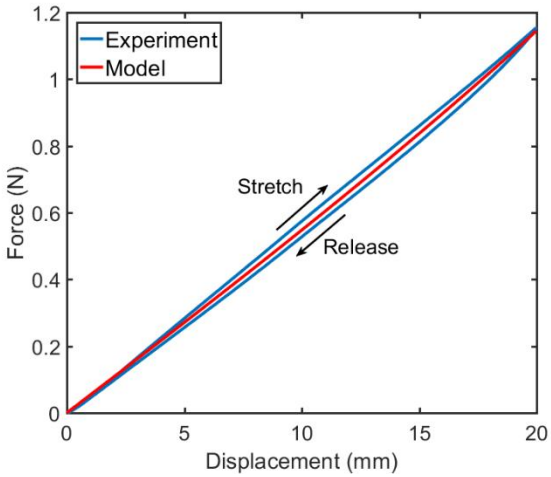

Figure 6.5. Single cone DEA force-displacement experimental result and model prediction. The membrane is deformed out-of-plane by 20 mm at the velocity of 0.01 mm/s and then released.

6.3.4.2 Configuration Optimization

With the parameters of the Ogden model determined, now a quasi-static DCDEA model can be used to optimize the design variable spacer length in terms of the maximum work output of a DCDEA. When an electric field is applied on one membrane, the Maxwell pressure reduces the stress of the membrane, which results in a force-displacement output of the DCDEA. The force output is largest when the displacement is zero and the force output reaches zero when the displacement reaches its maximum, as illustrated in **Figure 6.6** (**b**). The maximum work this actuator could exert is simply found by integrating the force-displacement curve: $W_{max} = \int_0^{\Delta d_{max}} F_{out}(d)\, d\Delta d$, where F_{out} is the output force and Δd is the actuation displacement. By using the quasi-static model (neglecting the electrical response and the viscoelasticity in the membrane), the maximum work output of the DCDEAs with the spacer lengths from 10 to 40 mm were evaluated and the result is shown in **Figure 6.6** (**a**). A fixed electric field of 80 MV/m was used in this evaluation.

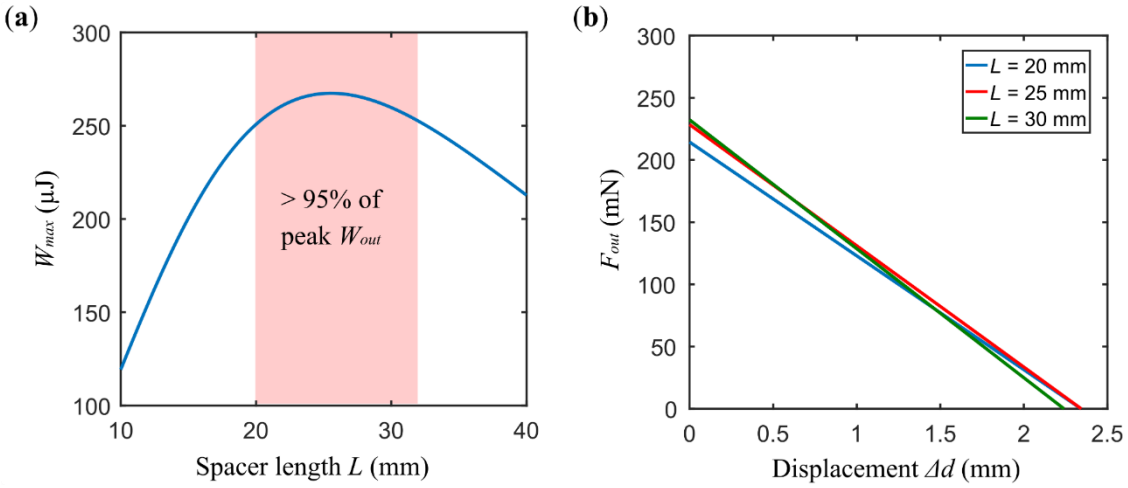

Figure 6.6. Work output optimization of a VHB DCDEA. (**a**) Comparison of the maximum work output from the DCDEAs with different spacer lengths. An optimal spacer length is found at 26 mm which generates the maximum work output. (**b**) Examples of the force-displacement output relationships of the DCDEAs with L = 20, 25, 30 mm.

As can be seen, the DCDEA has a peak in work output at L = 26 mm and within the range between 20 and 33 mm, the W_{max} remains within a high value range. Based on the optimal work output criteria, L = 26 mm is used in the rest of this work. **Figure 6.6** (**b**) shows the examples of the force-displacement curves of the DCDEAs with L = 20, 25 and 30 mm. Note that as the spacer height increases, the maximum force output increases, while the maximum displacement reduces. This suggests that apart from the optimal work output, the spacer height can be selected based on the specific applications where either a higher force or a longer stroke is desired. It is worth noting that in this optimization, only one membrane was actuated. For DCDEAs where two membranes can be actuated antagonistically, the total work output can be doubled.

6.3.4.3 DCDEA Dynamic Model Parameters Identification

With the quasi-static model parameters identified and the optimal spacer length value determined, the dynamic parameters in the model can then be identified by free oscillation experiments where two voltages with alternating current are applied across the top and bottom membranes to drive the DCDEA in translation along the vertical axis. The electrical model parameters are also identified in this process.

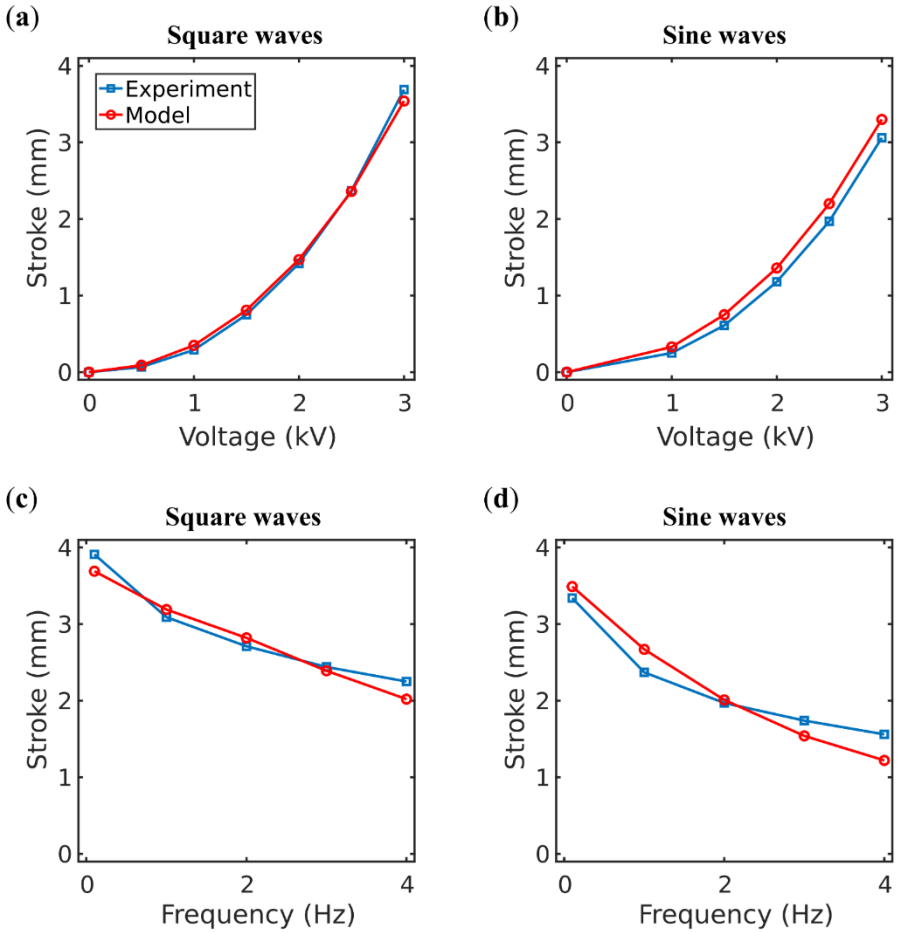

Figure 6.7. Validation of VHB based DCDEA dynamic model. Maximum stroke (bi-directional peak-to-peak) of the DCDEA against voltage amplitude of (**a**) square waves and (**b**) sinusoid waves (f = 0.25 Hz). Maximum stroke of the DCDEA as a function of actuation frequency of (**a**) square waves and (**b**) sinusoidal waves (Φ = 3 kV). No payload is included in this set of studies.

The dynamic model parameters were determined by the same least-error principle as above with varying actuation voltage amplitudes and frequencies. The identified values are μ_3 = 80 kPa, η_1 = 80 kPa·s, η_2 = 199.1 kPa·s. The measured strokes and the model predicted results under square and sine waves with different voltage amplitudes and frequencies are shown in **Figure 6.7**. The model prediction agrees very well with experimental results for both square and sine waves. Note that at a given voltage amplitude and frequency, the square wave can result in a larger stroke than the sinusoidal wave. Due to the high viscosity of the VHB material, the stroke reduces gradually with the increasing frequency. **Figure 6.8** shows the time series of the dynamic response of the DCDEA with a square and sinusoidal actuation wave. Again, the model matches very well with the measurement. Note that the DCDEA is clearly an overdamped system as there is no overshoot in the step response (**Figure 6.8** (**a**)).

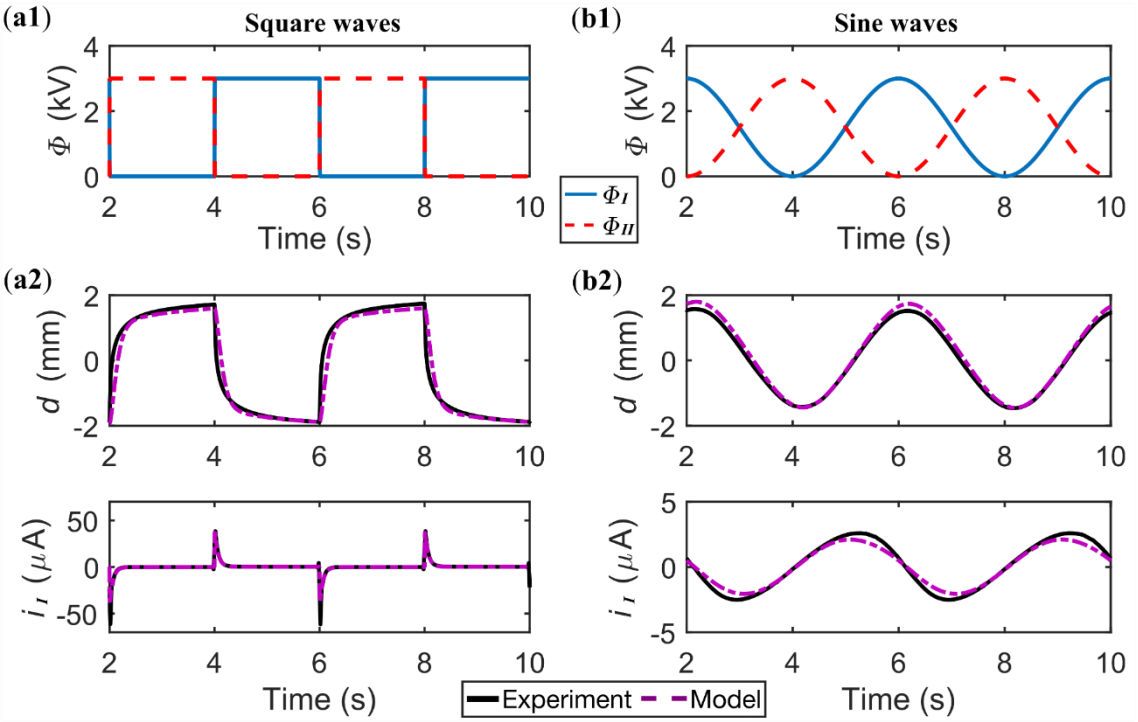

Figure 6.8. Time series of the measured and modelled displacement and current flow of the DCDEA with (**a**) square waves actuation signals and (**b**) sinusoidal wave actuation signals. No payload is included in this set of studies.

6.3.4.4 Electrical Model Parameters Identification

The measured and modelled current flow in the top DEA membrane are also shown in **Figure 6.8**. The model parameters were determined as: R_s = 35 MΩ, $\gamma = 7\times10^{-14}$ S/m, E_b = 20 MV/m and the capacitance was measured at C = 0.9 pF using a high-precision LCR meter (E4980AL, Keysight) which has an effective measuring range from 10^{-10} to 10^{3} F. The electrical model captures the charging and discharging current flows accurately. Note that the peak current flow in a square wave actuation is over one order of magnitude higher than the sinusoidal waves, which suggests a significantly higher peak power demand for the square wave. **Figure 6.9** shows a close comparison of the measured and simulated charging current of the top DEA membrane, i_I, as a function of time in a square wave actuation. Both the experimental result and the model simulation show that the current is greater than zero (~0.3 μA) after the DCDEA is charged. This leakage current results in an energy loss when the DEA reaches a steady state and is maintaining a position. This energy loss needs to be considered in any practical applications of DEAs.

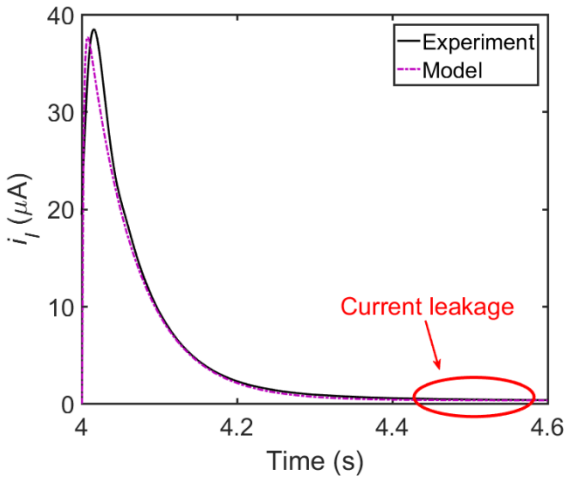

Figure 6.9. Charging current of the DEA showing a clear current leakage after the DEA reaches a steady charged state.

6.3.4.5 Compliant Actuation of DCDEA

The inherent compliance of the DCDEA can offer an advantage over other actuators since it can still function even it is initially deformed by an external force. In this subsection, the dynamic performance of the DCDEA is further investigated against the deformation of the actuator by letting the DCDEA drive a mass against gravity, as shown in **Figure 6.10** (**a**). With a mass attached to the actuator, the balancing position of the DCDEA will be lower than its reference position, as illustrated in **Figure 6.10** (**a**). In **Figure 6.10** (**b**), a clear difference can be noticed in the DCDEA position with and without a 40 g mass attached. **Figure 6.10** (**c**-**d**) shows the measured and modelled performance of the DEA as a function of mass respectively. As the mass becomes heavier, the balancing position of the DEA becomes lower, the upward stroke becomes smaller while the downward stroke increases. However, the total stroke (the difference between the top (red curve) and bottom (green curve) positions) remains approximately unchanged, which suggests that despite the balancing position of the DCDEA changing with the payload due to its inherent compliance, its actuation performance remains stable. This is particularly important for applications such as dynamic locomotion where the balancing position of the actuator is constantly changing due to the dynamic motion.

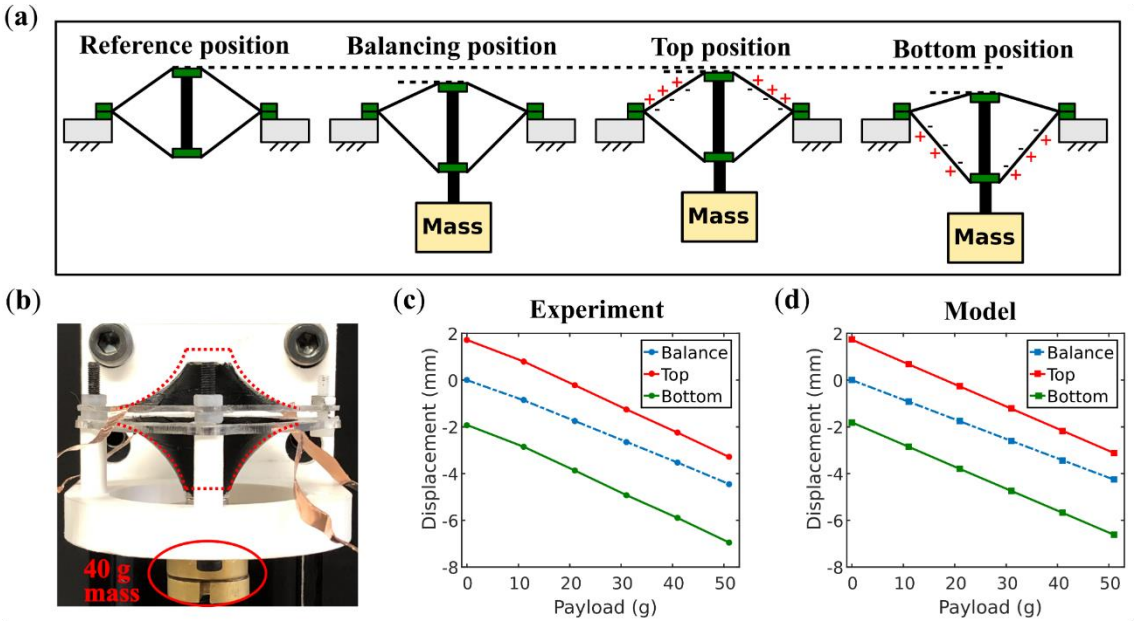

Figure 6.10. Performance of the VHB based DCDEA against payload. (**a**) Schematic diagrams of DCDEA actuation against a payload attached. (**b**) Photo of a DCDEA with 40 g mass attached, the red dash curves indicate the reference position of the DCDEA without payload. (**c**-**d**) Experimental and modelled positions (top, balancing, and bottom) of the DCDEA with varying weights attached. Square actuation waves with the amplitude of 3 kV and frequency of 0.25 Hz are used.

6.3.5 Energetic Study of VHB DCDEA

In the last subsection, the proposed dynamic model was compared with the experimental results with excellent accuracy. The DCDEA configuration was optimized in terms of work output in a quasi-static actuation. However, in applications such as robotic locomotion, the power output and the energy efficiency of the actuator are also critical. In this section, this model is utilized to perform an energetic study of the DCDEA which investigates the power and stroke output of the DCDEA and the electro-mechanical efficiency of the DCDEA. A novel strategy of utilizing the inherent elastic energy stored in the DEA membranes is also demonstrated.

6.3.5.1 Energetic Study Definition

This study focuses on a simple system where a DCDEA drives an inertial and dissipative payload, as illustrated in **Figure 6.11**. The DCDEA drives the mass, *M*, to move horizontally (gravity is neglected in this study for simplicity) and the mass is also rigidly connected to a dashpot with the damping coefficient, *c*. Note that in the setup in Section 6.3.4.5, the DCDEA drives the mass against gravity, the

work output in one complete cycle is zero as the mass returns to its initial position after one cycle, resulting in a zero change in its gravitational potential energy. However, in the setup used here, the added dashpot always absorbs energy, resulting in a positive work output from the DCDEA in one cycle. The dashpot in this setup is a simplified representation of the friction (e.g. crawling robot driven by DCDEAs, see Appendix C) or aerodynamic load (e.g. flapping wing mechanism driven by DCDEAs, see Section 6.4.3) in real systems. The different damping mechanisms or dissipation forces such as nonlinear viscous damping (aerodynamic load) or Coulomb damping (friction) in real systems can be replaced by the linear viscous damping (by ensuring the same energy dissipation per cycle) to enable the use of this study setup. In this study, the same DCDEA configuration from the preceding section was adopted (a = 5 mm, b = 20 mm, L = 26 mm). The mass, M, was fixed at 10 g. Here, the energetic performance of the DCDEA is investigated with varying actuation frequencies and damping coefficients representing different applications. The square and sinusoidal actuation signals with alternating current and amplitude of 3 kV were used here with the frequencies varying from 0.1 to 10 Hz. The damping coefficient, c, was varied from 0.1 to 100 N.s/m.

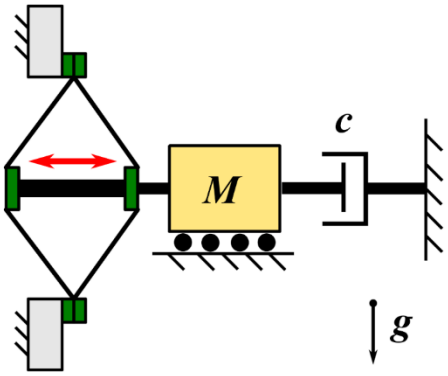

Figure 6.11. DCDEA energetic study setup.

Before conducting the study, the following parameters are defined.

The work output of the DCDEA in one cycle is

$$W_{out} = \int_0^T cv^2 \, dt \, , \tag{6.7}$$

where T is the period, v is the velocity, t is time.

The electrical energy input of the DCDEA in one cycle is

$$E_{in} = \int_0^T \Phi_{in}(t) i(t) \, dt \, . \tag{6.8}$$

Note that in this study, we assume there is no electrical energy recovery, i.e. current flowing back into the power supply ($i(t) < 0$) is not considered.

The average power output of the DCDEA is

$$P_{out} = \frac{W_{out}}{T}\,, \tag{6.9}$$

and the electromechanical efficiency over a cycle is

$$\eta_{em} = \frac{W_{out}}{E_{in}}\,. \tag{6.10}$$

In this system, during actuation, the kinetic energy of the mass, E_k, and the elastic stain energy of the DCDEA membranes, E_s, also fluctuate in one cycle, which are written as

$$E_k = \frac{1}{2}Mv^2\,, \tag{6.11}$$

$$E_s = W_s Vol\,. \tag{6.12}$$

where the strain energy density is given in Ogden model as

$$W_s = \frac{\mu_1}{2}\left(\lambda_{i\_1}^{\beta_1} + \lambda_{i\_2}^{\beta_1} + \lambda_{i\_1}^{-\beta_1}\lambda_{i\_2}^{-\beta_1} - 3\right) + \frac{\mu_2}{4}\left(\lambda_{i\_1}^{\beta_2} + \lambda_{i\_2}^{\beta_2} + \lambda_{i\_1}^{-\beta_2}\lambda_{i\_2}^{-\beta_2} - 3\right), \tag{6.13}$$

and the volume of the membrane is

$$Vol = \pi(b^2 - a^2)\frac{H_0}{\lambda_p^2}\,, \tag{6.14}$$

6.3.5.2 Energetic Study Findings

The simulated power output of the DCDEA as a function of the damping coefficient and the actuation frequency is shown in **Figure 6.12**. By comparing the square wave and sinusoidal wave results, it can be noted that square actuation signals result in higher average power outputs. For this DCDEA design, the maximum power output that can be achieved is about 0.4 mW at a frequency of 1 Hz using a square wave signal. The red curves in **Figure 6.12** show the frequency which generates the peak power output for each damping coefficient values. Note that for both square and sinusoidal waves, as the damping coefficient increases, the maximum power output occurs at a lower frequency but all within the frequency range of 0.5 to 2 Hz. **Figure 6.13** compares the power output as a function of damping coefficients with the frequency fixed at 1 Hz. The power output increases with the increasing damping coefficient and peaks at c = 20 N.s/m for both square and sinusoidal waves, as c increases further, P_{out} reduces gradually. It is worth noting that the power output with a square wave is almost twice that with a sinusoidal wave.

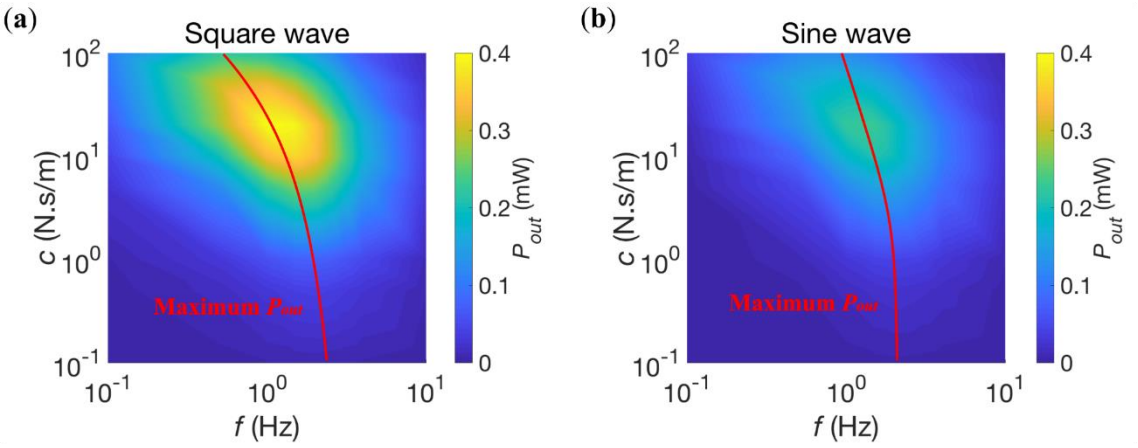

Figure 6.12. Power output of the DCDEA as a function of frequency and damping coefficient with (**a**) square actuation waves and (**b**) sinusoidal actuation waves.

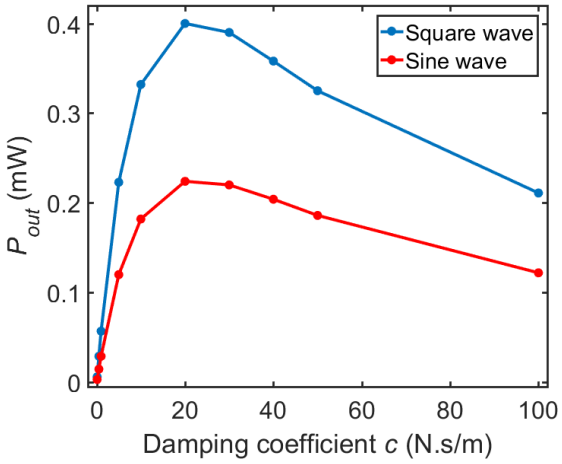

Figure 6.13. Comparison of the power output of the DCDEA with varying damping coefficients. f = 1 Hz.

Figure 6.14 shows the stroke output of the DCDEA and it can be noted that the square wave results in a larger stroke than the sinusoidal wave in all cases. At an extremely low frequency (e.g. f = 0.1 Hz), the stroke remains at a constant value regardless of the damping coefficient. However, as the actuation frequency and damping coefficient increases, the stroke drops gradually. It is worth noting that when c < 10 N.s/m, the stroke is dominated by the actuation frequency, and at 10 Hz, the stroke is close to zero even when the damping from the payload is negligible, which demonstrates that the substantial viscosity in the DEA itself restricts the application of the VHB based DCDEA at high frequencies.

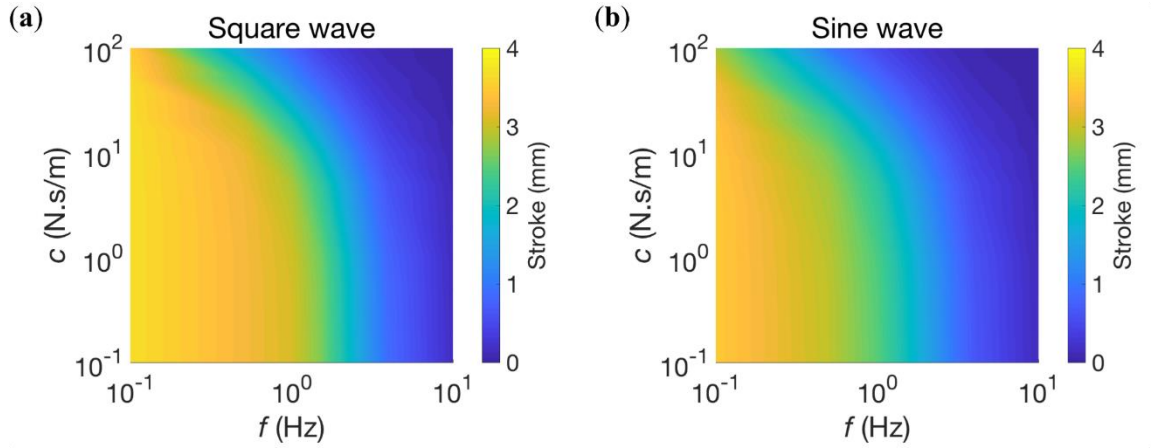

Figure 6.14. Stroke output of the DCDEA as a function of frequency and damping coefficient with (**a**) square actuation waves and (**b**) sinusoidal actuation waves.

Another parameter that describes the energetic characteristic of a DEA is its electromechanical efficiency. **Figure 6.15** compares the electromechanical efficiency of the DCDEA with square and sinusoidal actuation signals. It can be noticed that the highest efficiency occurs at the lowest frequency of 0.1 Hz and the highest damping coefficient of 100 N.s/m, which could be due to the low actuation frequency resulting in a larger stroke, and hence a greater work output, and the high damping coefficient, *c*, leading to a slower velocity and a lower viscous loss in the DEA, i.e. a higher proportion of velocity-dependent dissipation is lost to the load rather than within the membrane. As illustrated by the red curves, as *c* reduces, the maximum electromechanical efficiency occurs at a higher frequency but with a reducing value.

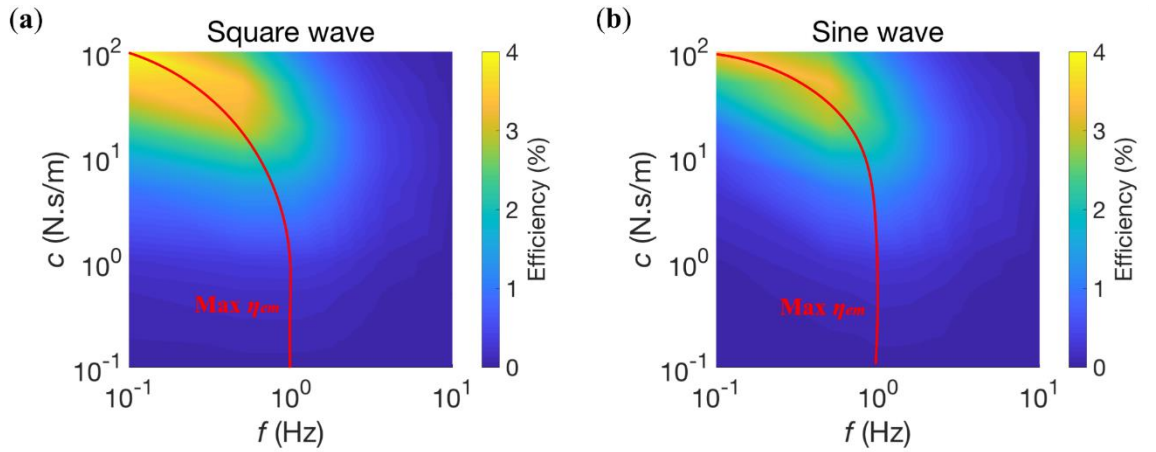

Figure 6.15. Electromechanical efficiency of the DCDEA as a function of frequency and damping coefficient with (**a**) square actuation waves and (**b**) sinusoidal actuation waves.

6.3.6 Utilizing Elastic Energy Recovery for Work Output

The inherent elasticity of the membrane means that DEAs differ from most types of conventional actuator in terms of elastic energy storage as no additional elastic element is required in a DEA to store and release elastic energy. **Figure 6.16** shows the simulated elastic strain energy fluctuation of the DCDEA in one actuation cycle. The elastic strain energy increases as the DEA is generating stroke (moving towards each end) and reduces as the DEA returns to its balance position ($\Delta d = 0$). Note that the kinetic energy of the mass, E_K, also fluctuates during one cycle, however, its value is found to be three orders of magnitude smaller than the change in the elastic strain energy and, hence, it is not studied here.

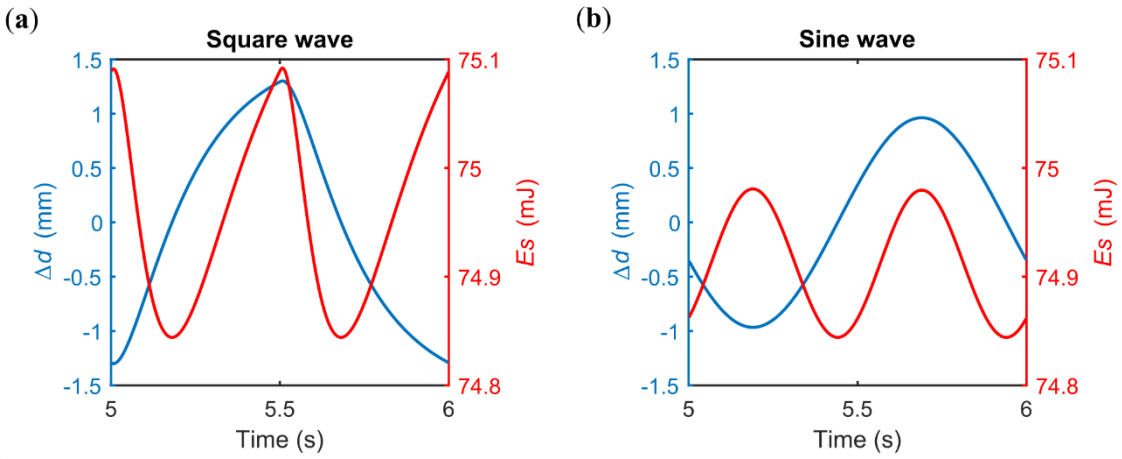

Figure 6.16. Time series of the displacement and strain energy in one cycle with (**a**) square wave and (**b**) sinusoidal wave. f = 1 Hz, c = 10 N.s/m.

To take advantage of the elastic strain energy fluctuation, the duty ratio (*DR*) of the two square actuation signals can be reduced such that a period is left passive after the elastic strain energy reaches its peak value and, during this passive period, this energy is released so that part of it is converted to the work output (driving the mass and dashpot). An example of this concept is illustrated in **Figure 6.17**. In this example, the duty ratio of the two signals are reduced from 0.5 to 0.3, so that a 0.2 s period is left passive after each DEA membrane is switched off. During this 0.2 s period, the DEA is driven by the elastic strain energy stored in its membranes towards its reference position, continuously outputting work without any electrical energy input. After this passive period, the DEA is switched on again, and the elastic strain energy is charged as part of the actuation process. **Figure 6.18** compares the contribution of the elastic strain energy in the work output in one complete cycle as a function of the duty cycle. As can be seen, a greater percentage of work is done during the passive period as the duty ratio reduces and about 28% of the total work output is contributed by the elastic strain energy stored in the DEA membranes during the passive period when *DR* is reduced to 0.2. However, it is worth

noting that the total work output reduces as the duty ratio becomes smaller due to the lower electrical energy input. This elastic energy recovery concept can be explored further in applications such as bio-inspired locomotion where elastic energy recovery can used to improve the energy efficiency.

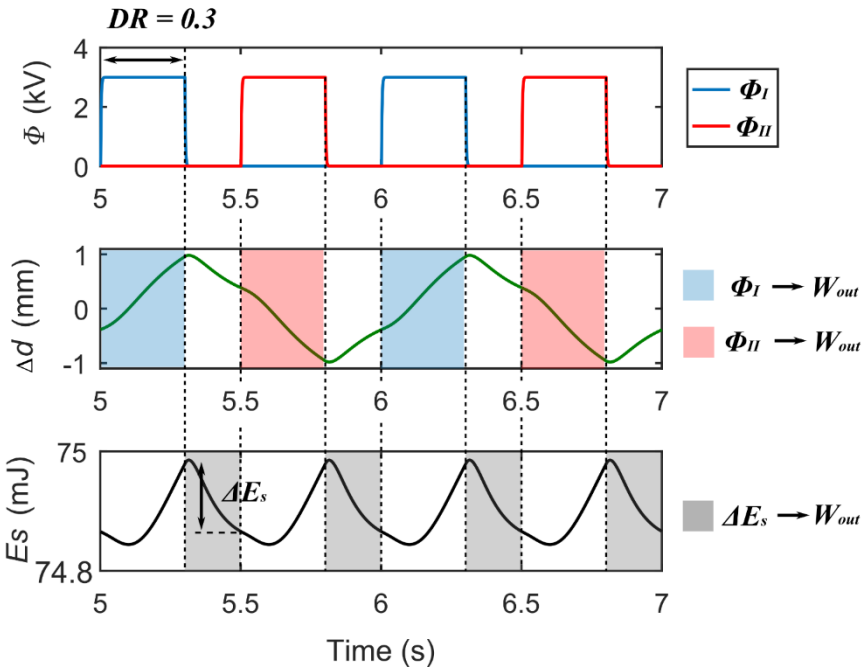

Figure 6.17. Principle of elastic energy recovery for VHB based DCDEAs. Reducing the duty ratio of the two actuation signals can result in more elastic strain energy stored in the DEA membranes to contribute to the work output.

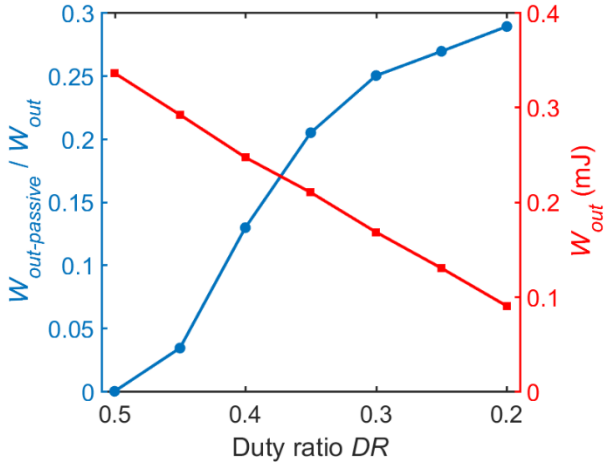

Figure 6.18. Contribution of the elastic strain energy on the work output and the total work output in one cycle as a function of duty ratio. f = 1 Hz, c = 10 N.s/m.

6.3.7 VHB DCDEA Driven Bioinspired Robotic Leg

In Section 6.3.4.5, the DCDEA was demonstrated to have beneficial compliance where its actuation performance showed negligible dependence on the deformation of its balancing position. In Section 6.3.6, we demonstrated that the inherent elastic energy stored in the DEA membranes can be recovered to produce work output. In this subsection, to demonstrate the feasibility of utilizing VHB based DCDEAs for bioinspired robotics, we present a leg design powered by DCDEAs to showcase the advantage of the compliance and elastic energy recovery of the DCDEA.

6.3.7.1 DCDEA Driven Robotic Leg Design Overview

The proposed bio-inspired robotic leg is shown in **Figure 6.19**. The leg design is a biologically inspired three-segment configuration, which is commonly seen in the hind limbs in mammals [29] and has been adopted in quadrupedal robot designs such as BigDog [209] and Cheetah-cub [210]. The detailed design parameters and the fabrication process of this leg design is given in Appendix E. A kinematic model of the leg design is developed and verified, which can also be found in Appendix E.

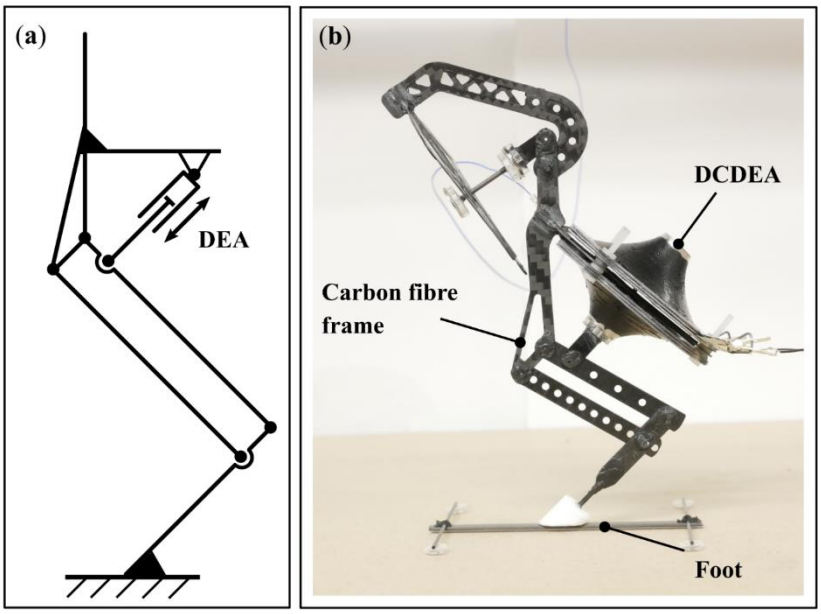

Figure 6.19. DCDEA driven bioinspired robotic leg design. (**a**) Schematic diagram of the leg design. (**b**) Photo of a fabricated leg prototype.

6.3.7.2 DCDEA Driven Robotic Leg Demonstration

Compliant actuation demonstration. In the first demonstration, the DCDEA powers the knee joint and generates a squat motion. **Figure 6.20** (**a-b**) shows the leg doing a squat with its bodyweight and with 5 g mass attached respectively. The 5 g mass caused the leg to lower its position and the DCDEA was deformed further from its initial position. However, the DEA was still functioning and driving the leg together with the payload down and upwards thanks to the inherent compliance of the DEA.

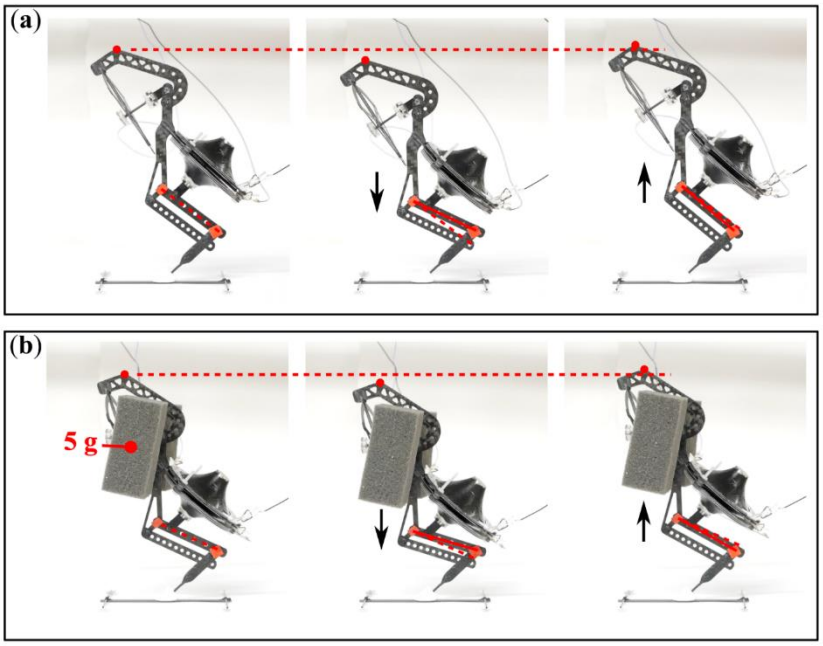

Figure 6.20. Robotic leg demonstrating a squat motion with (**a**) no additional payload attached and (**b**) 5 g mass attached. (f = 1 Hz in both cases).

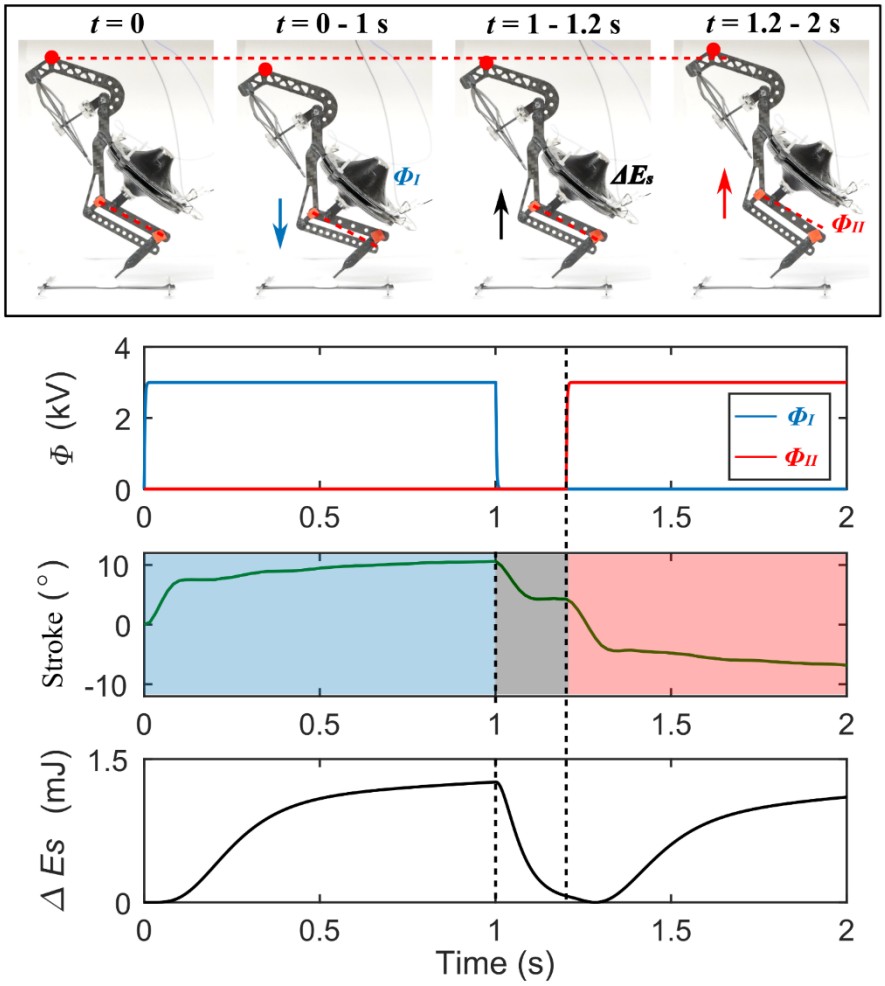

Figure 6.21. Demonstration of elastic energy recovery with the bio-inspired robotic leg. The input voltages to each membrane, Φ_I and Φ_{II}, the knee angle, and the sum of changes to the elastic strain energy across both membranes from the passive state, ΔE_s, are plotted against time.

Elastic energy recovery demonstration. In the second demonstration, the same squat motion was repeated, but with a reduced duty ratio in the actuation signals to demonstrate its elastic energy recovery. **Figure 6.21** shows the snapshots of the leg in actuation and the time series of the two actuation signals, change in knee angles and the fluctuation in the elastic strain energy in the DEA membranes in one cycle with the period of 2 s. In the first second, voltage Φ_I is on, which causes the DEA to lower the leg, and the elastic strain energy in the antagonistically coupled membranes is increased in this process. Between t = 1 – 1.2 s, both voltage signals are off, and the elastic strain energy stored during the first second is released, causing the leg to lift up. The passive release of stored strain energy in this period generates a knee joint stroke of 6.5˚, which highlights the benefits of taking inspiration from principles of biological legged locomotion (where the natural muscle-tendon complex performs a similar function [29]). Note that the leg does not entirely return to its initial passive position in this 0.2 s, which could be due to the friction in the joint and the viscoelasticity of the DEA. During t = 1.2 to 2 s, the Φ_{II} is

turned on, which forces the leg to stand up and drive the knee joint through a further 11.5˚. The total stroke of the knee joint in one cycle is 18˚ with a reduced duty ratio in the actuation signals.

6.3.8 VHB DCDEA Summary

To summarize, in this subsection an in-depth study on the dynamic performance of the VHB based double cone DEA was conducted. With the verified numerical model, the first energetic characterization and optimization study on VHB based DCDEAs was performed and the key findings are list as follows:

i. The configuration of the double cone DEA was optimized in terms of work output and the optimal configuration found was to be a 1.3 height-to-radius ratio.

ii. By using a DEA-mass-dashpot system, square wave actuation signals were found to lead to a higher power output with a better electromechanical efficiency than sinusoidal wave signals.

iii. The double cone DEA made with VHB material has a peak power output at a frequency between 0.5 to 2 Hz and the actuation bandwidth of this DEA was found to be less than 10 Hz due to the inherent viscosity of the material.

iv. Elastic strain energy stored in the DEA membranes can be recovered by reducing the duty ratio of the actuation signals thus allowing the released elastic strain energy to contribute to the work output.

With the optimal double cone DEA configuration, we developed a bioinspired robotic leg with the DCDEAs as a demonstrator to prove the feasibility of utilizing the compliant actuation and elastic energy recovery for bioinspired or soft robotics.

6.4 Silicone DCDEA

In the last subsection, the dynamic performance of a VHB acrylic DCDEA is characterized, and an optimal actuation frequency range of 0.5 to 2 Hz was found for VHB based DCDEAs, and their performance decrease dramatically with the increasing frequency due to the high viscoelasticity. Silicone elastomers, on the other hand, have significantly lower viscoelasticity than VHB and allow a higher actuation bandwidth. The resonant actuation of silicone DCDEAs can potentially increase the power output and energy efficiency of the actuator. This subsection focuses on (**i**) characterization the dynamic response of silicone DCDEA using the model developed in Section 6.2; (**ii**) using the same setup in Section 6.3.5 to investigate the power output of the DCDEA against actuation frequencies; (**iii**) optimizing the DCDEA configuration for maximum power output; (**iv**) demonstrating the resonance actuation in flapping wing robots.

6.4.1 Silicone DCDEA Model Validation

DCDEA fabrication. The DCDEA prototypes were fabricated with 100 μm thick off-the-shelf silicone elastomer (ELASTOSIL, Wacker Chemie AG) and the geometrical parameters were determined as a = 7.5 mm, b = 15 mm, L = 7 mm. Three sets of specimens with the pre-stretch ratios of 1×1, 1.2×1.2 and 1.4×1.4 were prepared. Detailed fabrication process is similar to Section 5.1.2 and is not repeated here.

Characterization of quasi-static force-displacement of a single membrane. **Figure 6.22** (**a-c**) shows the experimental setup, experimental and modelled results of the quasi-static force-displacement of a single DEA membrane respectively. The experimental setup follows the previous study in Section 5.1.2 where the DEA membrane was deformed out-of-plane at a low velocity of 0.05 mm/s to minimize the effect of viscoelasticity. Electric fields with the value of 0 and 50 V/μm were tested. The detailed experimental setup can be found in Section 5.3.1. It should be pointed out that the Gent model with the Maxwell rheological viscoelastic model introduced in Section 4.4.1 (Eq. (4.26 – 4.32)) was adopted for silicone material instead of the Kelvin-Voigt-Maxwell model as in Section 6.3.1 due to the reduced viscoelasticity. As shown in **Figure 6.22** (**b-c**), the model prediction agrees well with the experimental results. The Gent model parameters were determined by a least-mean-squares algorithm in MATLAB (Mathworks). The identified Gent model parameters are: μ_A = 415.5×10^3 Pa, J_A = 16. A dielectric constant of ε_r = 2.8 was used in this model as reported by the manufacturer.

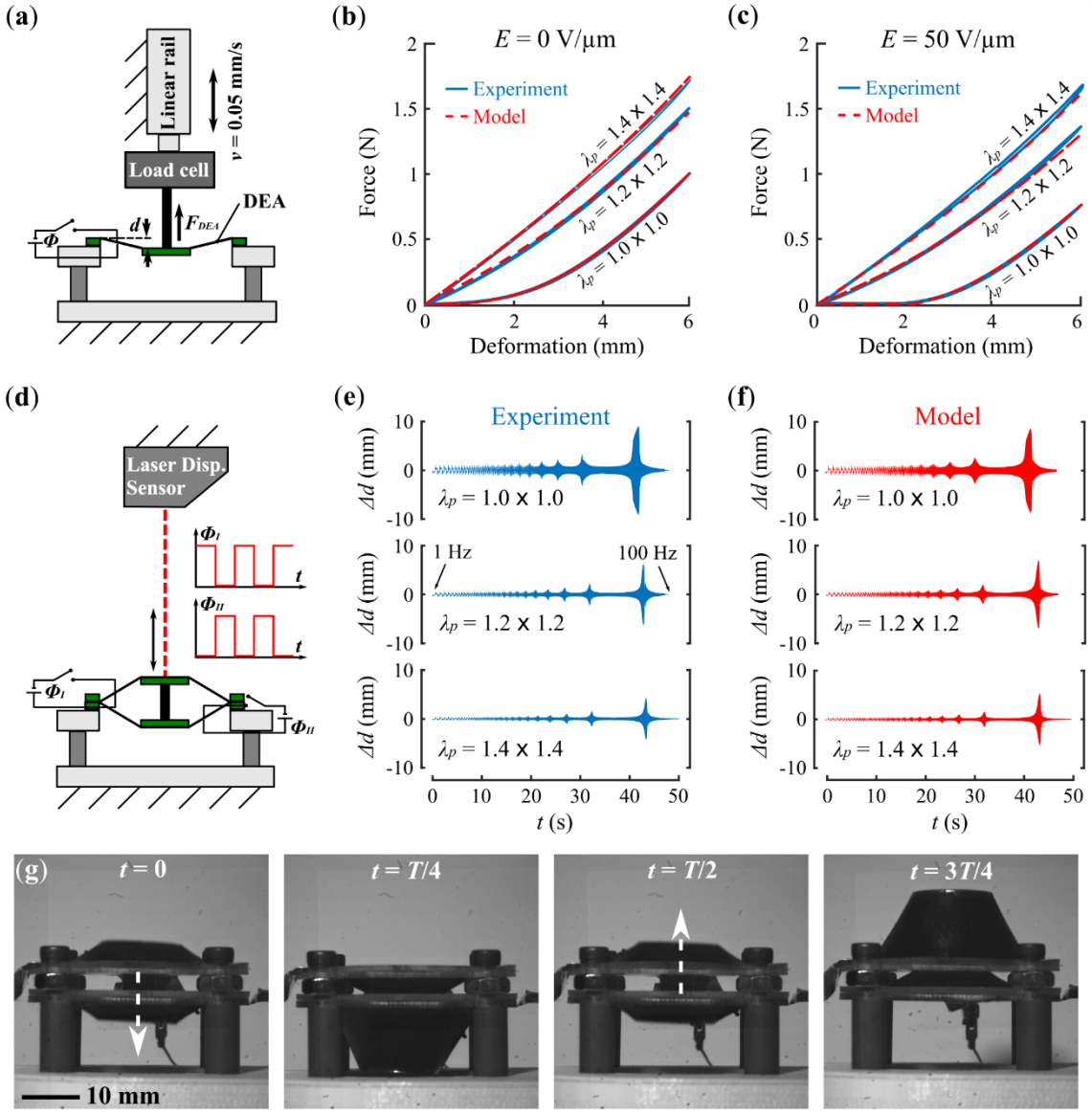

Figure 6.22. Silicone DCDEA dynamic model validation. (**a**) Experimental setup of quasi-static force-displacement measurement of a single cone DEA membrane. (**b-c**) Comparison of measured and modelled force-displacement relationship of the single cone DEA with different pre-stretch ratios when (**b**) $E = 0$ and (**c**) $E = 50$ V/μm. (**d**) Experimental setup of free oscillation of the DCDEA. (**e-f**) Measured and modelled dynamic response of DCDEAs with different pre-stretch ratios. (**g**) Series of photos of a DCDEA oscillating at its resonance.

Characterization of dynamic response of the DCDEA. Frequency sweep tests from 1 to 100 Hz with the square waveform were used (due to the superior performance over sinusoidal waves, as found in Section 6.3.5) to investigate the dynamic response of the DCDEAs and the experimental setup is shown in **Figure 6.22** (**d**). A detailed description is available in Section 5.3.1 and 6.3.3. Experimental and modelled results of the dynamic response of the DCDEAs with different pre-stretch ratios are shown in

Figure 6.22 (**e-f**) respectively. The identified viscoelasticity parameters are: μ_B = 90×10^3 Pa, J_B = 20, η = 117 Pa·s and the surface resistance R_s is estimated at 2 MΩ. Excellent accuracy was found between the modelled and measured dynamic response with all three sets of pre-stretch ratios, demonstrating the validity of this numerical model. The dynamic motion of the DCDEA was also recorded by a high-speed camera at 5000 frames-per-second (SA1.1, Photron), and a series of photos demonstrating the motion of the DCDEA at its resonance are shown in **Figure 6.22** (**g**). Due to the low viscoelasticity of the silicone material, the oscillation amplitude is extremely high at resonance, and the total stroke can pass 100 % relative to its height (second and fourth plot in **Figure 6.22** (**g**)). For example, for the DCDEA design with λ_p = 1×1, a stroke of 257 % was measured, which, to the best of the author's knowledge, was the highest linear stroke reported in DCDEAs to date. As a comparison, a maximum stroke of ~ 15 % was found for VHB based DCDEAs in Section 6.3.4.

6.4.2 Silicone DCDEA Power Output Study

The theorical power study follows the same setup as in Section 6.3.5. A payload with a mass, *M*, and a linear dashpot, *c*, is rigidly attached to one end of the DCDEA. The payload is constrained to allow horizontal translations so that gravitational force can be neglected in this study. The geometrical parameters of the DCDEA, *a* and *b*, are fixed at 7.5 mm and 15 mm respectively with the spacer length, *L*, varying from 5 to 30 mm and pre-stretch ratio varying from 1.0 to 1.4. The spacer is assumed to have a mass of 1 g and the payload has a mass of 2 g and a damping coefficient of 1 N.s/m. Two antiphase alternating current voltages are applied to the two membranes, and the frequency of the actuation voltages are stepped from 20 to 200 Hz with an increment of 0.2 Hz and 10 cycles are repeated at each frequency to ensure a steady state response. The average power output of the DCDEA per cycle is $P_{out} = \frac{1}{T}\int_0^T cv^2\,dt$, where *T* is the period and *v* is the velocity of the DCDEA.

Increasing the voltage amplitude can improve the output of a DEA, however, breakdown can happen when the corresponding electric field passes the threshold E_b. Hence, the amplitude of the voltage in this study is determined based on the breakdown electric field and the nominal thickness of the membrane. The breakdown electric field of the ELASTOSIL silicone elastomer was shown in [101] [211] [212] to be a function of two principle stretches and increases with the increasing stretch ratios. An empirical scale law was proposed in [101] based on the experimental measurement. However, it is worth noting that all existing measurements were based on equal biaxial stretches. To cope with the different principle stretches in cone DEAs, the breakdown electric field is proposed as a product of both λ_1 and λ_2, and is written as $E_b = E_{b0}(\lambda_1\lambda_2)^{0.615}$, where E_{b0} = 80 V/μm is the breakdown electric field with no pre-stretch and as reported by the manufacturer (Wacker Chemie AG). It is noteworthy that the E_{b0} adopted in this study is relatively conservative as a breakdown strength of 90 V/μm with no pre-

stretch was reported in [212]. The voltage amplitude is $\Phi_{peak} = 0.8E_bH$, a safe margin of 20% is considered in determining the voltage amplitude to further minimize the failure rate.

The power optimization strategy in this study is summarized as follows. Two parameters: λ_p and L are varied while the others are kept constant. By using the geometrical relationship (Eq. (4.42 – 4.44)), the two principle stretches, membrane thickness and force transmission angle can be obtained. Based on the breakdown strength scale law, E_b and Φ_{peak} are determined. By using the dynamic model of DCDEA (Eq. (6.1 - 6.2)), the average power output of the DCDEA at different excitation frequencies can be estimated. By comparing the power output performance, the optimal λ_p and L values can be determined.

Effects of pre-stretch ratios. The power output of the DCDEA with different λ_p and L values are shown in **Figure 6.23** with each subplot showing P_{out} as a function of f and L with λ_p fixed. It can be noted that for any sets of (λ_p, L), P_{out} increases with the increasing excitation frequency, reaches a peak value, P_{peak}, then decreases as f increases further. The peak power output demonstrates the advantages of resonant actuation of the inherent elastic DEAs. By comparing the subplots with different pre-stretch ratios, the maximum power output, P_{max}, the DCDEA can generate reduces with the increasing λ_p. For example, P_{max} is 73.6 mW when λ_p = 1×1 and drops to 58.3 mW when λ_p is increased to 1.4×1.4. This suggests that the DCDEA could have an optimal performance with no additional pre-stretch and the stretch caused by the spacer protrusion can be sufficient. This finding echoes the author's previous quasi-static work output optimization study on cone DEAs [213].

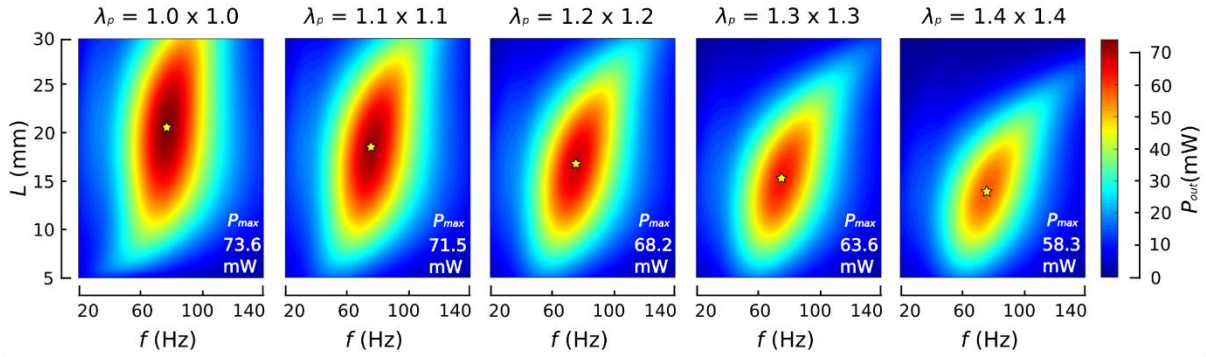

Figure 6.23. Silicone DCDEA power output optimization result. Comparison of P_{out} against f, L for λ_p from 1×1 to 1.4×1.4. Yellow stars mark the maximum P_{out} value for each λ_p. c = 1 N.s/m, M = 1 g.

Effects of spacer lengths. The peak power output, P_{peak}, and the peak stroke, Δd_{peak}, for DCDEAs with λ_p = 1×1 and varying L are plotted in **Figure 6.24** (**a**). P_{peak} shows an increase with the increasing L and peaks at 21 mm, then drops while Δd_{peak} fluctuates and shows a peak at L = 19 mm. The different L values where power and stroke peaks at suggests DCDEA design should be tailored based on the desired output (i.e. stroke/ power). **Figure 6.24** (**b**) shows the power and stroke output as a function of excitation

frequencies with L = 21 mm and λ_p = 1×1. The stroke and power output are found to have peaks at two separate frequencies with the frequency corresponding to Δd lower than that with maximum P_{out}. This is also noticed in our experimental study on the DEA driven pump in Section 7.5.6, where the peak pressure output occurs at a slightly higher frequency than the largest stroke. The difference between the peak in oscillation amplitude and power output can be explained by the different 'amplitude resonance' (the amplitude of the forced oscillator is maximum) and 'velocity resonance' (the velocity of the forced oscillator is maximum) of a dynamic system. For a forced vibration system with damping, the amplitude resonant frequency is lower than the natural frequency without damping, while the velocity resonant frequency equals the natural frequency without damping [214]. As a result, the peak amplitude occurs at a lower frequency than the velocity-dependent power output ($P_{out} \sim v^2$) in this DEA-mass-damper system.

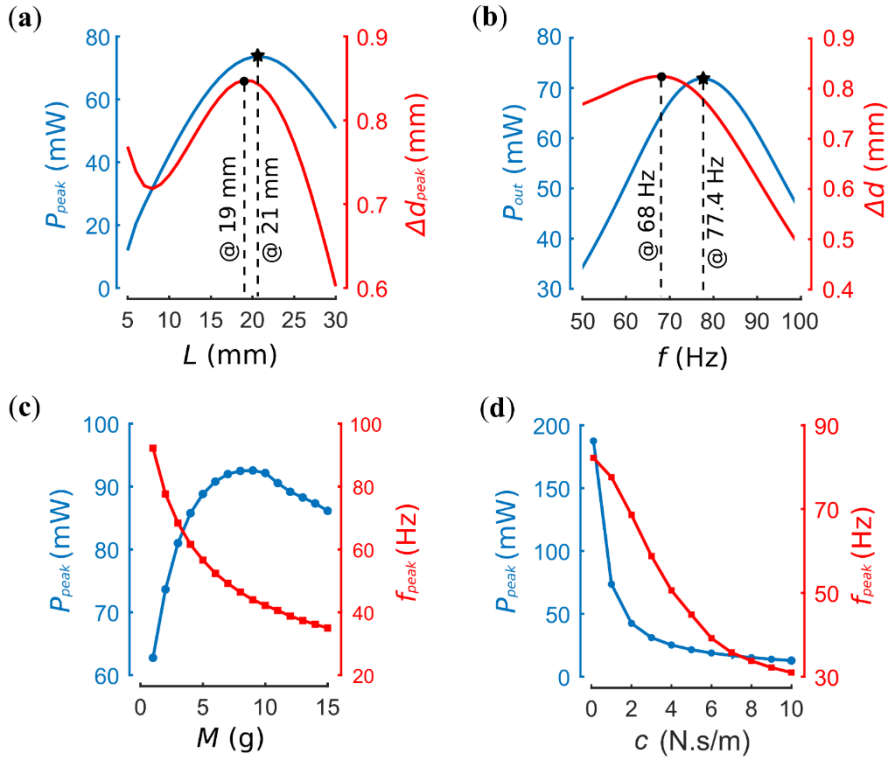

Figure 6.24. Silicone DCDEA power output optimization results. (**a**) Maximum P_{out} and Δd against L. λ_p = 1× 1, c = 1 N.s/m, M = 1 g. (**b**) P_{out} and Δd against f. λ_p = 1×1, L = 21 mm, c = 1 N.s/m, M = 1 g. (**c**) P_{peak} and the corresponding frequency against M. λ_p = 1×1, L = 21 mm, c = 1 N.s/m. (**d**) P_{peak} and the corresponding frequency against c. λ_p = 1×1, L = 21 mm, M = 1 g.

Effects of payloads. In the above studies, the mass, M, and damping coefficient, c, in the payload were fixed. Here we investigate the effects of these two parameters on the performance of the DCDEA. L is

fixed at 21 mm and λ_p is 1×1. **Figure 6.24** (**c**) shows the maximum power output and the corresponding frequency against M. As M increases, P_{peak} also rises while the frequency decreases and when M is heavier than 10 g, P_{peak} value also reduces. Increasing damping in the payload significantly decreases the P_{peak}, as plotted in **Figure 6.24** (**f**), and f_{peak} also decreases with the increasing c. The sharp reduction in power output is believed to be due to the force generated by the DCDEA which cannot overcome the velocity-proportional damping force when the damping coefficient is large, which results in greatly reduced actuation amplitude thus low power output. In applications where high damping exists, multiple layers of membranes can be stacked to achieve the desired power output. It is noteworthy that the peak power output demonstrated by the silicone DEA is significantly higher than VHB counterparts (over 70 mW for silicone DEAs and 0.4 mW for VHB ones with the same size). Such higher specific power of silicone DEAs also indicates a much higher electromechanical efficiency that could potentially approach the upper limit of 50% if no electrical energy recovery is taken into account.

6.4.3 Silicone DCDEA Flapping Wing Mechanism Design

To demonstrate the resonant actuation principle of silicone based DCDEAs, in this section the DCDEA is applied to drive a flapping wing mechanism. The design concept is illustrated in **Figure 6.25** (**a**), where a silicone DCDEA stack drives the wings via a rack and pinion mechanism. A fabricated prototype of the flapping wing mechanism is shown in **Figure 6.25** (**b**). The optimal silicone DCDEA configuration found in the last subsection (a = 7.5 mm, b = 15 mm, L = 21 mm, and λ_p = 1 × 1) was adopted here. The main structure was fabricated via 3D printing (Eden 350V printer, Objet Geometries). Rack and pinions have a pitch of 0.5 MOD and the pinions are precision spur gears with the pitch circle diameter of 6 mm (Accu, UK). The wings are 50 mm in length and 20 mm in width and are made of 0.05 mm thickness Mylar (DuPont).

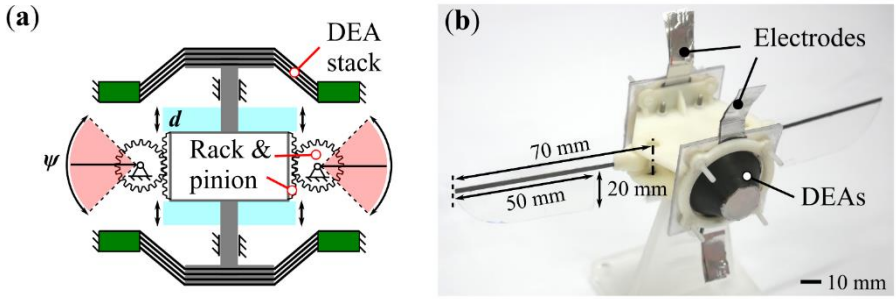

Figure 6.25. DCDEA driven flapping wing mechanism design. (**a**) Schematic diagram of DCDEA driven flapping wing mechanism design. (**b**) Photo of fabricated prototype.

Experiments were conducted to measure the performance of the DCDEA driven flapping wing mechanism and the experimental setup is illustrated in **Figure 6.26** (**a**). The prototype was fixed to a lever mechanism and its weight was balanced by counterweights. A load cell (NO.1004, TEDEA) was used to measure the lift generated by the flapping wing mechanism and a laser displacement sensor (LK-G152 and LKGD500, Keyence) measured the displacement of the DCDEA. The flapping stroke was estimated based on the measured DCDEA stroke and the pitch circle diameter of the spur gears.

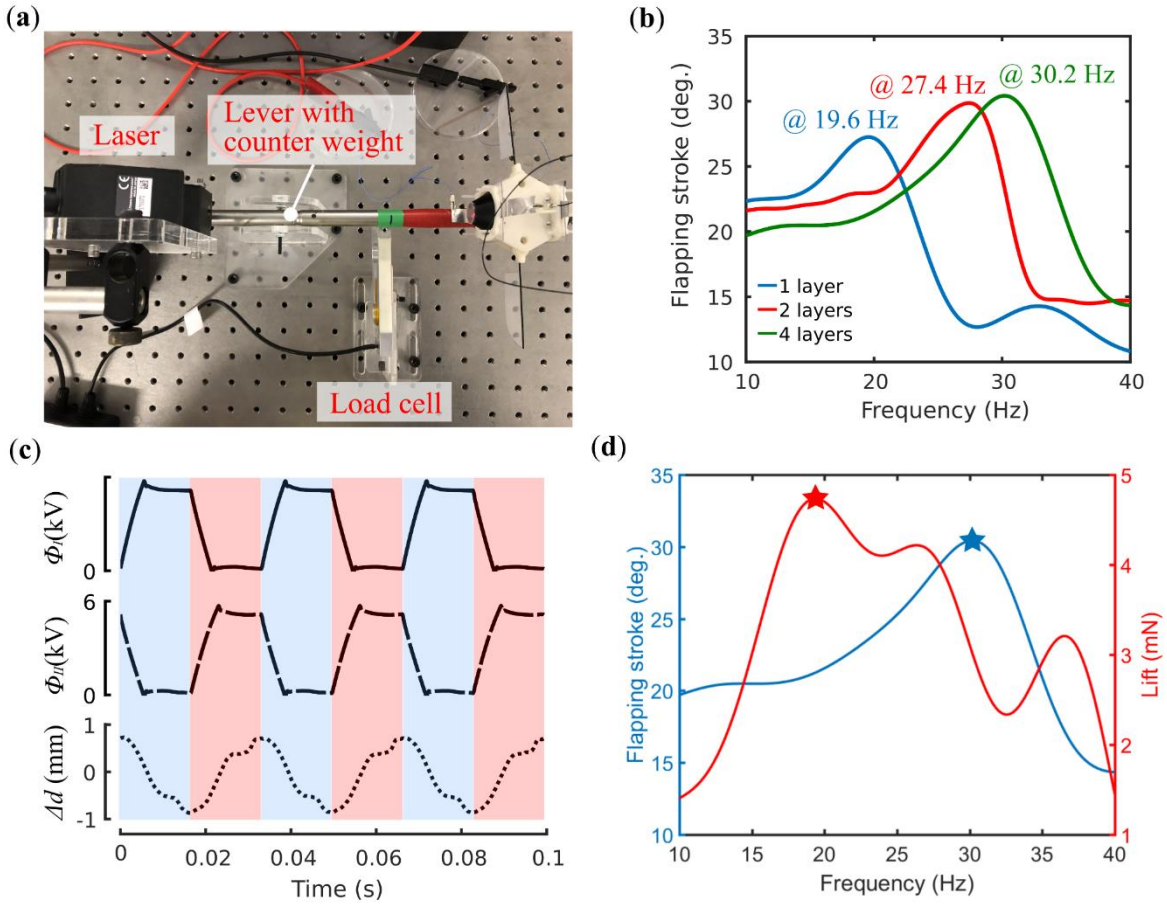

Figure 6.26. Experimental setup and results of flapping wing mechanism. (**a**) Experimental setup for flapping wing mechanism tests. (**b**) Flapping stroke against excitation frequency of DCDEA with different layers. (**c**) Measured flapping stroke and lift force against flapping frequency. 4 layers DCDEA was used. (**d**) Example of actuation voltages and DEA displacement at 30.2 Hz.

Figure 6.26 (**b**) shows the flapping stroke against actuation frequency for 1, 2, and 4 layers of silicone DCDEAs. Distinguishable stroke peaks can be observed for all three cases, showing clear resonance of the system. To the best of the author's knowledge, this is the first time a resonant peak was shown in a DEA driven flapping mechanism, which proves the feasibility of resonant actuation of DEAs for high power applications. As the number of layers increases, both the flapping stroke peak and its

corresponding frequency increases. For the 4-layer one, the flapper has a highest flapping stroke of 31˚ at 30.2 Hz. As the number of layers increases further, the high voltage amplifier used in this work is not capable of driving the increasing electrical payload. As a result, a maximum of 4 layers were used in the experiment. The detailed actuation voltages and the displacement of DCDEA with 4-layer stack are shown in **Figure 6.26** (**c**), where the blue and red colours represent the up and downstroke of the wings. It can be noted that due to the electrical payload, the programmed square waves turned trapezoidal, which demonstrates the need for a higher power amplifier in order to maximize the power output of the DEAs. The measured lift force against the actuation frequency for the 4-layer prototype is shown in **Figure 6.26** (**d**). A maximum of 4.7 mN lift was generated by this prototype, however, it is noteworthy that, the maximum lift is not correlated to the maximum flapping stroke, as indicated by the two different stars in **Figure 6.26** (**d**). This could be due to the wing membranes being too flexible, as the wings are flapping at a high frequency and the high aerodynamic load deforms the wing membranes significantly, causing a decrease in the angle-of-attack, and leading to reduced lift. This finding indicates the complicity of flapping wing mechanism designs and requires in-depth study for future optimization and integration of the system.

The flapping motion of the flapper at 30 Hz was recorded using a high-speed camera and **Figure 6.27** shows a series of footages in one cycle. It can be noted that the wings pitch passively during the up and downstrokes due to the aerodynamic load, and during the stroke reversal, the wings pitch passively to change the direction of angle-of-attack due to the inertial of the wings and the added mass of the air [215], such passive wing pitch reversal was observed in insect flights [216].

The flapping wing mechanism design proposed in this section serves as a demonstrator of the resonant actuation of DCDEAs with the configuration optimized to generate the maximum power output. Resonant peaks have been observed the first time in DEA driven flappers, which proves the feasibility of utilizing the inherent elasticity in DEAs to achieve resonant flapping motion, as found in natural counterparts. The flapping performance of this design outperforms previous DEA driven flappers (e.g. a flapping amplitude of 15˚ in [217] and 10˚ at 5Hz in [10]). It should be noted that this design is only a proof-of-concept. In the future work, optimization can be done to minimize the weight of the support structure [218], optimize the angle-of-attack [215][219], and improve motion transmission efficiency. Developing miniature yet high-power high voltage amplifiers is also an essential aspect for enabling untethered DEA driven flapping wing mechanisms.

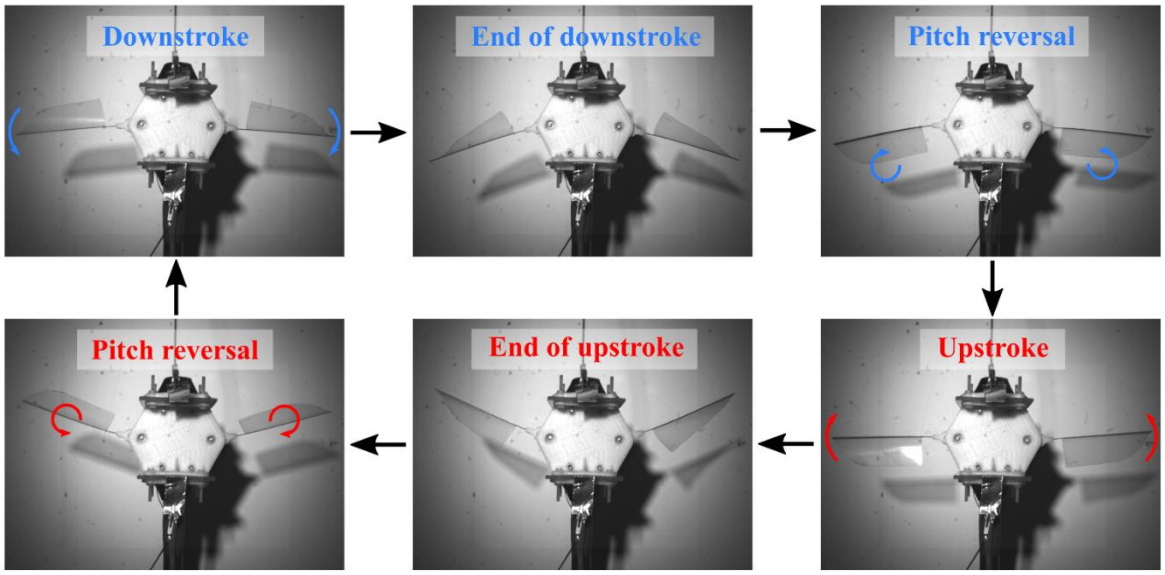

Figure 6.27. Series of flapping motion in one cycle demonstrating up and downstrokes and passive pitch reversals.

6.4.4 Silicone DEA Summary

The inherent elasticity in DEAs offers clear advantages in achieving resonant actuation over conventional actuators as no additional elastic elements are required. In this subsection, by using the verified numerical model, the first power optimization study on a silicone based DCDEA was conducted against its pre-stretch ratios and spacer length. The key findings are as follows:

i. The optimal DCDEA in terms of power output found was to have no pre-stretch and a 1.4 height-to-radius ratio.

ii. Peak power output occurs at a higher frequency than the peak stroke output for DCDEAs.

iii. Increasing the mass in the payload can reduce the frequency corresponding to the peak power output and can also affect the value of the peak power output.

iv. Increasing the damping coefficient in the payload can significantly reduce both the peak power output and the corresponding frequency.

With the optimal DCDEA configuration, we developed a bioinspired flapping wing mechanism driven by the resonating DCDEAs as a demonstrator to prove the feasibility of utilizing resonant actuation for bioinspired or soft robotics.

6.5 VHB vs Silicone DCDEA

In the last two subsections, VHB acrylic and ELASTOSIL silicone based DCDEAs were analysed in depth. It can be noted that despite the smaller size, silicone DCDEAs can generate a higher power output than VHB ones (**Figure 6.12** and **6.23**), which indicates the clear advantage of resonant actuation of silicone DEAs over VHB designs at high frequencies. This allows the silicone DEAs to be used in dynamic applications including flapping wing robots, soft motors and vibration shakers.

However, this finding does not suggest the silicone material is fully superior to VHB. As is demonstrated in **Figure 6.28**, by comparing the quasi-static output of silicone and VHB DCDEAs with identical size and membrane thickness, it can be noted that under the same electric field, VHB DEA has a much higher force and stroke output, leading to a greater work output at low frequencies. Note that the results were simulated based on the parameter values identified in Section 6.3.4 and 6.4.1. The high force/stroke/work output of VHB DEAs at low frequencies suggests that VHB material is better in quasi-static applications such as valves, binary robotics and active origami smart structures.

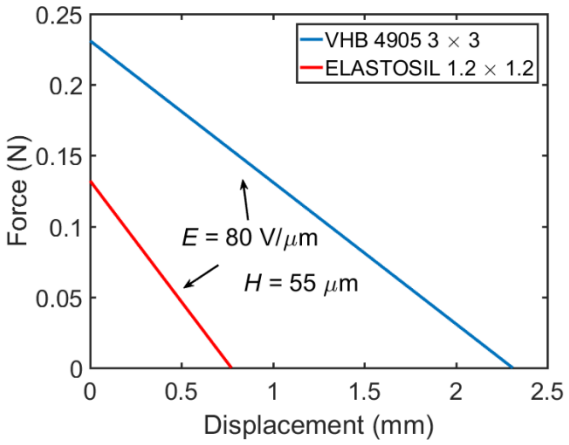

Figure 6.28. Comparison of the quasi-static force-displacement relationship of VHB DCDEA and silicone DCDEA with identical actuator size, membrane thickness and actuation electric field.

6.6 Chapter Summary

In this chapter, a double cone DEA configuration was investigated. A numerical model adopted from the generalized cone DEA model developed in Chapter 4 was developed. The DCDEAs made with VHB acrylic and ELASTOSIL silicone were investigated separately by using the numerical model and experimental study. Optimizations were performed the first time for the two types of DCDEAs. For VHB based DCDEA, its performance was optimized in terms of quasi-static work output while for silicone DCDEA, its performance was optimized in terms of maximum power output. Two novel principles of utilizing the inherent elasticity in the DEAs for cyclic actuations were also proposed. For VHB material with high viscoelasticity, its elasticity was utilized by taking advantage of the elastic energy recovery where the actuation duty ratio was reduced to allow a passive period for the elastic energy to contribute solely to the work output. This principle was also demonstrated on a bioinspired robotic leg. For silicone materials with low viscoelasticity, its elasticity was unitized by creating resonant actuation to allow the maximum power output from the actuator. The resonant actuation was demonstrated on a bioinspired flapping wing mechanism for the first time on a DEA driven flappers with the peak flapping stroke of 31˚ at 30 Hz.

Chapter 7: A Magnetically Coupled Double Cone DEA

The rigidly coupled double cone DEAs (DCDEAs) studied in Chapter 6 allow bidirectional actuation, however, the rigid coupling mechanism restricts the actuation of the two membranes to be in-phase, resulting in a single DOF system. In this chapter, a novel double cone DEA configuration is presented which eliminates the restriction of in-phase motion of the two DEA membranes, hence generating a 2-DOF system. This design features the compliant coupling of magnetic repulsion, which results in several emerging actuation behaviours, which could potentially be suitable for controllable shape changing actuations, active vibration damping and bioinspired/soft locomotion. The dynamic response of the magnetically coupled DEA (MCDEA) is fully characterized both experimentally and using the generalized cone DEA model. Its performance driving a dissipative payload is compared against a rigidly coupled DCDEA. The first DEA driven pneumatic pump is developed by using the MCDEA. Its performance is evaluated and potential applications of this pump in soft robotics are demonstrated.

Statement: The MCDEA design presented in Section 7.1 in this chapter is adapted from the following publication where C. Cao is the first author.

- **Cao, C**., Gao, X. and Conn, A.T., 2019. A compliantly coupled dielectric elastomer actuator using magnet repulsion. *Applied Physics Letters*. 114(1) p.011904.

Contribution: Fabrication and testing methodology, investigation, data curation, joint formal analysis, joint writing original draft; joint review & editing.

The MCDEA dynamic study presented in Section 7.2-7.3 in this chapter is adapted from the following publication where C. Cao is the first author.

- **Cao, C**., Hill, T.L., Conn, A.T. and Gao, X. Nonlinear dynamics of a magnetically coupled dielectric elastomer actuator. (submit soon)

Contribution: Fabrication and testing methodology, investigation, data curation, formal analysis, writing original draft; review & editing.

The MCDEA pump design presented in Section 7.5 in this chapter is adapted from the following publication where C. Cao is the co-first author with Dr Xing Gao.

- **Cao, C**., Gao, X. and Conn, A.T., 2019. A magnetically-coupled dielectric elastomer pump for soft robotics. *Advanced Materials Technologies*. (Accepted/In press).

Contribution: Fabrication and testing methodology, joint investigation, data curation, formal analysis, joint writing original draft; joint review & editing.

7.1 MCDEA Design

7.1.1 Design Overview and Actuation Principle

Here, we present a novel magnetically-coupled DEA (MCDEA) where the two membranes are compliantly-coupled using the repulsion of two permanent magnets. This design follows the same footprint of the DCDEAs but with complaint coupling which adds one extra DOF to the system. This novel 2-DOF DEA system allows two outputs with tunable amplitude and relative phases which lead to emerging dynamic behaviours and novel applications.

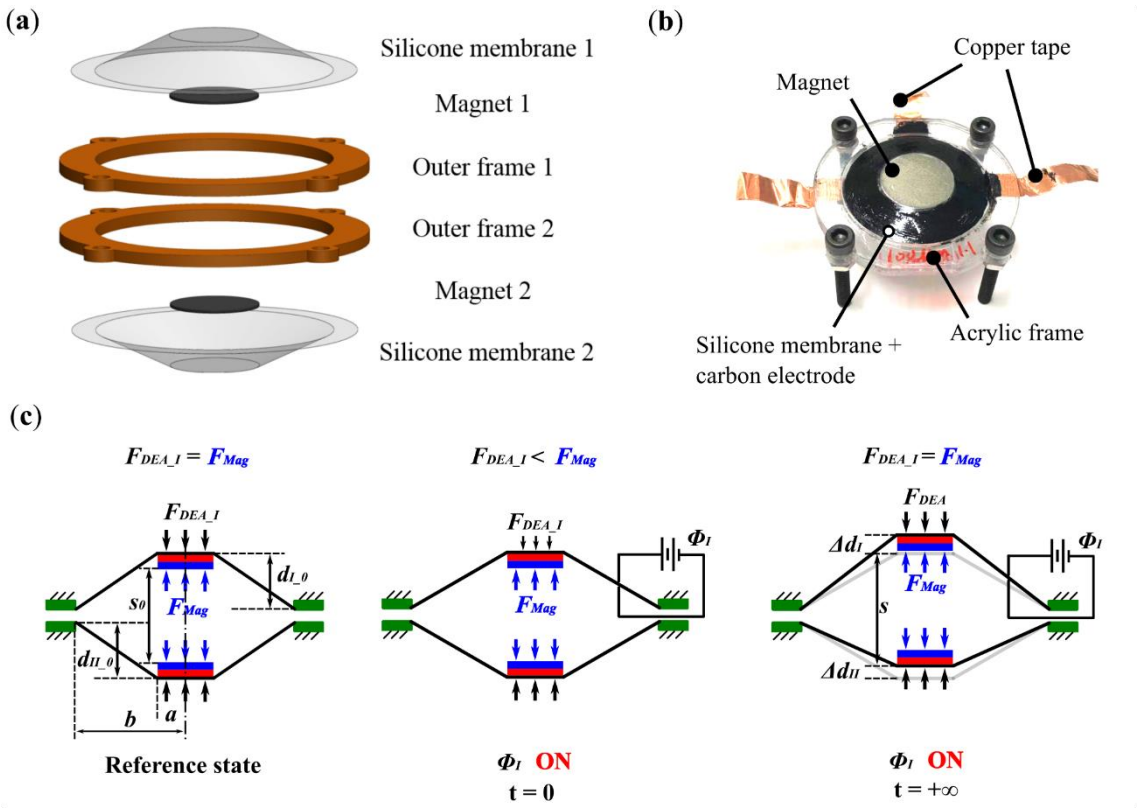

Figure 7.1. Design overview of a MCDEA. (**a**) Structure of the MCDEA (for clarity, electrodes are in absence). (**b**) Fabricated prototype of the MCDEA. (**c**) Actuation principle of the MCDEA.

The MCDEA configuration consists of two pre-stretched silicone membranes bonded to the rigid circular frames and disk permanent magnets in the centre, as shown in **Figure 7.1** (**a**). The two magnets are positioned to ensure the same pole are facing each other when the two membranes are assembled such that the membranes are deformed out-of-plane by the repulsion force. The reaction force of the DEA membrane in the vertical axis, F_{DEA}, and the magnetic repulsion, F_{Mag}, is balanced in its rest state (**Figure 7.1** (**c**) left). When a voltage is applied across one DEA membrane, the reaction force exerted

by the membrane reduces. The force imbalance between the F_{Mag} and the F_{DEA} causes the membrane to deform out-of-plane further until another force balance is achieved (**Figure 7.1** (**c**) middle and right). The same force imbalance also exists on the passive membrane, and it will deform together with the active membrane, but possibly by a different displacement due to the lack of Maxwell pressure and the compliant coupling.

By using this compliant coupling, this MCDEA has the capacity for different modalities with two separate inputs and an adjustable phase difference between them from 0 to 2π, which can result in several emerging actuation behaviours. For example, when the actuation voltage waveforms on the two membranes are in-phase, the double cone DEA expands in both directions as the two membranes are placed in symmetry (**Figure 7.2** (**a**)). Alternatively, when the actuation voltage waveforms are in antiphase, the DEA cones expand on one side and shorten on the other (**Figure 7.2** (**b**)).

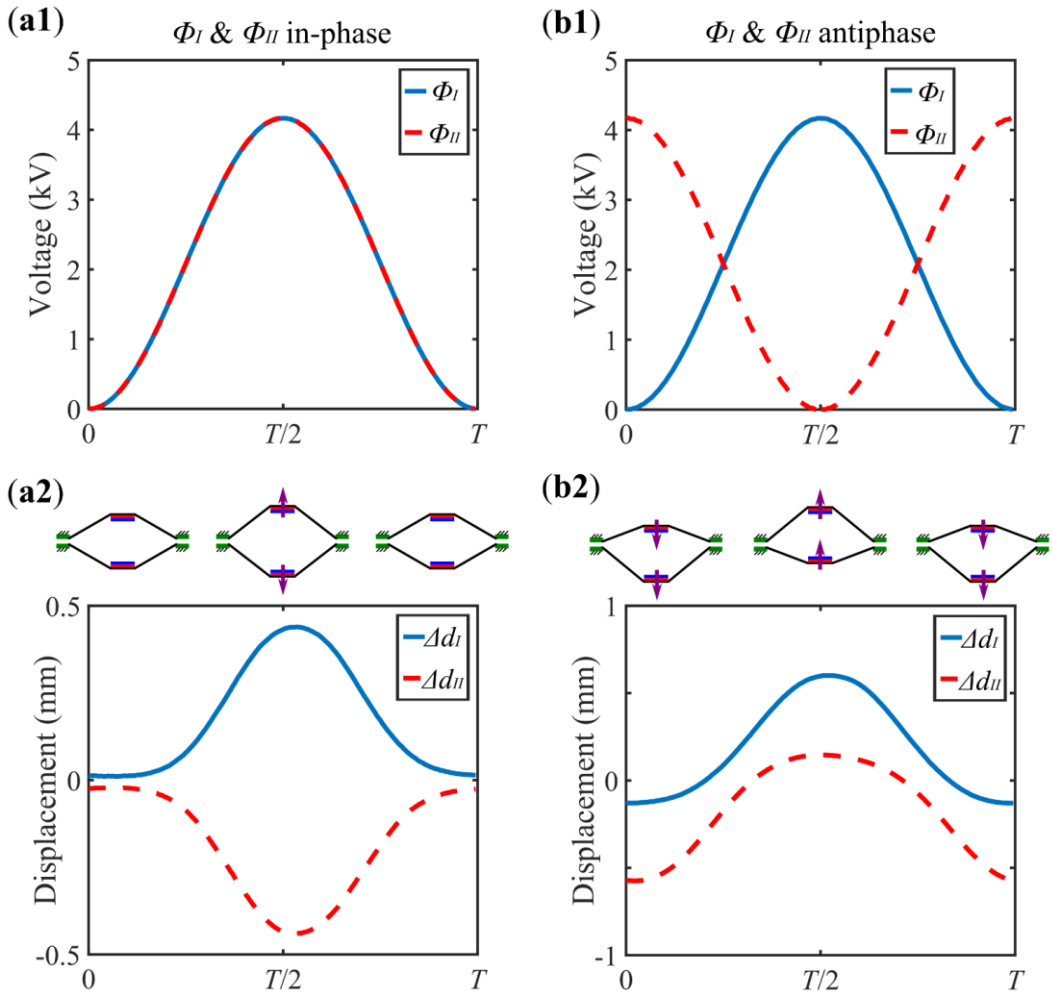

Figure 7.2. Examples of the applied voltages and measured displacements of the MCDEA. (**a**) The two membranes' actuation voltages are in-phase. (**b**) Two actuation voltages are antiphase.

7.1.2 MCDEA Fabrication

The fabrication of MCDEA prototypes follows the same steps described in Chapters 5 and 6. 100 μm thickness ELASTOSIL silicone elastomer with a 1.2 × 1.2 pre-stretch ratio was chosen here. The acrylic frame has an inner radius of 15 mm for prototype testing. Disk magnet with the radius of 7.5 mm, a thickness of 1 mm and weighs 1.35 g was attached to the centre of the membrane (N42 Neodymium magnets, First4Magnets). The custom carbon grease developed in Chapter 5 was adopted. Two DEA frames were connected using bolts and fasteners with 2 mm gaps in between.

7.2 MCDEA Performance Characterization

7.2.1 MCDEA Dynamic Model

As illustrated in **Figure 7.1** (**c**), in the passive equilibrium of the MCDEA, the magnetic repulsion, F_{Mag}, is balanced by the tension of membranes in the vertical axis, F_{DEA_n}, where $n = I, II$ for top and bottom membranes respectively (neglecting gravitational force). This force balance can be written as

$$F_{DEA\_\mathrm{I}} = F_{Mag}\ , \tag{7.1a}$$

$$F_{Mag} = F_{DEA\_\mathrm{II}}\ . \tag{7.1b}$$

The two membranes are deformed by d_{I_0} and d_{II_0} respectively and the distance between the two magnets is s_0 in this equilibrium, and can be expressed as

$$s_0 = \left|\overrightarrow{d_{\mathrm{I}\_0}} - \overrightarrow{d_{\mathrm{II}\_0}}\right|\ . \tag{7.2}$$

The arrows indicate the direction of deformation, for clarity, an upward deformation is defined as positive. The thickness of the magnets is neglected.

Letting $\overrightarrow{\Delta d_I}$ and $\overrightarrow{\Delta d_{II}}$ be the deformation of the top and bottom membranes from each passive equilibrium positions when actuation voltages are applied. The total out-of-plane deformation of the two membranes are $\overrightarrow{d_I} = \overrightarrow{d_{I\_0}} + \overrightarrow{\Delta d_I}$ and $\overrightarrow{d_{II}} = \overrightarrow{d_{II\_0}} + \overrightarrow{\Delta d_{II}}$. The distance between two magnets becomes $s = \left|\overrightarrow{d_I} - \overrightarrow{d_{II}}\right|$.

This magnetically coupled system can be simplified as the 2-DOF system shown in **Figure 7.3**, where m represents the mass of the magnet, nonlinear springs and dashpots represent the nonlinear reaction force and damping of the two DEA membranes. The nonlinear spring in the middle represents the

nonlinear magnetic repulsion. Here, it is assumed that there is no damping between magnetic interactions.

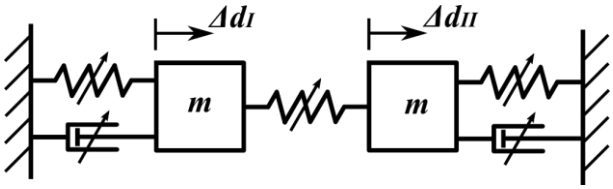

Figure 7.3. A schematic diagram illustrating this 2-DOF MCDEA system.

The equation of motions of the two masses can be readily expressed as

$$-\begin{bmatrix} m & 0 \\ 0 & m \end{bmatrix}\begin{pmatrix} \ddot{d}_I \\ \ddot{d}_{II} \end{pmatrix} + \begin{pmatrix} -F_{DEA\_I} \\ F_{DEA\_II} \end{pmatrix} + \begin{pmatrix} F_{Mag} \\ -F_{Mag} \end{pmatrix} = 0 \,, \tag{7.3}$$

where $\ddot{d}_n$ (n = *I*, *II*) is the vertical acceleration of the magnets.

The reaction force of two DEA membranes in the vertical axis can be described using the same model as in Section 6.2 (with the Gent hyperelastic model as well as the Maxwell rheological viscoelastic model introduced in Section 4.4.1 (Eq. (4.26 – 4.32))).

A simplified magnetic repulsion model [220] is adopted here to ensure that when the two magnets are in contact, the force becomes infinite and when the distance between two magnets tends to infinity, the force tends to zero. This model can be written as

$$F_{mag} = k/s^x \,, \tag{7.4}$$

where k is a constant to be determined, and x is an exponent to be determined from experimental testing.

With the actuation voltages defined, and the initial conditions known, the dynamic response of the MCDEA can be estimated by solving Eq. (7.3 – 7.4) numerically with the same process illustrated in **Figure 4.6**.

7.2.2 Model Validation

7.2.2.1 Experimental Setups

The quasi-static force-displacement relationship of a single DEA membrane was measured by following the same steps in Section 5.3.1 and 6.4.1, where the DEA was deformed at a very slow rate of 0.05

mm/s by a linear rail and the reaction force of the membrane was measured by a load cell. The experimental setup is shown in **Figure 7.4** (**a**). The magnetic repulsion was measured in the same way, one magnet was fixed to the load cell while the other one moved relative to this magnet by the linear actuator.

The dynamic response of the MCDEA was measured by fixing the frames of the DEA to the testing rig, with a frequency varying alternating current voltage applied to one DEA membrane while leaving the opposite membrane to oscillate passively. Two laser displacement sensors measured the displacements of the two membranes at a sampling rate of 40,000 Hz. The amplitude of the voltage single was set at 3.5 kV, which is equivalent to an electric field of 50 V/μm. The experimental setup is shown in **Figure 7.4** (**b**). Detailed experimental setup can be found in Section 5.3.1.

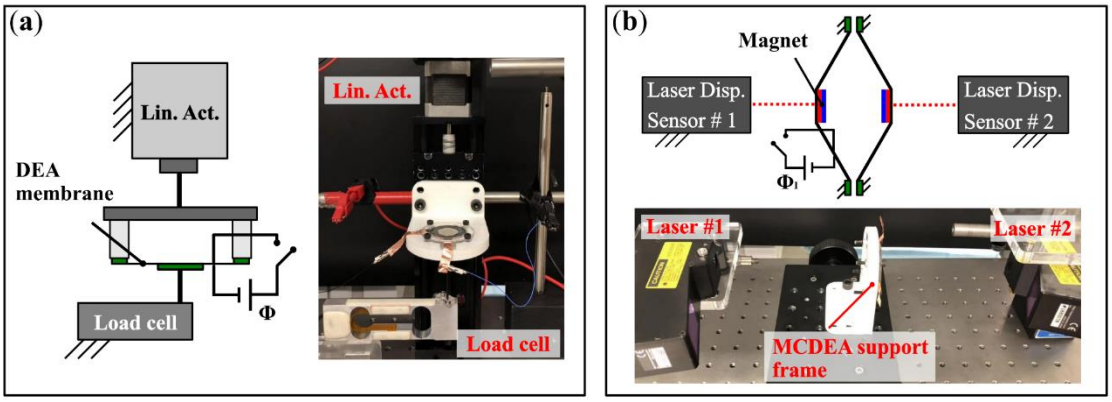

Figure 7.4. Experimental setup for MCDEA analysis. (**a**) Quasi-static force-displacement response of a single DEA membrane. (**b**) Dynamic frequency response of the MCDEA.

7.2.2.2 Model Parameters Identification

Figure 7.5 (**a1-2**) shows the measured and modelled quasi-static force-displacement response of a single membrane, F_{DEA}, and the magnet repulsion, F_{Mag}, respectively. The model parameters were determined by fitting to the experimental results using a least-mean-squares algorithm in MATLAB. The identified Gent model parameters are: μ_A = 431.5×10^3 Pa, J_A = 11.35. The magnetic repulsion is described using power curving fitting such that $F_{mag} = 0.0025s^{-0.93}$ (s in metres and F_{mag} in Newtons). An excellent fit can be found between the experimental result and model prediction for both DEA model and magnetic repulsion model, proving their effectiveness despite the simplifying assumptions.

Figure 7.5 (**b1-2**) and (**c1-2**) show the measured and modelled dynamic response of the MCDEA in a forward and backward frequency sweep. In this test, only one membrane was actively excited by a frequency varying sinusoidal voltage while the other membrane was left passive. The results shown in **Figure 7.5** (**b-c**) shows the displacement of the active membrane. The frequency of the sinusoidal excitation voltage is swept forward from 0 to 120 Hz at a rate of 1 Hz/s and then backward to 0 Hz at the same rate. The viscoelasticity of the elastomer was determined using the same fitting approach and the values adopted are μ_B = 145×10^3 Pa, J_B = 12 and η = 290 Pa·s. Again, an excellent match can be seen between the experimental result and the model prediction. Note that four peaks were observed in both forward and backward sweeps, which, to the best of the author's knowledge, have not been observed in previous rigidly coupled DEA systems. The distinguishing four resonant peaks are believed to be the result of the complex interactions between the two DEA membranes and the magnets and will be investigated in-depth in the next section.

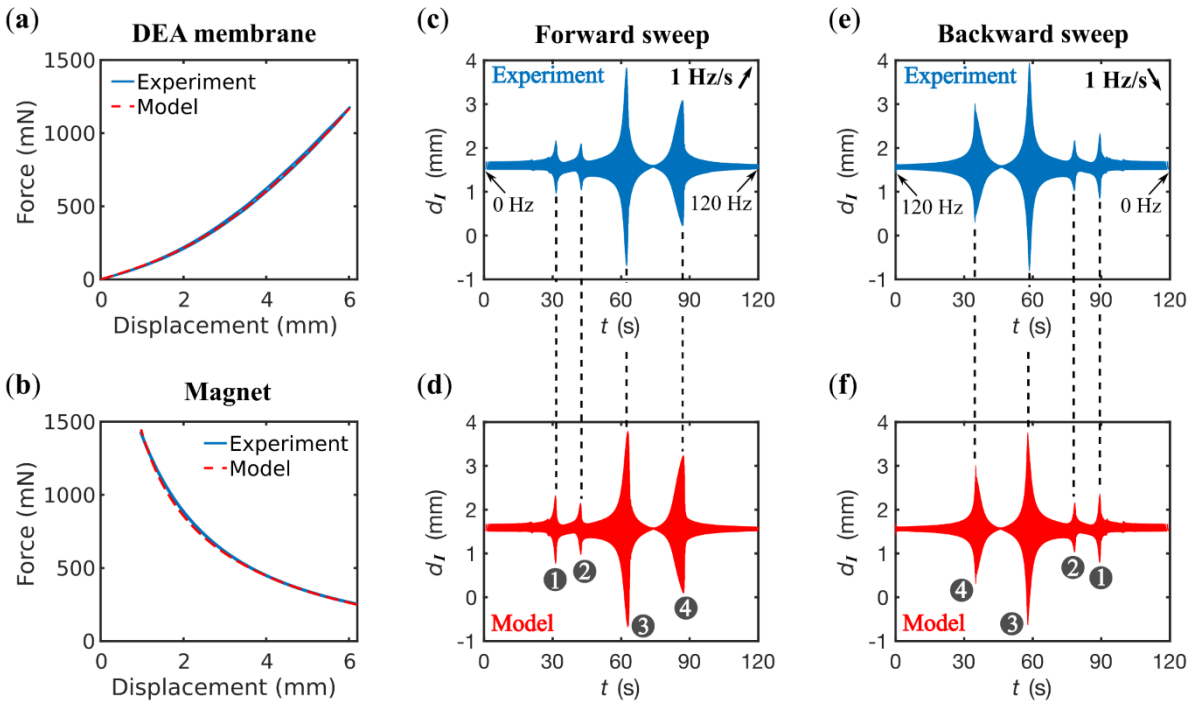

Figure 7.5. MCDEA model validation. Quasi-static force-displacement relationship of (**a1**) single DEA membrane and (**a2**) magnetic repulsion. Experimental results of the dynamic response of the MCDEA (displacement d_1) in (**b1**) forward frequency sweep and (**b2**) backward frequency sweep. (**c1-c2**) Model simulated response of the same frequency sweep test.

7.3 Dynamic Study on MCDEA

In this section, by using the developed dynamic model, the complex dynamic responses of the MCDEA system are analysed in-depth with the following two cases:

1. Φ_I = AC, Φ_{II} = 0. This is the fundamental case where one membrane is excited by an AC voltage while the other membrane remains passive.
2. Φ_I = AC, Φ_{II} = AC of the same frequency (i.e. $f_I = f_{II} = f$) but with varying relative phase. A distinguishing feature of the compliantly coupled MCDEA is that the two inputs signals can be tuned freely which can potentially result in interesting dynamic phenomena. Hence in this case, we investigate the effects of two input signals with the same frequency but different phases from 0 to π.

7.3.1 Case 1: Φ_I = AC, Φ_{II} = 0

The detailed time series of the actuation signal Φ_I and the displacements of the two magnets, d_I and d_{II}, of the four peaks found in **Figure 7.5** (**c1**) are shown in **Figure 7.6** (**a-d**) respectively. It can be noted that the two outputs are in-phase in peaks 1 and 3 and are antiphase in peaks 2 and 4. These correspond to the responses of the two underlying linear modes, as commonly found in 2-DOF oscillation systems [193]. As the excitation frequency is close to the resonant frequency of one of the resonant modes, the response of the system will be dominated by this specific resonant mode.

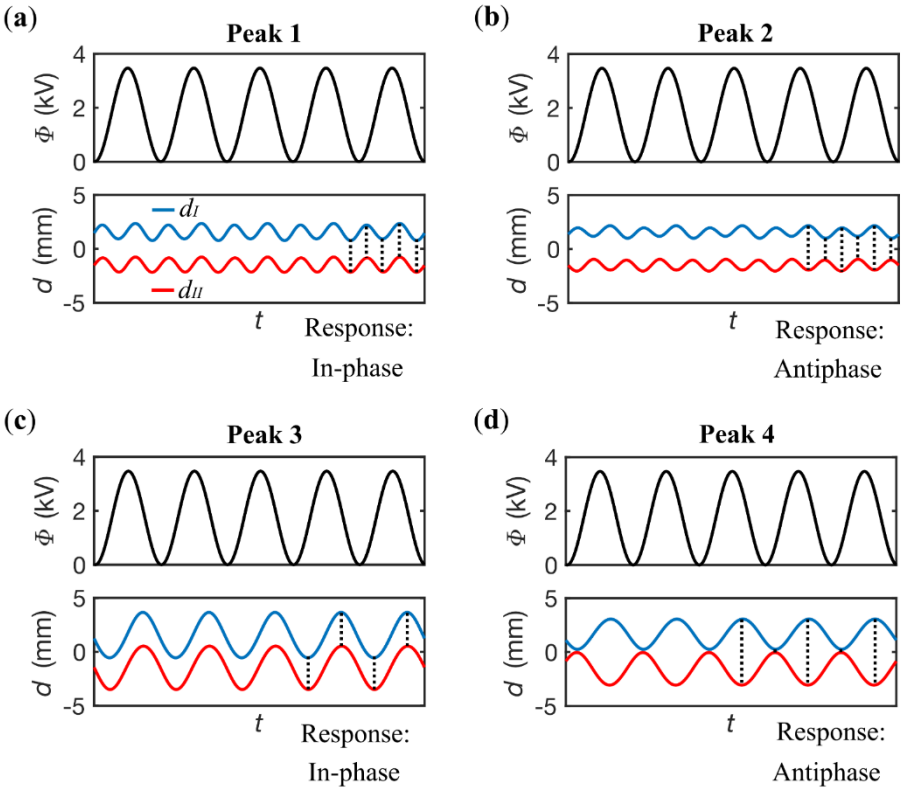

Figure 7.6. Simulated time series of the actuation signal Φ_I and the displacements of the two outputs, d_I and d_{II}, in the forward frequency sweep in **Figure 7.5** (**c1**). (**a**) Peak 1, f_I = 31.2 Hz, two outputs are in-phase; (**b**) Peak 2, f_I = 42.2 Hz, two outputs are antiphase; (**c**) Peak 3, f_I = 62.9 Hz, two outputs are in-phase; and (**d**) Peak 4, f_I = 87.1 Hz, two outputs are antiphase.

Also note that the excitation frequency of peak 1 is close to half that of peak 3, and the same is true for peaks 2 and 4. Also, in peaks 1 and 2, the two outputs oscillate at a frequency twice that of the driving frequency, demonstrating a super-harmonic response, while in peaks 3 and 4 where the oscillation amplitudes are higher, the oscillation frequency equals to the driving frequency, showing a harmonic resonance.

To understand the occurrence of multiple resonant peaks in this 2-DOF system, firstly recall (from Eq. (4.17)) that the excitation force is given by $p = \varepsilon_0 \varepsilon_r \frac{\Phi^2}{H^2}$, where p is the Maxwell pressure – i.e. the force experienced by the mass is a function of the square of the driving voltage signal, Φ. Therefore, recalling that the voltage signal for the first mass is given by $\Phi_I = \Phi_{DC} + \Phi_{AC} \cos(2\pi f_I t)$, the force experienced by the first mass is a function of

$$\Phi_I^2 = E_a + E_b \cos(2\pi f_I t) + E_c \cos(2\pi (2f_I) t) \,, \tag{7.5}$$

where

$$E_a = \Phi_{DC}^2 + \frac{\Phi_{AC}^2}{2} \,, \tag{7.6}$$

$$E_b = \Phi_{DC} \Phi_{AC} \,, \tag{7.7}$$

$$E_c = \frac{\Phi_{AC}^2}{2} \,. \tag{7.8}$$

This demonstrates that the forces experienced by the mass contain two time-varying components: one at frequency f_I and another at frequency $2f_I$. As a result, when the excitation frequency, f_I, is close to either $f_{rs}/2$ or f_{rs} (where f_{rs} is one of the resonant frequencies of this system), resonance could occur. The super-harmonic response of this MCDEA system can be potentially useful for engineering systems where high frequency oscillations can be generated by lower frequency signals.

The phase portraits and Poincaré maps of the four peaks are shown in **Figure 7.7** to allow further analysis of the dynamic response. These phase portraits and Poincaré maps are drawn based on the response over 100 excitation cycles. It can be noted for each peak, all 100 points in the Poincare maps overlap to one point, which suggests that at each peak, the MCDEA experiences a steady periodic vibration [193].

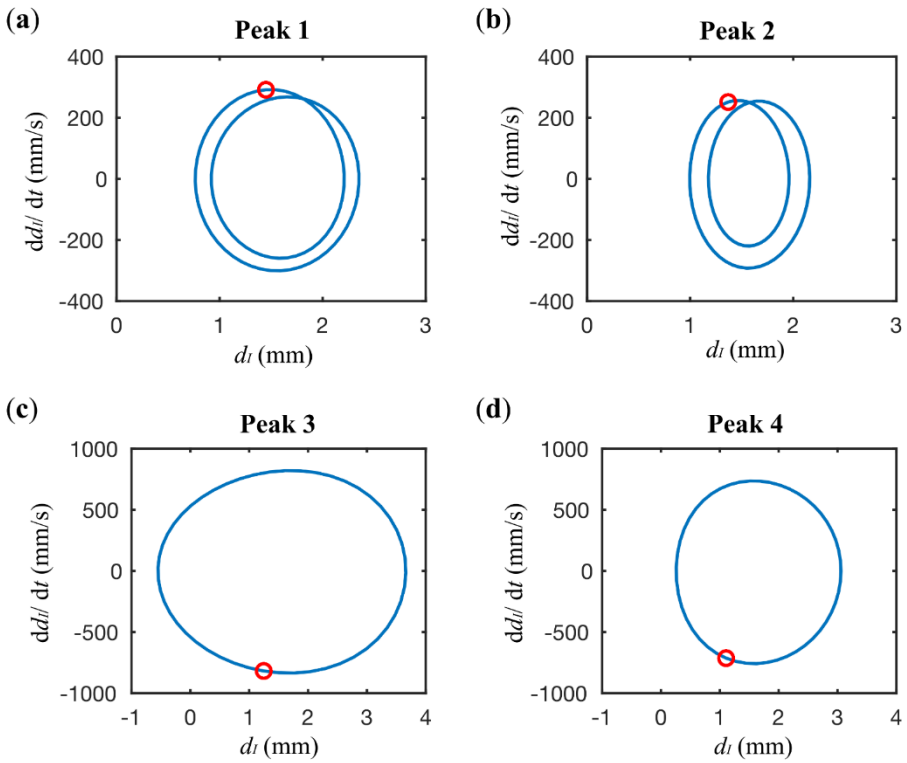

Figure 7.7. Phase portraits and the Poincare sections of the response of d_I in **Figure 7.6**.

Case 2: Φ_I = AC, Φ_{II} = AC, Varying Relative Phases

In the previous study, one DEA membrane was driven by an actuation signal while the other membrane remained passive. However, the MCDEA has the potential for allowing two membranes driven by two actuation signals with different relative phases. As a result, here the effects of the phase difference of the actuation signals on the dynamic response of the MCDEA are investigated by conducting the same forward frequency sweep from 0 to 120 Hz at a rate of 1 Hz/s. Two actuation signals were set as: $\Phi_I = \Phi_{DC} + \Phi_{AC}\cos(2\pi ft)$, $\Phi_{II} = \Phi_{DC} + \Phi_{AC}\cos(2\pi ft + \theta)$, and θ is varied from 0 to π (π to 2π will be similar to 0 to π hence not included in the study). Φ_{AC} = Φ_{DC} = 1.74 kV following Case 1.

The square of the two actuation voltage signals in this case study are written as

$$\Phi_I^2 = E_a + E_b\cos(2\pi ft) + E_c\cos(2\pi(2f)t)\,, \tag{7.9}$$

$$\Phi_{II}^2 = E_a + E_b\cos(2\pi ft + \theta) + E_c\cos(2\pi(2f)t + 2\theta)\,, \tag{7.10}$$

where E_a = 4.54 kV^2, E_b = 3.02 kV^2, E_c = 1.51 kV^2 (following Case 1).

The measured and simulated dynamic response of the MCDEA with θ = 0, π/6, π/3, π/2, 2π/3, 5π/6 and π are shown in **Figure 7.8** (**a1-g1**) and (**a2-g2**) respectively. Note that the change in phase not only affects the amplitudes of the resonant peaks but can also determine the existence of all the resonances. For example, at θ = 0, peaks 1 and 3, (i.e. the super-harmonic and primary resonances of the first mode, where d_I and d_{II} oscillate in-phase) completely vanish, while peaks 2 and 4, (i.e. the super-harmonic and primary resonances of the second mode, where d_I and d_{II} oscillate in antiphase) reach their maximum amplitudes. This can be explained by the fact that both the f and 2f components of the forcing (Φ_I^2 and Φ_{II}^2) are multiplied by coefficients that are opposite in sign (the two DEA membranes are facing each other, hence a similar actuation voltage will cause the two membranes to move in opposite directions, see **Figure 7.2** (**a**)). As a result, when θ = 0 the excitation forces are in antiphase and hence only excite the antiphase resonances. When θ = π/2, the phase of the 2f component of the excitation is 2θ = π (Eq. (7.9 & 7.10)), which leads to an in-phase excitation. Hence the first super-harmonic, peak 1 (exhibiting an in-phase response) reaches its maximum amplitude. Similarly, the case θ = π strongly excites the in-phase primary response, peak 3, and the antiphase super-harmonic resonance, peak 2 (as the phase of the 2f component is 2θ = 2π, which generates an antiphase excitation force).

The phase tuning demonstrated in this case represents a novel approach beyond voltage amplitude tuning to control the dynamic behavior of a 2-DOF DEA. Adjusting the phase difference between the two actuation signals not only controls the amplitudes but also the occurrence of a specific resonant peak. This phase tuning strategy is believed to be advantageous in future vibration control and energy harvesting applications, where a specific mode of oscillation and resonance is required for a potentially unpredictable external forcing frequency.

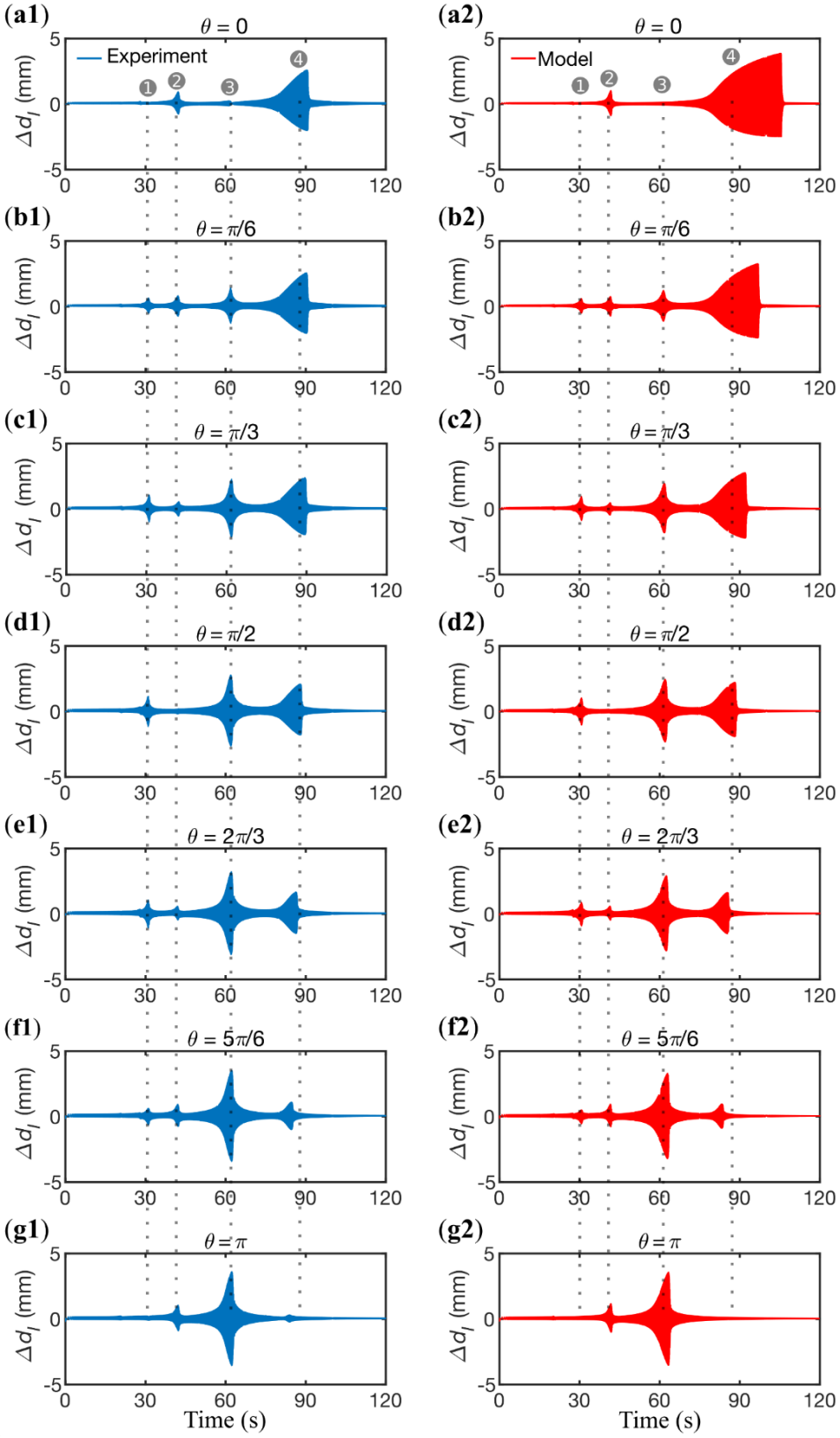

Figure 7.8. Experimental result (blue) and model simulation (red) of the dynamic response of the MCDEA with relative phase between two driving signals of (**a**) $\theta = 0$; (**b**) $\theta = \pi/6$; (**c**) $\theta = \pi/3$; (**d**) $\theta = \pi/2$; (**e**) $\theta = 2\pi/3$; (**f**) $\theta = 5\pi/6$ (**g**) $\theta = \pi$.

7.3.2 Summary of MCDEA Dynamics

By adopting the generalized cone DEA model and experimental approach, the emerging dynamics of MCDEAs were investigated in this section, and the results of the MCDEA dynamic study can be summarized as follows:

- This MCDEA system contains two vibration modes: antiphase and in-phase, which is due to the 2-DOF in this system.
- Due to the electromechanical coupling of the MCDEA, super-harmonic and primary hormonic resonance are observed.
- The MCDEA exhibits steady periodic oscillation, even at high amplitude resonant vibrations.
- Apart from tuning the actuation voltage amplitude as demonstrated in Section 5.3, the amplitude and resonant frequency of MCDEA can also be tuned by the relative phase between the two actuation signals.
- The phase tuning of MCDEA can control the existence of the resonance of a specific mode.
- Phase tuning offers a novel control scheme for the dynamics of DEAs.

7.4 Performance Comparison Against Rigidly Coupled DCDEA

In this section, the power output of the rigidly coupled DCDEA developed in last chapter and the compliantly coupled MCDEA are compared by driving a dissipative payload using the verified dynamic model.

7.4.1 Numerical Model Study Setup

The theorical study setup is described as follows. For both rigidly coupled DCDEA and MCDEA, a single layer of 100 μm thickness silicone membrane with a pre-stretch ratio of 1.2 × 1.2 was used. The rigid frame has the inner radius of 15 mm, the central disk/ magnet has the radius of 7.5 mm (after the model validation setup in Section 7.2.2.1). Each disk/magnet weighs 1.5 g. One disk/magnet is attached to a linear dashpot with the damping coefficient of *c*. The spacer length for DCDEA is set at 8 mm, the magnetic repulsion force coefficient *k* is set at 0.01 which ensures the MCDEA has an initial height as the DCDEA. An illustration of the setup is shown in **Figure 7.9**.

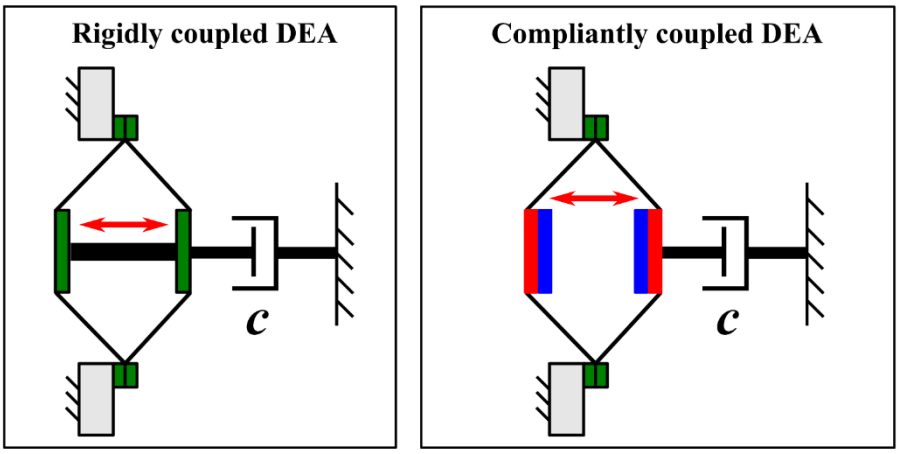

Figure 7.9. Performance comparison setup for rigidly coupled double cone DEA and compliantly coupled MCDEA.

The actuation signals for the two DEA membranes of both the DCDEA and MCDEA are antiphase with the amplitude of $E_{DC} = E_{AC} = 36$ V/μm. The damping coefficient is increased from 0.1 to 10 N.s/m and for each value of damping coefficient, the DEA is actuated to drive the dashpot while the excitation frequency is swept from 0 to 200 Hz. The average power at each frequency is $P_{out} = \frac{1}{T}\int_0^T cv^2 dt$, where *v* is the velocity of the dashpot, and *T* is the excitation period.

7.4.2 Modelling Results

The simulated average power output of the DCDEA and MCDEA as a function of excitation frequency and damping coefficients are shown in **Figure 7.10** and **7.11** respectively. For payloads with very low damping (e.g. c = 0.1 N.s/m), both the rigidly coupled DCDEA and MCDEA exhibits a peak in power output at resonance, as indicated by the bright yellow colour in both figures. However, as the damping coefficient in the payload becomes larger, DCDEA shows a dramatic drop in its power output (also demonstrated in **Figure 6.24**). When the damping coefficient reaches 10 N.s/m, the DCDEA exerts negligible power output and no resonant peak can be observed. On the contrary, the increasing damping in the payload shows no effect on the power output of the MCDEA. In fact, the maximum power output at the resonance increases with the increasing damping coefficient, suggesting its excellent performance is caused by the compliant coupling mechanism.

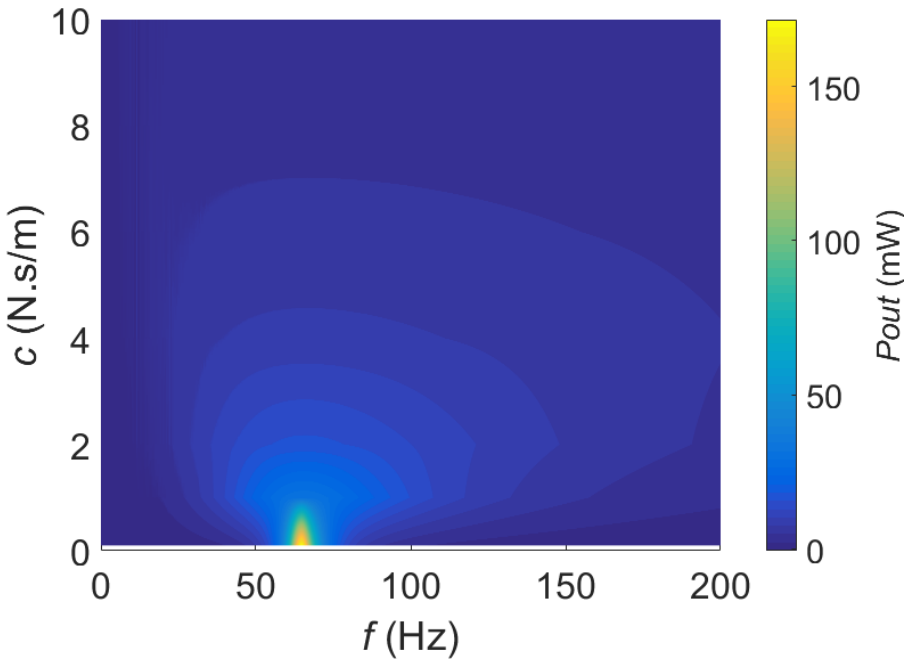

Figure 7.10. Average power output of a rigidly coupled DCDEA as a function of excitation frequency and damping coefficients.

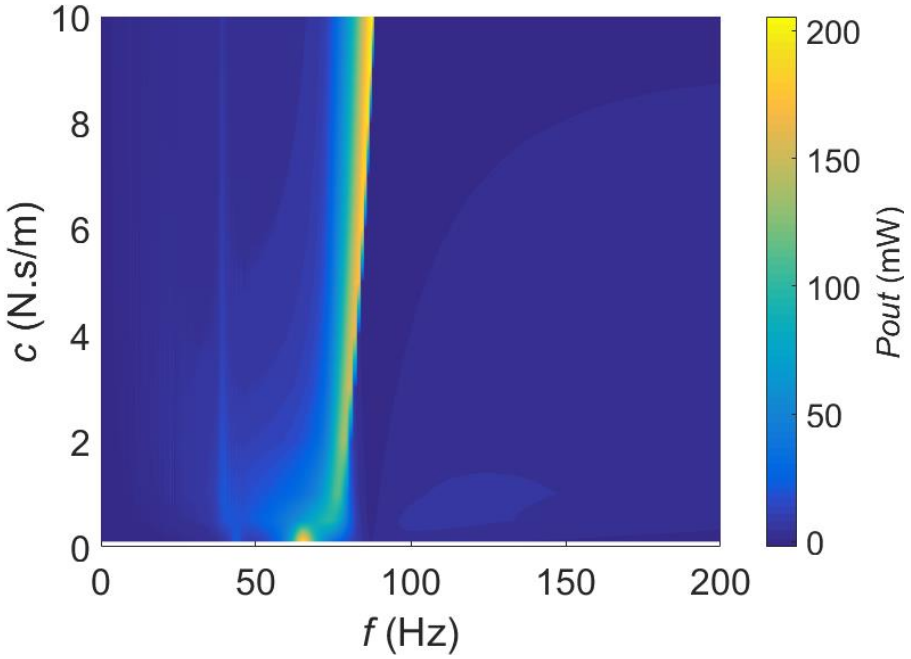

Figure 7.11. Average power output of a compliantly coupled MCDEA as a function of excitation frequency and damping coefficients.

7.4.3 Discussion

In this section, the power output of a rigidly coupled DCDEA and a MCDEA with identical shape and mass are compared in simulation. The MCDEA configuration is found to not be affected by the increasing damping in the payload, while the DCDEA is affected strongly by the damping. This is believed to be due to the force generated by the DCDEA not being able to overcome the velocity-dependent damping force when the damping coefficient is large, which results in greatly reduced actuation amplitude and thus low power output. For the MCDEA, because of the extra DOF added by the compliant coupling, even while one mass (magnet) is directly attached to the viscous payload, the other mass can still oscillated freely with a large amplitude, and the large damping force of the payload can be overcome by the large inertia force from the free oscillating mass. This feature allows the MCDEA to be used in applications with high damping. One example is a DEA pump, due to the viscosity of the fluid and the high pressure inside the pump chamber, where traditional DEA configurations such as the rigidly coupled DCDEAs might not have a good pumping performance, while the novel MCDEA configuration can be advantageous in this case. To demonstrate the feasibility, a MCDEA driven pneumatic pump is developed and will be described in detail in the next section.

However, it is worth noting that despite the high power output under the highly viscous payload, MCDEA has the problem of position drifting when the damping coefficient is high, as illustrated in **Figure 7.12**, this could be fine for applications such as the pneumatic pump where the amplitude/power

is essential while a fixed balancing position is less important. However, for applications such as flapping wing mechanisms, a fixed balancing position is crucial to ensure a minimum pitch motion during hovering. In this aspect, rigidly coupled DCDEA shows clear advantage over compliantly coupled MCDEA, and to some extent, the low power output of a DCDEA can be compensated by having multilayers stacked.

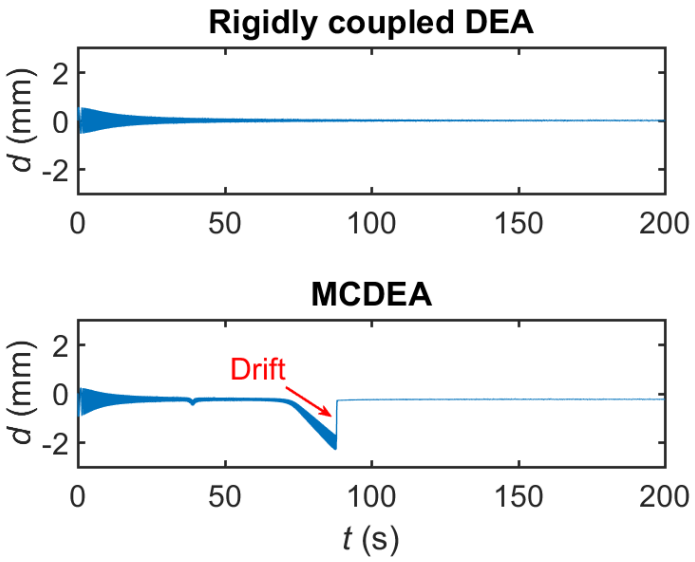

Figure 7.12. Comparison of the displacement of the payload driven by the DCDEA and MCDEA in a frequency sweep from 0 – 200 Hz at 1 Hz/s. The damping coefficient is 10 N.s/m. Drifting can be clearly noticed for MCDEA at resonance.

Another potential disadvantage for the MCDEA is the weight of the coupling magnets which can significantly increase the overall weight of the actuator. The DEA membranes and compliant electrodes tend to be extremely light (< 0.1 g in this size), and the circular frame can be made of high strength-to-weight ratio materials (such as glassfibres as shown in Chapter 6 to be less than 0.3 g). However, to ensure a sufficient out-of-plane deformation, the coupling magnet has to weigh over 1 g even when the high strength Neodymium N42 magnets are used. The heavier weight caused the coupling magnets can reduce its mass-specific power-density which could potentially limit its application in extremely weight sensitive applications such as flapping wing mechanisms.

7.5 MCDEA Application: MCDEA Driven Pneumatic Pump

7.5.1 Introduction

The fast growing fluidic elastomer actuation technique in soft robotics has the advantages of low-cost, inherent compliance and multiple degree-of-freedom operations [1]. Fluidic actuators are typically pneumatic and usually adopt bulky and rigid air compression systems that restrict their application in untethered mobile and wearable devices [65] [221]. The conventional setup of a single centralized air compressor with multiple distributed pneumatic actuators are further limited by the scaling of pressure losses as the air supply channels become thinner and longer. Miniature piezoelectric and electromagnetic pumps [222] have the potential to decentralize the air supply to compensate for the pressure loss. However, their actuation mechanisms typically rely on rigid or inextensible components, which can introduce a hard discontinuity in soft robotic systems due to the stiffness mismatch. This can consequently compromise advanced behaviors such as computational morphology [223] and overcomplicate the system design.

Advancing embeddable soft pump technologies towards integrated fluidic elastomer networks requires novel solutions that move beyond the paradigm of rigid compressor technologies. DEAs have the advantages of large actuation strains and they are inherently compliant, which make them an ideal candidate for potential embeddable soft pump designs. In the last two decades, several DEA driven hydraulic pumps have been developed. For example, a DEA-driven fluidic micromixer demonstrated peristaltic pumping [224] but is less effective for soft robotics due to low flowrates (21.5 µL/min). DEA diaphragm pumps have shown the advantage that DE membranes can serve both as a chamber diaphragm and a compressor [225]. Diaphragm DEAs that exploit the snap-through phenomenon have demonstrated a large pumping volume and a good pressure output (~10-20 mbar, 0.84 L/min) [226], however, the large space occupation due to snap-through expansion limits its potential for embedded soft pump applications. A hydrostatically-coupled DEA micropump demonstrated good pumping performance (84.5 mbar, 77.4 µL/min) at its resonant oscillation [227], but it is not known how this performance will scale up to meso and macro-scales. It is notable that all current DEA pumps in the literature are hydraulic and no pneumatic pumps are available. Considering the compressibility of air, these pumps might not directly adapt to pneumatic pumping, which is a limitation for soft robotics as pneumatic operation offers reduced weight, lower viscous pumping losses and no need for a liquid container.

7.5.2 Design Overview and Working Principle

The MCDEA configuration is well suited for a diaphragm pump design as the lower DEA membrane can also serve as an active or passive diaphragm (depending on whether a voltage is applied to the lower membrane or not), which can reduce the overall size of the pump design and the component complexity. The MCDEA diaphragm pump design is illustrated in **Figure 7.13** (**a**). The bottom membrane of the MCDEA is attached to the pump chamber frame and serves as the pump diaphragm. The top DEA membrane is separated from the bottom membrane by a spacer with the distance, *h*. This open design ensures minimal air damping between the two membranes. Passive check valves are connected to the inlet and outlet of the pump, allowing air flow into the chamber when the chamber volume expands (filling stage) and pumping air out when the chamber compresses (venting stage) (**Figure 7.13** (**b**)).

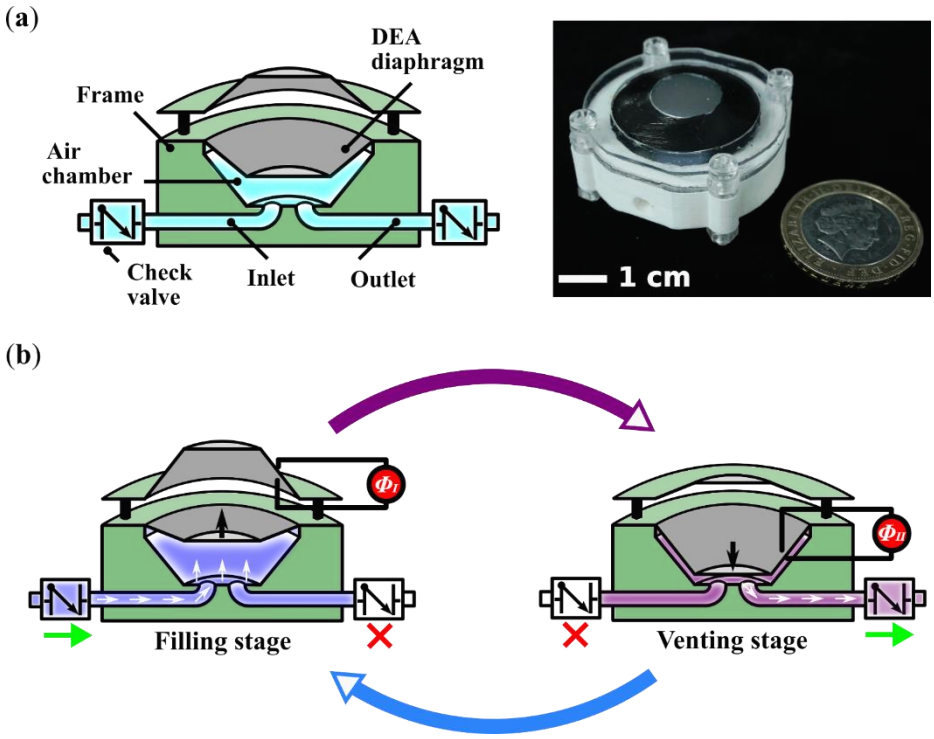

Figure 7.13. Proposed MCDEA driven pneumatic pump design. (**a**) Schematic diagram of the MCDEA pneumatic pump design and a fabricated prototype. (**b**) Working principle of the pump design.

7.5.3 MCDEA Pump Fabrication

The fabrication process of the DEA membranes follows the same steps in Section 5.1.2 and 7.1.2 and will not be repeated here. 1.2 × 1.2 pre-stretch ratio was chosen, and the frame has the inner radius of 15 mm. Four layers of membranes were stacked together on each side of the MCDEA and 7.5 mm

radius × 1 mm thick disc magnets (3×1.1 kg pull force, First4Magnets) were attached to the membranes. The top and bottom membrane stacks were separated by Nylon spacers. The main body of the pump was fabricated by 3D printing (PLA) with dimensions shown in **Appendix D**. Nylon miniature check valves (12.5 mbar breaking pressure, NO.7005, Cole-Parmer) were connected to the inlet and outlet. The MCDEA was attached to the pump frame via M3 bolts and fasteners.

7.5.4 Performance Characterization

7.5.4.1 Experimental Setup

The performance of the MCDEA diaphragm pump was characterized with the following setup. Two antiphase alternating sinusoidal waves ($\Phi_{DC} = \Phi_{AC} = 2.3$ kV) were applied to the two membrane stacks via two high-voltage amplifiers (Ultravolt, 5HC23-BP1). The pump was actuated to inflate a bespoke balloon (60 mm in diameter, 100 μm thickness ELASTOSIL membrane) where the pressure in the balloon was measured using a pressure sensor (SSCSNBN015PDAA5, Honeywell) and the flowrate was measured by a flowrate sensor (AWM5101VN Mass Air Flow Sensor, Honeywell). The power consumption of the DEA was estimated based on the measured actuation voltage and current flow into the DEA (measured from the high-voltage amplifier's feedback signal). The displacements of the two membranes were measured by two laser displacement sensors (LK-G152 and LKGD500, Keyence). All experiments were controlled by MATLAB (MathWorks) and all data was collected by a DAQ device (National Instruments, BNC-2111) at a sampling frequency of 20,000 Hz.

7.5.4.2 Experimental Results

The measured output pressure and flowrate of the MCDEA pump (h = 1.8 mm) as a function of excitation frequency are shown in **Figure 7.14** (**a**). Both the maximum output pressure and the maximum flowrate increases to peaks of 24.3 mbar and 0.92 standard litres per minute (SLPM), respectively, at 77 Hz. It can be noted from **Figure 7.14** (**b**) that the power input decreases as the frequency increases due to the current limit of the power supply. Thanks to the resonant actuation of the MCDEA, the stroke reaches the peak at 77 Hz where the pump achieves its maximum output and this is also where power consumption drops to a global minimum of 41.5 mW at 79 Hz, which significantly increases the efficiency (**Figure 7.14** (**b**)). **Figure 7.14** (**c**) shows the effects of voltage amplitude on the output pressure and flowrate at the resonance of 77 Hz. Both output pressure and flowrate increased monotonically with increasing voltage amplitude at resonance.

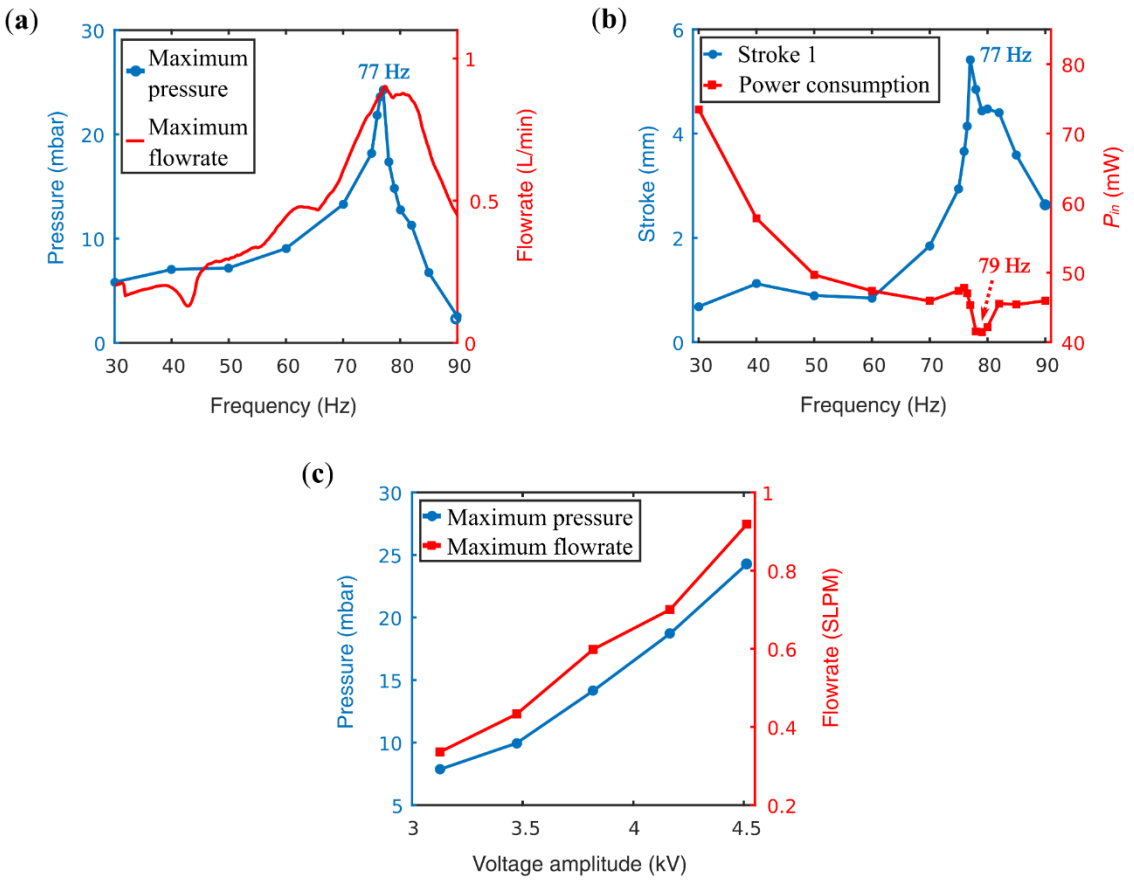

Figure 7.14. Performance characterization of the MCDEA pump against the actuation frequency and voltage amplitude. (**a**) Maximum output pressure and flowrate and (**b**) DEA stroke and power consumption as a function of frequency with h = 1.8 mm. The maximum pressure, flowrate and stroke occurred at 77 Hz which is believed to be resonant frequency, and the minimum power consumption at 79 Hz (note that power values do not include losses in the high-voltage amplifier). (**c**) Dependence of pressure and flowrate with voltage amplitude.

Figure 7.15 compares the effects of spacing between two DEA membranes on the performance of the pump. As the two membranes are separated further (increase of h), the magnetic repulsion force reduces and the lower DEA membrane tension results in a reduced elastic stiffness and resonant frequency. Consequently, the frequency at which the output pressure and peak flowrate occurs at reduces with increased membrane spacing (**Figure 7.15** (**a**)). The peak flowrate of the pump also reduces with increasing h. While the maximum output pressure also increases with h, it does so only up to h = 5.4 mm, where it has a peak of 30.2 mbar (total pumping pressure 42.7 mbar) (**Figure 7.15** (**b**)). As h increases further, the maximum output pressure reduces which is likely due to increased compression of the MCDEA's compliant coupling, since the magnetic repulsion force reduces with h. It also can be noticed in **Figure 7.15** (**b**) that as h increases, the peak becomes sharper. If a specific minimum pressure

output of, say, 10 mbar is required for potential soft robotic applications, then it can be concluded that a pump with a shorter *h* value can have a larger bandwidth where the pressure output is greater than 10 mbar (as indicated in black dash line in **Figure 7.15** (**b**)). **Figure 7.15** (**c**) shows the relationship between flowrate and output pressure during pumping at the frequencies where the peak pressures occur, which is approximately linear for this pump design.

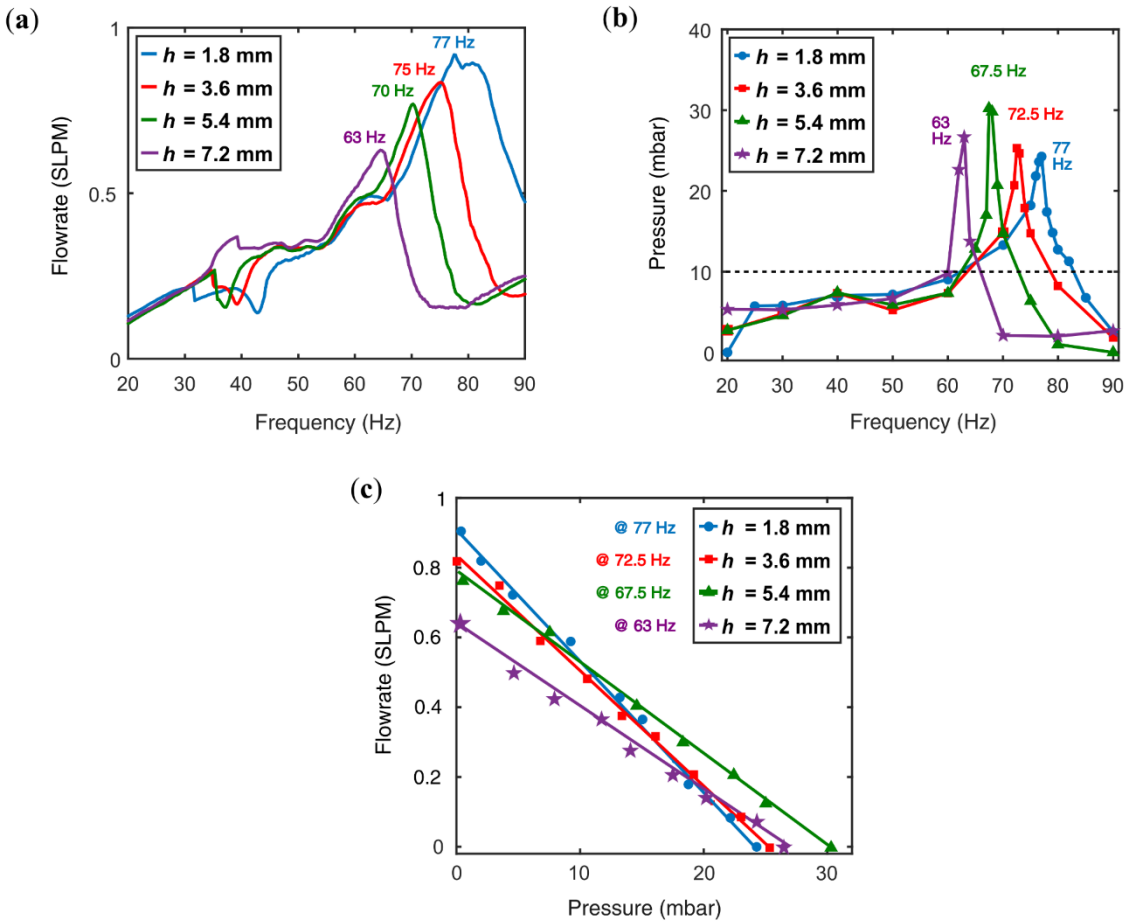

Figure 7.15. Performance comparison of the MCDEA pump against the spacer value. Pumping performance in terms of (**a**) flowrate and (**b**) output pressure as a function of frequency of excitation voltage at various spacer height, *h*. (**c**) Flowrate-pressure behavior of the MCDEA pump with various spacer height, *h*.

Figure 7.16 shows the design and performance of a similar pump design but with a DCDEA instead of MCDEA. No resonant peak in stroke or pressure was observed in the DCDEA version, which is due to the high damping in the compressed air. This result echoes the finding in the comparison of two cone DEA designs in Section 7.4.

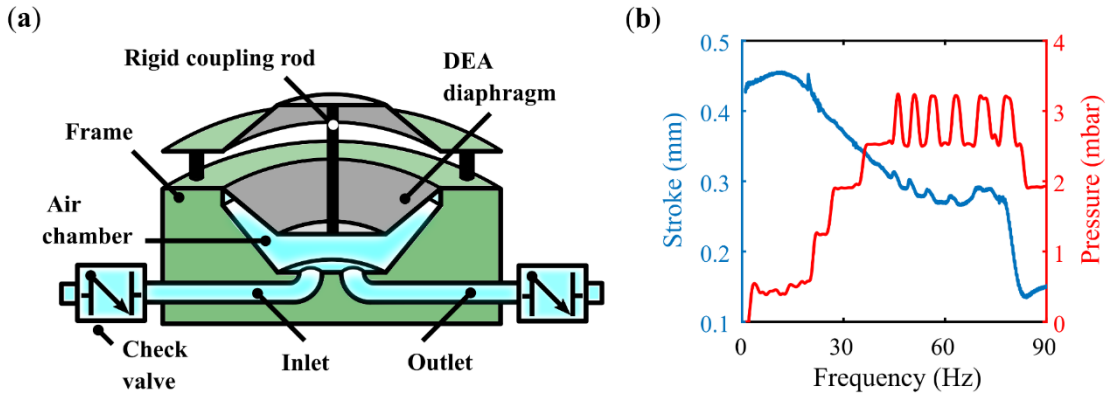

Figure 7.16. Rigidly coupled DCDEA driven pump. (**a**) Schematic diagram of the rigidly coupled DCDEA pump design. (**b**) Stroke and pressure output of this pump as a function of excitation frequency.

7.5.5 Application Demonstrations

Several demonstrations of the MCDEA pump for soft robotics are shown in **Figure 7.17**. In **Figure 7.17** (**a**), the MCDEA pump was used to inflate a silicone elastomer balloon with a diameter of 60 mm. Despite having a much larger size than the pump (diameter of 30 mm), a relative fast response was achieved e.g. 18.5 mbar within 4 secs. A two-finger soft gripper was designed (details in **Appendix D Figure D.2**), which was directly connected to the outlet of the pump and an object up to 68g could be firmly grasped (**Figure 7.17** (**b**)). The MCDEA pump can also be employed in a suction mode, as shown in **Figure 7.17** (**c**) where a 15g mass is lifted. **Figure 7.17** (**d**) illustrates a semi-soft version of the MCDEA pneumatic pump design where the DEA frames are made of flexible 0.2 mm PVC and the soft chamber was 3D printed with Tango Black rubber (Eden 350V printer, Objet Geometries). The 3D printable soft material allows the monolithic designs of soft robots with pump chambers embedded inside, which can significantly simplify the design and fabrication process.

Thanks to the contactless coupling between membranes by magnetic repulsion, the MCDEA pump can work in an electrically isolated mode, where the pump chamber interfaces with a passive membrane and the active DEA membrane is separated (details in **Figure 7.18**). This mode would be beneficial when the chamber needs to be embedded within a galvanically isolated condition e.g. biomedical applications.

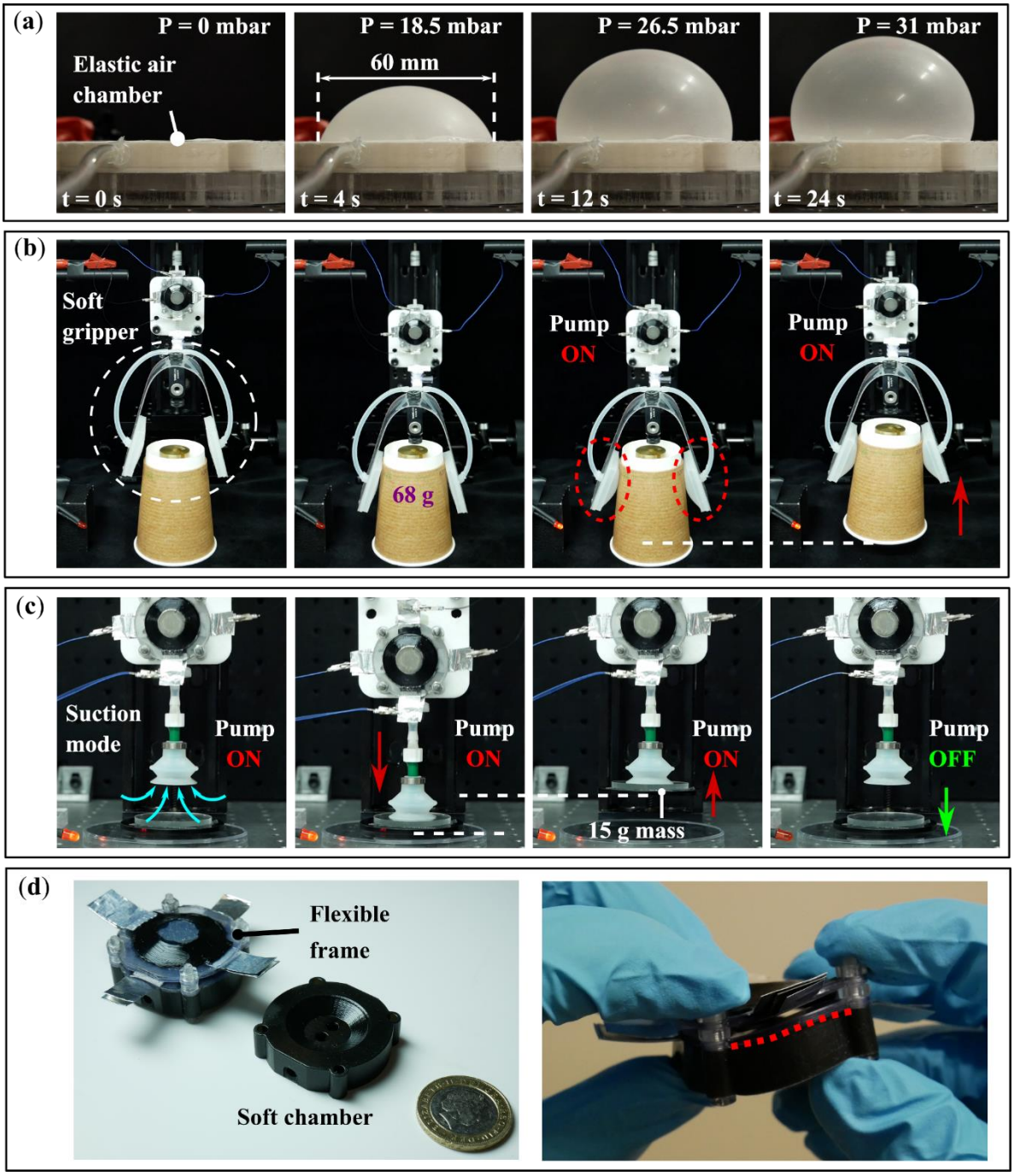

Figure 7.17. Demonstrations of potential applications for soft robotics. (**a**) Inflation of elastic balloon chamber. The MCDEA pump can function in both (**b**) inflation mode (soft gripper) and (**c**) suction mode (suction cup). (**d**) Semi-soft version of MCDEA pump.

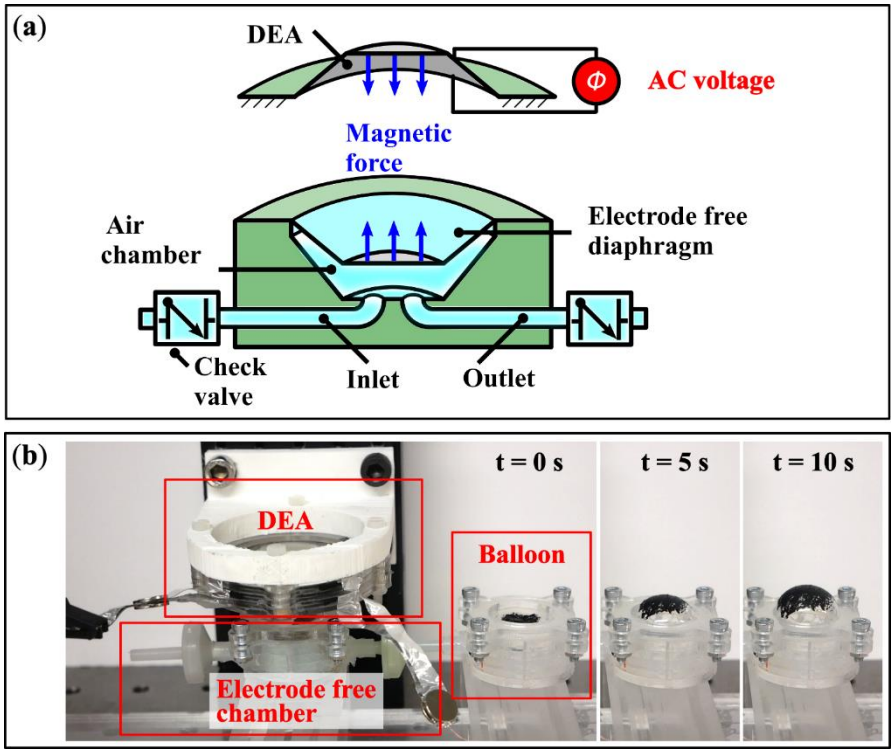

Figure 7.18. Contactless pumping of MCDEA. (**a**) Design concept. (**b**) Contactless DEA pump inflating a custom balloon.

7.5.6 Discussion

By characterizing the pumping performance against the actuation voltage amplitude, excitation frequency and DEA geometry, it can be concluded that this pump design can be easily customized to meet different demands for various applications. For example, output pressure and flowrate can be tuned by adjusting either the actuation voltage amplitude or frequency via a control signal. If a maximum flowrate or pressure is required, the height of the spacers between two membranes can be adjusted (h = 1.8 mm for maximum flow rate and h = 5.4 mm for maximum pressure for the current prototype).

The demonstrations of the MCDEA for balloon inflating, actuating a soft gripper and suction cup suggest that this novel pneumatic pump design can be readily used in various soft robotic applications. The semi-soft version of this pump design clearly illustrates the feasibility of embedding the micro pumps in the soft robots or devices where the robot/device itself can serve as the chamber.

The passive check valves may have some minimal leakage under back-pressure so there is potential to improve the pumping performance by replacing them with miniature active valves capable of crisp opening and closing. There is potentially also scope to optimize the chamber geometry further, but such improvements may be restricted by the rated power output of the high voltage power supply since its

load increases as the DEA membranes stack up with multiplied capacitance and resistance. Future work will explore how a fully soft embodiment of the pump performs during externally applied deformations.

7.6 Chapter Summary

This chapter presented a novel magnetically coupled double cone DEA configuration, its actuation principle was explained, its dynamic response was characterized both experimentally and using the generalized cone DEA model. Complex dynamic responses of the MCDEA, including super and primary harmonic response and resonance with two different modes were observed using experiments and captured by the dynamic model. Despite the compliance in its coupling, MCDEA exhibits a steady period oscillation with large amplitudes at resonance. The appearance and the amplitude and frequency of the resonance can be controlled by tuning the phase between the two actuation signals. By comparing it to a conventional rigidly coupled double cone DEA, the results showed that this MCDEA design has a clear advantage in having excellent power output performance at resonance even with significant damping in the payload. Based on this finding, the first DEA-driven pneumatic pump was developed. The proposed pump design exhibited a peak pressure output and flowrate at the resonance of the driving DEA. The current prototype demonstrated a maximum pressure output of 30.5 mbar and a flowrate of 0.9 SLPM at a relatively low power consumption of 40 mW. The performance of this pneumatic pump design was then demonstrated by integrating it with soft robotic demonstrators, including a soft gripper and a suction cup. In conclusion, this novel DEA driven pneumatic pump offers an alternative for efficient and high-performance soft pumps in future of soft robotics applications.

Chapter 8: Conclusion

In this thesis, the inherent elasticity of dielectric elastomer actuators (DEAs) and its potential application in soft/bioinspired robotics were investigated. The study was built on a comprehensive electromechanical dynamic model of generalized cone DEAs and three different configuration variations: (i) a novel circular and planar dielectric elastomer oscillator (DEO), (ii) a double cone dielectric elastomer actuator (DCDEA), (iii) a novel magnetically coupled dielectric elastomer actuator (MCDEA). Two different novel strategies for utilizing the elasticity in DEAs for cyclic operation were proposed: (1) for VHB acrylic material with high viscoelasticity, the actuation duty ratio can be reduced to allow the stored elastic energy in DEA membranes to contribute solely to the work output; (2) for silicone elastomers with low viscosity, resonant actuation can be used to maximize its stroke/power output. By using the three DEA configurations, along with the two strategies, novel applications were developed. These applications clearly demonstrate the feasibility and advantages of inherent elastic actuation of DEAs and are believed to expand the use of DEAs in soft/bioinspired robotics.

8.1 Summary

In Chapter 4, a generalized numerical model for conical shaped DEAs was developed which characterizes the electromechanical coupling, viscoelasticity and current leakage. This model can be readily applied to any specific cone DEA configurations by replacing the generalized protrusion force by the specific biasing element. This generalized model was verified against the experimental results in all three different cone DEA variations with excellent accuracy.

In Chapter 5, a custom carbon grease as the compliant electrodes for silicone DEAs was first developed. Commercially available carbon grease (such as MG 846, MG Chemicals) has the problem of diffusion into the silicone elastomer which can cause swelling of the elastomer, thus affecting the performance of the DEA. This novel custom carbon grease was made of carbon black powder and vegetable oil, which has the advantage of low cost, ease of fabrication and no swelling effects on the silicone material. The custom carbon grease was benchmarked against the widely used commercial counterpart (MG 846) and it was found that with the same carbon black concentration (20 wt. %), the custom carbon grease showed a lower surface resistance than MG 846 (2.1 kΩ/sq comparing to 3.2 kΩ/sq) and caused a less damping on the DEA. This custom carbon grease could benefit the DEA field by reducing the cost and facility barriers of traditional approaches (e.g. pad-printing) for applying electrodes on silicone membranes.

A novel circular and planar dielectric elastomer oscillator (DEO) was proposed in Chapter 5. This design consists of a pre-stretched membrane bonded to a circular frame with a disk mass attached in the

centre. The disk mass is too light to cause noticeable out-of-plane deformation, hence the DEO keeps a planar configuration in its passive state. However, as the DEO is excited by a voltage with the frequency close to its resonance, a large out-of-plane deformation was observed. That the maximum stroke of the DEO was measured at 13.5 mm, which is 67.5 % relative to the membrane diameter, is one order of magnitude of higher than the results reported in previous studies using VHB acrylic elastomer (~ 4 to 7 %). Multiple resonant peaks were observed using both experiments and numerical simulation. Further discrete Fourier transfer study exposed that at these resonant peaks, subharmonic of 1/2 and super-harmonics at 2, 3 and 4 could occur. This design has the advantages over existing DEA oscillators in its large oscillation amplitude, highly tunable oscillation amplitude/frequency, low profile structure and light weight and can be potentially applied in vibrational damping, noise cancellation and energy harvesting.

Based on the large out-of-plane actuation capability of the DEO, a novel monolithic electroadhesion (EA) DEO soft gripper was developed. Conventional EA grippers have the drawback of slow de-adhesion, which is due to the residual charge separation in the substrate after the applied voltage is removed. This design integrated the EA and DEO by dividing one DEO electrode into an EA pattern on a single membrane. EA was utilized to generate a grasping force to pick up substrates and the DEO served as the quick-release mechanism by utilizing its resonant excitation to rapidly detach substrates from the gripper. The performance of the EA-DEO gripper was tested on six different lightweight and flexible plastic substrates, which have the most severe release problems. Experimental results showed that for all six types of materials, the release speeds were sped up from several minutes to 100s of milliseconds, which demonstrated at least two orders of magnitude of improvement. This novel gripper demonstrated a clear use of the inherent elasticity of the actuator. The high performance, low-energy consumption (gripping ~2 mJ and releasing ~50 mJ), noise-free operation, low-cost and ease of fabrication also allow this gripper to be a promising candidate for industrial applications in the future.

In Chapter 6, the double cone DEAs (DCDEAs) were investigated. DCDEAs have the advantages of large stroke/force output, natural antagonistic and bidirectional actuation and ease of fabrication. Despite its wide use in the past, the energetic performance (work/power output and electromechanical efficiency) had not been investigated. To enable its practical application in soft/bioinspired robotics, its energetic performance requires characterization. By using the generalized cone DEA model developed in Chapter 4, we analysed the stroke, power and electromechanical efficiency of the DCDEA in this chapter with the setup of the DCDEA driving a dissipative payload. Without losing the generality, the two most common DEA materials: VHB acrylic and silicone were adopted.

For VHB DCDEA, it was found to have a peak power output at a frequency between 0.5 to 2 Hz and the actuation bandwidth is less than 10 Hz due to the inherent viscosity of the material. Square wave actuation signals were found to lead to a higher power output with a better electromechanical efficiency than sinusoidal wave signals. A strategy to utilize the elastic energy in the VHB DCDEA was proposed,

which is reducing the duty ratio of the actuation signals thus allowing the released elastic strain energy to contribute to the work output. A bioinspired robotic leg with the VHB DCDEAs as a demonstrator was developed to prove the feasibility of utilizing the compliant actuation and elastic energy recovery for bioinspired and soft robotics.

For ELASTOSIL silicone DCDEA, due to the reduced viscosity, resonant actuation can be utilized to improve the power/stroke output of the actuator. By using the same energetic study setup, the silicone DCDEA performance was optimized in terms of power output by varying its pre-stretch ratio and rod length. The optimal design showed a peak power output of 73.6 mW for an actuator size of 30 mm diameter membrane and 21 mm actuator height. No pre-stretch was found to give the highest power output. A resonant actuation principle, which represents the second strategy to utilize the inherent elasticity of the DEA, was demonstrated by letting the DCDEA drive a flapping wing mechanism. Four layers of the optimized silicone DCDEA were used to drive the flapping wing mechanism and a peak flapping stroke of 31˚ at the resonant of 30.2 Hz was observed for the first time in DEA driven flappers. A maximum lift force of 4 mN was measured using the current prototype, again, to the best of the author's knowledge, it is the first time a lift has been reported for a DEA driven flapper.

In Chapter 7, a novel magnetically coupled DEA was proposed. This design features the compliant coupling of magnetic repulsion, which differs from conventional DCDEAs as the compliant magnetic coupling allows the outputs of the DEA membranes on the two sides to have independent phases by adjusting the phase difference between the two actuation signals. A numerical model based on the generalized cone DEA model was developed to characterize its dynamic response. This MCDEA design exhibited two vibrational modes and super-harmonic and primary harmonic resonances. A novel phase tuning strategy was proposed which can tune the amplitude and resonant frequency and also control the existence of the resonance of a specific mode. A theoretical study was conducted to compare the performance of the DCDEA and MCDEA. The results showed that for a dissipative payload, the MCDEA is not affected by the damping in the payload and can maintain a high power output in highly dissipative payload conditions. On the contrary, the performance of DCDEAs is strongly affected by the damping, which suggests the clear advantage of this novel MCDEA design in high damping applications. Based on this finding and the resonant actuation principle, the first diaphragm pneumatic pump driven by the MCDEAs was developed. The proposed pump design exhibited a peak pressure output and flowrate at the resonance of the driving DEA. The current prototype demonstrated a maximum pressure output of 30.5 mbar and a flowrate of 0.9 SLPM at a relatively low power consumption of 40 mW. The performance of this pneumatic pump design was then demonstrated by integrating it with soft robotic demonstrators, including a soft gripper and a suction cup. In conclusion, this novel DEA driven pneumatic pump offers an alternative for efficient and high-performance soft pumps in future of soft robotics applications.

The key contributions of this PhD are summarized as follows:

1. Developing a generalized model for conical shaped DEAs that characterizes the electromechanical dynamics.
2. Proposing a novel dielectric elastomer oscillator and characterizing its nonlinear dynamic responses.
3. Developing a novel soft monolithic electroadhesion – dielectric elastomer oscillator gripper which improved the release speed by at least two orders of magnitude.
4. Conducting the first energetic study and work/power optimization of both VHB and silicone based double cone DEAs.
5. Demonstrating the elastic recovery principle for highly viscous VHB DEAs by using a bioinspired robotic leg.
6. Demonstrating the resonant actuation principle for silicone DEAs by using a novel bioinspired flapping wing mechanism.
7. Proposing a novel magnetically coupled DEA with freely controllable phase difference between two outputs.
8. Developing the first DEA driven pneumatic pump for soft robotics applications.

8.2 Future Works

The EA-DEO design can also be used in several other applications where fast EA release is desired. For example, for crawling robots where EA pads are used as feet (e.g. the author's paper in [228]), its crawling speed can be significantly improved by having the EA pads to release at a fast rate. The EA-DEO design offers a simple solution to achieve this without overcomplicating the system design. Another potential application for the EA-DEO device is fully soft flapping wing micro air vehicles (FWMAVs) with active perching capabilities (after [229]). The resonant DEO can be used as an elastic artificial muscle to drive the flapping wing mechanism. When the FWMAV is close to the target object and is ready to perch, the DEO can be switched off while turning the EA on. When the FWMAV is preparing to take-off, the DEO can be actuated, which flaps the wings and causes the release in the same time.

In the current design, two antagonist DEA membranes coupled by magnetic repulsions were used for the MCDEA configuration. Future work could explore the complex interactions and emerging behaviours of multiple magnetically coupled DEA membranes. For example, magnetically coupled energy harvesting devices that are input-independent, as demonstrated in [230]. The output phase and amplitude tuning capability of MCDEAs can also be explored in crawling robot designs where multiple

MCDEAs are attached in series (see for example, serial-coupling DCDEAs in crawling robots in the author's paper [231]). Such MCDEAs driven robot can switch between two-anchor crawling and peristaltic crawling or alter its direction by controlling the phases between each MCDEA segments. This expands the applications of DEA driven crawling robots in machine inspection, search-and-rescue, and minimally- invasive surgical robots.

Future work for the MCDEA driven pump can focus on a fully 3D printed soft robotic devices. A 3D printed soft chamber was already demonstrated in this work, by having the soft robotic device and the pump chamber printed together, the overall design and fabrication process can be simplified, and totally embedded pumping can be achieved.

The low dissipative loss and the high vibration amplitude at resonance of silicone elastomer suggests a promising potential for high efficiency dielectric elastomer generators (DEGs). By carefully designing the DEGs (e.g. pre-stretch ratio and weight of central mass, as shown in Chapter 5) or tuning the control signals (e.g. phase difference between two membranes, as shown in Chapter 7), the DEGs can have resonant frequencies matching the frequency of the vibrational source (e.g. car engine), resulting in a higher efficiency energy generation.

Appendix A: Quasi-Static Numerical Model for Cone DEAs

In this appendix, we briefly describe a quasi-static numerical model of the conical DEA which characterizes its nonhomogeneous strain/stress distributions on the DEA membrane. This model was original developed in [184] based on the thermodynamic equilibrium and geometry relationships. Differing from the generalized cone DEA model developed in Chapter 4 which assumes a homogeneous stress distribution on the membrane and a truncated cone shape, this model is able to capture the true strain-stress distribution on the cone membranes. However, the limitation of this model is also clear. The heavy computational cost limits its applications in dynamic simulations.

Statement: The model presented in this appendix is adapted from the following publication where C. Cao is the first author.

- **Cao, C**. and Conn, A.T., 2018, June. Performance Optimization of a Conical Dielectric Elastomer Actuator. *Actuators.* 7(2) p. 32.

Contribution: Fabrication and testing methodology, investigation, data curation, formal analysis, writing original draft; review & editing.

A.1 Model Development

This quasi-static model is described as follows. In its initial state, the elastomer membrane has an initial thickness H_0 and is stress and constraint free. The membrane is pre-stretched biaxially by a stretch ratio of λ_p. The pre-stretched membrane is then bonded to a rigid ring of radius b and a disk of radius a, as illustrated in **Figure A.1 (a)**. Both sides of the membrane are coated with compliant electrodes. An external force F and a voltage Φ are applied which move the membrane out of plane by a distance h and cause it to form a conical structure, as shown in **Figure A.1 (b)**. After the out-of-plane deformation, a particle on the membrane at radius R in **Figure A.1 (a)** now occupies the position of ($r(R)$, $z(R)$), where r is the current radius and z is the distance to the undeformed plane. The coordinates of (r, z) for $R = [a, b]$ describe the geometry of the conical DEA shape, and are developed as follows (after [184]). The coordinates of (r, z) are expressed as follows

$$\frac{dr}{dR} = \lambda_1' \cos\alpha \,, \tag{A.1}$$

$$\frac{dz}{dR} = -\lambda_1' \sin\alpha \,, \tag{A.2}$$

where λ_1' is the radial stretch due to the out-of-plane deformation and α is the angle between membrane tangent and horizontal plane at point (r, z) and is described as

$$\frac{d\alpha}{dR} = -\frac{s_2}{Rs_1}\sin\alpha \,, \tag{A.3}$$

where s_1 and s_2 are the nominal radial and circumferential stress. The external force F and membrane reaction force are equal in a quasi-static state, and this relationship is expressed as

$$2\pi \frac{H}{\lambda_1 \lambda_2} r\sigma_1 \sin\alpha = F \,, \tag{A.4}$$

where σ_1 is the radial stress at point (r, z), and λ_1 and λ_2 are the total radial and circumferential stretches, respectively, and are given as

$$\lambda_1 = \lambda_p \lambda_1' \,, \tag{A.5}$$

$$\lambda_2 = \lambda_p \lambda_2' \,. \tag{A.648}$$

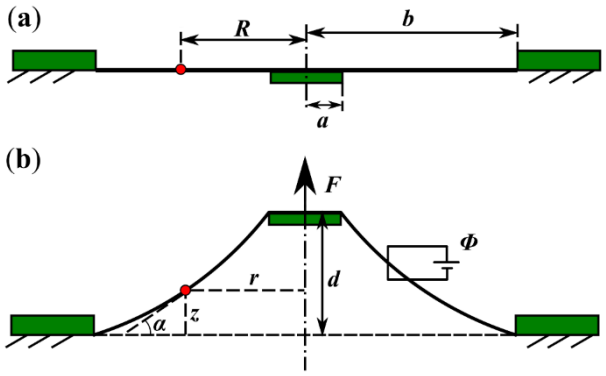

Figure A. 1. The cross-sectional illustrations of a conical DEA: (**a**) Pre-stretched membrane is bonded to a rigid ring and a central disk; (**b**) out-of-plane deformation of the membrane caused by a force F and a voltage Φ.

The stresses s_1 and s_2, can be described using the hyperelastic models introduced in Section 4.3. Then, the state of the conical DEA can be solved by three differential equations (A.1) – (A.3) and an algebraic equation (A.4), together with boundary conditions

$$r(R = a) = a, r(R = b) = b, z(R = b) = 0. \tag{A.7}$$

The model is numerically solved in Matlab (Mathworks) using shooting method and the '*ode15*' function.

A.2 Stress and Electrical Field Analysis of a Conical DEA

Owing to its complex three-dimensional geometry and boundary conditions, the strain–stress distribution on a conical DEA is very inhomogeneous. In this section, we attempt to reconstruct the

stress distribution along the DEA using the analytical model. Here we set b = 20 mm, a = 4 mm, h = 10 mm and λ_p = 1.2 × 1.2. **Figure A.2** compares the radial and circumferential stress σ_1 and σ_2 when Φ = 0 and Φ = 1.5 kV. When a voltage is applied to the DEA, a clear reduction in both radial and circumferential stresses can be observed, and the DEA is closer to a truncated conical shape. The lowest circumferential stress is near the edge with the central disk. If the voltage increases further, the circumferential stress near the inner edge will become negative first, which results in a wrinkled membrane in this region.

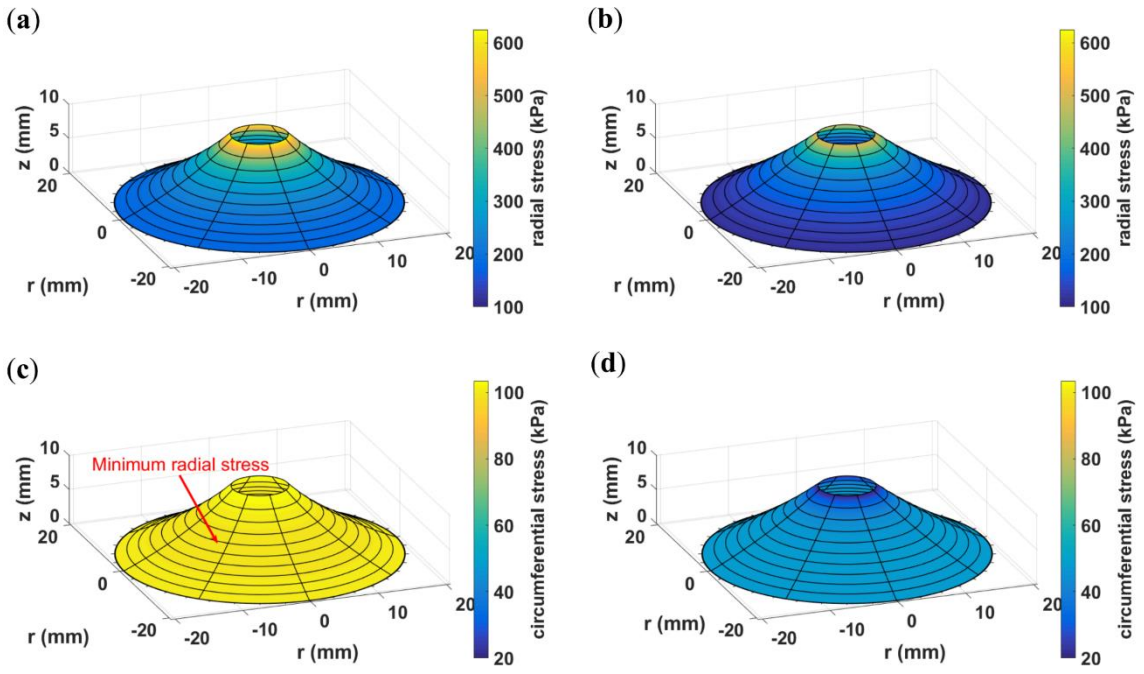

Figure A. 2. Demonstration of inhomogeneous stress distribution on a cone DEA. Radial stress distribution on a cone DEA when actuation voltage is (**a**) OFF and (**b**) ON. Circumferential stress distribution on a conical DEA when voltage is (**c**) OFF and (**d**) ON. Parameters: a = 4 mm, b = 20 mm, d = 10 mm, λ_p = 1.2 × 1.2.

Appendix B: Electroadhesion Gripper Release Study

This appendix characterizes the de-adhesion performance of an electroadhesion (EA) gripper against various lightweight objects.

Statement: This study presented in this appendix is adapted from the following publication where C. Cao is the co-first author with Dr Xing Gao.

- **Cao**, C., Gao, X. (joint first author), Guo, J. and Conn, A.T., 2019. De-electroadhesion of flexible and lightweight materials: an experimental study. *Applied Sciences*. (Under review).

Contribution: Joint fabrication and testing methodology, joint investigation, joint data curation, joint formal analysis, joint writing original draft; joint review & editing.

B.1 EA Gripper Design and Experimental Setup

The EA pad design utilized in this work follows a concentric-comb pattern. It has an effective diameter of 56 mm with an electrode width and gap of 4 mm, as shown in **Figure B.1 (a)**. The electrodes were made of off-the-shelf electrically conductive silicone sheet (0.5 mm thickness, 4.3 Ω•cm volume resistivity, J-Flex, UK). The electrodes were bonded to the base materials via a thin layer of silicone adhesive (Sil-Poxy, Smooth-On). Six different base materials were used: poly (methyl methacrylate) acrylic, medium-density fibreboard (MDF), silicone elastomer (ELASTOSIL, Wacker Chemie AG), polyacrylate elastomer (VHB 4910, 3M), polyethylene terephthalate film (Mylar, Dupont), and polystyrene foam (Styrofoam, Dow Chemical), as illustrated in **Figure B.1 (b-g)** respectively. Eight different object materials were used: balsa wood, polyethylene foam, cardboard, polyvinyl chloride (PVC) sheet, Mylar, paper tissue, paper sheet, and silicone film. The material properties, dimensions, and mass of object materials can be found in **Table B.1**.

The experimental procedure is summarized as follows and is illustrated in **Figure B.2**. First, the EA pad was moved downward along a linear rail to enable contact with the substrate. A voltage of 3.5 kV was then applied across the electrodes for a total period of 10 seconds, and after 5 seconds of actuation, the EA pad, together with the object, was lifted upwards. The EA system was turned off after 10 seconds charging and the release time measurement began. The release time was defined as the time required to drop off the object from the EA pads after turning off the applied voltage.

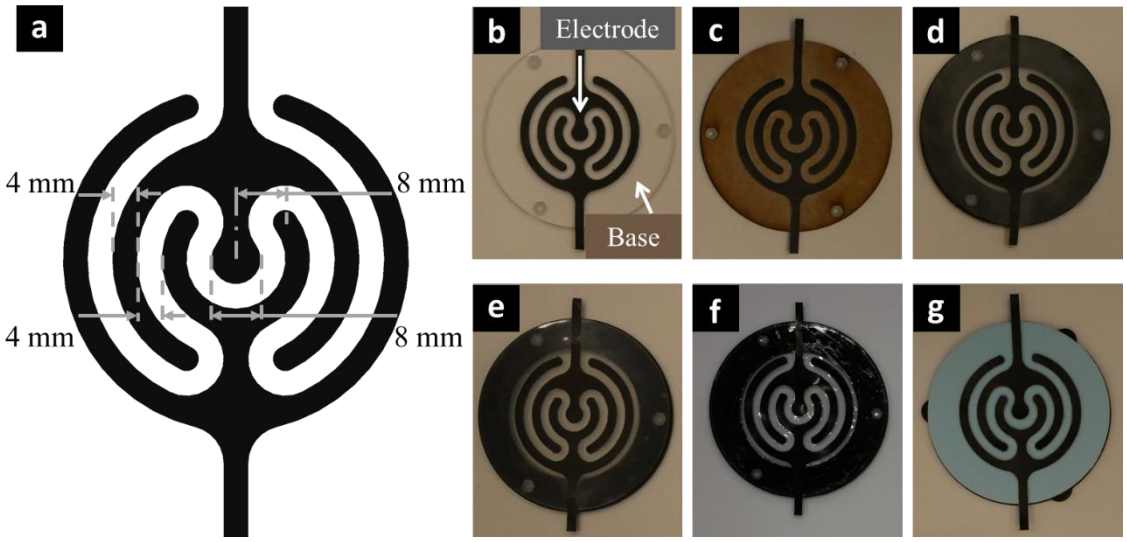

Figure B. 1. EA gripper design. (**a**) Dimensions of the EA gripper. Fabricated EA grippers with different base materials: (**b**) acrylic; (**c**) MDF; (**d**) silicone; (**e**) VHB; (**f**) Mylar film; and (**g**) Styrofoam.

Table B. 1. Parameters of tested substrate materials.

Substrate materials	Diameter (mm)	Thickness (mm)	Mass (g)	Relative permittivity (ε_r)
Balsa wood	70	1.00	0.48	1.40
Polyethylene foam	70	1.30	0.10	1.80
Cardboard	70	1.80	1.92	1.80
PVC sheet	70	0.15	0.74	3.20
Mylar sheet	70	0.05	0.26	3.30
Paper tissue	70	0.08	0.08	N/A
Paper sheet	70	0.10	0.31	1.80
ELASTOSIL silicone film	70	0.05	0.23	2.80

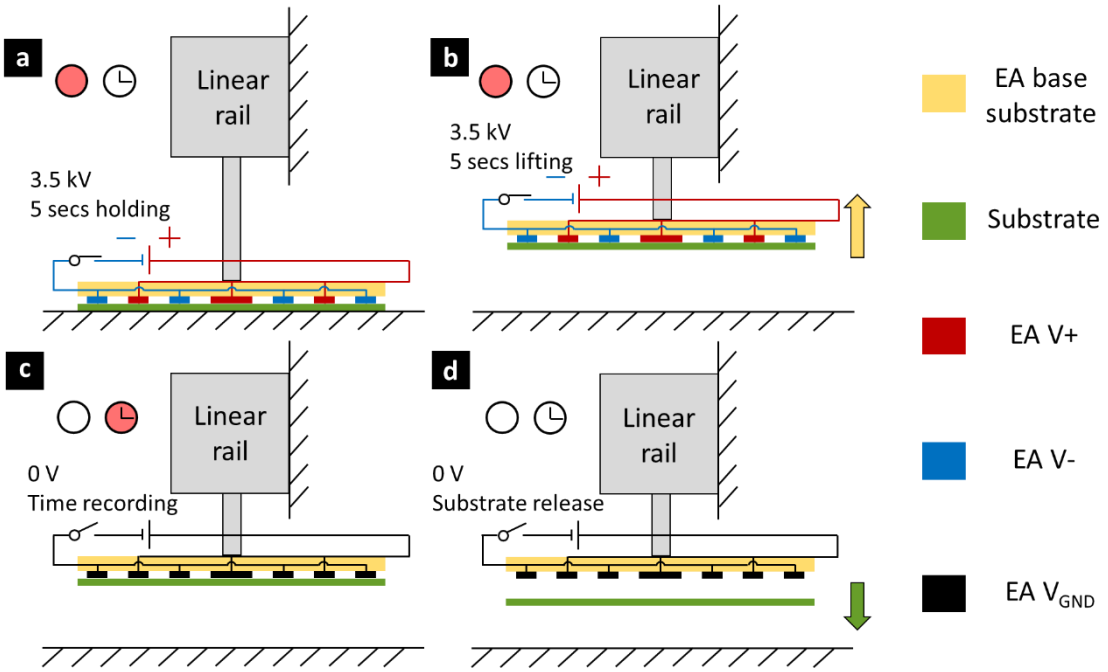

Figure B. 2. Schematic diagrams of experimental procedure.

B.2 Experimental Results

The de-adhesion behavior of the EA gripper is characterized by its release speed and the experimental results are shown in **Figure B.3**. As can be seen, the de-adhesion behavior is strongly dependent on the material type of the objects. The release time results can be divided into three different time categories: over 10s (including Mylar and PVC film), between 1s and 10s (including PE foam and silicone film) and under 1s (including balsa wood, paper sheet and cardboard). Plastic-based materials demonstrate a longer release period (Mylar shows the worst release behavior) than foam, silicone, and cellulose-based materials, which have the shortest release periods. The key findings are summarized as follows.

1. *The effect of the dielectric constant of the object*. Cellulose-based materials have the lowest dielectric constants and the fastest release speed among all objects while plastic materials have the highest dielectric constants and demonstrate the slowest release behaviors. This suggests that dielectric constant correlates with the de-adhesion property of a material.

2. *The effect of the weight of the object*. PE foam shows a similar dielectric constant to cellulose-based materials, while its low mass-specific density probably leads to the longer release period than cellulose-based materials.

3. *The effect of the compliance of the object*. Although silicone film demonstrates a dielectric constant close to plastics, its release period is significantly shorter than plastics, which might be partially

due to its softness. Peeling was observed during the release of the silicone object, which indicates that for an extremely compliant material, a peeling effect could also speed up the release period.

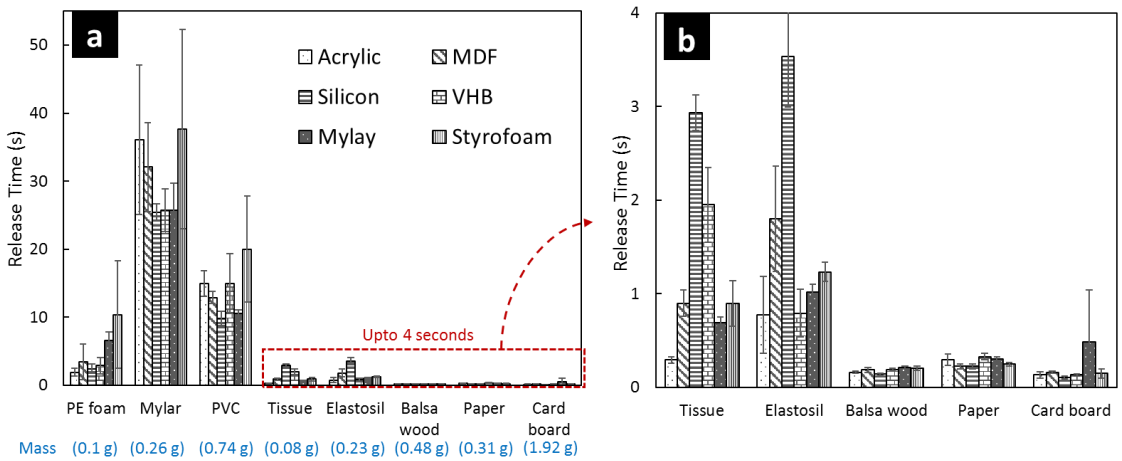

Figure B. 3. Experimental results of EA pad de-adhesion speed. (**a**) Comparison of the release time six EA pads on eight objects. (**b**) Expanded comparison of objects with release time less than 4 seconds.

During the actuation of an EA pad, polarization not only happens on the object, but also on the base material, causing residual EA force on the base when the electric field is removed. The results demonstrate that the de-adhesion behaviors of the six EA pads are clearly dependent on the base material. The EA pad with silicone as the base material has the best performance (fastest average release speed), which offers valuable suggestions for future EA gripper designs. This also demonstrates that silicone elastomer as the base material not only can serve as the dielectric elastomer oscillator to force the de-adhesion, as demonstrated in Chapter 5, but also the material itself can reduce the residue adhesion force during the release stage, hence speeding up the de-adhesion.

B.3 Discussion

These findings will enable the design of cost-effective EA based robotic end effectors with rapid release capability. EA grippers with quicker de-adhesion ability could significantly improve the overall throughput of assembly lines where material pick-and-place tasks are involved. In addition, more efficient and faster locomotion speeds could be achieved for crawling or climbing robots where EA is employed as their active adhesion and de-adhesion feet.

Appendix C: A Reconfigurable Crawling Robot

In this appendix, we develop a reconfigurable modular soft robot design driven by double cone DEAs that can be configured into both vibrational crawling and two-anchor crawling motions.

Statement: This robot presented in this appendix is adapted from the following publication where C. Cao is the co-first author with Mr R. S. Diteesawat.

- **Cao, C**., Diteesawat, R.S (joint first author), Rossiter, J., and Conn, A.T., 2019, April. A reconfigurable crawling robot driven by electroactive artificial muscle. In 2019 IEEE International Conference on Soft Robotics (RoboSoft). IEEE.

Contribution: Joint fabrication and testing methodology, joint investigation, data curation, formal analysis, writing-original draft; joint review & editing.

C.1 Design Overview

This modular design combines the advantages of the fast speed of vibrational crawling motion (**Figure C.1** (**a**)) and the payload transportation capability of the two-anchor crawling motion (**Figure C.1** (**b**)) that are silent in operation and have the potential to ensure completely soft vibratory robots.

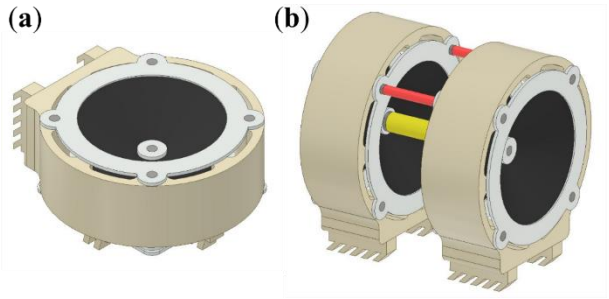

Figure C. 1. The proposed DEA-driven crawling robot prototype in (**a**) vibrational crawling mode and (**b**) two-anchor crawling mode.

C.2 Locomotion Principle

The locomotion principle for the vibrational crawling mode is illustrated in **Figure C.2** (**a**). In this mode, the robot is excited by a harmonic oscillating mass that is driven vertically by the double cone

DEA at its resonance. The bristles can be modelled as rigid legs connected to the robot body via torsional springs. In one cycle, as the mass oscillates downward then upwards, normal forces F_{N1} and F_{N2} ($F_{N1} > F_{N2}$) are exerted consecutively on the bristles with corresponding friction force F_{f1} and F_{f2}. Due to the anisotropic friction coefficients in forwards and backward directions, F_{f2} is smaller than F_{f1}, leading to a forward displacement *dx* in one cycle.

In the two-anchor crawling mode, the same principle of anisotropic friction principle is also utilized, but with two robot segments. Each segment is placed orthogonally to the ground such that the double cone DEA actuates parallel to the ground. The two segments are coupled with a rigid rod attached to the end-effectors of the DEAs. As illustrated in **Figure C.2** (**b**), when the two DE membranes on the outside are actuated, the distance between the two segments increases and Segment 1 is pushed forward while Segment 2 remains stationary due to the anisotropic friction on the bristles. The two segments are then driven towards each other by actuating the DE membranes on the inside. Now Segment 1 anchors while Segment 2 is pulled forward. The robot travels a forward distance *dx* in one actuation cycle.

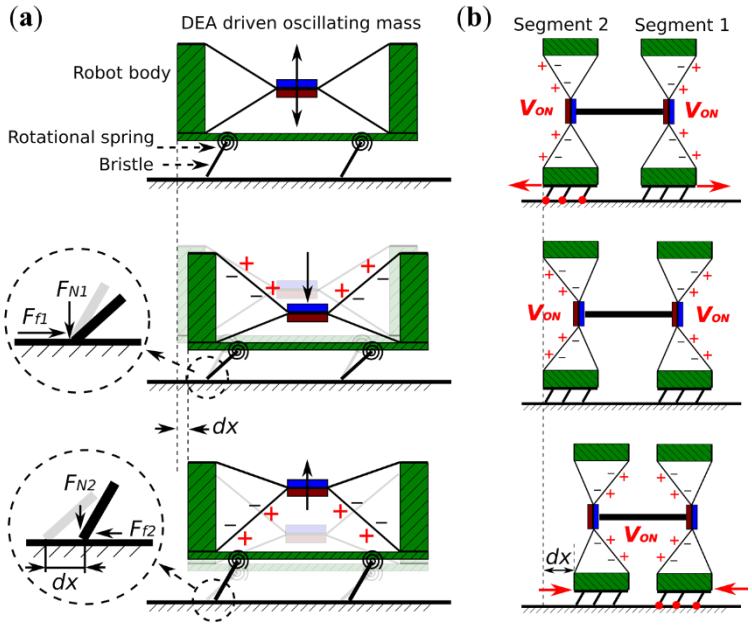

Figure C. 2. Locomotion principles. (**a**) Locomotion principle of the vibrational crawling mode. (**b**) Locomotion principle of the two-anchor crawling mode.

C.3 Robot Fabrication

A single robot module consists of three main parts: a double cone DEA, a soft robot body and bristles as demonstrated in **Figure C.3 (a)**. All components are connected to each together via magnets, which

allows easy assembly and disassembly and reduces the complexity in fabrication. Individual DEA frames are attached to the top and the bottom of the robot body; their central disks are connected via magnets. Two long bristles are connected to the flat surface on the robot body for two-anchor crawling mode and four short bristles were attached to the bottom of the robot body for vibrational crawling. For the two-anchor crawling mode, two modules are placed orthogonally to the ground and are coupled via a plastic core at the central disks of the DEAs and two plastic rods on the top of the robot body, as illustrated in **Figure C.3 (b)**. These rods connect the two segments of the robot to perform two-anchor crawling.

The soft robot body has a cylinder shape with an outer radius of 30 mm and a wall thickness of 2.5 mm. One side was modified to form a 37 mm wide flat surface for attaching bristles. The height of the body is 20 mm. Four 18 mm long plastic rods with magnets (radius = 1.5 mm, thickness = 1.0 mm) at both ends were inserted in the robot body as reinforcement. DEA frames were made of 1 mm thickness acrylic with the inner radius of 20 mm and an outer radius of 26 mm. Bristles were attached to the robot body by Sil-poxy (Smooth-On). The soft robot body and bristles were made of PDMS (Sylgard 184, DOWSIL). Each fabricated robot module (including DEAs) weighs 26 g.

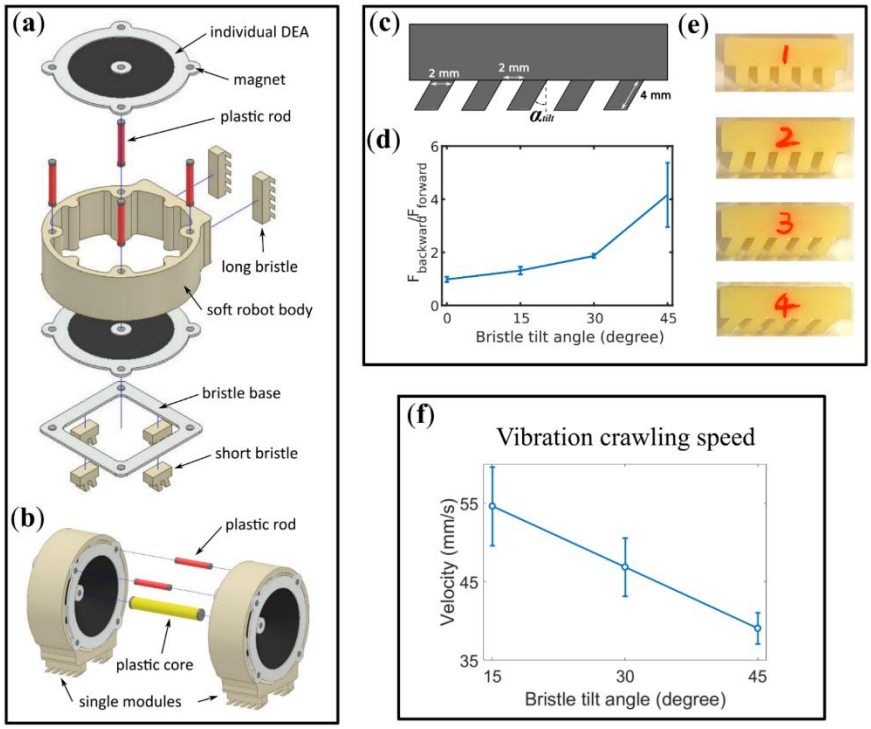

Figure C. 3. Robot design and characterization. (**a**) Exposed view of one robot module. (**b**) Two modules assembled. (**c**) Bristle design parameters. (**d**) Backward to forward friction ratio $F_{backward}/F_{forward}$, as a function of bristle tilt angle α_{tilt} from 0˚ to 45˚. (**e**) Fabricated bristles. (**f**) Velocity in vibrational crawling mode against bristle tilt angle.

The bristle design is demonstrated in **Figure C.3** (**c**) where the bristle tilt angle is the variable to be optimized. For the two-anchor crawling mode which relay on the anisotropic friction of the bristle, a higher backward to forward friction ratio is essential for a robust two-anchor gait. **Figure C.3** (**d**) shows the forward to backward friction ratio of different tilt angles. As can be seen, the friction ratio increases to over 4 when the tilt angle is at 45˚. A larger tilt angle was not included in this study due to the increasing difficulty in the moulding fabrication process. As a result, a tilt angle of 45˚ was selected for two-anchor crawling. However, as demonstrated in **Figure C.3** (**f**), a smaller tilt angle can lead to a faster vibrational crawling velocity, hence a small tilt angle of 15˚ was chosen for vibrational crawling.

C.4 Robot Demonstration

Figure C.4 (a) illustrates the robot motion of the robot in vibrational crawling mode. The DEA was driven at the resonance of 124 Hz, leading to a peak velocity of 55 mm/s (0.9 body length / s) with a power consumption of 40 mW. **Figure C.4 (b)** shows the two-anchor crawling motion with the peak velocity of 6.6 mm/s (0.1 body length / s) at 35 Hz. The two-anchor velocity against actuation frequency is shown in **Figure C.5 (a)**. The velocity increases with the increasing frequency and reaches a peak of 6.6 mm/s (0.1 body length / s) at 35 Hz and then drops sharply at 40 Hz due to the insufficient charging and discharging of the DEAs (a limitation of the high voltage supplies and electrodes). The detailed displacement of the front segment of the robot as a function of time at 2 Hz crawling is shown in **Figure C.5 (b)**. To demonstrate the payload transportation capability using the two-anchor mode, two 10 g weights were placed on the robot, which is equivalent to 35% of the robot's body weight. The robot was able to achieve a speed of 0.09 mm/s, as is shown in **Figure C.4 (c)**.

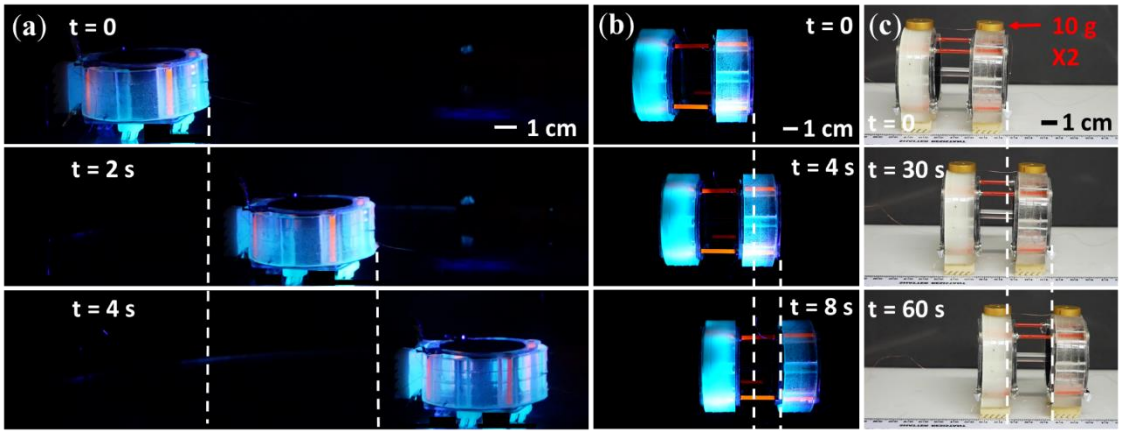

Figure C. 4. Robot in motion. (**a**) Vibrational crawling motion of the robot at 124 Hz actuation frequency (side view). (**b**) Two-anchor crawling motion at 35 Hz actuation frequency (top view). (**c**) Two-anchor crawling motion with 20 g payload (side view).

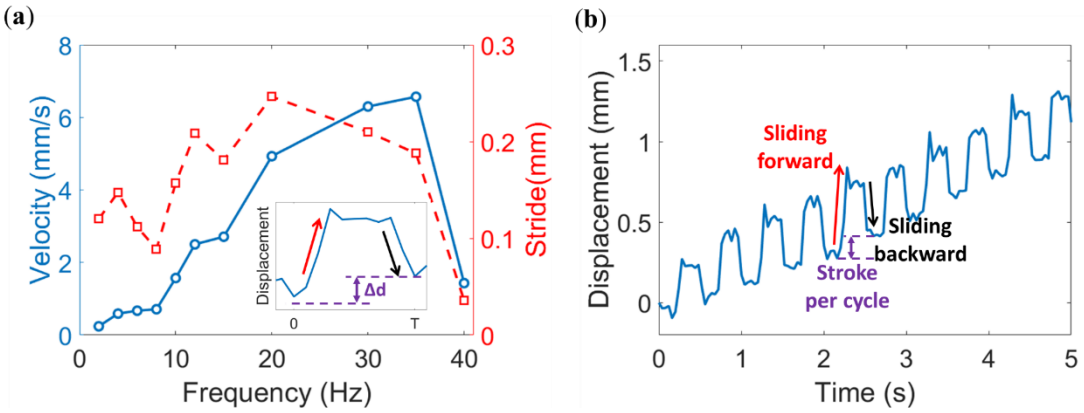

Figure C. 5. Robot locomotion speed analysis. (**a**) Velocity and stride in two-anchor mode against actuation frequency. (**b**) Displacement of the robot in 2 Hz crawling.

Appendix D: Pneumatic Pump and Soft Gripper Design

This appendix describes the detailed design of the DEA driven pneumatic pump and the soft gripper in Chapter 7.

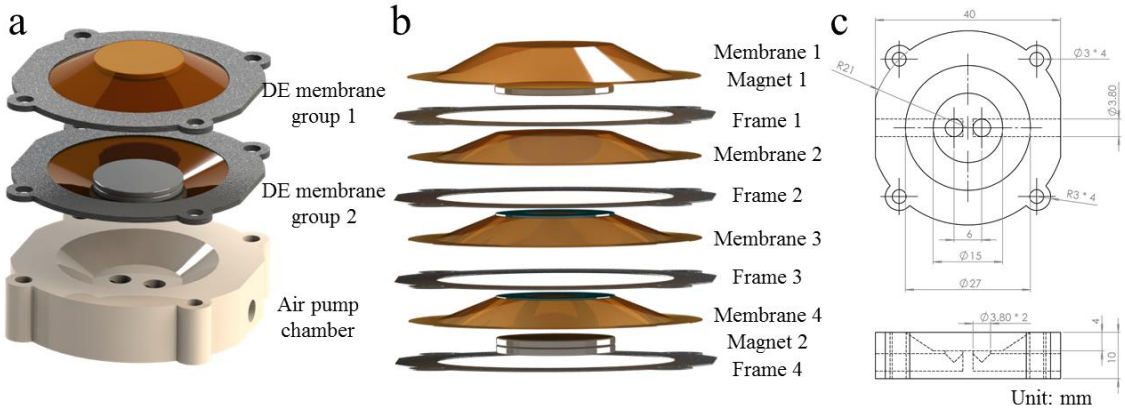

Figure D. 1. Assembly of (**a**) the MCDEA pump and (**b**) DE membranes and magnets. (**c**) Dimensions of the 3D printed pump chamber.

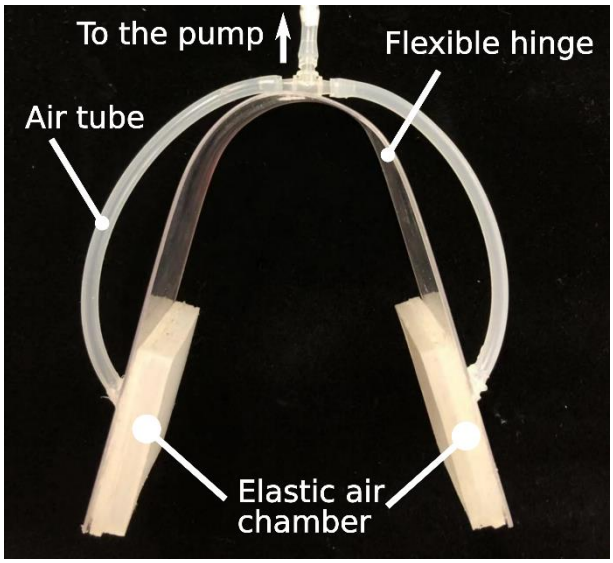

Figure D. 2. The two-finger soft gripper used in pump demonstration. This design consists of two elastic air chambers (Ecoflex 00-30, Smooth-On) fixed on a flexible hinge (1 mm thick acrylic).

Appendix E: DCDEA Driven Quadruped Robot

Statement: This study presented in this appendix is adapted from the following publication where C. Cao is the first author.

- **Cao, C**., Gao, X. and Conn, A.T., 2019. Towards efficient elastic actuation in bio-inspired robotics using dielectric elastomer artificial muscles. *Smart Materials and structures*. (Under review).

Contribution: Fabrication and testing methodology, investigation, data curation, formal analysis, writing original draft; review & editing.

The DCDEA driven quadruped robot design follows the same design as shown in Section 6.3.7. One additional DCDEA is added to drive the hip joint, as illustrated in **Figure E.1** (**a**). The detailed values of all design parameters are listed in **Table E.1** below.

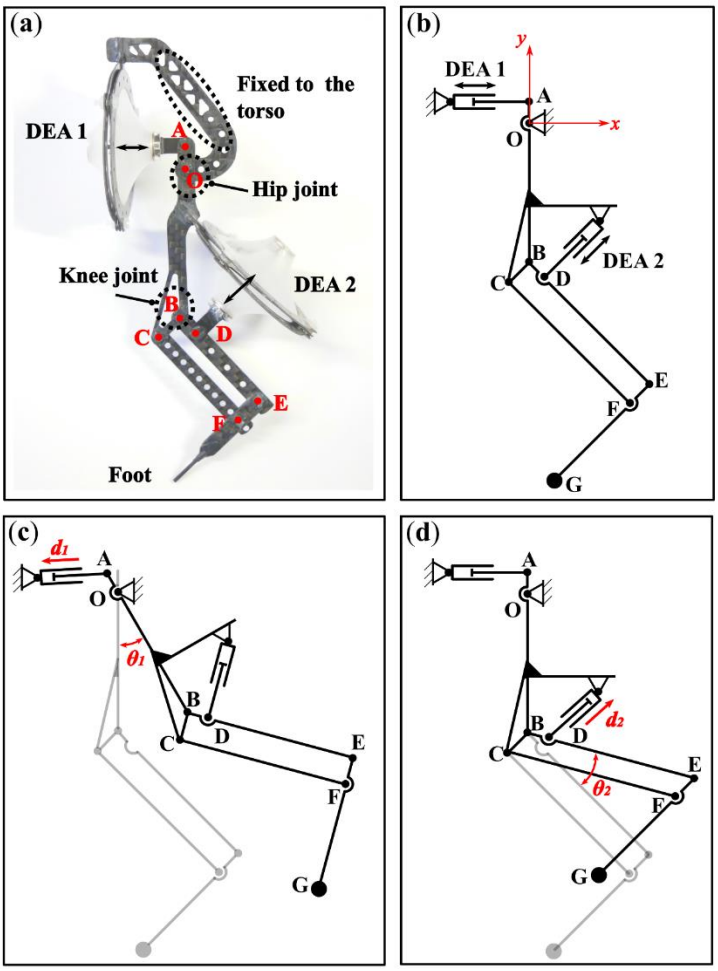

Figure E. 1. Leg design illustration. (**a**) Photo of a fabricated leg prototype. (**b**) Schematic diagram of the leg design. (**c**) DEA 1 drives the hip joint of the leg. (**d**) DEA 2 drives the knee joint of the leg.

Table E. 1. Design parameter values of the bio-inspired robotic leg.

Parameter	AO	OB	BC/EF	BE/CF	BD	EG	$\angle OBD_0$
Value	8 mm	52 mm	10 mm	48 mm	8 mm	42 mm	135˚

E.1 Kinematic Model of the Robotic Leg

In this subsection, a kinematic model is developed to describe the location of the foot with two given displacements of the DEAs d_1 and d_2.

The first step is to convert the linear displacement of the DEA into the rotational angle of the corresponding joint, which can be obtained from the geometrical relationship

$$\theta_i = \sin^{-1}(d_i/L), \tag{E.49}$$

where θ_i (i = 1, 2 for hip and knee joint respectively (**Figure E.1** (**b**))), d is the displacement of the DEA and L is the length of the linkage (L = AO and BD for hip and knee respectively)

In this leg design, the joint O is fixed to the torso and, as a result, this point is set as the origin, with the coordinate system illustrated in **Figure E.1** (**b**). Now considering the motion where only DEA 2 is actuated, the linkage BE is driven to rotate around joint B by an angle θ_2. Here we define that a counterclockwise angle is positive. The coordinate of point E can be described as

$$\overrightarrow{OE} = \overrightarrow{OB} + \overrightarrow{BE} = \begin{pmatrix} B_{x0} \\ B_{y0} \end{pmatrix} + \begin{pmatrix} |BE| \cos\left(-\frac{\pi}{4} + \theta_2\right) \\ |BE| \sin\left(-\frac{\pi}{4} + \theta_2\right) \end{pmatrix}, \tag{E.50}$$

where $\begin{pmatrix} B_{x0} \\ B_{y0} \end{pmatrix}$ is the initial coordinate of B prior to any rotation, -π/4 is the initial angle between $\overrightarrow{BE}$ and positive x axis.

The vector $\overrightarrow{EG}$ is always parallel to $\overrightarrow{BC}$, so that $\overrightarrow{EG} = \begin{pmatrix} |EG| \cos\left(\frac{-3\pi}{4}\right) \\ |EG| \sin\left(\frac{-3\pi}{4}\right) \end{pmatrix}$ and the coordinate of point G can be written as

$$\overrightarrow{OG} = \overrightarrow{OB} + \overrightarrow{BE} + \overrightarrow{EG} = \begin{pmatrix} B_{x0} + |BE| \cos\left(-\frac{\pi}{4} + \theta_2\right) + |EG| \cos\left(\frac{-3\pi}{4}\right) \\ B_{y0} + |BE| \sin\left(-\frac{\pi}{4} + \theta_2\right) + |EG| \sin\left(\frac{-3\pi}{4}\right) \end{pmatrix}. \tag{E.51}$$

Next, the transformation of the rotation caused by θ_1 is considered. θ_1 causes the whole system to rotate around the origin O, as a result, a rotational coordinate transformation can be employed to obtain the final coordinate of point G

$$\overrightarrow{OG} = \begin{pmatrix} \cos\theta_1 & -\sin\theta_1 \\ \sin\theta_1 & \cos\theta_1 \end{pmatrix} \begin{pmatrix} B_x + |BE|\cos\left(-\frac{\pi}{4}+\theta_2\right) + |EG|\cos\left(\frac{-3\pi}{4}\right) \\ B_y + |BE|\sin\left(-\frac{\pi}{4}+\theta_2\right) + |EG|\sin\left(\frac{-3\pi}{4}\right) \end{pmatrix} = \begin{pmatrix} B_{x0}\cos\theta_1 - B_{y0}\sin\theta_1 + |BE|\cos\left(-\frac{\pi}{4}+\theta_2+\theta_1\right) + |EG|\cos\left(\frac{-3\pi}{4}+\theta_1\right) \\ B_{x0}\sin\theta_1 + B_{y0}\cos\theta_1 + |BE|\sin\left(-\frac{\pi}{4}+\theta_2+\theta_1\right) + |EG|\sin\left(\frac{-3\pi}{4}+\theta_1\right) \end{pmatrix}. \quad \text{(E.52)}$$

With the actuation signals of DEA1 and DEA2 known, the displacement output of the two DEAs, d_1 and d_2, can be estimated from the dynamic DCDEA model, then the position of the foot, G, can be calculated.

E.2 Leg Kinematic Model Validation

The leg was mounted to a testing rig and four actuation signals drove the two DEAs to move the foot in the air. A red marker was attached to the end of the foot and its motion was filmed by a camera at 60 frames per second and then tracked using a custom tracking script in MATLAB. **Figure E.2** (**a**) shows a sequence of leg motion during one cycle and **Figure E.2** (**b**-**c**) illustrates the tracked position and the estimated position using the kinematic model with square and sinusoid waves respectively. It can be noted that despite the square wave resulting in a larger stroke of the robot foot than with sinusoid signals, the motion is discontinuous while the sinusoidal waves lead to a very smooth motion, which can be advantageous in stable dynamic legged locomotion.

E.3 Quadruped Robot

A DCDEA driven quadruped robot was developed based on the bioinspired leg design and **Figure E.3** shows a fabricated prototype. The quadruped has a size of 210 × 160 mm and weighs 100 g. Initial tests were performed with the quadruped robot. However, the legs were found to be unable to support the total weight of the robot when two legs are trying to lift up, which is due to an insufficient number of layers of DEA membranes used. Hence no successful step was recorded. In the future, novel fabrication techniques will be explored to allow simple fabrication of multilayer DEAs with lightweight that can support the overall weight of the robot and enable walking and even running gaits of the quadruped robot.

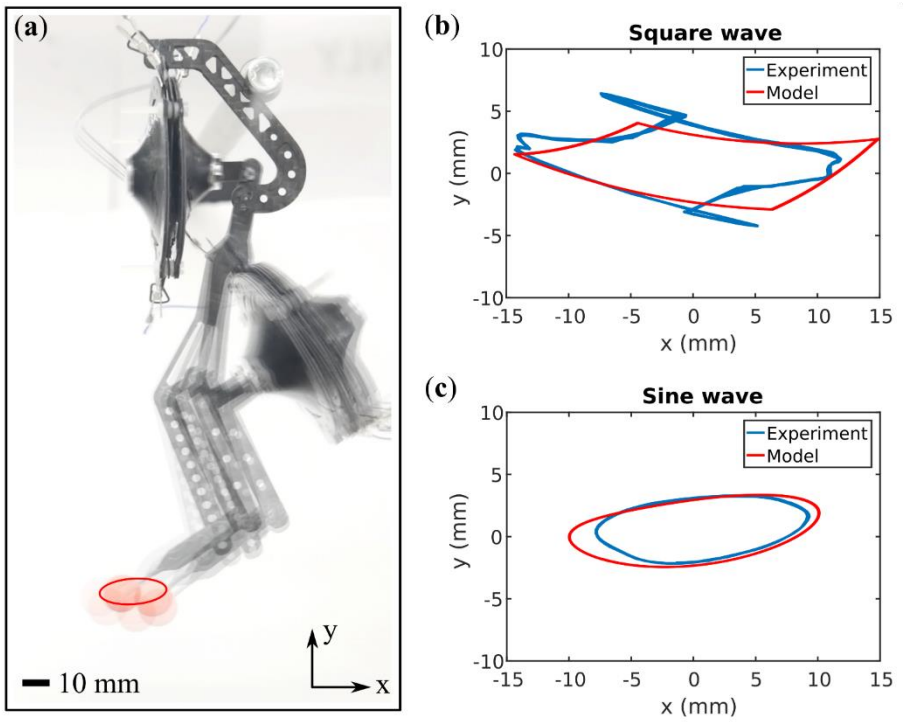

Figure E. 2. (**a**) Free swing of the bio-inspired leg using sinusoidal actuation waves. Tracked and modelled foot position relative to its passive location using (**b**) square waves and (**c**) sinusoidal waves.

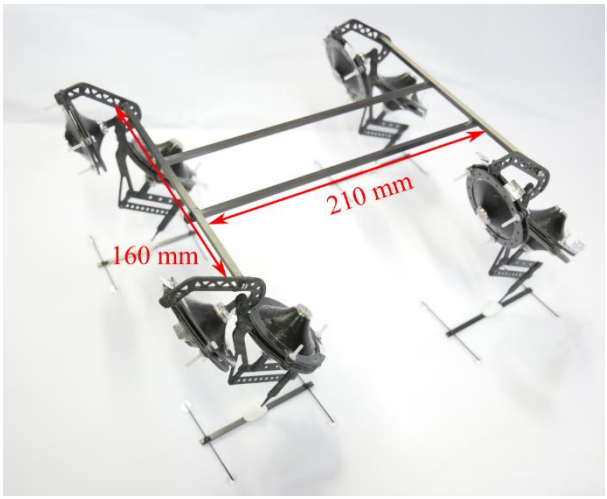

Figure E. 3. DCDEA driven quadruped robot prototype.

References

[1] D. Rus and M. T. Tolley, “Design, fabrication and control of soft robots,” *Nature*, vol. 521, no. 7553, pp. 467–475, 2015.

[2] G. M. Whitesides, “Soft Robotics,” *Angew. Chemie - Int. Ed.*, vol. 57, no. 16, pp. 4258–4273, 2018.

[3] S. . Morin, R. . Shepherd, S. . Kwok, A. . Stokes, A. Nemiroski, and G. M. Whitesides, “Camouflage and Display for Soft Machines,” *Science (80-.).*, vol. 337, no. 6096, pp. 828–832, 2012.

[4] R. Pelrine, R. Kornbluh, Q. Pei, and J. Joseph, “High-speed electrically actuated elastomers with strain greater than 100%,” *Science (80-.).*, vol. 287, no. 5454, pp. 836–839, 2000.

[5] K. Jung, J. C. Koo, J. Do Nam, Y. K. Lee, and H. R. Choi, “Artificial annelid robot driven by soft actuators,” *Bioinspiration and Biomimetics*, vol. 2, no. 2, 2007.

[6] Q. Pei, M. Rosenthal, S. Stanford, H. Prahlad, and R. Pelrine, “Multiple-degrees-of-freedom electroelastomer roll actuators,” *Smart Mater. Struct.*, vol. 13, no. 5, pp. N86–N92, 2004.

[7] C. T. Nguyen *et al.*, “Printable monolithic hexapod robot driven by soft actuator,” in *IEEE International Conference on Robotics and Automation (ICRA)*, 2015, pp. 189–190.

[8] J. Shintake, V. Cacucciolo, H. Shea, and D. Floreano, “Soft biomimetic fish robot made of dielectric elastomer actuators,” *Soft Robot.*, vol. 5, no. 4, pp. 466–474, 2018.

[9] T. Li *et al.*, “Fast-moving soft electronic fish,” *Sci. Adv.*, vol. 3, no. 4, pp. 1–8, 2017.

[10] G. K. Lau, H. T. Lim, J. Y. Teo, and Y. W. Chin, “Lightweight mechanical amplifiers for rolled dielectric elastomer actuators and their integration with bio-inspired wing flappers,” *Smart Mater. Struct.*, vol. 23, no. 2, p. 025021, 2014.

[11] J. Shintake, S. Rosset, B. E. Schubert, D. Floreano, and H. R. Shea, “A Foldable Antagonistic Actuator,” *IEEE/ASME Trans. Mechatronics*, vol. 20, no. 5, pp. 1997–2008, 2015.

[12] G. Kofod, W. Wirges, M. Paajanen, and S. Bauer, “Energy minimization for self-organized structure formation and actuation,” *Appl. Phys. Lett.*, vol. 90, no. 8, pp. 1–4, 2007.

[13] O. A. Araromi *et al.*, “Rollable multisegment dielectric elastomer minimum energy structures for a deployable microsatellite gripper,” *IEEE/ASME Trans. Mechatronics*, vol. 20, no. 1, pp. 438–446, 2015.

[14] G. K. Lau, K. R. Heng, A. S. Ahmed, and M. Shrestha, “Dielectric elastomer fingers for versatile grasping and nimble pinching,” *Appl. Phys. Lett.*, vol. 110, no. 18, 2017.

[15] J. Shintake, S. Rosset, B. Schubert, D. Floreano, and H. Shea, “Versatile Soft Grippers with Intrinsic Electroadhesion Based on Multifunctional Polymer Actuators,” *Adv. Mater.*, vol. 28, no. 2, pp. 231–238, 2016.

[16] P. Lotz, M. Matysek, and H. F. Schlaak, “Fabrication and application of miniaturized dielectric elastomer stack actuators,” *IEEE/ASME Trans. Mechatronics*, vol. 16, no. 1, pp. 58–66, 2011.

[17] F. A. Mohd Ghazali, C. K. Mah, A. AbuZaiter, P. S. Chee, and M. S. Mohamed Ali, “Soft dielectric elastomer actuator micropump,” *Sensors Actuators, A Phys.*, vol. 263, pp. 276–284, 2017.

[18] D. McCoul and Q. Pei, “Tubular dielectric elastomer actuator for active fluidic control,” *Smart Mater. Struct.*, vol. 24, no. 10, p. 105016, 2015.

[19] C. Keplinger, J.-Y. Sun, C. C. Foo, P. Rothemund, G. M. Whitesides, and Z. Suo, “Stretchable, Transparent, Ionic Conductors,” *Science (80-.).*, vol. 341, no. 6149, pp. 984–987, 2013.

[20] P. Rothemund, X. P. Morelle, K. Jia, G. M. Whitesides, and Z. Suo, “A Transparent Membrane for Active Noise Cancelation,” *Adv. Funct. Mater.*, vol. 28, no. 29, pp. 1–8, 2018.

[21] L. Maffli, S. Rosset, M. Ghilardi, F. Carpi, and H. Shea, “Ultrafast all-polymer electrically tunable silicone lenses,” *Adv. Funct. Mater.*, vol. 25, no. 11, pp. 1656–1665, 2015.

[22] S. Nam *et al.*, “A Robust Soft Lens for Tunable Camera Application Using Dielectric Elastomer Actuators,” *Soft Robot.*, vol. 5, no. 6, pp. 777–782, 2018.

[23] C. Xu, G. T. Stiubianu, and A. A. Gorodetsky, “Adaptive infrared-reflecting systems inspired by cephalopods,” *Science (80-.).*, vol. 359, no. 6383, pp. 1495–1500, 2018.

[24] S. Hau, G. Rizzello, M. Hodgins, A. York, and S. Seelecke, “Design and control of a high-speed positioning system based on dielectric elastomer membrane actuators,” *IEEE/ASME Trans. Mechatronics*, vol. 22, no. 3, pp. 1259–1267, 2017.

[25] J. Zou, G. Y. Gu, and L. M. Zhu, “Open-loop control of creep and vibration in dielectric elastomer actuators with phenomenological models,” *IEEE/ASME Trans. Mechatronics*, vol. 22, no. 1, pp. 51–58, 2017.

[26] J. Zou and G. Gu, “High-precision tracking control of a soft dielectric elastomer actuator with inverse viscoelastic hysteresis compensation,” *IEEE/ASME Trans. Mechatronics*, vol. 24, no. 1, pp. 36–44, 2019.

[27] A. Poulin and S. Rosset, “An open-loop control scheme to increase the speed and reduce the viscoelastic drift of dielectric elastomer actuators,” *Extrem. Mech. Lett.*, vol. 27, pp. 20–26, 2019.

[28] Z. Suo, X. Zhao, and W. H. Greene, “A nonlinear field theory of deformable dielectrics,” *J. Mech. Phys. Solids*, vol. 56, no. 2, pp. 467–486, 2008.

[29] R. M. N. Alexander, “Three Uses for Springs in Legged Locomotion,” *Int. J. Rob. Res.*, vol. 7, no. 2, pp. 53–61, 1990.

[30] C. P. Ellington, “The novel aerodynamics of insect flight: applications to micro-air vehicles,” *J. Exp. Biol.*, vol. 202, no. 23, pp. 3439–3448, 1999.

[31] A. T. Conn and J. Rossiter, “Towards holonomic electro-elastomer actuators with six degrees of freedom,” *Smart Mater. Struct.*, vol. 21, no. 3, p. 035012, 2012.

[32] M. Hodgins, G. Rizzello, D. Naso, A. York, and S. Seelecke, “An electro-mechanically coupled model for the dynamic behavior of a dielectric electro-active polymer actuator,” *Smart Mater. Struct.*, vol. 23, no. 10, p. 104006, 2014.

[33] G. Rizzello, M. Hodgins, D. Naso, A. York, and S. Seelecke, “Dynamic Modeling and Experimental Validation of an Annular Dielectric Elastomer Actuator With a Biasing Mass,” *J. Vib. Acoust.*, vol. 137, no. 1, p. 011005, 2015.

[34] M. Hodgins, A. York, and S. Seelecke, “Experimental comparison of bias elements for out-of-plane DEAP actuator system,” *Smart Mater. Struct.*, vol. 22, no. 9, p. 094016, 2013.

[35] X. Q. Li, W. B. Li, W. M. Zhang, H. X. Zou, Z. K. Peng, and G. Meng, “Magnetic force induced tristability for dielectric elastomer actuators,” *Smart Mater. Struct.*, vol. 26, no. 10, p. 105007, 2017.

[36] S. M. Mirvakili and I. W. Hunter, “Artificial Muscles: Mechanisms, Applications, and Challenges,” *Adv. Mater.*, vol. 30, no. 6, pp. 1–28, 2018.

[37] L. Hines, K. Petersen, G. Z. Lum, and M. Sitti, “Soft Actuators for Small-Scale Robotics,” *Adv. Mater.*, vol. 29, no. 13, p. 1603483, 2017.

[38] S. Bauer, S. Bauer-Gogonea, I. Graz, M. Kaltenbrunner, C. Keplinger, and R. Schwödiauer, “25th anniversary article: A soft future: From robots and sensor skin to energy harvesters,” *Adv. Mater.*, vol. 26, no. 1, pp. 149–162, 2014.

[39] M. Taghavi, T. Helps, and J. Rossiter, “Electro-ribbon actuators and electro-origami robots,” *Sci. Robot.*, vol. 3, no. 25, p. eaau9795, 2018.

[40] S. K. Mitchell *et al.*, “Hydraulically amplified self-healing electrostatic actuators with muscle-like performance,” *Science (80-.).*, vol. 359, no. 6371, pp. 61–65, 2018.

[41] A. Ölander, “An electrochemical investigation of solid cadmium-gold alloys,” *J. Am. Chem. Soc.*, vol. 54, no. 10, pp. 3819–3833, 1932.

[42] B. Holschuh, E. Obropta, and D. Newman, “Low spring index NiTi coil actuators for use in active compression garments,” *IEEE/ASME Trans. Mechatronics*, vol. 20, no. 3, pp. 1264–1277, 2015.

[43] J. Mohd Jani, M. Leary, A. Subic, and M. A. Gibson, “A review of shape memory alloy research, applications and opportunities,” *Mater. Des.*, vol. 56, pp. 1078–1113, 2014.

[44] W. Huang, “On the selection of shape memory alloys for actuators,” *Mater. Des.*, vol. 23, no. 1, pp. 11–19, 2002.

[45] S. Kim, E. Hawkes, K. Cho, M. Jolda, J. Foley, and R. Wood, “Micro artificial muscle fiber using NiTi spring for soft robotics,” in *2009 IEEE/RSJ International Conference on Intelligent Robots and Systems, IROS 2009*, 2009, pp. 2228–2234.

[46] M. Kovač, A. Guignard, J. D. Nicoud, J. C. Zufferey, and D. Floreano, “A 1.5g SMA-actuated microglider looking for the light,” in *Proceedings - IEEE International Conference on Robotics and Automation*, 2007, pp. 367–372.

[47] K. J. Cho, E. Hawkes, C. Quinn, and R. J. Wood, “Design, fabrication and analysis of a body-caudal fin propulsion system for a microrobotic fish,” in *Proceedings - IEEE International Conference on Robotics and Automation*, 2008, pp. 706–711.

[48] A. Villanueva, C. Smith, and S. Priya, “A biomimetic robotic jellyfish (Robojelly) actuated by shape memory alloy composite actuators,” *Bioinspiration and Biomimetics*, vol. 6, no. 3, p. 036004, 2011.

[49] H. T. Lin, G. G. Leisk, and B. Trimmer, “GoQBot: A caterpillar-inspired soft-bodied rolling robot,” *Bioinspiration and Biomimetics*, vol. 6, no. 2, p. 036007, 2011.

[50] C. Laschi, M. Cianchetti, B. Mazzolai, L. Margheri, M. Follador, and P. Dario, “Soft robot arm inspired by the octopus,” *Adv. Robot.*, vol. 26, no. 7, pp. 709–727, 2012.

[51] M. Noh, S. Kim, S. An, J. Koh, and K. Cho, “Flea-Inspired Catapult Mechanism for Miniature Jumping Robots,” *IEEE Trans. Robot.*, vol. 28, no. 5, pp. 1007–1018, 2012.

[52] P. G. Jablonski *et al.*, “Jumping on water: Surface tension-dominated jumping of water striders and robotic insects,” *Science (80-.).*, vol. 349, no. 6247, pp. 517–521, 2015.

[53] C.-P. Chou and B. Hannaford, “Measurement and modeling of McKibben pneumatic artificial muscles,” *IEEE Trans. Robot. Autom.*, vol. 12, no. 1, pp. 90–102, 1996.

[54] B. Tondu and P. Lopez, “Modeling and control of McKibben artificial muscle robot actuators,” *IEEE Control Syst. Mag.*, vol. 20, no. 2, pp. 15–38, 2000.

[55] P. Polygerinos *et al.*, “Soft Robotics: Review of Fluid-Driven Intrinsically Soft Devices; Manufacturing, Sensing, Control, and Applications in Human-Robot Interaction,” *Adv. Eng. Mater.*, vol. 19, no. 12, p. 170016, 2017.

[56] K. Suzumori, S. Iikura, and H. Tanaka, “Development of flexible microactuator and its applications to robotic mechanisms,” in *Proceedings. 1991 IEEE International Conference on Robotics and Automation*, 1191, pp. 1622–1627.

[57] R. V. Martinez *et al.*, “Robotic tentacles with three-dimensional mobility based on flexible elastomers,” *Adv. Mater.*, vol. 25, no. 2, pp. 205–212, 2013.

[58] R. V. Martinez, C. R. Fish, X. Chen, and G. M. Whitesides, “Elastomeric origami: Programmable paper-elastomer composites as pneumatic actuators,” *Adv. Funct. Mater.*, vol. 22, no. 7, pp. 1376–1384, 2012.

[59] R. Deimel and O. Brock, “A novel type of compliant and underactuated robotic hand for dexterous grasping,” *Int. J. Rob. Res.*, vol. 35, no. 1–3, pp. 161–185, 2016.

[60] J. Guo *et al.*, “Soft pneumatic grippers embedded with stretchable electroadhesion,” *Smart Mater. Struct.*, vol. 27, no. 5, p. 055006, 2018.

[61] A. T. Asbeck, S. M. M. De Rossi, K. G. Holt, and C. J. Walsh, “A biologically inspired soft exosuit for walking assistance,” *Int. J. Rob. Res.*, vol. 34, no. 6, pp. 744–762, 2015.

[62] P. Polygerinos *et al.*, “Towards a soft pneumatic glove for hand rehabilitation,” in *IEEE International Conference on Intelligent Robots and Systems*, 2013, pp. 1512–1517.

[63] P. Polygerinos, Z. Wang, K. C. Galloway, R. J. Wood, and C. J. Walsh, “Soft robotic glove for combined assistance and at-home rehabilitation,” *Rob. Auton. Syst.*, vol. 73, pp. 135–143, 2015.

[64] N. W. Bartlett *et al.*, “A Soft Robotic Orthosis for Wrist Rehabilitation,” *J. Med. Device.*, vol. 9, no. 3, p. 030918, 2015.

[65] M. T. Tolley *et al.*, “A Resilient, Untethered Soft Robot,” *Soft Robot.*, vol. 1, no. 3, pp. 213–223, 2014.

[66] A. D. Marchese, C. D. Onal, and D. Rus, “Autonomous Soft Robotic Fish Capable of Escape Maneuvers Using Fluidic Elastomer Actuators,” *Soft Robot.*, vol. 1, no. 1, pp. 75–87, 2014.

[67] K. M. Digumarti, A. T. Conn, and J. Rossiter, “Eumobot: Replicating euglenoid movement in a soft robot,” *J. R. Soc. Interface*, vol. 15, no. 148, p. 20180301, 2018.

[68] W. S. Chu *et al.*, “Review of biomimetic underwater robots using smart actuators,” *Int. J. Precis. Eng. Manuf.*, vol. 13, no. 7, pp. 1281–1292, 2012.

[69] R. K. Cheedarala, J. H. Jeon, C. D. Kee, and I. K. Oh, “Bio-Inspired All-Organic Soft Actuator Based on a π-π Stacked 3D Ionic Network Membrane and Ultra-Fast Solution Processing,” *Adv. Funct. Mater.*, vol. 24, no. 38, pp. 6005–6015, 2014.

[70] X. Ye, Y. Su, S. Guo, and L. Wang, “Design and realization of a remote control centimeter-scale robotic fish,” in *IEEE/ASME International Conference on Advanced Intelligent Mechatronics, AIM*, 2008, pp. 25–30.

[71] X. Tant *et al.*, “An autonomous robotic fish for mobile sensing,” in *IEEE International Conference on Intelligent Robots and Systems*, 2006, pp. 5424–5429.

[72] C. Zheng, S. Shatara, and X. Tan, “Modeling of robotic fish propelled by an ionic polymer-metal composite caudal fin,” *IEEE/ASME Trans. Mechatronics*, vol. 15, no. 3, pp. 448–459, 2010.

[73] J. Rossiter, B. Stoimenov, Y. Nakabo, and T. Mukai, “Three-phase control for miniaturization of a snake-like swimming robot,” in *2006 IEEE International Conference on Robotics and Biomimetics, ROBIO 2006*, 2006, pp. 1215–1220.

[74] S. W. Yeom and I. K. Oh, “A biomimetic jellyfish robot based on ionic polymer metal composite actuators,” *Smart Mater. Struct.*, vol. 18, no. 8, p. 085002, 2009.

[75] L. Shi, S. Guo, and K. Asaka, “A novel multifunctional underwater microrobot,” in *2010 IEEE International Conference on Robotics and Biomimetics, ROBIO 2010*, 2010, pp. 873–878.

[76] Y. F. Goh, S. Akbari, T. V. Khanh Vo, and S. J. A. Koh, “Electrically-Induced Actuation of Acrylic-Based Dielectric Elastomers in Excess of 500% Strain,” *Soft Robot.*, vol. 5, no. 6, pp. 675–684, 2018.

[77] T. A. Gisby, B. M. Obrien, and I. A. Anderson, “Self sensing feedback for dielectric elastomer actuators,” *Appl. Phys. Lett.*, vol. 102, no. 19, p. 193703, 2013.

[78] S. J. Dünki, Y. S. Ko, F. A. Nüesch, and D. M. Opris, “Self-repairable, high permittivity dielectric elastomers with large actuation strains at low electric fields,” *Adv. Funct. Mater.*, vol. 25, no. 16, pp. 2467–2475, 2015.

[79] S. R. Lafontaine *et al.*, “Artificial Muscle Technology: Physical Principles and Naval Prospects,” *IEEE J. Ocean. Eng.*, vol. 29, no. 3, pp. 706–728, 2004.

[80] T. Li *et al.*, “Agile and Resilient Insect-Scale Robot,” *Soft Robot.*, vol. 6, no. 1, pp. 133–141, 2018.

[81] J.-P. L. Lucking Bigué and J.-S. Plante, “Experimental Study of Dielectric Elastomer Actuator Energy Conversion Efficiency,” *IEEE/ASME Trans. Mechatronics*, vol. 18, no. 1, pp. 169–177, 2013.

[82] J. S. Plante and S. Dubowsky, “On the performance mechanisms of Dielectric Elastomer Actuators,” *Sensors Actuators, A Phys.*, vol. 137, no. 1, pp. 96–109, 2007.

[83] M. De Volder and D. Reynaerts, “Pneumatic and hydraulic microactuators: A review,” *J. Micromechanics Microengineering*, vol. 20, no. 4, p. 043001, 2010.

[84] S. Nemat-Nasser and Y. Wu, “Comparative experimental study of ionic polymer–metal composites with different backbone ionomers and in various cation forms,” *J. Appl. Phys.*, vol. 93, no. 9, pp. 5255–5267, 2003.

[85] K. J. Kim and M. Shahinpoor, “Ionic polymer – metal composites : II . Manufacturing techniques,” *Smart Mater. Struct.*, vol. 12, no. 1, pp. 65–79, 2003.

[86] S. J. Lee, M. J. Han, S. J. Kim, J. Y. Jho, H. Y. Lee, and Y. H. Kim, “A new fabrication method for IPMC actuators and application to artificial fingers,” *Smart Mater. Struct.*, vol. 15, no. 5, pp. 1217–1224, 2006.

[87] M. Duduta, E. Hajiesmaili, H. Zhao, R. J. Wood, and D. R. Clarke, “Realizing the potential of dielectric elastomer artificial muscles,” *Proc. Natl. Acad. Sci.*, vol. 116, no. 7, pp. 2476–2481, 2019.

[88] T. Li, C. Keplinger, R. Baumgartner, S. Bauer, W. Yang, and Z. Suo, “Giant voltage-induced deformation in dielectric elastomers near the verge of snap-through instability,” *J. Mech. Phys. Solids*, vol. 61, no. 2, pp. 611–628, 2013.

[89] R. Full and K. Meijer, “Metrics of Natural Muscle Function,” in *Electroactive Polymer (EAP) Actuators as Artificial Muscles: Reality, Potential, and Challenges, Second Edition*, 2010, pp. 73–89.

[90] R. E. Pelrine, R. D. Kornbluh, and J. P. Joseph, “Electrostriction of polymer dielectrics with compliant electrodes as a means of actuation,” *Sensors Actuators, A Phys.*, vol. 64, no. 1, pp. 77–85, 1998.

[91] R. Pelrine, R. Kornbluh, J. Joseph, R. Heydt, Q. Pei, and S. Chiba, “High-field deformation of elastomeric dielectrics for actuators,” *Mater. Sci. Eng. C*, vol. 11, no. 2, pp. 89–100, 2000.

[92] M. Wissler and E. Mazza, “Electromechanical coupling in dielectric elastomer actuators,” *Sensors Actuators, A Phys.*, vol. 138, no. 2, pp. 384–393, 2007.

[93] M. Wissler and E. Mazza, “Mechanical behavior of an acrylic elastomer used in dielectric elastomer actuators,” *Sensors Actuators, A Phys.*, vol. 134, no. 2, pp. 494–504, 2007.

[94] M. Duduta, R. J. Wood, and D. R. Clarke, “Multilayer Dielectric Elastomers for Fast, Programmable Actuation without Prestretch,” *Adv. Mater.*, vol. 28, no. 36, pp. 8058–8063, 2016.

[95] D. McCoul, S. Rosset, S. Schlatter, and H. Shea, “Inkjet 3D printing of UV and thermal cure silicone elastomers for dielectric elastomer actuators,” *Smart Mater. Struct.*, vol. 26, no. 12, p. 125022, 2017.

[96] S. Rosset, O. A. Araromi, S. Schlatter, and H. R. Shea, “Fabrication Process of Silicone-based Dielectric Elastomer Actuators,” *J. Vis. Exp.*, no. 108, pp. 1–13, 2016.

[97] C. T. Nguyen, H. Phung, T. D. Nguyen, H. Jung, and H. R. Choi, “Multiple-degrees-of-freedom dielectric elastomer actuators for soft printable hexapod robot,” *Sensors Actuators, A Phys.*, vol. 267, pp. 505–516, 2017.

[98] O. A. Araromi, A. T. Conn, C. S. Ling, J. M. Rossiter, R. Vaidyanathan, and S. C. Burgess, “Spray deposited multilayered dielectric elastomer actuators,” *Sensors Actuators, A Phys.*, vol. 167, no. 2, pp. 459–467, 2011.

[99] A. Poulin, S. Rosset, and H. R. Shea, “Printing low-voltage dielectric elastomer actuators,” *Appl. Phys. Lett.*, vol. 107, no. 24, p. 244104, 2015.

[100] H. Zhao, A. M. Hussain, M. Duduta, D. M. Vogt, R. J. Wood, and D. R. Clarke, “Compact Dielectric Elastomer Linear Actuators,” *Adv. Funct. Mater.*, vol. 28, no. 42, p. 1804328, 2018.

[101] D. Gatti, H. Haus, M. Matysek, B. Frohnapfel, C. Tropea, and H. F. Schlaak, “The dielectric breakdown limit of silicone dielectric elastomer actuators,” *Appl. Phys. Lett.*, vol. 104, no. 5, p. 052905, 2014.

[102] S. Rosset, O. A. Araromi, and H. R. Shea, “Maximizing the displacement of compact planar dielectric elastomer actuators,” *Extrem. Mech. Lett.*, vol. 3, pp. 72–81, 2015.

[103] F. B. Madsen, A. E. Daugaard, S. Hvilsted, and A. L. Skov, “The Current State of Silicone-Based Dieletric Elastomer Transducers,” *Macromol. Rapid Commun.*, vol. 37, pp. 378–413, 2016.

[104] S. Rosset and H. R. Shea, “Flexible and stretchable electrodes for dielectric elastomer actuators,” *Appl. Phys. A Mater. Sci. Process.*, vol. 110, no. 2, pp. 281–307, 2013.

[105] B. O’Brien, J. Thode, I. Anderson, E. Calius, E. Haemmerle, and S. Xie, “Integrated extension sensor based on resistance and voltage measurement for a dielectric elastomer,” *Electroact. Polym. Actuators Devices 2007*, vol. 6524, p. 652415, 2007.

[106] D. T. Kuhnel, J. M. Rossiter, and C. F. J. Faul, “Laser-Scribed Graphene Oxide Electrodes for Soft Electroactive Devices,” *Adv. Mater. Technol.*, vol. 4, no. 2, pp. 1–6, 2019.

[107] S. Shian, K. Bertoldi, and D. R. Clarke, “Dielectric Elastomer Based ‘grippers’ for Soft Robotics,” *Adv. Mater.*, vol. 27, no. 43, pp. 6814–6819, 2015.

[108] E. Hajiesmaili and D. R. Clarke, “Reconfigurable shape-morphing dielectric elastomers using spatially varying electric fields,” *Nat. Commun.*, vol. 10, no. 1, pp. 10–16, 2019.

[109] W. Yuan *et al.*, “Fault-tolerant dielectric elastomer actuators using single-walled carbon nanotube electrodes,” *Adv. Mater.*, vol. 20, no. 3, pp. 621–625, 2008.

[110] M. Zhang *et al.*, “Scar-Like Self-Reinforced and Failure-Tolerant Dielectric Elastomer Actuator With AgNWs Electrode,” *J. Appl. Mech.*, vol. 85, no. 3, p. 031006, 2018.

[111] S. P. Lacour, J. Jones, Z. Suo, and S. Wagner, “Design and Performance of Thin Metal Film Interconnects for Skin-Like Electronic Circuits,” *IEEE ELECTRON DEVICE Lett.*, vol. 25, no. 4, pp. 179–181, 2004.

[112] K. Wegner, P. Piseri, H. V. Tafreshi, and P. Milani, “Cluster beam deposition: A tool for nanoscale science and technology,” *J. Phys. D. Appl. Phys.*, vol. 39, no. 22, 2006.

[113] G. Kovacs, L. Düring, S. Michel, and G. Terrasi, “Stacked dielectric elastomer actuator for tensile force transmission,” *Sensors Actuators, A Phys.*, vol. 155, no. 2, pp. 299–307, 2009.

[114] C. T. Nguyen *et al.*, “A small biomimetic quadruped robot driven by multistacked dielectric elastomer actuators,” *Smart Mater. Struct.*, vol. 23, no. 6, 2014.

[115] H. S. Jung, K. H. Cho, J. H. Park, and S. Y. Yang, “Musclelike joint mechanism driven by dielectric elastomer actuator for robotic applications,” *Smart Mater. Struct.*, vol. 27, no. 7, p. 075011, 2018.

[116] F. Carpi, C. Salaris, and D. De Rossi, “Folded dielectric elastomer actuators,” *Smart Mater. Struct.*, vol. 16, no. 2, pp. S300–S305, 2007.

[117] A. D. Poole, J. D. Booker, C. L. Wishart, N. McNeill, and P. H. Mellor, “Performance of a prototype traveling-wave actuator made from a dielectric elastomer,” *IEEE/ASME Trans. Mechatronics*, vol. 17, no. 3, pp. 525–533, 2012.

[118] J. Maas, D. Tepel, and T. Hoffstadt, “Actuator design and automated manufacturing process for DEAP-based multilayer stack-actuators,” *Meccanica*, vol. 50, no. 11, pp. 2839–2854, 2015.

[119] J.-S. Plante, “Dielectric Elastomer Actuators for Binary Robotics and Mechatronics,” *IEEE/ASME Trans. Mechatronics*, vol. 17, no. 5, p. 186, 2006.

[120] T. Lu *et al.*, “Dielectric elastomer actuators under equal-biaxial forces, uniaxial forces, and uniaxial constraint of stiff fibers,” *Soft Matter*, vol. 8, no. 22, p. 6167, 2012.

[121] T. Lu, Z. Shi, Q. Shi, and T. J. Wang, “Bioinspired bicipital muscle with fiber-constrained dielectric elastomer actuator,” *Extrem. Mech. Lett.*, vol. 6, pp. 75–81, 2016.

[122] A. Wingert, M. D. Lichter, and S. Dubowsky, “On the design of large degree-of-freedom digital mechatronic devices based on bistable dielectric elastomer actuators,” *IEEE/ASME Trans. Mechatronics*, vol. 11, no. 4, pp. 448–456, 2006.

[123] G. Berselli, R. Vertechy, M. Babič, and V. Parenti Castelli, “Dynamic modeling and experimental evaluation of a constant-force dielectric elastomer actuator,” *J. Intell. Mater. Syst. Struct.*, vol. 24, no. 6, pp. 779–791, 2013.

[124] H. R. Choi, K. Jung, S. Ryew, J. Nam, and J. Jeon, “Biomimetic Soft Actuator : Design , Modeling , Control , and Applications,” *IEEE/ASME Trans. Mechatronics*, vol. 10, no. 5, pp. 581–593, 2005.

[125] C. Jordi, S. Michel, G. Kovacs, and P. Ermanni, “Scaling of planar dielectric elastomer actuators in an agonist-antagonist configuration,” *Sensors Actuators, A Phys.*, vol. 161, no. 1–2, pp. 182–190, 2010.

[126] Y. S. Teh and S. J. A. Koh, “Giant continuously-tunable actuation of a dielectric elastomer ring actuator,” *Extrem. Mech. Lett.*, vol. 9, pp. 195–203, 2016.

[127] L. Liu, C. Zhang, M. Luo, X. Chen, D. Li, and H. Chen, “A biologically inspired artificial muscle based on fiber-reinforced and electropneumatic dielectric elastomers,” *Smart Mater. Struct.*, vol. 26, no. 8, 2017.

[128] J. W. Fox and N. C. Goulbourne, “On the dynamic electromechanical loading of dielectric elastomer membranes,” *J. Mech. Phys. Solids*, vol. 56, no. 8, pp. 2669–2686, 2008.

[129] J. W. Fox and N. C. Goulbourne, “Electric field-induced surface transformations and experimental dynamic characteristics of dielectric elastomer membranes,” *J. Mech. Phys. Solids*, vol. 57, no. 8, pp. 1417–1435, 2009.

[130] F. Carpi, G. Frediani, and D. De Rossi, “Hydrostatically coupled dielectric elastomer actuators,” *IEEE/ASME Trans. Mechatronics*, vol. 15, no. 2, pp. 308–315, 2010.

[131] A. De Acutis, L. Calabrese, A. Bau, V. Tincani, and N. M. Pugno, “Design and proof of concept for multi degree of freedom hydrostatically coupled dielectric elastomer actuators with roto-translational kinematics for object handling,” *Smart Mater. Struct.*, 2018.

[132] F. Carpi, G. Frediani, M. Nanni, and D. De Rossi, “Granularly coupled dielectric elastomer actuators,” *IEEE/ASME Trans. Mechatronics*, vol. 16, no. 1, pp. 16–23, 2011.

[133] M. Follador, M. Cianchetti, and B. Mazzolai, “Design of a compact bistable mechanism based on dielectric elastomer actuators,” *Meccanica*, vol. 50, no. 11, pp. 2741–2749, 2015.

[134] K. McGough, S. Ahmed, M. Frecker, and Z. Ounaies, “Finite element analysis and validation of dielectric elastomer actuators used for active origami,” *Smart Mater. Struct.*, vol. 23, no. 9, 2014.

[135] J. Shintake, S. Rosset, B. Schubert, S. Mintchev, D. Floreano, and H. R. Shea, “DEA for soft robotics: 1-gram actuator picks up a 60-gram egg,” in *EAPAD*, 2015, p. 94301S.

[136] J. Shintake, B. Schubert, S. Rosset, H. Shea, and D. Floreano, “Variable stiffness actuator for soft robotics using dielectric elastomer and low-melting-point alloy,” *IEEE Int. Conf. Intell. Robot. Syst.*, vol. 2015-Decem, pp. 1097–1102, 2015.

[137] H. Imamura, K. Kadooka, and M. Taya, “A variable stiffness dielectric elastomer actuator based on electrostatic chucking,” *Soft Matter*, vol. 13, no. 18, pp. 3440–3448, 2017.

[138] H. Shao, S. Wei, X. Jiang, D. P. Holmes, and T. K. Ghosh, “Bioinspired Electrically Activated Soft Bistable Actuators,” *Adv. Funct. Mater.*, vol. 28, no. 35, p. 1802999, 2018.

[139] M. Follador, A. T. Conn, and J. Rossiter, “Bistable minimum energy structures (BiMES) for binary robotics,” *Smart Mater. Struct.*, vol. 24, no. 6, p. 065037, 2015.

[140] G. Kofod, M. Paajanen, and S. Bauer, “Self-organized minimum-energy structures for dielectric elastomer actuators,” *Appl. Phys. A Mater. Sci. Process.*, vol. 85, no. 2, pp. 141–143, 2006.

[141] M. T. Petralia and R. J. Wood, “Fabrication and analysis of dielectric-elastomer minimum-energy structures for highly-deformable soft robotic systems,” in *IEEE/RSJ 2010 International*

Conference on Intelligent Robots and Systems, IROS 2010 - Conference Proceedings, 2010, pp. 2357–2363.

[142] J. Zhao, J. Niu, D. McCoul, Z. Ren, and Q. Pei, "Phenomena of nonlinear oscillation and special resonance of a dielectric elastomer minimum energy structure rotary joint," *Appl. Phys. Lett.*, vol. 106, no. 13, p. 133504, 2015.

[143] J. Zhao *et al.*, "Improvement on output torque of dielectric elastomer minimum energy structures," *Appl. Phys. Lett.*, vol. 063505, no. 2015, pp. 7–12, 2015.

[144] Y. Z. Wang, U. Gupta, N. Parulekar, and J. Zhu, "A soft gripper of fast speed and low energy consumption," *Sci. China Technol. Sci.*, vol. 62, no. 1, pp. 31–38, 2019.

[145] J. Zhao *et al.*, "Bistable dielectric elastomer minimum energy structures," *Smart Mater. Struct.*, vol. 25, no. 7, 2016.

[146] H. Wang, L. Li, Y. Zhu, and W. Yang, "Analysis and application of a rolled dielectric elastomer actuator with two degrees of freedom," *Smart Mater. Struct.*, vol. 25, no. 12, 2016.

[147] A. T. Conn, A. D. Hinitt, and P. Wang, "Soft segmented inchworm robot with dielectric elastomer muscles," in *Electroactive Polymer Actuators and Devices (EAPAD) 2014*, 2014, vol. 9056, p. 90562L.

[148] M. Duduta, D. R. Clarke, and R. J. Wood, "A high speed soft robot based on dielectric elastomer actuators," *2017 IEEE Int. Conf. Robot. Autom.*, pp. 4346–4351, 2017.

[149] E.-F. M. Henke, S. Schlatter, and I. A. Anderson, "Soft Dielectric Elastomer Oscillators Driving Bioinspired Robots," *Soft Robot.*, vol. 4, no. 4, pp. 353–366, 2017.

[150] J. Cao *et al.*, "Untethered soft robot capable of stable locomotion using soft electrostatic actuators," *Extrem. Mech. Lett.*, vol. 21, pp. 9–16, 2018.

[151] H. Jung, P. T. Hoang, H. Phung, T. D. Nguyen, C. T. Nguyen, and H. R. Choi, "Development of an Insect-Inspired Hexapod Robot Actuated by Soft Actuators," *J. Mech. Robot.*, vol. 10, no. 6, p. 061016, 2018.

[152] M. Artusi, M. Potz, J. Aristiźabal, C. Menon, S. Cocuzza, and S. Debei, "Electroactive elastomeric actuators for the implementation of a deformable spherical rover," *IEEE/ASME Trans. Mechatronics*, vol. 16, no. 1, pp. 50–57, 2011.

[153] W.-B. Li, W. Zhang, H.-X. Zou, Z.-K. Peng, and G. Meng, "A Fast Rolling Soft Robot Driven by Dielectric Elastomer," *IEEE Trans. Mechatronics*, vol. 23, no. 4, pp. 1630–1640, 2018.

[154] S. Dubowsky, S. Kesner, J. Plante, and P. Boston, “Hopping mobility concept for search and rescue robots,” *Ind. Robot An Int. J.*, vol. 35, no. 3, pp. 238–245, 2008.

[155] C. Christianson, N. N. Goldberg, D. D. Deheyn, S. Cai, and M. T. Tolley, “Translucent soft robots driven by frameless fluid electrode dielectric elastomer actuators,” *Sci. Robot.*, vol. 3, no. 17, p. eaat1893, 2018.

[156] T. Yang *et al.*, “A soft artificial muscle driven robot with reinforcement learning,” *Sci. Rep.*, vol. 8, no. 1, p. 14518, 2018.

[157] G.-K. Lau, Y.-W. Chin, and T.-G. La, “Development of elastomeric flight muscles for flapping wing micro air vehicles,” in *Electroactive Polymer Actuators and Devices (EAPAD) 2017*, 2017, p. 1016320.

[158] J. Zhao, J. Niu, D. McCoul, J. Leng, and Q. Pei, “A rotary joint for a flapping wing actuated by dielectric elastomers: design and experiment,” *Meccanica*, vol. 50, no. 11, pp. 2815–2824, 2015.

[159] J. Rossiter, B. Yap, and A. Conn, “Biomimetic chromatophores for camouflage and soft active surfaces,” *Bioinspiration and Biomimetics*, vol. 7, no. 3, 2012.

[160] X. Zhao and Z. Suo, “Method to analyze programmable deformation of dielectric elastomer layers,” *Appl. Phys. Lett.*, vol. 93, no. 25, pp. 91–94, 2008.

[161] Z. Suo, “Theory of dielectric elastomers,” *Acta Mech. Solida Sin.*, vol. 23, no. 6, pp. 549–578, 2010.

[162] C. Chiang Foo, S. Cai, S. Jin Adrian Koh, S. Bauer, and Z. Suo, “Model of dissipative dielectric elastomers,” *J. Appl. Phys.*, vol. 111, no. 3, p. 034102, 2012.

[163] T. He, X. Zhao, and Z. Suo, “Dielectric elastomer membranes undergoing inhomogeneous deformation,” *J. Appl. Phys.*, vol. 106, no. 8, p. 083522, 2009.

[164] B. Li, J. Zhou, and H. Chen, “Electromechanical stability in charge-controlled dielectric elastomer actuation,” *Appl. Phys. Lett.*, vol. 99, no. 24, p. 244101, 2011.

[165] H. Wang, S. Cai, F. Carpi, and Z. Suo, “Computational Model of Hydrostatically Coupled Dielectric Elastomer Actuators,” *J. Appl. Mech.*, vol. 79, no. 3, p. 031008, 2012.

[166] U. Gupta, H. Godaba, Z. Zhao, C. K. Chui, and J. Zhu, “Tunable force/displacement of a vibration shaker driven by a dielectric elastomer actuator,” *Extrem. Mech. Lett.*, vol. 2, no. 1, pp. 72–77, 2015.

[167] A. . Gent, “A New Constitutive Relation for Rubber,” *Rubber Chem. Technol.*, vol. 69, no. 1, pp. 59–61, 1996.

[168] T. Li, S. Qu, and W. Yang, “Electromechanical and dynamic analyses of tunable dielectric elastomer resonator,” *Int. J. Solids Struct.*, vol. 49, no. 26, pp. 3754–3761, 2012.

[169] G. Rizzello, M. Hodgins, D. Naso, A. York, and S. Seelecke, “Modeling of the effects of the electrical dynamics on the electromechanical response of a DEAP circular actuator with a mass-spring load,” *Smart Mater. Struct.*, vol. 24, no. 9, p. 094003, 2015.

[170] B. Li, J. Zhang, H. Chen, and D. Li, “Voltage-induced pinnacle response in the dynamics of dielectric elastomers,” *Phys. Rev. E*, vol. 93, no. 5, p. 052506, 2016.

[171] G. Y. Gu, U. Gupta, J. Zhu, L. M. Zhu, and X. Zhu, “Modeling of Viscoelastic Electromechanical Behavior in a Soft Dielectric Elastomer Actuator,” *IEEE Trans. Robot.*, vol. 33, no. 5, pp. 1263–1271, 2017.

[172] C. Tang, B. Li, W. Sun, Z. Li, and H. Chen, “Identification and characterization of the out-of-plane resonance in a dielectric elastomer to drive an agile robotic cube,” *J. Appl. Phys.*, vol. 122, no. 16, p. 165104, 2017.

[173] J. Zhang, H. Chen, and D. Li, “Nonlinear Dynamical Model of a Soft Viscoelastic Dielectric Elastomer,” *Phys. Rev. Appl.*, vol. 8, no. 6, p. 064016, 2017.

[174] J. Zhang, H. Chen, and D. Li, “Pinnacle elimination and stability analyses in nonlinear oscillation of soft dielectric elastomer slide actuators,” *Nonlinear Dyn.*, vol. 94, no. 3, pp. 1907–1920, 2018.

[175] R. W. Ogden, “Large Deformation Isotropic Elasticity—On the Correlation of Theory and Experiment for Incompressible Rubberlike Solids,” *Rubber Chem. Technol.*, vol. 326, no. 1567, pp. 565–584, 1972.

[176] G. Y. Gu, J. Zhu, L. M. Zhu, and X. Zhu, “A survey on dielectric elastomer actuators for soft robots,” *Bioinspiration and Biomimetics*, vol. 12, no. 1, p. 011003, 2017.

[177] P. Lochmatter, G. Kovacs, and S. Michel, “Characterization of dielectric elastomer actuators based on a hyperelastic film model,” *Sensors Actuators, A Phys.*, vol. 135, no. 2, pp. 748–757, 2007.

[178] P. Lochmatter, G. Kovacs, and M. Wissler, “Characterization of dielectric elastomer actuators based on a visco-hyperelastic film model,” *Smart Mater. Struct.*, vol. 16, no. 2, pp. 477–486, 2007.

[179] Y. Liu, L. Liu, Z. Zhang, and J. Leng, “Dielectric elastomer film actuators: Characterization, experiment and analysis,” *Smart Mater. Struct.*, vol. 18, no. 9, p. 095024, 2009.

[180] W. Hong, “Modeling viscoelastic dielectrics,” *J. Mech. Phys. Solids*, vol. 59, no. 3, pp. 637–650, 2011.

[181] J. Zhang, H. Chen, B. Li, D. McCoul, and Q. Pei, “Coupled nonlinear oscillation and stability evolution of viscoelastic dielectric elastomers,” *Soft Matter*, vol. 11, no. 38, pp. 7483–7493, 2015.

[182] X. ZHAO, S. J. A. KOH, and Z. SUO, “Nonequilibrium Thermodynamics of Dielectric Elastomers,” *Int. J. Appl. Mech.*, vol. 03, no. 02, pp. 203–217, 2011.

[183] S. Rosset, O. A. Araromi, J. Shintake, and H. R. Shea, “Model and design of dielectric elastomer minimum energy structures,” *Smart Mater. Struct.*, vol. 23, no. 8, p. 085021, 2014.

[184] T. He, L. Cui, C. Chen, and Z. Suo, “Nonlinear deformation analysis of a dielectric elastomer membrane–spring system,” *Smart Mater. Struct.*, vol. 19, no. 8, p. 085017, 2010.

[185] B. Wang, Z. Wang, and T. He, “Investigation on the viscoelastic behaviors of a circular dielectric elastomer membrane undergoing large deformation,” *AIP Adv.*, vol. 6, no. 12, p. 125127, 2016.

[186] H. M. Wang, “Viscoelastic analysis of a spring-connected dielectric elastomer actuator undergoing large inhomogeneous deformation,” *Int. J. Mech. Sci.*, vol. 136, pp. 17–23, 2018.

[187] U. K. Chakravarty, “On the resonance frequencies of a membrane of a dielectric elastomer,” *Mech. Res. Commun.*, vol. 55, pp. 72–76, 2014.

[188] C. Tang, B. Li, H. Fang, Z. Li, and H. Chen, “A speedy, amphibian, robotic cube: Resonance actuation by a dielectric elastomer,” *Sensors Actuators, A Phys.*, vol. 270, pp. 1–7, 2018.

[189] Y. Li, I. Oh, J. Chen, and Y. Hu, “A new design of dielectric elastomer membrane resonator with tunable resonant frequencies and mode shapes,” *Smart Mater. Struct.*, vol. 27, no. 6, p. 065029, 2018.

[190] L. M. Diamante and T. Lan, “Absolute Viscosities of Vegetable Oils at Different Temperatures and Shear Rate Range of 64.5 to 4835 s^{-1},” *J. Food Process.*, vol. 2014, pp. 1–6, 2014.

[191] J. Germann, B. Schubert, and D. Floreano, “Stretchable electroadhesion for soft robots,” in *IEEE International Conference on Intelligent Robots and Systems*, 2014, pp. 3933–3938.

[192] F. Carpi *et al.*, “Standards for dielectric elastomer transducers,” *Smart Mater. Struct.*, vol. 24, no. 10, p. 105025, 2015.

[193] D. Wagg and S. Neild, *Nonlinear vibration with control*. Dordrecht, 2009.

[194] M. L. Hammock, A. Chortos, B. C. K. Tee, J. B. H. Tok, and Z. Bao, “25th anniversary article: The evolution of electronic skin (E-Skin): A brief history, design considerations, and recent progress,” *Adv. Mater.*, vol. 25, no. 42, pp. 5997–6038, 2013.

[195] T. Sekitani, U. Zschieschang, H. Klauk, and T. Someya, “Flexible organic transistors and circuits with extreme bending stability,” *Nat. Mater.*, vol. 9, no. 12, pp. 1015–22, 2010.

[196] K. Nakajima, H. Hauser, T. Li, and R. Pfeifer, “Information processing via physical soft body,” *Sci. Rep.*, vol. 5, pp. 1–11, 2015.

[197] F. Ilievski, A. D. Mazzeo, R. F. Shepherd, X. Chen, and G. M. Whitesides, “Soft robotics for chemists,” *Angew. Chemie - Int. Ed.*, vol. 50, no. 8, pp. 1890–1895, 2011.

[198] E. Brown *et al.*, “Universal Robotic Gripper based on the Jamming of Granular Material,” *Proc. Natl. Acad. Sci.*, vol. 107, no. 44, pp. 18809–18814, 2010.

[199] G. Fantoni *et al.*, “Grasping devices and methods in automated production processes,” *CIRP Ann. - Manuf. Technol.*, vol. 63, no. 2, pp. 679–701, 2014.

[200] S. Song and M. Sitti, “Soft grippers using micro-fibrillar adhesives for transfer printing,” *Adv. Mater.*, vol. 26, no. 28, pp. 4901–4906, 2014.

[201] G. . Monkman, S. Hesse, R. Steinmann, and H. Schunk, *Robot Grippers*. 2007.

[202] J. Shintake, V. Cacucciolo, D. Floreano, and H. Shea, “Soft Robotic Grippers,” *Adv. Mater.*, vol. 30, no. 29, p. 1707035, 2018.

[203] K. Autumn and A. M. Peattie, “Mechanisms of Adhesion in Geckos,” *Integr. Comp. Biol.*, vol. 42, no. 6, pp. 1081–1090, 2002.

[204] G. . Monkman, “Robot Grippers for Use With Fibrous Matreials,” *Int. J. Rob. Res.*, vol. 14, no. 2, pp. 144–151, 1995.

[205] S. Ratchev and S. Koelemeijer, *Micro-assembly technologies and Applications*. 2008.

[206] G. Monkman, “Electroadhesive microgrippers,” *Ind. Rob.*, vol. 30, no. 4, pp. 326–330, 2003.

[207] H. Demaghsi, H. Mirzajani, and H. B. Ghavifekr, “Design and simulation of a novel metallic microgripper using vibration to release nano objects actively,” *Microsyst. Technol.*, vol. 20, no. 1, pp. 65–72, 2014.

[208] J. Zhang, J. Ru, H. Chen, D. Li, and J. Lu, “Viscoelastic creep and relaxation of dielectric elastomers characterized by a Kelvin-Voigt-Maxwell model,” *Appl. Phys. Lett.*, vol. 110, no. 4, p. 044104, 2017.

[209] R. P. Marc Raibert, Kevin Blankespoor, Gabriel Nelson, “BigDog, the Rough-Terrain Quadruped Robot,” in *Proceedings of the 17th World Congress The International Federation of Automatic Control*, 2008, pp. 1–8.

[210] A. Spröwitz, A. Tuleu, M. Vespignani, M. Ajallooeian, E. Badri, and A. J. Ijspeert, “Towards dynamic trot gait locomotion: Design, control, and experiments with Cheetah-cub, a compliant quadruped robot,” *Int. J. Rob. Res.*, vol. 32, no. 8, pp. 932–950, 2013.

[211] S. Zakaria, P. H. F. Morshuis, M. Y. Benslimane, L. Yu, and A. L. Skov, “The electrical breakdown strength of pre-stretched elastomers, with and without sample volume conservation,” *Smart Mater. Struct.*, vol. 24, no. 5, p. 055009, 2015.

[212] F. Forster-Zugel, S. Solano-Arana, F. Hlug, and H. Schlaak, “Dielectric breakdown strength measurements with silicone-based single-layer dielectric elastomer transducers,” *Smart Mater. Struct.*, 2019.

[213] C. Cao and A. T. Conn, “Performance Optimization of a Conical Dielectric Elastomer Actuator,” *Actuators*, vol. 7, no. 2, p. 32, 2018.

[214] J. L. Meriam and L. G. Kraige, *Engineering Mechanics Dynamics (7th Edition)*. John Wiley & Sons, Inc., 2012.

[215] S. P. Sane, “The aerodynamics of insect flight,” *J. Exp. Biol.*, vol. 206, no. 23, pp. 4191–4208, 2003.

[216] A. J. Bergou, S. Xu, and Z. J. Wang, “Passive wing pitch reversal in insect flight,” *J. Fluid Mech.*, vol. 591, pp. 321–337, 2007.

[217] E.-F. M. Henke, K. E. Wilson, and I. A. Anderson, “Entirely soft dielectric elastomer robots,” in *Electroactive Polymer Actuators and Devices (EAPAD) 2017*, 2017, vol. 10163, p. 101631N.

[218] T. Van Truong, U. Kureemun, V. B. C. Tan, and H. P. Lee, “Study on the structural optimization of a flapping wing micro air vehicle,” *Struct. Multidiscip. Optim.*, vol. 57, no. 2, pp. 653–664, 2017.

[219] L. Zhao, Q. Huang, X. Deng, and S. P. Sane, “Aerodynamic effects of flexibility in flapping wings,” *J. R. Soc. Interface*, vol. 7, no. 44, pp. 485–497, 2010.

[220] S. Defrancesco and V. Zanetti, “Experiments on magnetic repulsion,” *Am. J. Phys.*, vol. 51, no. 11, pp. 1023–1025, 1983.

[221] A. A. Stokes, R. F. Shepherd, S. A. Morin, F. Ilievski, and G. M. Whitesides, “A Hybrid Combining Hard and Soft Robots,” *Soft Robot.*, vol. 1, no. 1, pp. 70–74, 2014.

[222] F. Amirouche, Y. Zhou, and T. Johnson, “Current micropump technologies and their biomedical applications,” *Microsyst. Technol.*, vol. 15, no. 5, pp. 647–666, 2009.

[223] H. Hauser, A. J. Ijspeert, R. M. Füchslin, R. Pfeifer, and W. Maass, “Towards a theoretical foundation for morphological computation with compliant bodies,” *Biol. Cybern.*, vol. 105, no. 5–6, pp. 355–370, 2011.

[224] S. Solano-arana, F. Klug, and H. Mö, “A novel application of dielectric stack actuators : a pumping micromixer,” *Smart Mater. Struct.*, vol. 27, p. 074008, 2018.

[225] L. Maffli, S. Rosset, and H. R. Shea, “Zipping dielectric elastomer actuators: Characterization, design and modeling,” *Smart Mater. Struct.*, vol. 22, no. 10, p. 104013, 2013.

[226] Z. Li, J. Zhu, C. C. Foo, and C. H. Yap, “A robust dual-membrane dielectric elastomer actuator for large volume fluid pumping via snap-through,” *Appl. Phys. Lett.*, vol. 111, no. 21, p. 212901, 2017.

[227] J. J. Loverich, I. Kanno, and H. Kotera, “Concepts for a new class of all-polymer micropumps,” *Lab Chip*, vol. 6, no. 9, pp. 1147–1154, 2006.

[228] K. M. Digumarti, C. Cao, J. Guo, A. T. Conn, and J. Rossiter, “Multi-directional crawling robot with soft actuators and electroadhesive grippers,” *2018 IEEE Int. Conf. Soft Robot. RoboSoft 2018*, pp. 303–308, 2018.

[229] K. Ma, P. Chirarattananon, S. B. Fuller, and R. J. Wood, “Controlled Flight of a Biologically Inspired, Insect-Scale Robot,” *Science (80-.).*, vol. 340, no. 6132, pp. 603–607, 2013.

[230] M. Hwang and A. F. Arrieta, “Input-Independent Energy Harvesting in Bistable Lattices from Transition Waves,” *Sci. Rep.*, vol. 8, no. 1, pp. 1–9, 2018.

[231] C. Cao, R. S. Diteesawat, J. Rossiter, and A. T. Conn, “A Reconfigurable Crawling Robot Driven by Electroactive Artificial Muscle,” in *2019 2nd IEEE International Conference on Soft Robotics (RoboSoft)*, 2019, pp. 840–845.